

Detecting, quantifying and interpreting irreversibility in linear systems

Grzegorz Aleksander Gradziuk



München 2022

Detecting, quantifying and interpreting irreversibility in linear systems

Grzegorz Aleksander Gradziuk

A dissertation submitted
to the Faculty of Physics at the
Ludwig–Maximilians–Universität München
for the degree of
DOCTOR RERUM NATURALIUM



Munich, 1st April 2022

First referee: Prof. Dr. Chase Broedersz
Second referee: Prof. Dr. Joachim Rädler
Day of the oral exam: 25th May 2022

Zusammenfassung

Irreversibilität ist dem Leben inhärent und charakteristisch für alle Nichtgleichgewichtsprozesse. Aus physikalischer Perspektive gesehen, steht diese Irreversibilität in einer engen Verbindung mit der Entropieproduktion, der Energiedissipation und der Struktur der Nichtgleichgewichtsfluktuationen. Wir sind jedoch immer noch dabei herauszufinden wie die Leistungsfähigkeit biologischer Prozesse von deren Energieverbrauch abhängt. Ebenso ist es rätselhaft, wie die aus der Energiedissipation auf einem mikroskopischen Niveau entstehende Irreversibilität durch alle Längenskalen bis hin zur Makrowelt propagiert. Wegen ihrer wichtigen Rolle haben Irreversibilität und die Dissipation ein großes wissenschaftliches Interesse erregt und es wurden vielfältige Messmethoden und mathematische Maße entwickelt um sie zu erkennen und zu quantifizieren.

In dieser Dissertation entwickeln wir Methoden zur Berechnung verschiedener Irreversibilitätsmaße in linearen Systemen mit externer Antreibung in der Form eines dynamischen Rauschens oder einer nicht-konservativen Kraft. Diese Maße charakterisieren die Irreversibilität auf unterschiedlichen Detailebenen. Vom zellulären Cytoskelett und von Biomembranen inspiriert, wenden wir unsere Methoden auf viskoelastische Netzwerke an. Wir diskutieren, ob eine Messung einfacher Irreversibilitätsmaße in solch einem Netzwerk die Eigenschaften der zugrundeliegenden externen Antreibung wie Amplitude, Momente oder Korrelationszeit enthüllen kann. Gleichzeitig sagen wir vorher, dass die gemessene Irreversibilität von einem im Netzwerk eingebettet Tracer-Paars im Durchschnitt schnell mit der Distanz zwischen den beiden Tracern abnimmt. Der Zusammenhang der Irreversibilität von der Distanz der beiden Tracer folgt dabei einem Potenzgesetz.

Abschließend zeigen wir, dass ein grobes Irreversibilitätsmaß, das komprimierte Information über die Struktur des Wahrscheinlichkeitsstroms enthält, die irreversibelsten Komponenten der Dynamik identifizieren kann. Diese Komponenten könnten dann potenziell zur Rekonstruktion von charakteristischen Moden der irreversiblen Dynamik verwendet werden. Zum Ende wenden wir diese Methoden dann als ersten Schritt einer unüberwachten Analyse von Zeitraffermikroskopie-Daten an.

Summary

Irreversibility is inherent to life and all nonequilibrium processes. From a physical perspective this irreversibility has been proved to be tightly related to the entropy production, energy dissipation, and the structure of nonequilibrium fluctuations. However, we are still building our understanding of how the performance of the vital biological processes hinges upon the level of energy consumption. Similarly, it is a puzzle how the irreversibility generated by energy dissipation at the microscopic level propagates across different length scales, all the way up to our macroscopic world. Given their important role, irreversibility and dissipation have been sought after and multiple techniques and measures have been introduced to detect and quantify them.

In this dissertation we develop a framework for calculating various measures of irreversibility in linear systems with external driving in form of dynamical noise or non-conservative forces. These measures reflect the irreversible behaviour at varying level of detail. We apply our framework in the context of driven viscoelastic networks inspired by the cytoskeleton, or biological membranes. We discuss whether a measurement of simple irreversibility metrics in such a network could reveal properties of the underlying driving, such as the amplitudes, the moment (monopoles vs. dipoles), or the correlation times of the active forces. At the same time we predict that the irreversibility displayed by a couple of tracers embedded in the network should on average decay rapidly as a power law in function of the distance between the tracers.

Finally, we demonstrate that a coarse grained measure of irreversibility that encodes simplified information about the structure of the probability currents could be used to identify the most irreversible components of the dynamics. These components could then potentially be used to reconstruct stereotypical irreversible modes of the dynamics. We then use this framework as a first step in an inference method for unsupervised analysis of time-lapse microscopy data.

Contents

Zusammenfassung	v
Summary	vii
1 Introduction	1
1 The origin of irreversibility	2
2 Irreversibility-dissipation relations and measurements	5
3 Dissipation setting bounds for biological processes	7
2 Mathematical framework	11
1 Classification of random processes	11
2 Descriptions for continuous state-space dynamics	13
2.1 Langevin equation	13
2.2 Fokker-Planck equation	15
2.3 Path integral formalism	16
3 Measures of irreversibility	18
3 Interpreting Irreversibility	23
1 Scaling laws in driven networks	24
2 Finding the most irreversible components	27
4 Outlook	31
Bibliography	35
Related Publications	47
A Nonequilibrium scaling behavior in driven soft biological assemblies	57
B Scaling behavior of nonequilibrium measures in internally driven elastic assemblies	69
C Irreversibility in linear systems with colored noise	83
D Learning the non-equilibrium dynamics of Brownian movies	97
Acknowledgements	123

Chapter 1

Introduction

*Nothing can ever happen twice.
In consequence, the sorry fact is
that we arrive here improvised
and leave without the chance to practice.
- Wisława Szymborska*

While the poet surely refers to something way deeper than the subject of this thesis, let us use our readers' rights to make our own interpretation. "Nothing can ever happen twice" – indeed, any process in nature is subject to fluctuations, and no two realisations of what we would classify as "the same process" will ever really be the same. Typically, the smaller the scale we look at, the larger the role of fluctuations. Take a ball and try throwing it at a target – after a bit of practice, as long as you throw the ball with roughly the same velocity in roughly the same direction, it will always hit the target. Now, go down the scale by 8 orders of magnitude and imagine you're responsible for delivering a cargo from the centre of a cell to its peripheries. First, your motion is strongly damped by the surrounding medium. Second, you're constantly being pushed back and forth by thermal fluctuations. In order to maintain a directed motion you must continuously consume energy. The more directed and regular you want your motion to be, the more energy you need to spend to counteract the random fluctuations. This and many other vital tasks are unceasingly performed inside our cells with a stunning precision, even though "we arrive here improvised". Indeed we do – the improvisation has continued for over 4 billion years, during which we, our building blocks, and surrounding forms of life evolved to efficiently turn energy into order and time-directed processes. This directionality, or "irreversibility", is typical of life and in general of processes that involve dissipation and transfer of energy. The degree of irreversibility and its explicitness depends on the process and on the scale at which we observe it. Our own life is manifestly irreversible when viewed on the time scale from "arriving" to "leaving". Even on a microscopic scale the dynamics can be clearly irreversible, as it is for a kinesin motor that under natural conditions never takes a step back. However, as soon as thermal fluctuations become strong enough, the time asymmetry of a process becomes less evident and the question of detecting and quantifying irreversibility gains relevance.

In this thesis we mathematically analyse such irreversible processes modelled as linear stochastic systems driven by dynamical noise with certain characteristics. The noise contains the inevitable thermal component and an active part that can produce irreversible dynamics. We derive formulas for a family of measures of irreversibility, relating the potential outcomes of a measurement to the properties of the underlying driving. We also develop a framework for inferring the irreversibility of the dynamics from time-lapse microscopy data. As a byproduct, we find a way to identify the most irreversible components of the dynamics, which could potentially reveal the stereotypical irreversible behaviour.

The thesis is structured as follows: in the introduction we first superficially discuss the origin of irreversibility based on a mechanical toy model. Then, in section 1.2 we review the established relations between the structure of fluctuations, irreversibility and heat dissipation, and discuss how these relations can be used to detect nonequilibrium behaviour and estimate the rate of energy consumption. The significance of the heat dissipation for the performance of biological processes is then discussed in section 1.3.

In chapter 2 we introduce the principal mathematical frameworks used to describe stochastic processes. We present a set of measures of irreversibility that characterize the irreversibility at various levels of detail. Finally, in chapter 3 we review our main results. The first set of the results concerns a model of actively driven viscoelastic network. We predict a scaling behaviour of certain measures of irreversibility as a function of distance. The specific functional form depends on the dimensionality of the system and the properties of the active driving. The second result is a dimensionality reduction scheme, designed to select the components of the dynamics that exhibit the strongest irreversibility. This reduction scheme was employed as the first step of the framework for analysing time-irreversibility of time-lapse microscopy data. The last chapter is a compilation of the publications representative of the work performed during my doctoral study and discussed in this thesis.

1 The origin of irreversibility

Time irreversibility is something equally common and unexpected in the world we live in. It definitely is common - otherwise, we probably wouldn't be using two different words, "past" and "future", when talking about "not now". Standard empirical examples of irreversibility in daily life include cells dividing, but never merging into one, glass breaking into pieces, but never spontaneously self-assembling back into one piece, or rain always falling down. These standard observations must be confronted with the fact that the equations of motion, at least the classical ones describing the world at our scales, are time reversible. This means that for any process that satisfies the equations of motion its time reversed counterpart also satisfies the equations of motion. In other words, there's nothing in the dynamics that would fundamentally disallow a broken glass to come together back into one piece.

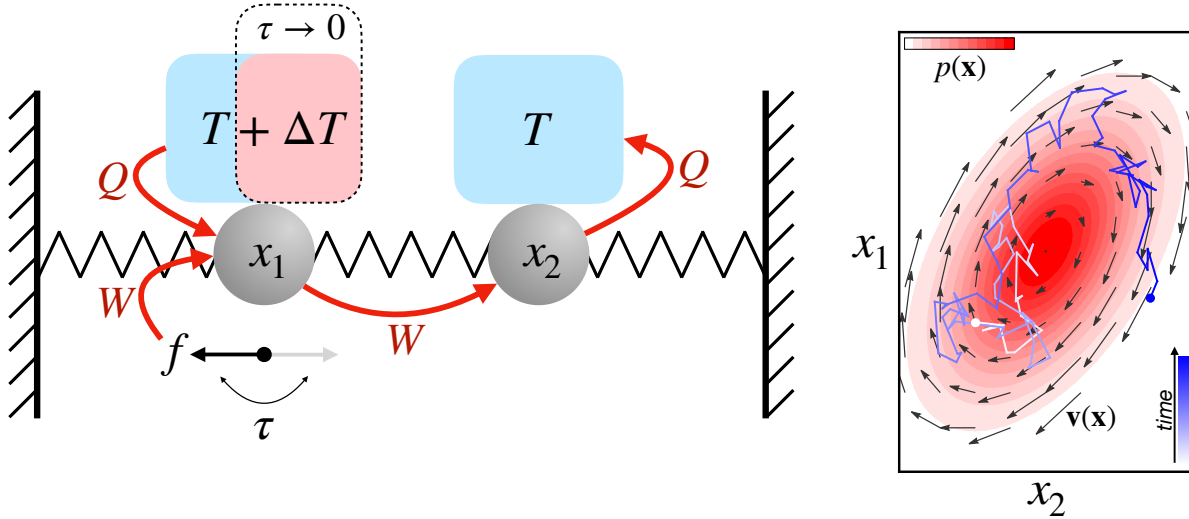
The origin of this irreversibility is not fully understood and we won't attempt a profound explanation either. One of the explanations makes reference to some special initial

conditions of the universe, but without specifying what these initial conditions should be like and why they would ever be so, it's difficult to consider this explanation satisfactory. Another explanation is based on the concept of entropy, first developed phenomenologically by Clausius and later redefined by Boltzmann, who gave a statistical meaning to it. The statistical meaning refers to the number of microstates that correspond to a considered macrostate, or equivalently the amount of information about the system that is missing. The second law of thermodynamics states that the entropy of an isolated system cannot decrease, therefore specifying the direction of the "arrow of time".

The word "irreversible" may suggest that during the process the system changes qualitatively, as in the standard example in which a wall dividing a container is removed and all the gas molecules initially confined to the left half spread over the entire container. However, there is a wide class of systems which exhibit irreversible dynamics despite not changing over time in a statistical sense. These are called non-equilibrium steady states and are precisely the class of systems we study in this thesis. The notion of "steady state" itself has a strong potential for leading to a confusion. Namely, the "steady state" refers to the state of our knowledge about the system and not the state of the system itself. A system at a steady state keeps transitioning through the configuration space and can be in any configuration at any time. The irreversibility then manifests itself in a typical order in which the system transitions between the states. What is "steady" is our knowledge about the system expressed in terms of the probability (density) $p(\mathbf{x})$ for the system being in configuration \mathbf{x} . The steady state is reached when the correlations between the current state of the system and its initial conditions vanish.

Let us now consider a toy model that well illustrates the idea of non-equilibrium steady states. Our toy model consists of two harmonically coupled beads immersed in a viscous fluid. As common in biophysical applications, we assume the Reynolds number to be very small and the motion of the beads to be overdamped. The beads are coupled to a thermal bath at temperature T that keeps them fluctuating around their average position. The motion of the beads is completely reversible - when presented with a time trajectory of the beads and its time-mirrored copy, one can't guess which one is the original one with probability higher than 0.5. Now, on top of the thermal motion someone applies an external force to one of the beads. The force has a constant amplitude f and at a certain rate τ^{-1} randomly flips the direction between left and right. The system is no longer in thermal equilibrium. The randomly flipping force keeps changing the potential landscape, performing work on the driven bead. The motion of the beads is no longer time-reversible. The driven bead is now more motile and the passive bead tends to follow the displacements of the driven one. This leads to an on average counterclockwise motion through the configuration space. With this in mind, given a sample trajectory, one can now distinguish with a higher probability between the original dynamics and the time-mirrored ones. Of course, there's still some probability of guessing incorrectly - whatever trend we see, it can be just a misleading coincidence of the thermal fluctuations, but the longer the analysed trajectory, the less likely it is for such a coincidence to occur.

As the next step consider a limit in which the force flips very fast compared to the relaxation times of the beads. One can construct such a limit mathematically by simulta-



neously increasing the force amplitude and the flipping rate (for details see Sec. 4.C). In this limit one obtains a driving in form of a Gaussian white noise, which is mathematically equivalent to the driven bead being coupled to a heat bath at an effective temperature $T + dT$. It can be anticipated and shown that the irreversible cycling behaviour prevails in the white noise limit. The higher the temperature difference, the more pronounced the irreversible dynamics. Moreover, treating the driving as an effective temperature offers an interpretation of the irreversibility in terms of a heat flow. The driven bead extracts heat from the warmer heat bath and transfers it to the other bead, which then dissipates the heat into the cooler heat bath [1, 2]. In fact, analogous models have been considered in the past to study the heat flow in a harmonic crystal [3, 4, 5].

In both cases, with the random external force and with a temperature difference, the system reaches a steady state - the probability for finding the beads at certain positions converges to a fixed distribution. At the same time the beads' positions exhibit irreversible dynamics that reflect the non-equilibrium nature of the system. The degree of irreversibility is tightly related to the heat flow and the amount of dissipated heat. This relation will be the topic of the following section.

2 Irreversibility-dissipation relations and measurements

Using a term like nonlinear science is like referring to the bulk of zoology as the study of non-elephant animals.

- Stanisław Ulam

An analogous quote about nonequilibrium physics is attributed John von Neumann. Both statements point at the awkwardness of using a name like "non-special" for something standard and diverse. Nonlinear systems are standard and diverse, and so are nonequilibrium dynamics. To start with, fairly all that's related to life is out of thermal equilibrium and it is the nonequilibrium together with nonlinearity that give rise to the observed richness of the life phenomena.

Given this richness, it may seem hopeless to search for universal principles [6] that would guide or constrain all the nonequilibrium processes, just as it would be hopeless, if not ridiculous, to look for common features shared by all the non-elephant animals. This task, however, becomes less absurd when we restrict ourselves to a subclass of non-elephant animals, such as birds, reptiles, or insects. Similarly, when considering certain subclasses of nonequilibrium systems it becomes easier to recognize the structure hidden underneath the details of the dynamics. In fact, over the last century the search for such universal principles in nonequilibrium systems has led to uncovering a multitude of rules, relations and bounds with various ranges of applicability. The field has flourished over the last decades, the results are constantly extended to ever wider classes of systems and further development can be expected in the following years. Here, we briefly review the existing results, with special emphasis on those relating the statistics of the fluctuations, dissipated heat and irreversibility of the dynamics.

Linear regime

Naturally, the first relations putting constraints on the nonequilibrium processes were discovered for the case of weakly driven systems, for which the response of the system is linear in the driving forces. First of the results concerns structure of the Onsager coefficients L_{ij} that describe the linear relations between thermodynamic forces and corresponding fluxes. Onsager demonstrated [7, 8] that the time reversibility of equilibrium dynamics imposes certain symmetries on the coefficients L_{ij} , known as Onsager reciprocal relations.

Another classical result, called the Fluctuation-Dissipation theorem [9], relates the spectrum of equilibrium fluctuations of a system with its temporal response to a weak external driving:

$$S_x(\omega) = \frac{2k_B T}{\omega} \text{Im}[\chi_x(\omega)]. \quad (1.1)$$

Here $S_x(\omega)$ is the power spectrum of position trajectories, T is the temperature and $\chi_x(\omega)$ the position response function in frequency space. Experimentally observed deviations from this relation have been used as a litmus paper for nonequilibrium activity [10, 11, 12, 13, 14, 15]. Apart from just detecting nonequilibrium, the degree and structure

of such deviations can deliver information about the properties of the active forces and about heat dissipation [16, 17, 18, 19], as will be discussed later on.

Beyond linear response

The end of the last century was marked by the discovery of fluctuation theorems that directly pointed at the stochastic nature of thermodynamic quantities, such as work, for small systems. One of the pioneering results, the Jarzynski equality [20], provides a relation between the free energy difference between two equilibrium states ΔF and the statistics of the work W done when moving the system between these states:

$$\exp(-\Delta F/k_B T) = \langle \exp(-W/k_B T) \rangle, \quad (1.2)$$

from which the classical inequality $\Delta F < \langle W \rangle$ follows. Importantly, this result did not require any assumptions about the external driving being weak. Apart from offering a useful tool for measuring the free energy landscape [21, 22, 23, 24], this result gave momentum to the development of Stochastic Thermodynamics [25, 26] and paved the way for the discovery of a family of fluctuation theorems. These theorems, initiated by Evans' et al. studies of the entropy production distribution [27] and then continued by others [28, 29, 30, 26], go a step further than Jarzynski equality and put constraints on the structure of the fluctuations of thermodynamic quantities. (For a review including experimental verifications see [31, 32, 26].) One of the most impactful theorems, the Crooks fluctuation theorem [33, 34], relates the entropy production, and so the dissipated heat, with the irreversibility of the dynamics. In its most general form that originates directly from the principle of microscopic reversibility [33] the Crooks theorem relates the probability of observing a time reversed trajectory $\tilde{P}[\tilde{X}(t)]$ with the entropy produced along the forward trajectory $s[X(t)]$.

$$\ln \left(\frac{P[X(t)]}{\tilde{P}[\tilde{X}(t)]} \right) = s[X(t)] \quad (1.3)$$

To obtain the average entropy production, or entropy production rate, one simply has to average the left hand side of Eq. (1.3) with respect to $P[x(t)]$. This gives an expression reminiscent of the Kullback-Leibler divergence, which allows to interpret this measure of irreversibility in terms of how easy it is to distinguish a forward trajectory from a reversed one [35]. Not surprisingly, if $X(t)$ does not include all the relevant degrees of freedom, the available information is reduced, the distinction between forward and backward more difficult, and Eq. (1.3) provides only a lower bound to the total entropy production.

The entropy production rate, expressed in terms of trajectory probabilities, as in Eq. (1.3), is considered to be the most general measure of irreversibility. Methods for estimating steady state entropy production that derive directly from Eq. (1.3) have been developed and applied to systems with discrete [36, 37, 38] and continuous [39, 40] state space, as well as for nonequilibrium dynamics of fields [41, 42]. The most recent variants of these methods employ artificial neural networks [43].

Alternative ways to estimate dissipation are based on expressing the entropy production rate as $\dot{s} \sim \langle \text{force} \times \text{velocity} / \text{temperature} \rangle$, which in terms of a Fokker-Planck-like

description can be rewritten in a form $\dot{s} \sim j^2 D^{-1}$, with j the probability current and D the diffusion constant (for details see Sec. 2.3). While equivalent to the expression based on Eq. (1.3) for Markovian systems with all degrees of freedom available, a difference can be seen in case of dynamics with hidden degrees of freedom. In [38] it is demonstrated how positive entropy production can be inferred despite vanishing probability currents. Nevertheless, the formula based on the probability currents can also be successfully applied to infer entropy production [44, 45], especially when reinforced with smart inference of the force, velocity and diffusion fields [46, 47].

Finally, there exist an method for quantifying the dissipation rate, that does not make any direct use of irreversibility. It employs the Harada-Sasa relation [16, 17] which remarkably binds the dissipated heat to the deviations from the Fluctuation-Dissipation theorem (Eq. (1.1)). This relation has been verified experimentally [48] and applied to study simple biological systems such as molecular motors [18, 19]. The applicability of this method is limited by the necessity to measure the linear response function for a range of frequencies, in contrast to the aforementioned non-invasive methods.

The relations between the structure of the fluctuations, irreversibility and entropy production rate offer a set of ways to experimentally quantify the amount of heat dissipated in a driven mesoscopic system. This energy dissipation is crucial for maintaining processes in living system, but the way these processes hinge upon the level of energy consumption turns out to be a multifaceted problem.

3 Dissipation setting bounds for biological processes

Vital biological processes that break the time-reversal symmetry setting the direction of the arrow of time inevitably require constant supply of energy. The necessity to dissipate heat is obvious for example in case of a molecular motor like kinesin that drags a cargo through a viscous medium. The directed motion with an average velocity v results in a heat dissipation proportional to v^2 , due to counteracting the drag force [49]. Because of their manifest non-equilibrium dynamics, relative simplicity and the possibility to experimentally investigate isolated single motor molecules, molecular motors became a model system for studying active dynamics [50, 51]. The analogy between molecular machines and classical engines [26] raised questions about the efficiency of molecular motors, which was studied at maximal power [52], as a function of the applied load [53], and considering different definitions of the efficiency [49]. An experimental study of a rotary molecular motor F₁-ATPase revealed that the free energy coming from ATP hydrolysis is almost entirely transferred to the rotational motion of the motor [18]. This estimate was made based on application of the Harada-Sasa relation [16, 17]. In contrast, similar approach applied to kinesin-1 suggested that around 80% of the consumed energy is dissipated internally by the motor [19].

In fact, it turns out to be a more general rule that the energy is not simply invested in completing a task, but also in achieving certain speed or accuracy. A classical example is that of kinetic proof reading [54]. This mechanism, first suggested by Hopfield, aims

to explain the exceptionally low error rates observed in protein synthesis ($\sim 10^{-4}$) or DNA replication ($\sim 10^{-9}$) [54]. Similar models of kinetic proof reading were considered in context of a trade-off between error, speed and dissipation [55]. Such models are based on a reaction network with reaction rates biased by an external energy source. Of course the pure dissipation would not be enough, if not accompanied by clever architecture of the reaction network. The reaction networks behind crucial biological processes are believed to be designed in a way that makes the performance robust to changes in the concentrations of the substrates [56].

Dissipation and robustness also plays a central role in reaction networks responsible for chemical sensing, making a biological device sensitive to changes in concentration of chemicals over a wide range. Studies on chemical sensing, pioneered by Berg and Purcell [57], showed that such cellular computation hinges upon the energy consumption [58], and revealed trade-offs between energetic costs, speed and accuracy of sensory adaptation [59]. The principles behind chemical sensing were further connected to cell signaling [60], or the kinetic proofreading [61].

Perhaps one of the most extravagant examples of how dissipation bounds biological processes is that presented in [62]. There the relation between dissipation and irreversibility was employed to estimate the amount of energy needed for bacterial replication. Those results suggest that the actual energy budget of *E. coli* is only at most 6 times larger than the minimal energy required to maintain and replicate bacteria at the rate observed in nature.

Finally, results were obtained for how energy consumption is related to the precision of biochemical oscillations [63, 64] and so called Brownian clocks [65] - cyclic reaction networks capable of measuring time. It was shown that in such systems the necessary rate of energy input diverges with decreasing target precision, which relates to a series of theorems discovered in the recent past.

Thermodynamic uncertainty relations

Recent years have witnessed the advent of a family of relations that bound the fluctuations of a generalized accumulated current by the amount of produced entropy [66]. The generalized accumulated currents can represent diverse quantities such as the distance travelled by a kinesin molecular motor, the number of produced molecules, or the entropy itself. These thermodynamic uncertainty relations, first proposed in [67] and subsequently proven [68] and generalized to finite times [69, 70], typically take the following form:

$$\frac{\text{Var}[j_\tau]}{\langle j_\tau \rangle^2} \geq \frac{2k_B}{s_\tau}, \quad (1.4)$$

where j_τ is a generic current integrated over time τ , and s_τ the total entropy produced in the time interval τ . The origin of the uncertainty is twofold: it comes partially from the fluctuations of the direction in which the steps of a process are made, and partially from the distribution of waiting times between the steps. [66]. While the unidirectionality of a

process can be augmented by increasing the energy input, the fluctuations due to random waiting times cannot be tempered this way [71].

It has been quickly recognized that apart from setting general theoretical bounds for precision the thermodynamics uncertainty relations can be used as a tool for inference. For example, it allows one to put an estimate on the efficiency of a molecular motor based on its kinetics only [72]. Furthermore, a comparison between current fluctuations and its mean offers a lower bound to the dissipated heat [2]. This idea was further refined by noting that the inequality in Eq. (1.4) can be improved for short [69] and saturated for infinitesimal times [73]. The most recent variants of this method employ machine learning techniques [74] also in case of time dependent dynamics [75].

From a biological perspective it is relevant to ask how constraining these thermodynamic uncertainty relations are in practice. For example, it is estimated that molecular motors consume 2.5-10 times more energy than the necessary minimum implied by the uncertainty relations [76, 77]. While this could at first sight suggest that the performance of such motors is far from optimal, one should keep in mind that correct operation of a motor is just one out of countless tasks that a living cell needs to take care of. In fact, given two generalized currents, they cannot simultaneously saturate their corresponding bounds of type Eq. (1.4) [78]. To address the fact that nature typically needs to simultaneously optimize several, somewhat correlated processes, a multidimensional variant of the thermodynamic uncertainty relation was developed [79, 78]. These advances combined with recent work [77] show that accounting for the correlations in the considered currents yields improved thermodynamic bounds on the entropy production. With this in mind, given the complexity of biological systems, it may turn out tricky in many cases to disprove or argue for optimality of a certain mechanism. Nevertheless, the domain of thermodynamic uncertainty relations keeps developing in a way similar to how the fluctuation theorems were evolving in the past, and one can expect tighter bounds and more widely applicable relations to appear in the near future.

Chapter 2

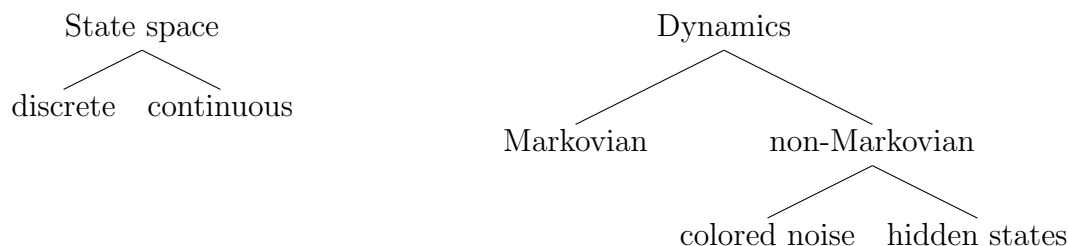
Mathematical framework

In this chapter we first present a classification of stochastic processes based on the structure of the state space and the way in which a system transitions between the states. Next, we restrict the discussion to systems with continuous state space and briefly review three mathematical frameworks employed to describe the stochastic dynamics of such systems. Finally, we give expressions for different measures of irreversibility derived using the aforementioned frameworks.

1 Classification of random processes

Before we proceed to classifying the stochastic processes that can describe a physical system, let us emphasise that associating a physical system with a certain class is relative and really depends on the level of description we use. To begin with, within classical physics no process is truly random and all the stochasticity originates from our ignorance of the initial conditions, or the dynamics of some "hidden" degrees of freedom that couple to the observed subsystem. The canonical example here would be the random motion of a Brownian particle resulting from the collisions with invisible water molecules.

Based on the structure of the phase space and the way in which the system transitions between the states we can classify random processes as follows.



From a fundamental point of view, physical processes represent continuous motion through space in continuous time, which naturally suggests the use of a continuous state space. However, it often happens that the dynamics consist of series of fast transitions

between which the system spends a long time dwelling in limited subregions of the state space. It can be, that while the system keeps transitioning within a subregion, for us – subjective observers – it stays fixed in a macrostate defined by our idea of what’s relevant. Such a discretised perspective is applied, for example, to the motion of a kinesin motor, where depending on our level of description, the transitions can represent consecutive steps of the motor, or more detailed conformational changes of the molecule. This way of describing the dynamics as transitions within a network of states was the starting point for many entropy inference methods and thermodynamic uncertainty relations discussed in Secs. 1.2, 1.3.

Sometimes the use of state space other than discrete may even seem ridiculous, as in the case of population dynamics, where we are interested in the number of individuals of certain species. Amusingly, in this case further coarse graining may lead us again to a continuous state space description, when considering the dynamics of large populations.

Regarding the way the system transitions between the states, the key criterion seems to be the Markovianity. A system is called Markovian, or memoryless, if the present state gives us the best possible information about the future and our predictions can’t be improved by any information about the past. Slightly more formally, if \mathbf{x} is the state of the system and $p(\mathbf{x})$ the probability distribution, then $p(\mathbf{x}_{\text{future}} | \mathbf{x}_{\text{now}}, \mathbf{x}_{\text{past}}) = p(\mathbf{x}_{\text{future}} | \mathbf{x}_{\text{now}})$. Non-Markovianity typically results from lack of access to degrees of freedom that form an important part of the dynamics. A silly, yet transparent example could be an underdamped Brownian motion, where we only track the position of a particle. Knowing just the present position of the particle, there’s little we can say about its future. However, knowing where the particle was a while ago, we can estimate its velocity and make a better guess for where it’s going to go further. A more practical example would be the dynamics of a particle diffusing in a viscoelastic medium, such as a polymer network. There, the motion of the particle is coupled to the dynamics of the network, and eliminating the network from our description leads to an effective equation with a memory kernel and with thermal noise correlated in time.

In this thesis we will focus exclusively on dynamics in continuous state space. The mathematical frameworks used to describe such systems are reviewed in the following section 2.2. We will face two types of non-Markovian effects. In Secs. A, B and D the non-Markovianity results from tracking only a few nodes, or a part of a full network. In Sec. C we will be dealing with more intrinsically non-Markovian systems – we will consider random external driving in form of a time-correlated dynamical noise. We should note that this distinction between origin of non-Markovianity is rather subjective, since one can also view the dynamics of the noise as a hidden degree of freedom.

2 Descriptions for continuous state-space dynamics

*You can never understand one language
until you understand at least two.*
- Geoffrey Willans

In the realm of stochastic processes various languages are used to talk about the unpredictable. And even though all these languages describe the same dynamics with its uncertainties and statistics, each of them takes a different perspective and opens up a different way of thinking about a problem. However, learning a set of languages offers more than just a deeper understanding of stochastic processes. Typically, the choice of particular language in a given context is not so much a matter of taste, but rather of convenience – a certain result may be trivial to obtain within one description, while seemingly inaccessible within another. This suitability of different languages for approaching different classes of problems explains why multiple equivalent descriptions remain in use and why the following subsections are dedicated to discussing them in detail. Specifically, we present the three most commonly employed frameworks in their basic form with possible extensions:

- Langevin framework - using a random variable for the driving force in the equation of motion
- Fokker-Planck or Smoluchowski framework - focusing on the dynamics of the probability density
- Path integral framework - assigning probability to every possible realisation of the dynamics

All three frameworks are used in deriving the expressions for various measures of irreversibility presented in section 2.3. For a comprehensive overview of these frameworks in the setting of Brownian motion we refer the reader to [80, 81].

2.1 Langevin equation

The framework pioneered by Paul Langevin is the oldest of the three presented here. In his 1908 paper [82, 83] Langevin first briefly discusses the successful explanation of Brownian motion and derivation of the diffusion coefficient by Einstein [84] and Smoluchowski [85]. He then claims to have corrected Smoluchowski's result which now coincided with the one obtained by Einstein, and finally proceeds to what he himself refers to as "an infinitely more simple demonstration by means of an entirely different method". Nowadays we can identify the core of his "entirely different method" as the first stochastic differential equation ever written down, which later served as a cornerstone for an entire new branch of science. Once again the pursuit of simplicity paid off.

In its basic version the Langevin equation takes the following form:

$$\dot{\mathbf{x}}(t) = \mathbf{f}(\mathbf{x}) + \sqrt{2\mathbf{D}}\boldsymbol{\xi}(t). \quad (2.1)$$

Here, $\mathbf{x}(t)$ is the position in phase space at time t , which for a mechanical system can represent velocity (as in Langevin’s paper), position (in overdamped case), or both. In general, however, it can represent other quantities varying randomly in time, such as voltage, temperature or stock price. The term $\mathbf{f}(\mathbf{x})$ is the deterministic driving experienced by the system at state $\mathbf{x}(t)$. For Langevin this deterministic force was the drag force proportional to the velocity of the Brownian particle. Finally, $\sqrt{2\mathbf{D}}\boldsymbol{\xi}(t)$ represents the random force, also called the dynamical noise, satisfying

$$\langle \xi_i(t)\xi_j(t') \rangle = \delta_{ij}\mathcal{G}(t-t'). \quad (2.2)$$

The matrix \mathbf{D} encodes the amplitudes and correlations between the random forces acting on different degrees of freedom. In case of Brownian motion \mathbf{D} has the interpretation of a diffusion matrix. The function $\mathcal{G}(t)$ represents the temporal correlations in the noise, which in case of the thermal noise are often assumed to be delta-peaked, that is $\mathcal{G}(t-t') = \delta(t-t')$. Such an assumption was also implicitly present in Langevin’s demonstration, where he argued that $\langle \mathbf{x}(t)\mathbf{f}^\top(t) \rangle = 0$. In general the time correlations can of course be long lived and the functional form may differ for different degrees of freedom, requiring us to specify $\mathcal{G}_{ij}(t-t')$ for all pairs of degrees of freedom i, j separately. In any case one should keep in mind that \mathbf{D} and \mathcal{G} alone do not uniquely define the dynamics of the noise, as discussed in Sec. C.

Before reviewing the possible extensions of Eq. (2.1), let us ponder a bit upon the philosophy behind the Langevin approach. In this approach the random dynamics is defined through an ordinarily looking equation of motion with a time-dependent driving force $\boldsymbol{\xi}(t)$. Although the force $\boldsymbol{\xi}(t)$ is defined to be a random variable, at the level of the equation of motion it can be treated as an ordinary deterministic function. This aspect makes Langevin approach perfectly suited for numerical simulations, where an ensemble of randomly generated force protocols $\{\boldsymbol{\xi}(t)\}$ can be used to create an ensemble of trajectories $\{\mathbf{x}(t)\}$, from which the desired statistics can be obtained. Another advantage of the Langevin approach is the ease with which formal calculations can be performed. For linear Langevin equations one can write the formal solution for $\mathbf{x}(t)$ in terms of the noise protocol $\boldsymbol{\xi}(t)$ and then calculate moments and correlations of \mathbf{x} referring to the statistics of $\boldsymbol{\xi}$. We shall use this strategy extensively in section 2.3.

In the Langevin framework all the difficulties and peculiarities of the stochastic process are hidden under the hood. In fact, a student with no experience in stochastic processes would typically feel comfortable about Langevin-like explanation of the Brownian motion. Of course the same student can easily get confused, when confronted with the fact that the white noise used as the random force is zero on average, but has an infinite amplitude at all times – enough to be called a ”mathematical freak” [86]. This and other peculiarities had to wait 15 years for Norbert Wiener to give them more mathematical rigour [87, 88], and another 20 years for Kiyosi Ito and later Ruslan Stratonovich to build proper stochastic calculus as we know it [89]. From a physical perspective the white noise becomes much more intuitive, when viewed as a limit of random functions with decreasing, but finite time correlations.

Below we list possible extensions and generalizations of the Langevin equation.

Multiplicative noise

The diffusion matrix can in general be a function of the position in phase space, $\mathbf{D}(\mathbf{x})$. A noise defined in this way is then called "multiplicative" as opposed to "additive" for $\mathbf{D}(\mathbf{x}) = \text{const}$. Such a scenario would be realised for instance in case of a particle diffusing in a temperature gradient. Allowing for multiplicative noise leads to additional subtlety in case of the white noise - the Langevin equation is no longer unambiguous and one needs to additionally specify the integration convention. We refer the reader to [89] for more details.

Memory kernel

The deterministic force term can include a dependence on the values of \mathbf{x} in the past and not only the instantaneous value. Up to linear order such deterministic force takes the form $\int_{-\infty}^t \Gamma(t-t')\mathbf{x}(t')dt'$ as in the generalized Langevin equation derived by Mori [90]. $\Gamma(t)$ is called the memory kernel and can be used to describe the retarded response of the medium in case of diffusion in a complex medium.

Dynamics of fields

The Langevin framework can be naturally extended to describe the dynamics of fields. Then the noise function gains dependence on the position in space, $\xi(\mathbf{x}, t)$, and one needs to specify both temporal and spatial correlations. This generalisation is commonly used in the theory of interfacial growth [91], for example in the form of Edwards-Wilkinson or KPZ equations. The Edwards-Wilkinson equation could be of special interest to us – with some adjustments of the noise correlator it could represent a continuous limit of the models considered in Secs. A, B and C.

2.2 Fokker-Planck equation

The central object in the Fokker-Planck language is the conditional probability density $p(\mathbf{x}, t | \mathbf{x}_0, t_0)$ of finding the system in state \mathbf{x} at time t , given it's initial state \mathbf{x}_0 at time t_0 . This is radically different from the Langevin approach, which specified the equation for random trajectories. In the Fokker-Planck approach there are no trajectories. Moreover, while the dynamics of the system itself is stochastic, the time evolution of the probability density is fully deterministic. Specifically, for a system that evolves according to a Langevin equation Eq. (2.1) with white noise, the time evolution of the probability is given by

$$\partial_t p(\mathbf{x}, t) = -\partial_i [f_i(\mathbf{x})p(\mathbf{x}, t)] + \partial_i \partial_j D_{ij} p(\mathbf{x}, t), \quad (2.3)$$

where we omitted the initial condition to simplify the notation. This equation, called the Fokker-Planck equation, bears striking resemblance to the diffusion equation. In fact it was this similarity that allowed Smoluchowski to write down an equation for the evolution of the probability density in case of an overdamped particle in a potential [92]. He noticed that the probability density for the position of a single diffusing particle should follow the

same dynamics as particle density field, leading to the diffusive term $\partial_i \partial_j D_{ij} p(\mathbf{x}, t)$. The remaining term, $-\partial_i [f_i(\mathbf{x}) p(\mathbf{x}, t)]$, corresponds to particles being convected by a deterministic velocity field $f_i(\mathbf{x})$.¹ Although these original arguments make direct reference to the described system - a particle diffusing in a potential, the equivalence between Eq. (2.1) and Eq. (2.3) can be proved rigorously in general as long as the dynamical noise is white. The equivalence persists in the case of spatially varying diffusion tensor - when replacing \mathbf{D} with $\mathbf{D}(\mathbf{x})$, Eq. (2.3) is equivalent to Eq. (2.1) interpreted in the Ito convention. In case of colored noise the dynamics is not Markovian and the evolution of the probability density can no longer be described by Eq. (2.3). Under certain assumptions it is possible, however, to formulate a generalized Fokker-Planck equation that captures the non-markovian effects. For a thorough review, we refer the reader to [93].

As can be anticipated from the relation to the diffusion equation, the Fokker-Planck equation can be interpreted as a continuity equation for the probability density. Defining $\mathbf{j}(\mathbf{x}, t)$ as the probability current, Eq. (2.3) can be rewritten as

$$\partial_t p(\mathbf{x}, t) = -\nabla \cdot \mathbf{j}(\mathbf{x}, t), \quad \text{with} \quad \mathbf{j}(\mathbf{x}, t) = \mathbf{f}(\mathbf{x}) p(\mathbf{x}, t) - \nabla^\top \mathbf{D} p(\mathbf{x}, t). \quad (2.4)$$

The ratio $\mathbf{j}(\mathbf{x}, t)/p(\mathbf{x}, t)$ can be identified with the mean phase space velocity $\mathbf{v}(\mathbf{x}, t)$.

The great advantage of the Fokker-Planck approach is that it offers access to the full time dependent probability density, from which other statistics such as correlations and moments of the distribution can be calculated. Of course, the access to $p(\mathbf{x}, t)$ requires solving a partial differential equation (Eq. (2.3)), which can in general be a challenging task, if one aims for an analytical solution. A profound treatment of the Fokker-Planck equation and review of methods to solve it can be found in [94].

We close this subsection, by mentioning an interesting correspondence between the Fokker-Planck approach and quantum mechanics. The characteristic diffusive-like term $\partial_x^2[\dots]$ appears also in the Schrödinger equation, and consequently operator methods for solving the Schrödinger equation can be adapted to solve the Fokker-Planck equation. In fact, the correspondence between Fokker-Planck and Langevin approaches can be compared to that between quantum mechanics and Bohmian mechanics [95]. Within each pair of frameworks the latter gives a recipe for calculating the trajectories, while the former stays at the level of probability density. Curiously, there also exists a "classical" version of quantum mechanics by Nelson, where a type of Brownian motion of the particles is assumed to form a fundamental part of the dynamics [96].

2.3 Path integral formalism

The last approach we present, based on path integrals, originates from the efforts to find a mathematically rigorous grounds for the Langevin equation. The idea of this approach initiated by Wiener [87, 88] and further developed by Onsager and Machlup [86, 97] is to

¹Note, this does not mean that $f_i(\mathbf{x})$ is the mean velocity at point \mathbf{x} . This will become clear in Sec. 2.3

assign a probability weight to every possible trajectory of the system. We will now present this idea in a plain setup.

For simplicity let us consider a one-dimensional system driven by Gaussian white noise: $\dot{x}(t) = f(x) + \xi(t)$, with $\langle \xi(t)\xi(t') \rangle = 2T\delta(t-t')$ (we set k_B and mobility equal to 1). Before assigning probability to the trajectories of $x(t)$ let us consider the probability $P[\{\xi(t)\}_{t_i}^{t_f}]$ of a certain realisation of the noise $\{\xi(t)\}_{t_i}^{t_f}$. Since the noise is Gaussian and uncorrelated in time, we can easily calculate this probability as

$$P[\{\xi(t)\}_{t_i}^{t_f}] = \mathcal{N}_\xi \exp \left[- \int_{t_i}^{t_f} \frac{\xi^2(t')}{4T} dt' \right], \quad (2.5)$$

where \mathcal{N}_ξ is a normalisation constant. However, what we are actually interested in is the probability $P[\{x(t)\}_{t_i}^{t_f}]$ for a certain trajectory of the observed variable $\{x(t)\}_{t_i}^{t_f}$. This can be obtained by noting that the random variable $x(t)$ is in fact a function (or rather a functional) of another random variable $\xi(t)$ allowing us to apply the standard rules for transformation of probability densities: $P(x) = P(\xi) |\frac{\partial x}{\partial \xi}|$, where $|\frac{\partial x}{\partial \xi}|$ is the Jacobian of the transformation. We then obtain:

$$P[\{x(t)\}_{t_i}^{t_f}] = \mathcal{N}_x \exp \left\{ - \int_{t_i}^{t_f} \frac{[\dot{x}(t') - f(x(t'))]^2}{4T} dt' - \int_{t_i}^{t_f} \frac{1}{2} \partial_x f(x(t')) dt' \right\}, \quad (2.6)$$

where the second integral in the exponential function comes from the Jacobian of the transformation calculated using the Stratonovich convention. For a guidebook on switching between conventions and doing calculus in the path integral framework see [98]. The calculation of the Jacobian requires a discretisation of the trajectory into infinitesimal pieces and a limiting procedure, which reduce the problem of dealing with functionals to standard multivariable calculus.

One of the great advantages of the path integral formalism is that it allows us to prove statements about probabilities of trajectories such as Eq. (1.3), which compares the probabilities of forward vs. inverse trajectories. Using Eq. (2.6) we can calculate

$$\ln \left(\frac{P[\{x(t)\}]}{\tilde{P}[\{\tilde{x}(t)\}]} \right) = - \int_{t_i}^{t_f} \frac{[\dot{x}(t') - f(x(t'))]^2}{4T} dt' + \int_{t_i}^{t_f} \frac{[-\dot{x}(t') - f(x(t'))]^2}{4T} dt' \quad (2.7)$$

$$= \int_{t_i}^{t_f} \frac{\dot{x}(t') f(x(t'))}{T} dt' = \frac{Q}{T}, \quad (2.8)$$

which confirms that the ratio of probabilities of forward and time reversed trajectories equals to the change of the entropy of the medium. Here we used the fact that the velocity \dot{x} is odd under time reversal. Analogous calculation can be found in [26]. Let us clarify that Eq. (2.6) only defines the probability of observing a specific series of transitions conditioned on starting at position $x_i = x(t_i)$. The probability of observing a trajectory $\{x(t)\}_{t_i}^{t_f}$ can be calculated as $p(x_i, t_i) P[\{x(t)\}_{t_i}^{t_f}]$. As a cross check, assuming that $f(x)$ derives from a potential and that $p(x) \sim \exp(-F(x)/T)$, one can verify that $x(t)$ satisfies the condition of

microscopic reversibility. Equipped with the expression for the probability of a trajectory one can then calculate, or at least write formal expressions for averages of any observable being a function of $x(t)$.

While here we considered the simplest case of Gaussian white noise, similar expressions for the probability of observing a specific trajectory can be derived for systems with colored noise [99, 100]. In these approaches one accounts for the correlations in the noise essentially by including an inverse of the time correlation of the noise in an analogue of Eq. (2.5).

3 Measures of irreversibility

Having introduced the three principal frameworks for describing stochastic dynamics in a continuous phase space, we will now demonstrate how they can be used to define measures of irreversibility, which capture the irreversibility at different levels of detail. The analytical expressions will be given for systems in which the deterministic driving is a linear function of the position in phase space: $\mathbf{f}(\mathbf{x}) = \mathbf{A}\mathbf{x}$. Whenever possible, apart from considering the white noise scenario ($\mathcal{G}(s) = \delta(s)$), we will show how the formulas generalize to the colored noise case. A more detailed overview can be found in Secs. A, B, C.

Entropy production rate

In section 1.2 we described the entropy production rate as the most general measure of irreversibility – it can be defined in terms of distinguishability of forward vs. time reversed dynamics (see Eq. (1.3)). This means that any sort of irreversibility, even if not manifest in form of probability currents, must necessarily reveal itself in the entropy production rate. For a system described by a Fokker-Planck equation, or equivalently a Langevin equation with white noise, the steady state entropy production rate can be expressed as [101, 26]

$$\dot{S} = \int \frac{\mathbf{j}^\top(\mathbf{x})\mathbf{D}^{-1}\mathbf{j}(\mathbf{x})}{p(\mathbf{x})} d\mathbf{x}. \quad (2.9)$$

This steady state entropy production rate can be interpreted in terms of the rate at which heat Q is dissipated to the surrounding medium at temperature T , namely $\dot{S} = \langle \dot{Q} \rangle / T$. This can be roughly seen in the structure of formula (2.9):

$$\dot{S} \sim \int j^2 D^{-1} / p \sim \langle v^2 D^{-1} \rangle \sim \langle v f / T \rangle \sim \langle \dot{Q} / T \rangle. \quad (2.10)$$

In general, beyond the steady state, the increase of the entropy of the medium represented by Eq. (2.9) is accompanied by a term corresponding to the dynamics of the probability distribution [101, 26]. We ought to note that when writing \dot{S} we actually meant the mean value of the entropy production rate. The produced entropy itself is a stochastic quantity, as substantiated by the fluctuation theorems described in Sec. 1.2. In fact, since the produced entropy is a function of the trajectory $\mathbf{x}(t)$, it itself evolves according to a drift-diffusion Langevin equation [102].

In what follows we shall see that for linear systems the entropy production rate can be expressed in terms of other, coarse grained measures of irreversibility.

Probability currents and mean velocity field

One of the standard indicators of non-equilibrium and irreversibility is the principle of detailed balance, which states that for a system at thermal equilibrium transitions between any two states statistically balance each other. For overdamped dynamics an immediate consequence is that the probability currents and the mean velocity fields must vanish for a system at thermal equilibrium. For a white-noise linear system ($\mathbf{f}(\mathbf{x}) = \mathbf{A}\mathbf{x}$) the mean velocity field $\mathbf{v}(\mathbf{x})$ is a linear function of the position in phase space [103]:

$$\mathbf{v}(\mathbf{x}) = \mathbf{\Omega}\mathbf{x}, \text{ with } \mathbf{\Omega} = \mathbf{A} + \mathbf{D}\mathbf{C}^{-1}, \quad (2.11)$$

where $\mathbf{C} = \langle \mathbf{x}\mathbf{x}^T \rangle$ is the covariance matrix. The covariance itself can be obtained from the Lyapunov equation $\mathbf{A}\mathbf{C} + \mathbf{C}\mathbf{A}^T = -2\mathbf{D}$. A modified Lyapunov equation can be used to find the time dependent auto-covariance function, also for systems with colored noise (see Sec. C).

The expression for the mean velocity field (Eq.(2.11)) can be read out directly from the Fokker-Planck equation viewed as a continuity equation for the probability, using the fact that the steady state probability distribution is Gaussian (fully determined by \mathbf{C}) and that $\mathbf{j}(\mathbf{x}) = \mathbf{v}(\mathbf{x})p(\mathbf{x})$ (the probability is advected by the velocity field). Alternatively, the mean velocity can be obtained within the Langevin picture in terms of a conditional average: $\mathbf{v}(\mathbf{x}) = \lim_{\Delta t \rightarrow 0} \langle [\mathbf{x}(t + \Delta t) - \mathbf{x}(t - \Delta t)] / (2\Delta t) \mid \mathbf{x}(t) = \mathbf{x} \rangle$ [26]. Note the importance of the symmetrized, Stratonovich-like form of the infinitesimal difference. Calculating the derivative in a different way gives $\lim_{\Delta t \rightarrow 0} \langle [\mathbf{x}(t + \Delta t) - \mathbf{x}(t)] / \Delta t \mid \mathbf{x}(t) = \mathbf{x} \rangle = \mathbf{f}(\mathbf{x})$. Of course, this distinction is of relevance only if the dynamical noise has a white-noise component. For systems driven by colored noise, however, the velocity $\mathbf{v}(\mathbf{x})$ is in general not simply linear in \mathbf{x} . Such a linear dependence persists in case of the Ornstein-Uhlenbeck kind of noise (Gaussian and exponentially correlated in time), as discussed in Sec. C.

For white-noise driven systems the linear relation between $\mathbf{v}(\mathbf{x})$ and \mathbf{x} allows us to rewrite the formula for the steady state entropy production rate (Eq. (2.9)) in a simplified form:

$$\dot{S} = \text{Tr}(\mathbf{\Omega}\mathbf{C}\mathbf{\Omega}^T\mathbf{D}^{-1}), \quad (2.12)$$

which after an appropriate change of coordinates can help finding the most irreversible components of the dynamics (Sec. 3.2).

Experimentally, the mean velocity field can be obtained by a simple binning procedure [104], or more efficiently by inferring the expansion of the velocity field in a set of basis functions [46]. Since the inference of the full velocity field is difficult with limited data, one may consider using different, coarse grained measures of irreversibility.

Cycling frequencies and area enclosing rates

Given the conservation of probability, non-vanishing currents can only exist if they form closed cycles in phase space. The structure of these cycles is particularly plain for linear systems, as implied by Eq. (2.11). Instead of measuring the full velocity field one can then measure the frequency of such circulation [104]. This leads to the definition of the cycling frequencies ω_{ij} , which measure the mean angular velocity in a 2-dimensional subspace of a pair of degrees of freedom $\{i, j\}$. Not surprisingly, for white-noise linear systems the cycling frequencies are related to the matrix Ω . In coordinates for which $\mathbf{C} = \mathbb{1}$, we simply have $\Omega_{ij} = \omega_{ij}$. In general, however, the relation is more complex: derivation of ω_{ij} requires projecting the mean velocity field onto the 2-dimensional subspace, eventually leading to (see Secs. A, B):

$$\omega_{ij} = \frac{(\mathbf{AC} - \mathbf{CA}^\top)_{ij}}{2\sqrt{C_{ii}C_{jj} - C_{ij}^2}}. \quad (2.13)$$

A related metric for irreversibility, the area enclosing rate, is defined as:

$$\mathcal{A} = \frac{1}{2} \langle \dot{\mathbf{x}}\mathbf{x}^\top - \mathbf{x}\dot{\mathbf{x}}^\top \rangle. \quad (2.14)$$

They were considered already by Mori and Kubo [90, 9] in the derivation of the Generalised Langevin equation. The area enclosing rates combine the frequency of circulation with the size and correlations of fluctuations, as quantified by the relation:

$$\mathcal{A} = \Omega\mathbf{C} \quad (2.15)$$

whenever $\mathbf{v}(\mathbf{x}) = \Omega\mathbf{x}$. In general \mathcal{A} carries the same information as a projection of the mean velocity field on the subspace of linear functions of \mathbf{x} [46]. The area enclosing rates are considerably easier to deal with than the cycling frequencies: to start with, they transform in a simpler way, since

$$\mathcal{A} = \frac{1}{2}(\mathbf{AC} - \mathbf{CA}^\top). \quad (2.16)$$

Comparing this formula with Eq. (2.13) reveals that the cycling frequencies can be calculated as the area enclosing rates normalized by the average area enclosed during a single revolution around the origin. Moreover, unlike the cycling frequencies, the area enclosing rates can be calculated for systems driven by colored noise with given time correlation function $\mathcal{G}(t)$ using

$$\mathcal{A} = \frac{1}{2}(\mathbf{BAC} - \mathbf{CA}^\top\mathbf{B}^\top), \quad (2.17)$$

where $\mathbf{B}(t) = 2 \int_0^\infty e^{\mathbf{A}t} \mathcal{G}(t) dt$. Apart from mathematical convenience, \mathcal{A} is probably easier to measure in practice, since it doesn't depend on the position of the origin. On the contrary, the measured number of full revolutions, or the mean angular velocity may be strongly affected by small changes in origin's position.

The coarse grained measures of irreversibility have been used to detect nonequilibrium dynamics in biological systems [104] and some of the mentioned formulas were verified

experimentally [105] for the dynamics of RC circuits. Moreover, these coarse grained measures have been considered as tools of studying the properties of driven polymer networks. First, it has been suggested to measure the cycling frequencies for the bending modes of embedded filamentous probes [106, 107]. Second, we proposed a method inspired by the two-point microrheology, which relates the properties of the active driving in the network to a scaling behaviour predicted for ω 's and \mathcal{A} [108, 109, 110, 111]. This potential application will be discussed in detail in Sec. 3.1.

Chapter 3

Interpreting Irreversibility

We know already that the irreversibility of dynamics can be quantified by the entropy production rate. We also know how the irreversibility and heat dissipation are related and how both can be measured, as discussed in Sec. 1.2. In Sec. 1.3 we then explained how the rate of heat dissipation resulting from energy consumption not only maintains nonequilibrium processes, but also controls their speed or accuracy. It can therefore be of interest to quantify the irreversibility, or the rate of heat dissipation in a biological process, first, to learn to what extent it is actively driven, and second, to find out how close to optimal a process is, given the fundamental theoretical limits. These kinds of studies are feasible for small, well controlled systems such as an isolated molecular motor. However, even in such a relatively simple system the measurement of the entropy production rate may pose a challenge. Every missing information about the state of the system can decrease the inferred entropy production. In particular, transitions between internal states of a motor that can't be resolved within the applied measurement technique may contribute to an entropy production higher than the one estimated experimentally.

The situation only gets worse when instead of an isolated molecular motor one considers a complex system such as a cell membrane, or cytoskeletal network driven by hundreds or thousands of molecular motors. To start with, it is not clear what one could actually learn from the inferred entropy production rate in this case. One could in principle measure the dissipation under different conditions, for instance at varying levels of ATP, but since the inferred entropy production offers only a lower bound to the true value, no fair comparison between the values inferred at different conditions is really be possible. Second, the study of entropy production, mechanical properties of the system, or properties of the driving must always be based on an analysis of time trajectories of the system. This in turn requires a choice of a set of degrees of freedom for which the trajectories are recorded. The problem with a system such as a filament network is that there are extremely many degrees of freedom (in principle a continuum) and it is not clear how to choose the most informative variables.

A conventional approach in such systems is to use tracers - small objects embedded in the investigated medium. These can either occur naturally in the medium [112, 113], for example in form of lipid granules or small organelles, or can be introduced artificially.

The most commonly introduced tracers are synthetic beads [11, 114, 115] or filaments [116, 117, 118]. The beads can be simply tracked, or manipulated to measure the mechanical response of the medium [14, 119]. In case of tracer filaments one can register the dynamics of the bending modes resulting from the active forces. The features of the dynamics and of the mechanical response often take the form of a scaling law as a function of time difference or frequency. These scaling laws can reveal the properties of both the medium the driving activity. In the following section 3.1 we explain that similar scaling laws that encode the properties of the system and the active driving can in principle be observed for some coarse grained measured of irreversibility defined in Sec. 2.3.

An alternative to these conventional approaches would be to employ a method that automatically selects the most informative degrees of freedom in an unsupervised way. Here, the exact meaning of "the most informative" depends on the posed problem. In Sec. 3.2 we present such a framework that identifies the most irreversible modes of the dynamics [45]. This framework could be applied to infer the dynamics and the entropy production rate directly from time-lapse microscopy images.

1 Scaling laws in driven networks

Polymer networks constitute a fundamental building material of living matter. The cytoskeleton spanning the interior of cells is in essence a mesh of filaments of varying length and stiffness held together by crosslinkers, often in form of motors, that apart from binding the filaments can exert active forces on them [120, 121, 122]. This complex scaffolding must on one hand allow the cell to maintain its shape, but on the other permit deformations and motion – rather demanding requirements for the mechanical response. The mechanical behaviour may be different on different time scales, but the cell might also be able to tune its mechanical properties. Indeed, it has been shown that changes in the dynamics of the crosslinkers alone can qualitatively change the cell behaviour [123, 124]. Given the complexity of the actual cytoskeleton it is remarkable that a vast range of mechanical behaviours is observed also for reconstituted cytoskeletal networks composed just of a few ingredients [121]. Varying the concentrations and properties of the filaments and crosslinkers one can drastically change the network properties: relatively small changes in crosslinker's concentration can increase the stiffness by orders of magnitude [125]. The role of motors for mechanical properties is very subtle: they can either fluidize [126] or stiffen the network [11, 127, 128]. The complex role of crosslinkers, motors, and their binding times on the mechanical properties was confirmed by theoretical models [129, 130, 131].

To study the mechanics of such networks, both *in vivo* and *in vitro* a series of experimental techniques called microrheology has been developed. These methods rely on tracking the dynamics of microscopic probes such as beads embedded in the medium and aim to quantify the mechanical properties of the medium in terms of the complex shear modulus $G^*(\omega)$. Additionally, such measurements can reveal the spectrum of thermal and active forces present in the network. The functional forms of the complex shear modulus $G^*(\omega)$, the mean square displacement of the probes $\Delta x^2(t)$ or the internal force spectrum

$f^2(\omega)$ often take form of power laws with different exponents in different time and frequency regimes. The corresponding exponents can then be used to classify the behaviour of the medium at a given time scale, for example by comparing the exponents to those of a purely viscous or purely elastic medium. The points at which the exponent changes can reveal the typical time scales of the active processes [132]. Varying the size of the tracers beads allows to probe the mechanical properties at different length scales [133].

The first microrheology method, called active microrheology [134, 133], measures the response of the embedded tracers to force applied with magnetic field or optical tweezers. The measured response function is then translated to the complex shear modulus using the Generalized Stokes relation. A follow-up, non-invasive method, the passive microrheology, bypasses the necessity of directly measuring the response function, by relating it to the spontaneous fluctuations of the tracers via Fluctuation-Dissipation theorem [135, 114]. Naturally, the Fluctuation-Dissipation theorem only applies to systems at equilibrium, which excludes the use of passive microrheology alone to study actively driven networks. However, a combination of active and passive microrheology can still give insightful results through force spectrum microscopy. If the complex shear modulus is known, for example from an active microrheology experiment, the measurement of spontaneous fluctuations of the probe give access to the spectrum of forces in the network, both thermal and active ones [112, 136, 132]. Finally, to measure the bulk properties of the material, and not the local ones (possibly affected by the presence of the probe) one can use the two-point microrheology [137, 114, 112], which in contrast to the aforementioned methods uses the cross-correlations in displacements of pairs of tracers.

Inspired by the two-point microrheology, in Secs. A, B, C and in [110] we ask whether a non-invasive measurement of the irreversibility of probes' dynamics can deliver information about the network and the features of the active driving. Specifically, we propose measuring the cycling frequencies, or the area enclosing rates (see Sec. 2.3) for pairs of tracer beads at distance r from each other. To make a prediction for what such a measurement would yield we considered a simplified model of d -dimensional spring network embedded in a viscous fluid. The tracer particles are present at all the nodes of the network and obey overdamped dynamics. On top of the thermal noise experienced by all the beads we model the nonequilibrium activity as random monopole or dipole forces [110]. These active random forces are primarily modeled with Gaussian white noise. We analyze the effects of time correlations in the driving in Sec. C. We consider various types of activity distribution: single active agent, and a uniform distribution of active agents with randomly chosen force amplitudes. The case of spatially correlated activity amplitudes is treated in [110]. The behaviour of the cycling frequencies in an actively stressed isostatic network [138] was studied in [139].

We predict that the cycling frequencies and the area enclosing rates follow a power law as a function of distance between the probes. Overall, the values of the irreversibility measures are proportional to the standard deviation of the active force amplitudes, but independent of specific probability distribution of the amplitudes. The exponent of the power law depends on the dimensionality of the system (network, membrane, or a stretched polymer), but not on the exact geometry of the network. Importantly, the exponent

strongly depends on the moment of the active forces: dipoles (as for a contractile motor) vs. monopoles (as for an ion pump in a membrane [140]). This is not straightforward – fitting a model to experimental data is not necessarily conclusive about the moment of the forces [14].

The predictions described above are derived based on the formulas presented in Sec. 2.3 and exploit a mapping between the Lyapunov equation for the covariance matrix and Poisson equation in a $2d$ -dimensional space. The predicted exponents surely inherit from the exponents describing deformations of an elastic medium, but those don't explain everything. First, the scaling behaviour is observed also for the cycling frequencies, which quantify the mean angular velocity and as such are independent of the size of fluctuations. Second, the exponents are different for a single active agent and for a random distribution of forces.

The framework presented in Sec. C allowed us to account for temporal correlations in the active noise, which are known to be present for example in the contractile forces generated by myosin filaments. We found that the scaling behaviour remains unchanged for large distances between the tracers, for which the relaxation times of the network are large compared to the correlation times of the active forces. At such large distances the active noise can indeed be effectively described as white. At shorter distances, however, the behaviour of the area enclosing rates as a function of distance is no longer monotonic and displays a maximum at distance $r \sim \tau^{1/2}$, where τ is the correlation time of the active forces. Such measurements of irreversibility could therefore give access to the processivity times of the motors driving the network. Here we should however note that there are arguably simpler ways of estimating the processivity time, such as concluding it from the active force spectrum and mean the square displacements [132], or by directly observing the local deformations of the network [117]. Recent studies suggest that the processivity times can be obtained from a simplistic caging model, which assumes that a tracer is confined to a harmonic trap driven by a single colored noise process [115, 13, 141]. Finally, the correlation times of the active forces were reflected in a very recent experiment designed to identify the time scales relevant to dissipation [142]. There, the authors measured the irreversibility of time series of consecutive displacements of the tracer particles for varying lag times.

The τ -dependent position of the maximum of the area enclosing rates may therefore be rather of theoretical than practical interest. Still, it is recognised that the correlation times of the driving force can have crucial effects on active processes. The way in which the time correlations affect the irreversibility may once prove important in some biological context, given the connections between irreversibility, dissipation, work and precision (see Sec. 1.2). The original results discussed above show how the irreversibility originating from microscopic driving propagates across different length scales. However, the relevance of this phenomenon to biological processes remains an open question.

2 Finding the most irreversible components

We discussed how various types of tracers are used to study the dynamics of mesoscopic driven systems. However, introducing tracers without perturbing the investigated system may not always be possible. Instead of using artificial tracers one can try tracking objects already present in the medium, but what if no such clearly distinguishable, discrete objects appear in the experimental image? Let us, nevertheless, be optimistic for a second and assume we managed to insert and track a hundred of beads. How should we analyse their trajectories now? Should we look at the beads one by one, or rather in pairs, as in the aforementioned two-point methods? And what if it's actually beneficial to look at some linear combination of the displacements of multiple beads? This could for example represent a Fourier mode of the network.

It is not obvious in general what degrees of freedom to choose. In general, there may not even be an obvious set of degrees of freedom to choose from. This choice, however, though not straightforward, can be decisive for what and how much we learn from an observation. The optimal choice may depend on the context and on our objective, that is on what we want to learn. In [45] (Sec. D) we took up the challenge of identifying and inferring the irreversible dynamics, and estimating the entropy production rate of a driven elastic network directly from a manufactured experimental movie. Given this objective, we developed a framework for identifying the most irreversible components of the dynamics, which we briefly present below (a detailed explanation can be found in Sec. D).

Our idea there was to refrain from making any biased choice for what to track and instead to treat the entire experimental movie as the input. That is, the data we work on is the time trajectory of pixel intensities, while we are ignorant of what the images actually represent. By analysing the movie as a whole, we are sure not to miss out on anything, but run into a different problem. The framework for stochastic force inference [46] that we eventually want to apply to our data suffers from high dimensionality of the phase space, which is a common limitation of inference schemes in general. In our case the dimensionality is equal to the number of pixels in a frame, which in principle can even exceed the actual number of the physical degrees of freedom. We therefore need to reduce the number of the degrees of freedom, keeping only the most informative ones, in our case the ones displaying high irreversibility.

To this end we resort to the properties of the covariance matrix \mathbf{C} , the area enclosing rate matrix \mathcal{A} , and a particular formula for the entropy production rate valid for linear systems:

$$\dot{S} = \text{Tr}(\mathcal{A}\mathbf{C}^{-1}\mathcal{A}\mathbf{D}^{-1}), \quad (3.1)$$

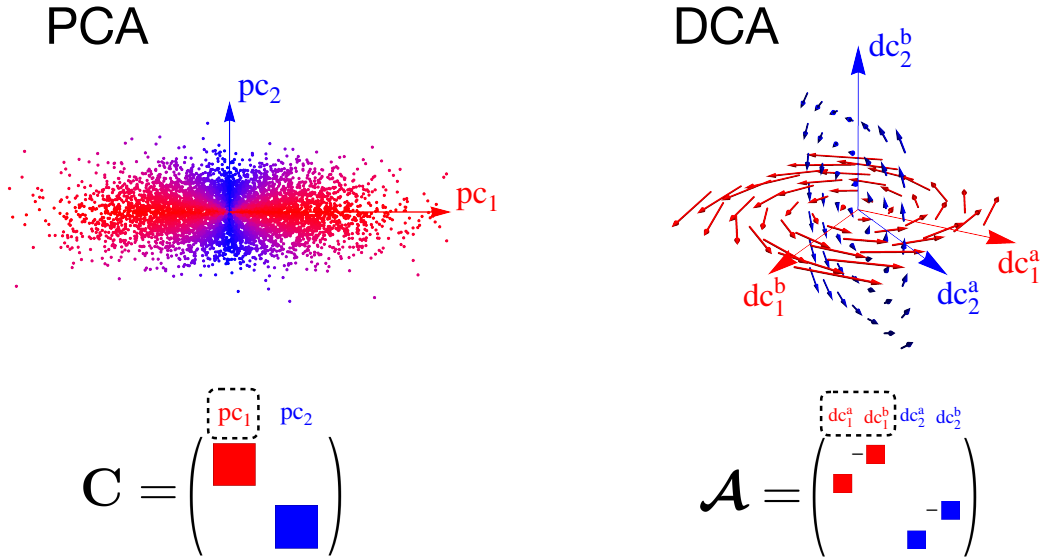
with \mathbf{D} being the diffusion matrix. This relation follows directly from Eqs. (2.12), (2.15). The matrix \mathcal{A} (see Sec. 2.3) in essence encodes the covariance of pairs of degrees of freedom and their circulation rate. The properties of \mathbf{C} and \mathcal{A} imply existence of a linear transformation which simultaneously brings these matrices into a favourable, simplified form. Specifically, in these special coordinates $\mathbf{C} = \mathbb{1}$ and \mathcal{A} becomes block diagonal with blocks of the form $\{0, -\omega_{2i-1,2i}\}, \{\omega_{2i-1,2i}, 0\}$. We used the symbol ω , since in these

coordinates the non-zero elements of \mathcal{A} are actually equal to the cycling frequencies (again, assuming linear dynamics). The entropy production rate then takes the form

$$\dot{S} = \sum_i \omega_{2i-1,2i}^2 [(D^{-1})_{2i-1,2i-1} + (D^{-1})_{2i,2i}], \quad (3.2)$$

where \mathbf{D} is to be taken in the special coordinates. The advantage of using this basis is that now the total entropy production rate splits into a sum of independent contributions corresponding to pairs of basis vectors $\{\mathbf{dc}_i^a, \mathbf{dc}_i^b\}$. The elements of \mathcal{A} can be calculated from the trajectories and \mathbf{D} estimated from short time mean squared displacements. We can then use these estimated values to calculate the expected contributions to the entropy production rate in Eq. (3.2) and arrange them in decreasing order. Applying the same ordering to the corresponding pairs of basis vectors allows us to identify the components of the movie that display the most irreversible dynamics.

The reasoning behind our dissipative component analysis (DCA) can be illustrated by comparing it to the commonly applied principal component analysis (PCA), as visualised in the figure below.



In the PCA one diagonalizes the covariance matrix to find a reduced number of components that account for most of the variance in the data. In DCA we instead bring the area enclosing rate matrix \mathcal{A} to a block diagonal form. In these special coordinates the probability currents are disentangled, allowing us to independently assess the irreversibility for pairs of the basis vectors and only keep the most irreversible ones. Note that the irreversibility is not only set by the circulation rate ω^2 – the weights $\sim D^{-1}$ account for

the fact that with larger dynamical noise an observed time directionality is more likely to be just a result of a fluctuation (compare with Eq. (2.6)).

Having found a set of most irreversible modes we can feed them to the stochastic force inference framework and obtain an improved estimate of the entropy production rate. However, it feels unsatisfactory to confine our findings to a single scalar number - the entropy production rate, given all the information about the irreversible dynamics we obtained on the way. Wouldn't it be possible to use the information about the inferred mean velocity fields of corresponding modes to reconstruct the typical irreversible dynamics? We can think of the stereotypical irreversible dynamics as following the integral curves of the mean velocity field. For a linear system, in the special coordinates the integral curves are just circles and the stereotypical image dynamics $\mathcal{I}_i(t)$ could be represented as

$$\mathcal{I}_i(t) = \mathbf{dc}_i^a \cos(\omega_{2i-1,2i}t) + \mathbf{dc}_i^b \sin(\omega_{2i-1,2i}t). \quad (3.3)$$

Note that the dissipative components $\{\mathbf{dc}_i^a, \mathbf{dc}_i^b\}$ correspond to a set of pixel intensities in a frame, so a superposition, as in Eq. (3.3) can really be used to construct a movie and visualise what the most irreversible dynamics actually represent.

The presented dimensionality reduction scheme relies on the assumption that the dynamics is linear, which is unlikely to be the case in practice. With nonlinearities a rigorous decomposition of the entropy production is no longer possible and applying Eq. (3.2) to sort the inferred modes is just an educated guess. Similarly, the integral curves of the velocity field are no longer simple circles, which complicates the reconstruction of stereotypical irreversible dynamics. Nevertheless, for the nonlinear example studied in Sec. D) the DCA still performs visibly better than the standard PCA. Possible directions for dealing with nonlinearities and interpreting the inferred image dynamics will be further discussed in the following Outlook chapter.

Chapter 4

Outlook

In this thesis we looked at irreversibility as a distinctive feature of nonequilibrium dynamics, that can not only unveil the presence of active processes, but also deliver quantitative information about them. In the introduction we discussed the connections between irreversibility, entropy production and the structure of fluctuations. These connections are expressed in terms of a series of fluctuation theorems that put constraints on the possible course of nonequilibrium processes. We discussed how the speed and precision of a process are generally bounded by the amount of consumed energy. Further we reviewed a class of thermodynamic uncertainty relations. This continually improved family of inequalities defines the minimal entropic costs of suppressing generalized current fluctuations at various time scales. Apart from setting theoretical bounds for precision, these relations can themselves be used to infer the entropy production rate. Measuring the produced entropy in alternative ways, for example in terms of irreversibility of the trajectories, can then be used to assess the degree of optimality of a biological process, or efficiency of a molecular motor.

This modus of investigation, while insightful for small, isolated systems, seems less promising in case of complex systems with many degrees of freedom, many of which may not even be accessible experimentally. In such a system the identification of relevant degrees of freedom may pose a problem of its own. Given this limited accessibility and informativeness of the entropy production rate, in Sec. 3.1 we reflected on whether some coarse grained measures of irreversibility (area enclosing rates and cycling frequencies) could instead reveal some features of the active driving. Within a simplistic model of a driven viscoelastic network we showed that a measurement akin to two-point microrheology could in principle deliver such information. We expect the measures of irreversibility to decrease on average as a power law in function of distance between the tracers. The exponents and regimes of the power law encode features of the active driving such as the moment of the active forces, or their correlation times. Here we should note that our predictions for the results of the suggested measurement implicitly assume a certain complex shear modulus of the medium. It would be interesting to investigate how the predicted nonequilibrium scaling behaviour is modified in media with different complex shear moduli, for example when memory effects come into play. Further modifications could account for the hydrodynamic

interactions in the network. For this purpose the two-fluid model [143, 129, 144] could be a useful tool. Our preliminary numerical study for a lattice of harmonically trapped and hydrodynamically interacting beads suggested presence of similar power laws but with reduced exponents. There we approximated the hydrodynamic interactions by a constant Oseen tensor, as in [145, 146].

If the proposed measurement were to be performed, it is relevant to ask how difficult it would be to actually measure the cycling frequencies, or the area enclosing rates. These and related quantities have been measured experimentally for simple electronic circuits [105] and even for the dynamics of a beating flagella, or primary cilium [104]. However, to our knowledge, no such measurement was ever successfully performed for a driven network, or similar system. Indeed, the power law behaviour we predict suggests that the quantities to be measured decay very fast with increasing distance r between the tracers, making it increasingly difficult to bring the signal beyond the noise level. Specifically, if the cycling frequency scales as $\omega(r) \sim r^{-\alpha}$ then the time required to measure it would be $t \sim r^{2\alpha}$. Another potential problem here is the limited measurement time. The cycling frequency for a certain pair of tracers is a steady state entity set by the specific distribution of the active agents. If the spatial distribution of the active forces changes, so does the steady state value of the cycling frequency. The maximal measurement time is therefore limited by the time it takes for the active agents to rearrange.

Although the scaling behaviour of the irreversibility metrics may be difficult to observe experimentally, it tells us that irreversibility generated locally by active forces decays quickly as we move to larger scales. Persistent irreversibility of the dynamics can in general be used to extract work – imagine coupling the irreversible degrees of freedom to a mechanism like a spinning reel. Our results seem to suggest that such work could not be efficiently extracted at a large scale when powered by uncorrelated local forces. Spatial correlations between active force amplitudes and temporal correlations between the active agents could change things qualitatively.

Even if the area enclosing rates or the cycling frequencies can never be measured for internally driven networks, it does not yet rule out the use of irreversibility metrics for studying such systems - some other measures of irreversibility may turn out to be more practical. In fact, in a very recent study of actomyosin cortex [142] the authors measure the irreversibility of trajectories of single tracers. Specifically, they take the trajectories of consecutive displacements of the tracer for varying time resolution. They argue that the time resolution at which the measured irreversibility is maximized reveals the time scales of the active agent, in that case myosin. While this approach cannot be considered an established method yet, the successful measurement of irreversibility for a complex driven network is already a great progress.

The characteristic time scales of the active agents appear to play a significant role in the dynamics of driven systems. We already mentioned the example where the dissociation times of the crosslinkers control the mechanical properties of the network [123]. It is also known that the active dynamics of the molecular motors in the cytoskeleton can substantially increase the effective diffusivity [147, 132, 144], and may therefore play a side role

in the undirected cellular transport. However, it has not been studied how the correlation times of the motors affect this diffusivity. Based on simple arguments we expect that for a fixed amplitude of the active forces the effective diffusivity may be maximized for intermediate values of the correlation times.

Automatized analysis of active systems

The available methods for studying active biological systems typically require the use of tracers in form of small particles or filaments. In the optimistic scenario one can use some constituents of the system as tracers - in case of the cytoskeleton these could be small organelles, or lipid granules. Otherwise, the tracers have to be inserted manually, which may not be simple without disturbing the scrutinized system. Moreover, many approaches require measuring the response function by actively manipulating the inserted probes, which brings further hazard of spoiling the object of investigation. In any case, the particular choice of tracers is dictated by convenience or necessity rather than by asking what would be the most informative set of variables.

In Sec. D we presented what is meant to be the first, humble step in the quest of the holy grail - a framework for non-invasive, system independent analysis of time-lapse microscopy data, that would reveal the deterministic and stochastic parts of the dynamics, their irreversible components and the energy dissipation. Of course there is a long way to go. In the presented framework instead of arbitrarily deciding on what degrees of freedom to track, we treat the entire movie, that is the time dependent pixel intensities, as a dynamical system. Since the existing methods for dynamical inference [46, 47] are only efficient for systems with limited dimensionality (definitely smaller than the number of pixels in a frame), we precede the inference by an educated dimensionality reduction. For this purpose we developed Dissipative Component Analysis aimed at selecting the most irreversible components of the system. While this reduction scheme is fully legitimate only for linear dynamics, it turns out to outperform the standard Principal Component Analysis also for nonlinear systems.

The identification of the most irreversible components of the dynamics may be of use on its own. It could be used at the early stage of investigation of a biological system as a proxy for the most active spots. Such spots could then be studied with special attention as potentially the most interesting ones. This seems to be the lowest-hanging fruit on the way to the "holy grail". The next step would be combining the selected components with the inferred mean phase space velocity field to visualise the stereotypical irreversible dynamics. The suggested reduction scheme was irreversibility oriented, since one of our main goals was inferring the entropy production rate. However, one can imagine that such reduction schemes could be modified and adjusted depending on the ultimate objective of the inference.

Having decided on the dimensionality reduction scheme optimal for our purpose, the remaining challenge is interpreting the inferred velocity and force fields. The problem is that the inferred forces describe the dynamics of the pixel intensities. It is not obvious how to transform this information into something more intuitive. One option would be to

somehow translate the force fields into how the objects or shapes visible in the image move on average.

At this point, along with the limited amount of data, the nonlinearities seem to be the major challenge in unsupervised analysis of experimental movies. The current version of the dissipative component analysis relies on a linear transformation and choosing an appropriate subset of basis vectors. The way this subset is chosen relies on the assumption of linear dynamics. This may easily become an issue – note that even if the underlying dynamics is linear in the physical space, the corresponding dynamics of pixel intensities may be highly nonlinear, especially for large displacements of objects in the movie. Furthermore, while the stochastic force inference is not limited to linear systems, the more complex the dynamics, the more difficult it is to infer the force, diffusion and velocity fields with all their details. A way to deal with nonlinearities could be to employ a neural network that would effectively invert the mapping from physical to image space. A machine learning approach was recently applied to infer the entropy production and irreversible components from an experimental movie [43, 148], however, the results are not convincing yet. Nevertheless, it may just be a matter of time for such unsupervised methods to become a standard tool for studying complex driven systems at mesoscopic scale, as it was the case with the study of stereotypical animal behaviour [149, 150, 151, 152]. If not by providing direct answers, such approaches could still guide the researchers by allowing them to see through the noise and find patterns in limited data.

Bibliography

- [1] S. Ciliberto, A. Imparato, A. Naert, and M. Tanase, “Heat flux and entropy produced by thermal fluctuations,” *Physical Review Letters*, vol. 110, p. 180601, 2013.
- [2] J. Li, J. M. Horowitz, T. R. Gingrich, and N. Fakhri, “Quantifying dissipation using fluctuating currents,” *Nature Communications*, vol. 10, p. 1666, 2019.
- [3] Z. Rieder, J. L. Lebowitz, and E. Lieb, “Properties of a harmonic crystal in a stationary nonequilibrium state,” *Journal of Mathematical Physics*, vol. 8, pp. 1073–1078, 1967.
- [4] H. Spohn and J. L. Lebowitz, “Stationary non-equilibrium states of infinite harmonic systems,” *Communications in Mathematical Physics*, vol. 54, pp. 97–120, 1977.
- [5] G. Falasco, M. Baiesi, L. Molinaro, L. Conti, and F. Baldovin, “Energy repartition for a harmonic chain with local reservoirs,” *Physical Review E*, vol. 92, p. 022129, 2015.
- [6] W. Bialek, *Biophysics: Searching for Principles*. Princeton University Press, 2012.
- [7] L. Onsager, “Reciprocal Relations in Irreversible Processes I,” *Physical Review*, vol. 37, p. 405, 1931.
- [8] L. Onsager, “Reciprocal Relations in Irreversible Processes II,” *Physical Review*, vol. 38, p. 2265, 1931.
- [9] R. Kubo, “The fluctuation-dissipation theorem,” *Reports on Progress in Physics*, vol. 29, p. 255, 1966.
- [10] P. Martin, A. J. Hudspeth, and F. Jülicher, “Comparison of a hair bundle’s spontaneous oscillations with its response to mechanical stimulation reveals the underlying active process,” *Proceedings of the National Academy of Sciences*, vol. 98, no. 25, pp. 14380–14385, 2001.
- [11] D. Mizuno, C. Tardin, C. F. Schmidt, and F. C. MacKintosh, “Nonequilibrium mechanics of active cytoskeletal networks,” *Science*, vol. 315, pp. 370–373, 2007.

- [12] T. Betz, M. Lenz, J.-F. Joanny, and C. Sykes, “ATP-dependent mechanics of red blood cells,” *Proceedings of the National Academy of Sciences*, vol. 106, no. 36, pp. 15320–15325, 2009.
- [13] É. Fodor, W. W. Ahmed, M. Almonacid, M. Bussonnier, N. S. Gov, M. H. Verlhac, T. Betz, P. Visco, and F. Van Wijland, “Nonequilibrium dissipation in living oocytes,” *Europhysics Letters*, vol. 116, p. 30008, 2016.
- [14] H. Turlier, D. A. Fedosov, B. Audoly, T. Auth, N. S. Gov, C. Sykes, J. F. Joanny, G. Gompper, and T. Betz, “Equilibrium physics breakdown reveals the active nature of red blood cell flickering,” *Nature Physics*, vol. 12, pp. 513–520, 2016.
- [15] F. S. Gnesotto, F. Mura, J. Gladrow, and C. P. Broedersz, “Broken detailed balance and non-equilibrium dynamics in living systems: a review,” *Reports on Progress in Physics*, vol. 81, p. 066601, 2018.
- [16] T. Harada and S. I. Sasa, “Equality connecting energy dissipation with a violation of the fluctuation-response relation,” *Physical Review Letters*, vol. 95, p. 130602, 2005.
- [17] T. Harada and S. I. Sasa, “Energy dissipation and violation of the fluctuation-response relation in nonequilibrium Langevin systems,” *Physical Review E*, vol. 73, p. 026131, 2006.
- [18] S. Toyabe, T. Okamoto, T. Watanabe-Nakayama, H. Taketani, S. Kudo, and E. Muneyuki, “Nonequilibrium energetics of a single F1-ATPase molecule,” *Physical Review Letters*, vol. 104, p. 198103, 2010.
- [19] T. Ariga, M. Tomishige, and D. Mizuno, “Nonequilibrium Energetics of Molecular Motor Kinesin,” *Physical Review Letters*, vol. 121, p. 218101, 2018.
- [20] C. Jarzynski, “Nonequilibrium equality for free energy differences,” *Physical Review Letters*, vol. 78, no. 14, pp. 2690–2693, 1997.
- [21] J. Liphardt, S. Dumont, S. B. Smith, I. Tinoco, and C. Bustamante, “Equilibrium information from nonequilibrium measurements in an experimental test of Jarzynski’s equality,” *Science*, vol. 296, pp. 1832–1835, 2002.
- [22] G. Hummer and A. Szabo, “Free energy reconstruction from nonequilibrium single-molecule pulling experiments,” *Proceedings of the National Academy of Sciences*, vol. 98, no. 7, pp. 3658–3661, 2001.
- [23] G. Hummer and A. Szabo, “Free Energy Surfaces from Single-Molecule Force Spectroscopy,” *Accounts of Chemical Research*, vol. 38, pp. 504–513, 2005.
- [24] R. F. Fox, “Using nonequilibrium measurements to determine macromolecule free-energy differences,” *Proceedings of the National Academy of Sciences*, vol. 100, no. 22, pp. 12537–12538, 2003.

- [25] K. Sekimoto, *Stochastic Energetics*. Springer, Berlin, Heidelberg, 2010.
- [26] U. Seifert, “Stochastic thermodynamics, fluctuation theorems and molecular machines,” *Reports on Progress in Physics*, vol. 75, p. 126001, 2012.
- [27] D. J. Evans, E. G. Cohen, and G. P. Morriss, “Probability of second law violations in shearing steady states,” *Physical Review Letters*, vol. 71, no. 15, pp. 2401–2404, 1993.
- [28] G. Gallavotti and E. G. Cohen, “Dynamical ensembles in nonequilibrium statistical mechanics,” *Physical Review Letters*, vol. 74, no. 14, pp. 2694–2697, 1995.
- [29] J. Kurchan, “Fluctuation theorem for stochastic dynamics,” *Journal of Physics A*, vol. 31, p. 3719, 1998.
- [30] J. L. Lebowitz and H. Spohn, “A Gallavotti-Cohen-type symmetry in the large deviation functional for stochastic dynamics,” *Journal of Statistical Physics*, vol. 95, no. 1/2, pp. 333–365, 1999.
- [31] F. Ritort, “Nonequilibrium fluctuations in small systems: From physics to biology,” *Advances in Chemical Physics*, vol. 137, pp. 31–123, 2008.
- [32] S. Ciliberto, S. Joubaud, and A. Petrosyan, “Fluctuations in out-of-equilibrium systems: from theory to experiment,” *Journal of Statistical Mechanics*, p. P12003, 2010.
- [33] G. E. Crooks, “Nonequilibrium measurements of free energy differences for microscopically reversible Markovian systems,” *Journal of Statistical Physics*, vol. 90, no. 5/6, pp. 1481–1487, 1998.
- [34] G. E. Crooks, “Entropy production fluctuation theorem and the nonequilibrium work relation,” *Physical Review E*, vol. 60, no. 3, pp. 2721–2726, 1999.
- [35] J. M. Parrondo, C. Van Den Broeck, and R. Kawai, “Entropy production and the arrow of time,” *New Journal of Physics*, vol. 11, p. 073008, 2009.
- [36] É. Roldán and J. M. Parrondo, “Entropy production and Kullback-Leibler divergence between stationary trajectories of discrete systems,” *Physical Review E*, vol. 85, p. 031129, 2012.
- [37] É. Roldán, *Irreversibility and Dissipation in Microscopic Systems*. Springer, Cham, 2014.
- [38] I. A. Martínez, G. Bisker, J. M. Horowitz, and J. M. Parrondo, “Inferring broken detailed balance in the absence of observable currents,” *Nature Communications*, vol. 10, p. 3542, 2019.
- [39] É. Roldán, J. Barral, P. Martin, J. M. R. Parrondo, and F. Jülicher, “Arrow of Time in Active Fluctuations,” *arXiv preprint*, p. 1803.04743, 2018.

- [40] É. Fodor, C. Nardini, M. E. Cates, J. Tailleur, P. Visco, and F. Van Wijland, “How Far from Equilibrium Is Active Matter?,” *Physical Review Letters*, vol. 117, p. 038103, 2016.
- [41] C. Nardini, É. Fodor, E. Tjhung, F. van Wijland, J. Tailleur, and M. E. Cates, “Entropy production in field theories without time-reversal symmetry: quantifying the non-equilibrium character of active matter,” *Physical Review X*, vol. 7, p. 021007, 2017.
- [42] D. S. Seara, B. B. Machta, and M. P. Murrell, “Irreversibility in dynamical phases and transitions,” *Nature Communications*, vol. 12, p. 392, 2021.
- [43] D. K. Kim, Y. Bae, S. Lee, and H. Jeong, “Learning Entropy Production via Neural Networks,” *Physical Review Letters*, vol. 125, p. 140604, 2020.
- [44] B. Lander, J. Mehl, V. Blickle, C. Bechinger, and U. Seifert, “Noninvasive measurement of dissipation in colloidal systems,” *Physical Review E*, vol. 86, p. 030401(R), 2012.
- [45] F. S. Gnesotto, G. Gradziuk, P. Ronceray, and C. P. Broedersz, “Learning the non-equilibrium dynamics of Brownian movies,” *Nature Communications*, vol. 11, p. 5378, 2020.
- [46] A. Frishman and P. Ronceray, “Learning Force Fields from Stochastic Trajectories,” *Physical Review X*, vol. 10, p. 021009, 2020.
- [47] D. B. Brückner, P. Ronceray, and C. P. Broedersz, “Inferring the Dynamics of Underdamped Stochastic Systems,” *Physical Review Letters*, vol. 125, p. 058103, 2020.
- [48] S. Toyabe, H. R. Jiang, T. Nakamura, Y. Murayama, and M. Sano, “Experimental test of a new equality: Measuring heat dissipation in an optically driven colloidal system,” *Physical Review E*, vol. 75, p. 011122, 2007.
- [49] C. B. Li and S. Toyabe, “Efficiencies of molecular motors: a comprehensible overview,” *Biophysical Reviews*, vol. 12, pp. 419–423, 2020.
- [50] F. Jülicher, A. Ajdari, and J. Prost, “Modeling molecular motors,” *Reviews of Modern Physics*, vol. 69, no. 4, pp. 1269–1281, 1997.
- [51] H. Qian, “The mathematical theory of molecular motor movement and chemomechanical energy transduction,” *Journal of Mathematical Chemistry*, vol. 27, no. 3, pp. 219–234, 2000.
- [52] T. Schmiedl and U. Seifert, “Efficiency of molecular motors at maximum power,” *Europhysics Letters*, vol. 83, p. 30005, 2008.

- [53] U. Seifert, “Stochastic thermodynamics: From principles to the cost of precision,” *Physica A*, vol. 504, pp. 176–191, 2018.
- [54] J. Hopfield, “Kinetic Proofreading: A New Mechanism for Reducing Errors in Biosynthetic Processes Requiring High Specificity,” *Proceedings of the National Academy of Sciences*, vol. 71, no. 10, pp. 4135–4139, 1974.
- [55] A. Murugan, D. A. Huse, and S. Leibler, “Speed, dissipation, and error in kinetic proofreading,” *Proceedings of the National Academy of Sciences*, vol. 109, no. 30, pp. 12034–12039, 2012.
- [56] N. Barkai and S. Leibler, “Robustness in simple biochemical networks,” *Nature*, vol. 387, pp. 913–917, 1997.
- [57] H. C. Berg and E. M. Purcell, “Physics of chemoreception,” *Biophysical Journal*, vol. 20, no. 2, pp. 193–219, 1977.
- [58] P. Mehta and D. J. Schwab, “Energetic costs of cellular computation,” *Proceedings of the National Academy of Sciences*, vol. 109, no. 44, pp. 17978–17982, 2012.
- [59] G. Lan, P. Sartori, S. Neumann, V. Sourjik, and Y. Tu, “The energy-speed-accuracy trade-off in sensory adaptation,” *Nature Physics*, vol. 8, pp. 422–428, 2012.
- [60] W. Bialek and S. Setayeshgar, “Physical limits to biochemical signaling,” *Proceedings of the National Academy of Sciences*, vol. 102, no. 29, pp. 10040–10045, 2005.
- [61] D. Hartich, A. C. Barato, and U. Seifert, “Nonequilibrium sensing and its analogy to kinetic proofreading,” *New Journal of Physics*, vol. 17, p. 055026, 2015.
- [62] J. L. England, “Statistical physics of self-replication,” *The Journal of chemical physics*, vol. 139, p. 121923, 2013.
- [63] Y. Cao, H. Wang, Q. Ouyang, and Y. Tu, “The free-energy cost of accurate biochemical oscillations,” *Nature Physics*, vol. 11, pp. 772–778, 2015.
- [64] A. C. Barato and U. Seifert, “Coherence of biochemical oscillations is bounded by driving force and network topology,” *Physical Review E*, vol. 95, p. 062409, 2017.
- [65] A. C. Barato and U. Seifert, “Cost and precision of Brownian clocks,” *Physical Review X*, vol. 6, p. 041053, 2016.
- [66] J. M. Horowitz and T. R. Gingrich, “Thermodynamic uncertainty relations constrain non-equilibrium fluctuations,” *Nature Physics*, vol. 16, pp. 15–20, 2020.
- [67] A. C. Barato and U. Seifert, “Thermodynamic Uncertainty Relation for Biomolecular Processes,” *Physical Review Letters*, vol. 114, p. 158101, 2015.

- [68] T. R. Gingrich, J. M. Horowitz, N. Perunov, and J. L. England, “Dissipation Bounds All Steady-State Current Fluctuations,” *Physical Review Letters*, vol. 116, p. 120601, 2016.
- [69] P. Pietzonka, F. Ritort, and U. Seifert, “Finite-time generalization of the thermodynamic uncertainty relation,” *Physical Review E*, vol. 96, p. 012101, 2017.
- [70] G. Falasco, M. Esposito, and J. C. Delvenne, “Unifying thermodynamic uncertainty relations,” *New Journal of Physics*, vol. 22, p. 053046, 2020.
- [71] I. Di Terlizzi and M. Baiesi, “Kinetic uncertainty relation,” *Journal of Physics A*, vol. 52, p. 02LT03, 2019.
- [72] P. Pietzonka, A. C. Barato, and U. Seifert, “Universal bound on the efficiency of molecular motors,” *Journal of Statistical Mechanics: Theory and Experiment*, p. 124004, 2016.
- [73] S. K. Manikandan, D. Gupta, and S. Krishnamurthy, “Inferring Entropy Production from Short Experiments,” *Physical Review Letters*, vol. 124, p. 120603, 2020.
- [74] S. Otsubo, S. Ito, A. Dechant, and T. Sagawa, “Estimating entropy production by machine learning of short-time fluctuating currents,” *Physical Review E*, vol. 101, p. 062106, 2020.
- [75] S. Otsubo, S. K. Manikandan, T. Sagawa, and S. Krishnamurthy, “Estimating time-dependent entropy production from non-equilibrium trajectories,” *Communications Physics*, vol. 5, p. 11, 2022.
- [76] W. Hwang and C. Hyeon, “Energetic Costs, Precision, and Transport Efficiency of Molecular Motors,” *Journal of Physical Chemistry Letters*, vol. 9, pp. 513–520, 2018.
- [77] A. Dechant and S. I. Sasa, “Improving Thermodynamic Bounds Using Correlations,” *Physical Review X*, vol. 11, p. 41061, 2021.
- [78] J. Yan, “Achievability of thermodynamic uncertainty relations,” *arXiv preprint*, p. 1905.00929v2, 2019.
- [79] A. Dechant, “Multidimensional thermodynamic uncertainty relations,” *Journal of Physics A*, vol. 52, no. 3, p. 035001, 2019.
- [80] E. Nelson, *Dynamical Theories of Brownian Motion*. Princeton University Press, 1967.
- [81] E. Frey and K. Kroy, “Brownian motion: a paradigm of soft matter and biological physics,” *Annalen der Physik (Leipzig)*, vol. 14, no. 1-3, pp. 20–50, 2005.
- [82] P. Langevin, “Sur la théorie du mouvement brownien,” *Comptes-rendus de l’Académie des sciences*, vol. 146, pp. 530–533, 1908.

- [83] D. S. Lemons and A. Gythiel, “Paul Langevin’s 1908 paper “On the Theory of Brownian Motion”,” *American Journal of Physics*, vol. 65, pp. 1079–1081, 1997.
- [84] A. Einstein, “Über die von der molekularkinetischen Theorie der Wärme geforderte Bewegung von in ruhenden Flüssigkeiten suspendierten Teilchen,” *Annalen der Physik*, vol. 322, no. 8, pp. 549–560, 1905.
- [85] M. Smoluchowski, “Zur kinetischen Theorie der Brownschen Molekularbewegung und der Suspensionen,” *Annalen der Physik*, vol. 326, no. 14, pp. 756–780, 1906.
- [86] L. Onsager and S. Machlup, “Fluctuations and irreversible processes,” *Physical Review*, vol. 91, no. 6, pp. 1505–1512, 1953.
- [87] N. Wiener, “The Average of an Analytic Functional,” *Proceedings of the National Academy of Sciences*, vol. 7, pp. 253–260, 1921.
- [88] N. Wiener, “The average of an analytic function and the Brownian movement,” *Proceedings of the National Academy of Sciences*, vol. 7, pp. 294–298, 1921.
- [89] B. Øksendal, *Stochastic Differential Equations*. Springer, Berlin, Heidelberg, 1998.
- [90] H. Mori, “Transport, Collective Motion, and Brownian Motion,” *Progress of Theoretical Physics*, vol. 33, no. 3, p. 423, 1965.
- [91] A.-L. Barabási and H. E. Stanley, *Fractal Concepts in Surface Growth*. Cambridge University Press, 1995.
- [92] A. Fulinski, “On Marian Smoluchowski’s life and contribution to physics,” *Acta Physica Polonica B*, vol. 29, no. 6, pp. 1523–1537, 1998.
- [93] P. Hänggi and P. Jung, “Colored Noise in Dynamical Systems,” *Advances in Chemical Physics*, vol. 89, pp. 239–326, 1995.
- [94] H. Risken, *The Fokker-Planck equation*. Berlin: Springer, 1996.
- [95] D. Dürr and S. Teufel, *Bohmian Mechanics*. Springer-Verlag Berlin Heidelberg, 2009.
- [96] E. Nelson, “Comment on derivation of the Schrödinger equation from Newtonian mechanics,” *Physical Review*, vol. 150, no. 4, p. 1079, 1966.
- [97] S. Machlup and L. Onsager, “Fluctuations and irreversible process. II. Systems with kinetic energy,” *Physical Review*, vol. 91, no. 6, pp. 1512–1515, 1953.
- [98] L. F. Cugliandolo and V. Lecomte, “Rules of calculus in the path integral representation of white noise Langevin equations: The Onsager-Machlup approach,” *Journal of Physics A*, vol. 50, p. 345001, 2017.

- [99] H. S. Wio, P. Colet, M. San Miguel, L. Pesquera, and M. A. Rodríguez, “Path-integral formulation for stochastic processes driven by colored noise,” *Physical Review A*, vol. 40, no. 12, pp. 7312–7324, 1989.
- [100] L. Caprini, U. M. B. Marconi, A. Puglisi, and A. Vulpiani, “The entropy production of Ornstein-Uhlenbeck active particles: a path integral method for correlations,” *Journal of Statistical Mechanics*, p. 053203, 2019.
- [101] U. Seifert, “Entropy production along a stochastic trajectory and an integral fluctuation theorem,” *Physical Review Letters*, vol. 95, p. 040602, 2005.
- [102] S. Pigolotti, I. Neri, É. Roldán, and F. Jülicher, “Generic Properties of Stochastic Entropy Production,” *Physical Review Letters*, vol. 119, p. 140604, 2017.
- [103] J. B. Weiss, “Coordinate invariance in stochastic dynamical systems,” *Tellus A*, vol. 55, no. 3, pp. 208–218, 2003.
- [104] C. Battle, C. P. Broedersz, N. Fakhri, V. F. Geyer, J. Howard, C. F. Schmidt, and F. C. MacKintosh, “Broken detailed balance at mesoscopic scales in active biological systems,” *Science*, vol. 352, no. 6285, pp. 604–607, 2016.
- [105] J. P. Gonzalez, J. C. Neu, and S. W. Teitworth, “Experimental metrics for detection of detailed balance violation,” *Physical Review E*, vol. 99, p. 022143, 2019.
- [106] J. Gladrow, N. Fakhri, F. C. MacKintosh, C. F. Schmidt, and C. P. Broedersz, “Broken Detailed Balance of Filament Dynamics in Active Networks,” *Physical Review Letters*, vol. 116, p. 248301, 2016.
- [107] J. Gladrow, C. P. Broedersz, and C. F. Schmidt, “Nonequilibrium dynamics of probe filaments in actin-myosin networks,” *Physical Review E*, vol. 96, p. 022408, 2017.
- [108] F. Mura, G. Gradziuk, and C. P. Broedersz, “Nonequilibrium Scaling Behavior in Driven Soft Biological Assemblies,” *Physical Review Letters*, vol. 121, p. 038002, 2018.
- [109] G. Gradziuk, F. Mura, and C. P. Broedersz, “Scaling behavior of nonequilibrium measures in internally driven elastic assemblies,” *Physical Review E*, vol. 99, p. 052406, 2019.
- [110] F. Mura, G. Gradziuk, and C. P. Broedersz, “Mesoscopic non-equilibrium measures can reveal intrinsic features of the active driving,” *Soft Matter*, vol. 15, pp. 8067–8076, 2019.
- [111] G. Gradziuk, G. Torregrosa, and C. P. Broedersz, “Irreversibility in linear systems with colored noise,” *Physical Review E*, vol. 105, p. 024118, 2022.

- [112] A. W. C. Lau, B. D. Hoffman, A. Davies, J. C. Crocker, and T. C. Lubensky, “Microrheology, Stress Fluctuations, and Active Behavior of Living Cells,” *Physical Review Letters*, vol. 91, p. 198101, nov 2003.
- [113] S. Yamada, D. Wirtz, and S. C. Kuo, “Mechanics of living cells measured by laser tracking microrheology,” *Biophysical Journal*, vol. 78, pp. 1736–1747, 2000.
- [114] M. L. Gardel, M. T. Valentine, J. C. Crocker, A. R. Bausch, and D. A. Weitz, “Microrheology of entangled F-actin solutions,” *Physical Review Letters*, vol. 91, no. 15, p. 158302, 2003.
- [115] É. Fodor, M. Guo, N. S. Gov, P. Visco, D. A. Weitz, and F. Van Wijland, “Activity-driven fluctuations in living cells,” *Europhysics Letters*, vol. 110, p. 48005, 2015.
- [116] C. P. Brangwynne, G. H. Koenderink, E. Barry, Z. Dogic, F. C. MacKintosh, and D. A. Weitz, “Bending dynamics of fluctuating biopolymers probed by automated high-resolution filament tracking,” *Biophysical Journal*, vol. 93, pp. 346–359, 2007.
- [117] C. P. Brangwynne, G. H. Koenderink, F. C. MacKintosh, and D. A. Weitz, “Nonequilibrium Microtubule Fluctuations in a Model Cytoskeleton,” *Physical Review Letters*, vol. 100, p. 118104, 2008.
- [118] N. Fakhri, A. D. Wessel, C. Willms, M. Pasquali, D. R. Klopfenstein, F. C. MacKintosh, and C. F. Schmidt, “High-resolution mapping of intracellular fluctuations using carbon nanotubes,” *Science*, vol. 344, no. 6187, pp. 1031–1035, 2014.
- [119] B. Fabry, G. N. Maksym, J. P. Butler, M. Glogauer, D. Navajas, and J. J. Fredberg, “Scaling the microrheology of living cells,” *Physical Review Letters*, vol. 87, no. 14, p. 148102, 2001.
- [120] D. A. Fletcher and R. D. Mullins, “Cell mechanics and the cytoskeleton,” *Nature*, vol. 463, pp. 485–492, 2010.
- [121] A. R. Bausch and K. Kroy, “A bottom-up approach to cell mechanics,” *Nature Physics*, vol. 2, pp. 231–238, 2006.
- [122] K. E. Kasza, A. C. Rowat, J. Liu, T. E. Angelini, C. P. Brangwynne, G. H. Koenderink, and D. A. Weitz, “The cell as a material,” *Current Opinion in Cell Biology*, vol. 19, pp. 101–107, 2007.
- [123] A. J. Ehrlicher, R. Krishnan, M. Guo, C. M. Bidan, D. A. Weitz, and M. R. Pollak, “Alpha-actinin binding kinetics modulate cellular dynamics and force generation,” *Proceedings of the National Academy of Sciences*, vol. 112, no. 21, pp. 6619–6624, 2015.

- [124] W. W. Ahmed and T. Betz, “Dynamic cross-links tune the solid-fluid behavior of living cells,” *Proceedings of the National Academy of Sciences*, vol. 112, no. 21, pp. 6527–6528, 2015.
- [125] M. L. Gardel, J. H. Shin, F. C. MacKintosh, L. Mahadevan, P. Matsudaira, and D. A. Weitz, “Elastic behavior of cross-linked and bundled actin networks,” *Science*, vol. 304, pp. 1301–1305, 2004.
- [126] D. Humphrey, C. Duggan, D. Saha, D. Smith, and J. Käs, “Active fluidization of polymer networks through molecular motors,” *Nature*, vol. 416, pp. 413–416, 2002.
- [127] G. H. Koenderink, Z. Dogic, F. Nakamura, P. M. Bendix, F. C. MacKintosh, J. H. Hartwig, T. P. Stossel, and D. A. Weitz, “An active biopolymer network controlled by molecular motors,” *Proceedings of the National Academy of Sciences*, vol. 106, no. 36, pp. 15192–15197, 2009.
- [128] O. J. N. Bertrand, D. K. Fygenson, and O. A. Saleh, “Active, motor-driven mechanics in a DNA gel,” *Proceedings of the National Academy of Sciences*, vol. 109, no. 43, pp. 17342–17347, 2012.
- [129] F. C. MacKintosh and A. J. Levine, “Nonequilibrium Mechanics and Dynamics of Motor-Activated Gels,” *Physical Review Letters*, vol. 100, p. 018104, jan 2008.
- [130] C. P. Broedersz, M. Depken, N. Y. Yao, M. R. Pollak, D. A. Weitz, and F. C. MacKintosh, “Cross-link-governed dynamics of biopolymer networks,” *Physical Review Letters*, vol. 105, p. 238101, 2010.
- [131] N. Y. Yao, C. P. Broedersz, M. Depken, D. J. Becker, M. R. Pollak, F. C. MacKintosh, and D. A. Weitz, “Stress-Enhanced Gelation: A Dynamic Nonlinearity of Elasticity,” *Physical Review Letters*, vol. 110, p. 018103, 2013.
- [132] M. Guo, A. J. Ehrlicher, M. H. Jensen, M. Renz, J. R. Moore, R. D. Goldman, J. Lippincott-Schwartz, F. C. Mackintosh, and D. A. Weitz, “Probing the stochastic, motor-driven properties of the cytoplasm using force spectrum microscopy,” *Cell*, vol. 158, pp. 822–832, 2014.
- [133] F. Amblard, A. C. Maggs, B. Yurke, A. N. Pargellis, and S. Leibler, “Subdiffusion and Anomalous Local Viscoelasticity in Actin Networks,” *Physical Review Letters*, vol. 77, no. 21, p. 4470, 1996.
- [134] F. Ziemann, J. Rädler, and E. Sackmann, “Local measurements of viscoelastic moduli of entangled actin networks using an oscillating magnetic bead micro-rheometer,” *Biophysical Journal*, vol. 66, pp. 2210–2216, 1994.
- [135] T. G. Mason and D. A. Weitz, “Optical measurements of frequency-dependent linear viscoelastic moduli of complex fluids,” *Physical Review Letters*, vol. 74, no. 7, pp. 1250–1253, 1995.

- [136] D. Mizuno, D. A. Head, F. C. MacKintosh, and C. F. Schmidt, “Active and passive microrheology in equilibrium and nonequilibrium systems,” *Macromolecules*, vol. 41, pp. 7194–7202, 2008.
- [137] J. C. Crocker, M. T. Valentine, E. R. Weeks, T. Gisler, P. D. Kaplan, A. G. Yodh, and D. A. Weitz, “Two-point microrheology of inhomogeneous soft materials,” *Physical Review Letters*, vol. 85, no. 4, pp. 888–891, 2000.
- [138] M. Sheinman, C. P. Broedersz, and F. C. MacKintosh, “Actively stressed marginal networks,” *Physical Review Letters*, vol. 109, p. 238101, 2012.
- [139] F. S. Gnesotto, B. M. Remlein, and C. P. Broedersz, “Nonequilibrium dynamics of isostatic spring networks,” *Physical Review E*, vol. 100, p. 013002, 2019.
- [140] J. B. Manneville, P. Bassereau, S. Ramaswamy, and J. Prost, “Active membrane fluctuations studied by micropipet aspiration,” *Physical Review E*, vol. 64, p. 021908, 2001.
- [141] W. W. Ahmed, É. Fodor, M. Almonacid, M. Bussonnier, M. H. Verlhac, N. Gov, P. Visco, F. van Wijland, and T. Betz, “Active Mechanics Reveal Molecular-Scale Force Kinetics in Living Oocytes,” *Biophysical Journal*, vol. 114, no. 7, pp. 1667–1679, 2018.
- [142] T. H. Tan, G. A. Watson, Y.-C. Chao, J. Li, T. R. Gingrich, J. M. Horowitz, and N. Fakhri, “Scale-dependent irreversibility in living matter,” *arXiv preprint*, p. 2107.05701v1, 2021.
- [143] P. G. De Gennes, “II. Inclusion of Hydrodynamic Interactions,” *Macromolecules*, vol. 9, no. 4, pp. 594–598, 1975.
- [144] K. Yasuda, R. Okamoto, and S. Komura, “Anomalous diffusion in viscoelastic media with active force dipoles,” *Physical Review E*, vol. 95, p. 032417, 2017.
- [145] A. Berut, A. Petrosyan, and S. Ciliberto, “Energy flow between two hydrodynamically coupled particles kept at different effective temperatures,” *Europhysics Letters*, vol. 107, p. 60004, 2014.
- [146] A. Bérut, A. Imparato, A. Petrosyan, and S. Ciliberto, “Stationary and transient fluctuation theorems for effective heat fluxes between hydrodynamically coupled particles in optical traps,” *Physical Review Letters*, vol. 116, p. 068301, 2016.
- [147] C. P. Brangwynne, G. H. Koenderink, F. C. MacKintosh, and D. A. Weitz, “Cyttoplasmic diffusion: Molecular motors mix it up,” *Journal of Cell Biology*, vol. 183, no. 4, pp. 583–587, 2008.

- [148] Y. Bae, D.-K. Kim, and H. Jeong, “Attaining entropy production and dissipation maps from Brownian movies via neural networks,” *arXiv preprint*, p. 2106.15108v1, 2021.
- [149] G. J. Stephens, B. Johnson-Kerner, W. Bialek, and W. S. Ryu, “Dimensionality and dynamics in the behavior of *C. elegans*,” *PLoS Computational Biology*, vol. 4, no. 4, p. e10000028, 2008.
- [150] G. J. Stephens, M. B. De Mesquita, W. S. Ryu, and W. Bialek, “Emergence of long timescales and stereotyped behaviors in *Caenorhabditis elegans*,” *Proceedings of the National Academy of Sciences*, vol. 108, no. 18, pp. 7286–7289, 2011.
- [151] J. Kain, C. Stokes, Q. Gaudry, X. Song, J. Foley, R. Wilson, and B. De Bivort, “Leg-tracking and automated behavioural classification in *Drosophila*,” *Nature Communications*, vol. 4, p. 1910, 2013.
- [152] G. J. Berman, D. M. Choi, W. Bialek, and J. W. Shaevitz, “Mapping the stereotyped behaviour of freely moving fruit flies,” *Journal of the Royal Society Interface*, vol. 11, p. 20140672, 2014.

Related Publications

The following sections consist of reprints of the publications representative of the scientific work performed during my doctoral studies, and referred to throughout the preceding chapters. We first list the relevant publications, specifying the key results and the contributions of the authors.

Nonequilibrium scaling behavior in driven soft biological assemblies

Reference

Nonequilibrium scaling behavior in driven soft biological assemblies

Federica Mura*, Grzegorz Gradziuk*, and Chase P. Broedersz

Physical Review Letters **121**, 038002 (2018)

Author contributions

F.M. and C.P.B. conceived the project. G.G. developed the mathematical background. F.M. and G.G. performed numerical calculations. F.M., G.G. and C.P.B. wrote the paper.

Abstract

Measuring and quantifying nonequilibrium dynamics in active biological systems is a major challenge because of their intrinsic stochastic nature and the limited number of variables accessible in any real experiment. We investigate what nonequilibrium information can be extracted from noninvasive measurements using a stochastic model of soft elastic networks with a heterogeneous distribution of activities, representing enzymatic force generation. In particular, we use this model to study how the nonequilibrium activity, detected by tracking two probes in the network, scales as a function of the distance between the probes. We quantify the nonequilibrium dynamics through the cycling frequencies, a simple measure of circulating currents in the phase space of the probes. We find that these cycling frequencies exhibit power-law scaling behavior with the distance between probes. In addition, we show that this scaling behavior governs the entropy production rate that can be recovered from the two traced probes. Our results provide insight into how internal enzymatic driving generates nonequilibrium dynamics on different scales in soft biological assemblies.

Key results

- We propose a novel noninvasive measurement allowing to probe the nonequilibrium behaviour in actively driven soft networks. The measurement consists in tracking the positions of pairs of tracer particles and measuring the on average cyclic motion in the 2-dimensional position space.
- Using a simple model of an actively driven network, we show numerically that the proposed measure of irreversibility called *cycling frequency*, follows a power law as a

function of distance between the tracer beads. We verify that the scaling behaviour persists for various geometries of the network in various dimensions. The scaling exponent depends on the dimension, but not on the details of the network.

- We confirm the power-law decay analytically, by relating the cycling frequencies to the structure of the covariance matrix. The covariance matrix itself is obtained by exploiting an analogy between a class of Lyapunov equations and the diffusion equation.
- The cycling frequencies can be used to calculate a lower bound for the entropy production rate. This lower bound is shown to also follow a power law as a function of distance between the tracer beads.

Scaling behavior of nonequilibrium measures in internally driven elastic assemblies

Reference

Scaling behavior of nonequilibrium measures in internally driven elastic assemblies

Grzegorz Gradziuk, Federica Mura, and Chase P. Broedersz

Physical Review E **99**, 052406 (2019)

Author contributions

G.G., F.M. and C.P.B. conceived the project. G.G. developed the mathematical background. F.M. and G.G. performed numerical calculations. G.G., F.M. and C.P.B. wrote the paper.

Abstract

Detecting and quantifying nonequilibrium activity is essential for studying internally driven assemblies, including synthetic active matter and complex living systems such as cells or tissue. We discuss a noninvasive approach of measuring nonequilibrium behavior based on the breaking of detailed balance. We focus on “cycling frequencies”—the average frequency with which the trajectories of pairs of degrees of freedom revolve in phase space—and explain their connection with other nonequilibrium measures, including the area enclosing rate and the entropy production rate. We test our approach on simple toy models composed of elastic networks immersed in a viscous fluid with site-dependent internal driving. We prove both numerically and analytically that the cycling frequencies obey a power law as a function of distance between the tracked degrees of freedom. Importantly, the behavior of the cycling frequencies contains information about the dimensionality of the system and the amplitude of active noise. The mapping we use in our analytical approach thus offers a convenient framework for predicting the behavior of two-point nonequilibrium measures for a given activity distribution in the network.

Key results

In this publication we present in more detail and extend the results published in Physical Review Letters **121**, 038002 (2018).

- We study how measures of irreversibility defined for pairs of tracer beads embedded in a driven viscoelastic network depend on the distance between the beads. Apart from the cycling frequencies we consider a different measure called *area enclosing rates* and show how these two measures are related in general.

- For both of the measures we demonstrate analytically that they follow a power-law decay as a function of the distance between the tracer beads. We predict theoretically how the exponent of the power law depends on the dimensionality of the system. This prediction agrees with the previously obtained numerical results.
- In the limit of weak driving the cycling frequencies are proportional to the amplitude of the active driving and inversely proportional to the temperature of the bath. The area enclosing rates are proportional to the amplitude of the active driving even beyond the limit of weak driving, as long as the dynamics of the network can be treated as linear.
- We discuss how the mapping between the Lyapunov equation and the diffusion equation that we employ in our analytical derivations could be generalised to networks of different geometry.

Irreversibility in linear systems with colored noise

Reference

Irreversibility in linear systems with colored noise

Grzegorz Gradziuk, Gabriel Torregrosa, and Chase P. Broedersz

Physical Review E **105**, 024118 (2022)

Author contributions

G.G. and C.P.B. conceived the project. G.G. and G.T. developed the mathematical framework. G.G. and C.P.B. wrote the paper. Part of this work was presented in the Master thesis by G. Torregrosa, supervised by C. P. Broedersz and co-supervised by G. Gradziuk.

Abstract

Time-irreversibility is a distinctive feature of non-equilibrium dynamics and several measures of irreversibility have been introduced to assess the distance from thermal equilibrium of a stochastically driven system. While the dynamical noise is often approximated as white, in many real applications the time correlations of the random forces can actually be significantly long-lived compared to the relaxation times of the driven system. We analyze the effects of temporal correlations in the noise on commonly used measures of irreversibility and demonstrate how the theoretical framework for white noise driven systems naturally generalizes to the case of colored noise. Specifically, we express the auto-correlation function, the area enclosing rates, and mean phase space velocity in terms of solutions of a Lyapunov equation and in terms of their white noise limit values.

Key results

- We develop a framework for calculating various measures of irreversibility such as the autocovariance function, or the area enclosing rates for linear systems driven by colored noise. The results are exact for arbitrary correlations of the dynamical noise and not only close to the white-noise limit.
- We find that the considered measures of irreversibility depend only on the second order correlations of the dynamical noise, meaning that two qualitatively different types of driving can result in exactly the same measurement for the autocorrelation, or area enclosing rates, while also producing qualitatively different dynamics.

- We identify an object called *spreading matrix*, which encodes the temporal correlations of the dynamical noise combined with the way forces are transmitted in the system. The spreading matrix allows for easily transforming the white noise limit results into results for the corresponding colored noise problem.
- For the specific case of Ornstein-Uhlenbeck noise, often employed to model persistent motion, we find the full probability distribution and expressions for the mean velocity field.
- We revisit the problem of scaling behaviour of nonequilibrium measures in driven viscoelastic networks studies in [108, 109, 110], where the active noise was assumed to be white. We show that accounting for the time correlations in the driving qualitatively changes the scaling behaviour at short distances, giving rise to an emergent length. At larger distances, at which the relaxation times are large compared to the correlation times of the noise, the white noise behaviour is recovered.

Learning the non-equilibrium dynamics of Brownian movies

Reference

Learning the non-equilibrium dynamics of Brownian movies

Federico S. Gnesotto, Grzegorz Gradziuk, Pierre Ronceray, and Chase P. Broedersz
Nature Communications **11**, 5378 (2020)

Author contributions

P.R. and C.P.B. conceived the project. F.S.G. wrote the new codes developed in this manuscript and performed all simulations and Brownian movies analysis. P.R. provided support for the Stochastic Force Inference analysis and G.G. largely developed the derivations underlying the Dissipative Component Analysis (DCA). All authors contributed conceptually to developing the Brownian movie analysis and DCA frameworks, interpreting the results, and writing the paper.

Abstract

Time-lapse microscopy imaging provides direct access to the dynamics of soft and living systems. At mesoscopic scales, such microscopy experiments reveal intrinsic thermal and non-equilibrium fluctuations. These fluctuations, together with measurement noise, pose a challenge for the dynamical analysis of these Brownian movies. Traditionally, methods to analyze such experimental data rely on tracking embedded or endogenous probes. However, it is in general unclear, especially in complex many-body systems, which degrees of freedom are the most informative about their non-equilibrium nature. Here, we introduce an alternative, tracking-free approach that overcomes these difficulties via an unsupervised analysis of the Brownian movie. We develop a dimensional reduction scheme selecting a basis of modes based on dissipation. Subsequently, we learn the non-equilibrium dynamics, thereby estimating the entropy production rate and time-resolved force maps. After benchmarking our method against a minimal model, we illustrate its broader applicability with an example inspired by active biopolymer gels.

Key results

- We develop a novel tool for unsupervised analysis of time-lapse microscopy data. The presented framework allows for inferring the dynamics and estimating its irreversibility by treating the series of images as a noisy dynamical system.

- Before inferring the image dynamics, we employ a novel dimensionality reduction scheme aimed at selecting the modes of the dynamics that exhibit the strongest irreversibility. The reduction scheme relies on diagonalizing the area enclosing rates matrix.
- The inference scheme gives us access to configuration dependent deterministic force fields and diffusion tensor.
- We test our framework on a computer generated series of images imitating the dynamics of a driven cytoskeletal assembly. Within this example, the performance of our framework is robust to measurement noise and limited image resolution.

A Nonequilibrium scaling behavior in driven soft biological assemblies

This section is a reprint of the following publication:

Nonequilibrium scaling behavior in driven soft biological assemblies

Federica Mura*, Grzegorz Gradziuk*, and Chase P. Broedersz†

*equal contribution

† corresponding author

Physical Review Letters **121**, 038002 (2018)

Nonequilibrium Scaling Behavior in Driven Soft Biological Assemblies

Federica Mura, Grzegorz Gradziuk, and Chase P. Broedersz*
*Arnold-Sommerfeld-Center for Theoretical Physics and Center for NanoScience,
 Ludwig-Maximilians-Universität München, D-80333 München, Germany*

 (Received 30 January 2018; revised manuscript received 13 April 2018; published 18 July 2018)

Measuring and quantifying nonequilibrium dynamics in active biological systems is a major challenge because of their intrinsic stochastic nature and the limited number of variables accessible in any real experiment. We investigate what nonequilibrium information can be extracted from noninvasive measurements using a stochastic model of soft elastic networks with a heterogeneous distribution of activities, representing enzymatic force generation. In particular, we use this model to study how the nonequilibrium activity, detected by tracking two probes in the network, scales as a function of the distance between the probes. We quantify the nonequilibrium dynamics through the cycling frequencies, a simple measure of circulating currents in the phase space of the probes. We find that these cycling frequencies exhibit power-law scaling behavior with the distance between probes. In addition, we show that this scaling behavior governs the entropy production rate that can be recovered from the two traced probes. Our results provide insight into how internal enzymatic driving generates nonequilibrium dynamics on different scales in soft biological assemblies.

DOI: [10.1103/PhysRevLett.121.038002](https://doi.org/10.1103/PhysRevLett.121.038002)

Cells and tissue constitute a class of nonequilibrium many-body systems [1–5]. Indeed, nonequilibrium activity has been observed in various biological systems, including membranes [6,7], chromosomes [8], and the cytoplasm [9–11]. A distinguishing physical feature of such biological assemblies is that they are driven out of equilibrium collectively by internal enzymatic processes that break the detailed balance at the molecular scale. The active nature of living matter on larger scales can be determined noninvasively by observing the steady-state stochastic dynamics of mesoscopic degrees of freedom using time-lapse microscopy experiments: the nonequilibrium dynamics of these systems can manifest as circulating probability currents in a phase space of mesoscopic coordinates [2, 12–14]. However, it remains unclear how such nonequilibrium measures depend on the spatial scale on which the measurement is performed. A theoretical understanding of the spatial scaling behavior of broken detailed balance in internally driven biological assemblies may reveal how to extract quantitative information from measurable phase space currents to characterize the active nature of the system.

Here we consider a simple, yet general model for an internally driven elastic assembly to study nonequilibrium scaling behavior. This assembly is driven out of equilibrium by heterogeneously distributed stochastic forces, representing internal enzymatic activity (Fig. 1). We quantify the nonequilibrium dynamics of such an assembly by the cycling frequencies associated with steady-state circulating currents in phase space [13,14]. To study how broken detailed balance manifests on different scales in a given system, we investigate how the cycling frequency of a pair

of tracer probes depends on the spatial distance between these probes. Interestingly, the cycling frequencies in our model exhibit a power-law scaling with the distance between probes with an exponent that depends on the dimensionality of the system. To provide a conceptual understanding of this scaling behavior, we develop an analytical calculation of these exponents. Furthermore, we show that the exponent associated with the power law of the cycling frequencies also underlies the scaling behavior of the entropy production rate that can be recovered from measured trajectories. Therefore, we provide a framework to study the spatial scaling behavior of nonequilibrium measures in soft elastic assemblies.

Our model consists of a d -dimensional elastic network of N beads, immersed in a simple Newtonian liquid at temperature T [15–18]. We assume a lattice structure where each bead is connected to its nearest neighbours by springs of elastic constant k , as illustrated in Fig. 1. For simplicity, we model internal enzymatic activity by a Gaussian white noise with variance α_i at bead i . By assuming white noise, we effectively consider the dynamics of biological systems on timescales much longer than the characteristic timescales of the active processes [13,19,20]. Importantly, these activity amplitudes, $\alpha_i \geq 0$, are spatially heterogeneous, reflecting a spatial distribution of active processes in the system. These activity amplitudes are drawn independently from a distribution p_α with mean $\bar{\alpha} < \infty$ and standard deviation $\sigma_\alpha < \infty$ for each realization of the system. This description of a heterogeneously driven assembly is similar to bead-spring models in which the beads are coupled to distinct heat baths at different temperatures [21–23].

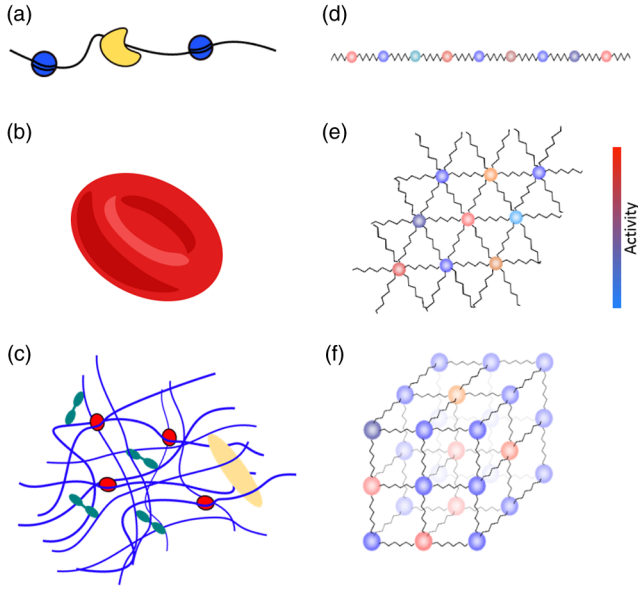


FIG. 1. Schematic illustrating soft viscoelastic networks with heterogeneous driving for various types of cellular systems. (a) Chromosome, (b) red blood cell membrane, (c) cytoskeletal network with (d)–(f) associated bead-spring models with heterogeneous active driving. The color of the bead indicates the intensity of activity, representing the variance (increasing from blue to red) of the associated active noise process.

The temporal evolution of the probability distribution $p(\mathbf{x}, t)$ of the beads' displacements \mathbf{x} , relative to their rest positions, is governed by a Fokker-Planck equation

$$\begin{aligned} \frac{\partial p(\mathbf{x}, t)}{\partial t} &= -\nabla \cdot [\mathbf{A}\mathbf{x}p(\mathbf{x}, t)] + \nabla \cdot \mathbf{D}\nabla p(\mathbf{x}, t), \\ &= -\nabla \cdot \mathbf{j}(\mathbf{x}, t), \end{aligned} \quad (1)$$

where $\mathbf{j}(\mathbf{x}, t) = \mathbf{A}\mathbf{x}p(\mathbf{x}, t) - \mathbf{D}\nabla p(\mathbf{x}, t)$ is the probability current. Here, \mathbf{A} is the elastic interaction matrix, incorporating all nearest neighbor spring interactions between beads; the mobility matrix is assumed to be diagonal to exclude hydrodynamic interactions between the beads and is absorbed in \mathbf{A} . The diffusion matrix \mathbf{D} is diagonal with elements $d_{ij} = \delta_{ij}[k_B(T + \alpha_i)/\gamma]$, where γ is the damping coefficient describing the viscous interaction between a bead and the immersing liquid. The steady-state dynamics of this active network is described by

$$p(\mathbf{x}) = \frac{1}{\sqrt{(2\pi)^{dN} \det \mathbf{C}}} e^{-\frac{1}{2}\mathbf{x}^T \mathbf{C}^{-1} \mathbf{x}}, \quad (2)$$

where $\mathbf{C} = \langle \mathbf{x} \otimes \mathbf{x} \rangle$ is the covariance matrix, which can be obtained by solving the Lyapunov equation $\mathbf{A}\mathbf{C} + \mathbf{C}\mathbf{A}^T = -2\mathbf{D}$ [24]. In the simplest limit, the activities are spatially homogeneous: $\alpha_i = \alpha \forall i$, resulting in effectively equilibrium dynamics, with $p(\mathbf{x})$ given by the Boltzmann distribution [$\mathbf{C}^{-1} = -\mathbf{A}/(T + \alpha)$] and $\mathbf{j} = \mathbf{0}$. By contrast, in

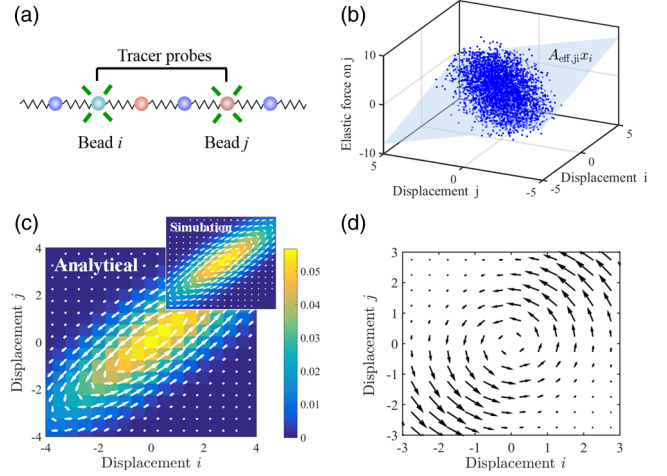


FIG. 2. Reduced system of tracked probed. (a) Schematic of two fluorescently labeled probe beads in a larger system. (b) Elastic force acting on bead j obtained at different time steps of a simulation of the Langevin dynamics of the full system (blue points) and the effective linear force $\mathbf{A}_{\text{eff}}\mathbf{x}_r$ from analytical calculations (light blue plane). (c) Probability density (color map) and probability current (white arrows) calculated analytically from the effective 2D system, together with results from simulating the full system in the inset. (d) The nonconservative part of the effective force field, $[(\mathbf{A}_{\text{eff}} - \mathbf{A}_{\text{eff}}^T)/2]\mathbf{x}_r$ (black arrows), can contribute to the rotation in phase space in nonequilibrium systems. Note, for $\alpha_i = \alpha \forall i$ (effective equilibrium scenario), \mathbf{A}_{eff} becomes symmetric.

heterogeneously driven systems with nonidentical α_i 's, we obtain nonequilibrium steady-state dynamics with $\mathbf{j} \neq \mathbf{0}$ [24].

If we were able to observe the stochastic motion of all beads in the network, we could directly measure the full probability current $\mathbf{j}(\mathbf{x})$ and extract information about the complete nonequilibrium dynamics of the system. However, in an actual experiment, typically only a small subset of the degrees of freedom can be tracked [Fig. 2(a)]. What information on the nonequilibrium dynamics of the system can be extracted from such limited observations? To address this question, we investigate a scenario where only a few degrees of freedom are accessible.

We start by reducing our description to the marginal distribution, $p_r(\mathbf{x}_r) = \int dx_{k \notin [r]} p(x_1, x_2, \dots, x_{dN})$, of a subset $[r]$ of n tracked degrees of freedom \mathbf{x}_r . By integrating out the subset $[l]$ of m unobserved degrees of freedom \mathbf{x}_l on both sides of Eq. (1) and taking the steady-state limit, we obtain (see Supplemental Material [25])

$$0 = -\nabla \cdot [\mathbf{A}_{\text{eff}}\mathbf{x}_r p_r(\mathbf{x}_r)] + \nabla \cdot \mathbf{D}_{[r,r]} \nabla p_r(\mathbf{x}_r), \quad (3)$$

where the subindex $[r, r]$ of a matrix indicates the submatrix corresponding to the reduced set of observed variables. In addition, we introduce the effective linear interaction [Fig. 2(b)], which can be written as $\mathbf{A}_{\text{eff}}\mathbf{x}_r$, with $\mathbf{A}_{\text{eff}} = \mathbf{A}_{[r,r]} + \mathbf{A}_{[r,l]}\mathbf{C}_{[l,r]}\mathbf{C}_{[r,r]}^{-1}$. Here, $\mathbf{A}_{[r,l]}$ and $\mathbf{C}_{[l,r]}$ are rectangular matrices of sizes $[n \times m]$ and $[m \times n]$, given by the

elements of indices $[r, 1]$ of \mathbf{A} and $[1, r]$ of \mathbf{C} , respectively. Thus, we obtain an effective stationary Fokker-Planck equation for the reduced system (3). From this, we obtain the exact steady-state reduced probability distribution $p_r(\mathbf{x}_r)$ and probability current density:

$$\mathbf{j}_r(\mathbf{x}_r) = \mathbf{A}_{\text{eff}} \mathbf{x}_r p_r(\mathbf{x}_r) + \mathbf{D}_{[r,r]} \mathbf{C}_{[r,r]}^{-1} \mathbf{x}_r p_r(\mathbf{x}_r), \quad (4)$$

which can, in principle, be measured from the trajectories of the observed degrees of freedom [Fig. 2(c)].

We can use this reduced description to investigate how broken detailed balance manifests at different scales in the network. In particular, we consider the simplest case of a reduced system of only two tracked beads in a larger system, as illustrated in Fig. 2(a). It is convenient to quantify the probability currents in the 2D phase space of these two tracer beads by a pseudoscalar quantity: the average cycling frequency around the origin [13,14,26]. For linear systems, we can express the reduced probability current as $\mathbf{j}_r(\mathbf{x}_r) = \mathbf{\Omega}_r \mathbf{x}_r p_r(\mathbf{x}_r)$, where $\mathbf{\Omega}_r$ is a 2D matrix with purely imaginary eigenvalues $\lambda = \pm i\omega$, with ω representing the cycling frequency.

This cycling frequency can be measured experimentally for a pair of degrees of freedom; e.g. the displacements in a certain direction of two probe beads at a distance r . This frequency will depend on the specific configuration of all activity amplitudes α_i . We aim to compute how this cycling frequency depends on r after averaging over all activity configurations. Since ω is expected to be distributed symmetrically around zero, we calculate $\sqrt{\langle \omega^2(r) \rangle_\alpha}$ for pairs of beads separated by a distance r . Here, the average $\langle \dots \rangle_\alpha$ is taken over an ensemble of activities $\{\alpha_i\}$ drawn from the distribution p_α . Intuitively, the magnitude of the circulation of currents in phase space typically decreases with the distance between the probes, as shown in Fig. 3(a). This reduction of the circulation is reflected by a decrease of the cycling frequency ω with distance. Remarkably, $\sqrt{\langle \omega^2(r) \rangle_\alpha}$ appears to depend on the distance between the tracer beads r as a power law, $\sqrt{\langle \omega^2(r) \rangle_\alpha} \propto r^{-\mu}$, with $\mu \approx 1.9$ for a 1D chain with a folded Gaussian or an exponential distribution of activities, as depicted in Fig. 3(b).

To investigate how the architecture of the system affects the scaling behavior of the cycling frequencies, we considered different network structures, including square, triangular, and cubic lattices. In particular, we determined the ensemble average $\langle \dots \rangle_\alpha$ by performing a spatial average for computational convenience (see Supplemental Material [25]). Interestingly, we find that the characteristic exponent μ appears to depend strongly on the dimensionality of the lattice, but not on its geometry, as shown in Figs. 3(b) and 3(c). These results suggest that the distance dependence of the cycling frequency is determined in part by the long wavelength elastic properties of the system. Importantly, however, the scaling of cycling frequency is sensitive to the spatial structure of the

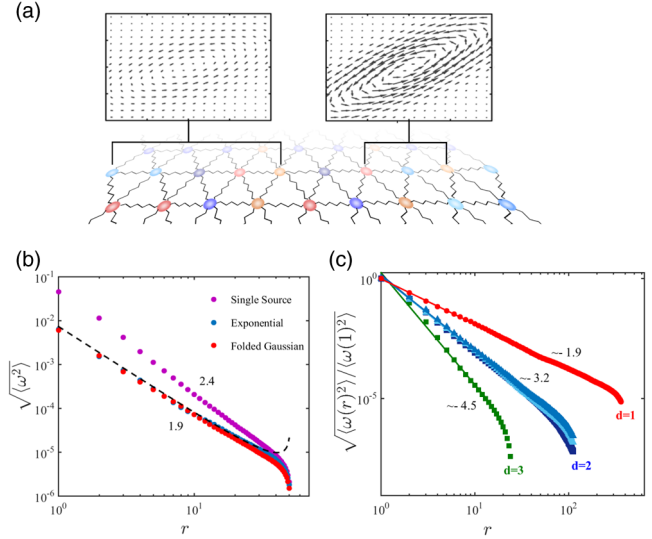


FIG. 3. Spatial scaling behavior of cycling frequencies. (a) Steady-state current cycles in phase space of the displacements (along the lattice direction) of two tracer beads for a nearby pair of probes (left) and distant pair of probes (right). (b) Scaling behavior of the cycling frequencies $\sqrt{\langle \omega^2(r) \rangle}$ of a pair of probes beads as a function of their spatial distances, obtained for a 1D chain and different activity distributions, as indicated in the legend. Black dashed line is obtained from Eq. (10). (c) Scaling behavior of the cycling frequencies $\sqrt{\langle \omega^2(r) \rangle} / \sqrt{\langle \omega^2(1) \rangle}$, obtained for different lattices and a folded Gaussian activity distribution. Triangular and square markers represent triangular and square lattices, respectively. Light (dark) blue triangles represent triangular networks with zero (finite) rest length springs. In both (b) and (c), we used $\bar{\alpha}/T = 0.15$.

activities. For example, in the simple case of a δ -distributed (single-source) activity on a 1D chain, we find $\mu_{\text{single}} \approx 2.4$ [Fig. 3(b)] in contrast to the value 1.9 obtained above for spatially distributed activities.

To obtain more insight into the scaling behavior of the cycling frequencies, we derive an analytical expression for the cycling frequency as a function of the distance between the observed beads $\omega(r)$. In general, it can be shown that, for a linear system described by a Fokker-Planck equation, the cycling frequencies are given by (see Supplemental Material [25])

$$\omega_{ij} = \frac{1}{2\gamma} \frac{\langle \tau_{ij} \rangle}{\sqrt{\det \mathbf{C}_{[r,r]}}, \quad (5)$$

where $\tau_{ij} := \mathbf{x}_r \times \mathbf{f}_r(\mathbf{x}) = x_i f_j(\mathbf{x}) - x_j f_i(\mathbf{x})$ is a generalized phase space torque in the x_i - x_j plane, with $f_i(\mathbf{x})$ denoting the deterministic force acting on the i th bead. This result is intuitive: for an overdamped system, the mean angular velocity is proportional to the mean torque and the factor $1/\sqrt{\det \mathbf{C}_{[r,r]}}$ ensures coordinate invariance. For the 1D chain of beads [Fig. 1(d)], Eq. (5) reduces to

$$\omega_{ij} = \frac{k}{\gamma} \frac{\tilde{\partial}_2^2 c_{ij}}{\sqrt{\det \mathbf{C}_{[r,r]}}}, \quad (6)$$

where c_{ij} is the i th, j th element of the covariance matrix \mathbf{C} , with the discrete second derivative across rows denoted as $\tilde{\partial}_2^2 c_{ij} = c_{i,j+1} - 2c_{i,j} + c_{i,j-1}$. Thereby, we have reduced the problem of calculating $\omega(r)$ to finding the covariance matrix of the system.

The structure of \mathbf{D} suggests a natural decomposition of the covariance matrix \mathbf{C} into equilibrium ($\bar{\mathbf{C}}$) and nonequilibrium (\mathbf{C}^*) contributions: $\mathbf{C} = (k_B T/k) \bar{\mathbf{C}} + (k_B \bar{\alpha}/k) \mathbf{C}^*$, such that $\bar{\mathbf{C}}$ and \mathbf{C}^* are dimensionless. Both $\bar{\mathbf{C}}$ and \mathbf{C}^* can be found by solving the Lyapunov equation, which for the 1D chain is given by

$$\tilde{\partial}_1^2 \bar{c}_{ij} + \tilde{\partial}_2^2 \bar{c}_{ij} = -2\delta_{ij}, \quad (7)$$

$$\tilde{\partial}_1^2 c_{ij}^* + \tilde{\partial}_2^2 c_{ij}^* = -2\delta_{ij} \frac{\alpha_i}{\bar{\alpha}}, \quad (8)$$

where $\tilde{\partial}_1^2$ indicates the discrete second derivative across columns. These equations represent discrete stationary diffusion equations, with sources of divergence given by δ_{ij} and $\delta_{ij}(\alpha_i/\bar{\alpha})$, respectively. This result prescribes how a spatial distribution of activities structures the covariance matrix.

We can make further progress by noting that the principle of detailed balance imposes $\omega_{ij} = 0$ at thermal equilibrium, which together with Eq. (6) implies $\tilde{\partial}_2^2 \bar{c}_{ij} = 0$. We can, therefore, substitute $\tilde{\partial}_2^2 \bar{c}_{ij}$ in Eq. (6) by $\tilde{\partial}_2^2 c_{ij}^*$, and then expand this equation up to linear order in $\bar{\alpha}/T$ to obtain

$$\omega_{ij} = \frac{k \bar{\alpha}}{\gamma T} \frac{\tilde{\partial}_2^2 c_{ij}^*}{\sqrt{\det \bar{\mathbf{C}}_{[r,r]}}}. \quad (9)$$

We proceed by calculating \mathbf{C}^* for a given distribution of activities $\{\alpha_i\}$. Because of the linearity of Eq. (8), \mathbf{C}^* is a superposition of steady-state solutions to single-source problem, i.e., a δ -distribution for which all but one of the activities would be set to zero. Denoting the element of \mathbf{C}^* at a distance r from the single activity source by $c^*(r)$, we obtain the ‘‘covariance current’’ $\partial_r c^*(r) \sim 1/r$. Here we employed a continuous approximation of the discrete diffusion problem in Eqs. (7) and (8). Thus, $c^*(r) = -a \ln(r) + b$ for a single-source problem, with integration constants a and b , representing the Green’s function for our problem. Using this expression for $c^*(r)$ together with Eq. (9), we obtain for the single-source case $\omega_{\text{single}}^2(r) = (k^2/\gamma^2)(\alpha^2/T^2)(a^2/r^4) \{1/\det \bar{\mathbf{C}}_{[r,r]}(r)\}$, where α is the source’s activity.

Next, we use a superposition of single-source solutions for $c^*(r)$ to obtain the nonequilibrium contribution of the covariance matrix \mathbf{C}^* for a specific configuration of many activity sources $\{\alpha_i\}$. Using this result in conjunction with Eq. (9) and performing an ensemble average over the

distribution of activity realizations, we arrive at the central result

$$\langle \omega^2(r) \rangle_\alpha = \frac{k^2 \sigma_\alpha^2 \pi a^2}{\gamma^2 T^2 2r^3} \frac{1}{\det \bar{\mathbf{C}}_{[r,r]}(r)}. \quad (10)$$

Finally, we note that the elements of the equilibrium covariance matrix are given by $\bar{c}_{i,j} = \min(i,j) - ij/(N+1)$ and find that, for $r \ll N$, $\det \bar{\mathbf{C}}_{[r,r]}(r)$ exhibits a power-law behavior $\det \bar{\mathbf{C}}_{[r,r]}(r) \sim Nr$. Therefore, from this analysis, we find for a 1D chain with heterogenous activities $\mu = 2$, independent of the activity distribution p_α . Furthermore, we find $\mu_{\text{single}} = 2.5$ for a single-source activity, in accord with our numerical result [see Fig. 3(b)]. This calculation provides insight into how a combination of features of the equilibrium and nonequilibrium contributions to the covariance matrix determine the spatial scaling behavior of cycling frequencies.

Nonzero cycling frequencies directly reflect broken detailed balance, suggesting a connection between ω and measures of the internal driving, including the rate of entropy production. For a Markovian system described by a Fokker-Planck equation, the total entropy production rate under steady-state conditions is given by [27]

$$\Pi_{\text{tot}} = k_B \int d\mathbf{x} \frac{\mathbf{j}^T(\mathbf{x}) \mathbf{D}^{-1} \mathbf{j}(\mathbf{x})}{p(\mathbf{x})}, \quad (11)$$

where k_B is Boltzmann’s constant. The validity of this result relies on the equivalence between the Fokker-Planck and Langevin descriptions. However, the marginal probability density of the reduced system is described by a Fokker-Planck equation only at steady state [see Eq. (3) and Supplemental Material [25]], reflecting the loss of Markovianity after coarse graining. Even if the real dynamics of the reduced system are non-Markovian, we can define an effective Markovian dynamics through the Langevin equation

$$\frac{d\mathbf{x}_r(t)}{dt} = \mathbf{A}_{\text{eff}} \mathbf{x}_r(t) + \sqrt{2\mathbf{D}_{[r,r]}} \boldsymbol{\xi}_r(t), \quad (12)$$

with Gaussian white noise $\boldsymbol{\xi}_r(t)$. This equation of motion results in the exact steady-state probability and current densities, but with an approximate stochastic dynamics. In particular, the effective interaction matrix \mathbf{A}_{eff} [see Eq. (3)] captures only the average interaction between the traced variables, as illustrated in Fig. 2(b). Furthermore, in contrast to the full deterministic forces ($\mathbf{A}\mathbf{x}$), these effective interactions [Fig. 2(c)] need not derive from a potential and thus may contain a nonconservative component [Fig. 2(d)].

The entropy production rate associated with the effective Markovian dynamics in Eq. (12) is given by

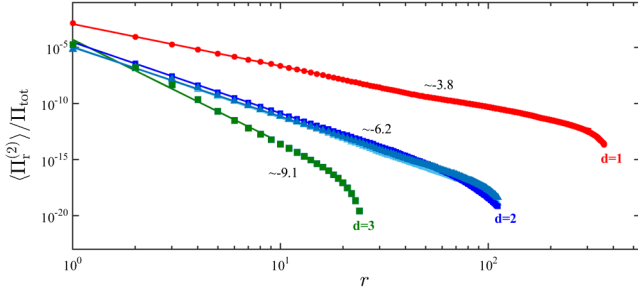


FIG. 4. Spatial scaling behavior of the average entropy production rate $\langle \Pi_r^{(2)} \rangle$ of a pair of probe beads as a function of their spatial distance r , obtained for different lattices, and a folded Gaussian activity distribution with $\bar{\alpha}/T = 0.15$. Note the entropy production rate of the reduced system is scaled by the total entropy production rate of the whole network Π_{tot} . Triangular and square markers represent triangular and square lattices, respectively. Light (dark) blue triangles represent triangular networks with zero (finite) rest length springs.

$$\Pi_r = k_B \int d\mathbf{x}_r \frac{\mathbf{j}_r^T(\mathbf{x}_r) \mathbf{D}_{[r,r]}^{-1} \mathbf{j}_r(\mathbf{x}_r)}{p_r(\mathbf{x}_r)} \leq \Pi_{\text{tot}}, \quad (13)$$

where $\mathbf{j}_r(\mathbf{x}_r)$ is defined in Eq. (4). Note, estimating Π_r by using the Markovian formalism allows us to set a lower bound for the total entropy production rate Π_{tot} (see Supplemental Material [25]), similar to what has already been shown for discrete systems [28]. In the $n = 2$ case with two traced degrees of freedom that we consider here, Eq. (13) reduces to (see Supplemental Material [25])

$$\Pi_r^{(2)} = k_B \omega^2 \text{Tr}(\mathbf{C}_{[r,r]} \mathbf{D}_{[r,r]}^{-1}). \quad (14)$$

This result provides an explicit relation between the partial entropy production rate and the cycling frequency ω . Note, all quantities in the expression for $\Pi_r^{(2)}$ can be observed in an experiment, providing a direct way to noninvasively determine the reduced rate of entropy production for a set of traced degrees of freedom. Since $\text{Tr}(\mathbf{C}_{[r,r]} \mathbf{D}_{[r,r]}^{-1})$ depends only weakly on r , as long as $1 \ll r \ll N$, we expect a scaling behavior $\langle \Pi_r^{(2)} \rangle \sim r^{-2\mu}$. This result shows that the spatial scaling behavior of the cycling frequencies directly determines the spatial scaling behavior of the entropy production rate [see Fig. 4].

In summary, we here demonstrate theoretically how experimental measures of nonequilibrium activity in internally driven linear networks are affected by the length scale at which the system is observed. Specifically, we developed a general framework to predict the scaling behavior of cycling frequencies and the entropy production rate that can be inferred by tracing pairs of degrees of freedom. We showed that the exponent μ that governs this behavior for a system with heterogeneous random activities is insensitive to the details of distribution of activities. However,

this exponent depends sensitively on the dimensionality of the system. The predicted scaling behavior can be tested, for instance, by analyzing the fluctuations of pairs of tracer particles embedded in biological [9–11,29,30] and artificial [31–36] systems under nonequilibrium steady-state conditions.

We thank S. Ceolin, E. Frey, J. Gladrow, F. Gnesotto, P. Ronceray, and C. Schmidt for stimulating discussions. This work was supported by the German Excellence Initiative via the program NanoSystems Initiative Munich (NIM), by a DFG Fellowship through the Graduate School of Quantitative Biosciences Munich (QBM). Part of this work was performed at the Aspen Center for Physics supported by NSF Grant No. PHY-1607611.

F. M. and G. G. contributed equally to this work.

*C.broedersz@lmu.de

- [1] E. Fodor and M. C. Marchetti, [arXiv:1708.08652](#).
- [2] F. Gnesotto, F. Mura, J. Gladrow, and C. P. Broedersz, *Rep. Prog. Phys.* **81**, 066601 (2018).
- [3] F. Jülicher, K. Kruse, J. Prost, and J.-F. Joanny, *Phys. Rep.* **449**, 3 (2007).
- [4] D. Needleman and Z. Dogic, *Nat. Rev. Mater.* **2**, 17048 (2017).
- [5] C. F. Schmidt and F. C. MacKintosh, *Curr. Opin. Cell Biol.* **22**, 29 (2010).
- [6] T. Betz, M. Lenz, J. F. Joanny, and C. Sykes, *Proc. Natl. Acad. Sci. U.S.A.* **106**, 15320 (2009).
- [7] H. Turlier, D. A. Fedosov, B. Audoly, T. Auth, N. S. Gov, J.-F. Joanny, G. Gompper, and T. Betz, *Nat. Phys.* **12**, 513 (2016).
- [8] S. C. Weber, A. J. Spakowitz, and J. A. Theriot, *Proc. Natl. Acad. Sci. U.S.A.* **109**, 7338 (2012).
- [9] A. W. C. Lau, B. D. Hoffman, A. Davies, J. C. Crocker, and T. C. Lubensky, *Phys. Rev. Lett.* **91**, 198101 (2003).
- [10] M. Guo, A. J. Ehrlicher, M. H. Jensen, M. Renz, J. R. Moore, R. D. Goldman, J. L. Schwartz, F. C. MacKintosh, and D. A. Weitz, *Cell* **158**, 822 (2014).
- [11] N. Fakhri, A. D. Wessel, C. Willms, M. Pasquali, D. R. Klopfenstein, F. C. MacKintosh, and C. F. Schmidt, *Science* **344**, 1031 (2014).
- [12] C. Battle, C. P. Broedersz, N. Fakhri, J. Howard, C. F. Schmidt, and F. C. MacKintosh, *Science* **352**, 604 (2016).
- [13] J. Gladrow, N. Fakhri, F. C. MacKintosh, C. F. Schmidt, and C. P. Broedersz, *Phys. Rev. Lett.* **116**, 248301 (2016).
- [14] J. Gladrow, C. P. Broedersz, and C. F. Schmidt, *Phys. Rev. E* **96**, 022408 (2017).
- [15] M. G. Yucht, M. Sheinman, and C. P. Broedersz, *Soft Matter* **9**, 7000 (2013).
- [16] C. P. Broedersz and F. C. MacKintosh, *Rev. Mod. Phys.* **86**, 995 (2014).
- [17] D. Osmanovic and Y. Rabin, *Soft Matter* **13**, 963 (2017).
- [18] X. Mao and T. C. Lubensky, *Annu. Rev. Condens. Matter Phys.* **9**, 413 (2018).

- [19] F. C. MacKintosh and A. J. Levine, *Phys. Rev. Lett.* **100**, 018104 (2008).
- [20] J. Ruostekoski and J. R. Anglin, *Phys. Rev. Lett.* **91**, 190402 (2003).
- [21] Z. Rieder, J. L. Lebowitz, and E. Lieb, *J. Math. Phys. (N.Y.)* **8**, 1073 (1967).
- [22] F. Bonetto, J. L. Lebowitz, and J. Lukkarinen, *J. Stat. Phys.* **116**, 783 (2004).
- [23] G. Falasco, M. Baiesi, L. Molinaro, L. Conti, and F. Baldovin, *Phys. Rev. E* **92**, 022129 (2015).
- [24] H. Risken, *The Fokker-Planck Equation* (Springer, Berlin, 1996).
- [25] See Supplemental Material at <http://link.aps.org/supplemental/10.1103/PhysRevLett.121.038002> for additional details on the derivations of the results in the main text.
- [26] J. B. Weiss, *Tellus A* **55**, 208 (2003).
- [27] U. Seifert, *Rep. Prog. Phys.* **75**, 126001 (2012).
- [28] G. Bisker, M. Poletini, T. R. Gingrich, and J. M. Horowitz, *J. Stat. Mech.* (2017) 093210.
- [29] D. Mizuno, C. Tardin, C. F. Schmidt, and F. C. MacKintosh, *Science* **315**, 370 (2007).
- [30] A. D. Wessel, M. Gumalla, J. Grosshans, and C. F. Schmidt, *Biophys. J.* **108**, 1899 (2015).
- [31] O. Liele, M. M. A. E. Claessens, and A. R. Bauch, *Soft Matter* **6**, 218 (2010).
- [32] J. Palacci, S. Sacanna, A. P. Steinberg, D. J. Pine, and P. M. Chaikin, *Science* **339**, 936 (2013).
- [33] I. Buttinoni, J. Bialké, F. Kümmel, H. Löwen, C. Bechinger, and T. Speck, *Phys. Rev. Lett.* **110**, 238301 (2013).
- [34] G. H. Koenderink, Z. Dogic, F. Nakamura, P. M. Bendix, F. C. MacKintosh, J. H. Hartwig, T. P. Stossel, and D. A. Weitz, *Proc. Natl. Acad. Sci. U.S.A.* **106**, 15192 (2009).
- [35] M. H. Jensen, E. J. Morris, and D. A. Weitz, *Biochim. Biophys. Acta* **1853**, 3038 (2015).
- [36] V. Schaller, C. Weber, C. Semmrich, E. Frey, and A. R. Bausch, *Nature (London)* **467**, 73 (2010).
- [37] Y. L. Tong, *Springer Series in Statistics* (Springer-Verlag, Berlin, 1990).

Supplement: Non-equilibrium scaling behaviour in driven soft biological assemblies

Federica Mura,^{1,*} Grzegorz Gradziuk,^{1,*} and Chase P. Broedersz^{1,†}

¹*Arnold-Sommerfeld-Center for Theoretical Physics and Center for NanoScience,
Ludwig-Maximilians-Universität München, D-80333 München, Germany.*

(Dated: July 6, 2018)

DERIVATION OF EQ. (3)

Here, we derive Eq. (3), which describes the steady state distribution of traced variables. Integrating out the unobserved degrees of freedom on both sides of the Fokker-Plank equation (Eq. (1)), and using the Einstein notation for summing over repeated indexes, we obtain:

$$\overbrace{\int d\mathbf{x}_1 \partial_t p(\mathbf{x})}^{(I)} = - \overbrace{\int d\mathbf{x}_1 \partial_i [a_{ij} x_j p(\mathbf{x}, t)]}^{(II)} + \overbrace{\int d\mathbf{x}_1 d_{ij} \partial_i \partial_j p(\mathbf{x}, t)}^{(III)} \quad (S1)$$

where a_{ij} and d_{ij} are the elements of the interaction matrix \mathbf{A} and the diffusion matrix \mathbf{D} , respectively. Rewriting the probability as $p(\mathbf{x}, t) = p(\mathbf{x}_1 | \mathbf{x}_r, t) p_r(\mathbf{x}_r, t)$, we can separately calculate each term in Eq.(S1). The first term (I) gives:

$$\int d\mathbf{x}_1 \partial_t p_r(\mathbf{x}_r, t) p(\mathbf{x}_1 | \mathbf{x}_r, t) = \partial_t p_r(\mathbf{x}_r, t) \int d\mathbf{x}_1 p(\mathbf{x}_1 | \mathbf{x}_r, t) = \partial_t p_r(\mathbf{x}_r, t) \quad (S2)$$

For the second term (II), we obtain

$$\begin{aligned} \int d\mathbf{x}_1 \partial_i [p_r(\mathbf{x}_r, t) p(\mathbf{x}_1 | \mathbf{x}_r, t) a_{ij} x_j] &= \delta_{i,[r]} \partial_i [p_r(\mathbf{x}_r, t) \int d\mathbf{x}_1 p(\mathbf{x}_1 | \mathbf{x}_r, t) a_{ij} x_j] \\ &= \delta_{i,[r]} \partial_i [p_r(\mathbf{x}_r, t) a_{ij} \langle x_j | \mathbf{x}_r, t \rangle] \end{aligned} \quad (S3)$$

where $\delta_{i,[r]} = 1$ if x_i is one of the observed coordinates and zero otherwise. In the first line we use that the probability density vanishes at infinity faster than $1/x$. Similarly, the third term (III) can be written as

$$\begin{aligned} \int d\mathbf{x}_1 d_{ij} \partial_i \partial_j [p_r(\mathbf{x}_r, t) p(\mathbf{x}_1 | \mathbf{x}_r, t)] &= \delta_{i,[r]} \delta_{j,[r]} d_{ij} \partial_i \partial_j [p_r(\mathbf{x}_r, t) \int d\mathbf{x}_1 p(\mathbf{x}_1 | \mathbf{x}_r, t)] \\ &= \delta_{i,[r]} \delta_{j,[r]} d_{ij} \partial_i \partial_j p_r(\mathbf{x}_r, t) \end{aligned} \quad (S4)$$

We seek a description for the stochastic dynamics, which only depends on the observed degrees of freedom. This can be achieved by taking the steady-state limit. In this case, the conditional average appearing in Eq.(S3) yields $\langle \mathbf{x}_1 | \mathbf{x}_r \rangle = \mathbf{C}_{[1,r]} \mathbf{C}_{[r,r]}^{-1} \mathbf{x}_r$ [S1]. We substitute Eqs. (S2)-(S4) in Eq. (S1) to obtain Eq. (3), which therefore holds only at steady-state.

DERIVATION OF EQ. (5)

Here we derive the expression in Eq. (5) for the cycling frequencies. To this end, we first show that the right hand side of this equation is invariant under orientation preserving linear transformations restricted to the 2-dimensional reduced subspace. Let us consider such a transformation: $\mathbf{x}'_r = \mathbf{B} \mathbf{x}_r$, $\mathbf{f}'_r = \mathbf{B} \mathbf{f}_r$, and denote by $\mathbf{C}'_{[r,r]}$ the reduced covariance matrix in the transformed coordinates.

$$\mathbf{B} \mathbf{C}_{[r,r]} \mathbf{B}^T = \mathbf{C}'_{[r,r]} \quad \implies \quad \det \mathbf{B} = \sqrt{\frac{\det \mathbf{C}'_{[r,r]}}{\det \mathbf{C}_{[r,r]}}} \quad (S5)$$

Using this result together with the transformation properties of the vector product, we obtain

$$\frac{\langle \tau_{ij} \rangle}{\sqrt{\det \mathbf{C}_{[r,r]}}} = \frac{\langle \mathbf{x}_r \times \mathbf{f}_r(\mathbf{x}) \rangle}{\sqrt{\det \mathbf{C}_{[r,r]}}} = \frac{\langle \mathbf{x}'_r \times \mathbf{f}'_r(\mathbf{x}') \rangle}{\sqrt{\det \mathbf{C}_{[r,r]}}} \frac{1}{\det \mathbf{B}} = \frac{\langle \tau'_{ij} \rangle}{\sqrt{\det \mathbf{C}'_{[r,r]}}} \quad (S6)$$

The coordinate invariance of this term allows us to specifically consider the convenient coordinates in which $\mathbf{C}_{[r,r]} = \mathbf{I}$:

$$\frac{1}{\gamma} \langle \tau_{ij} \rangle = \frac{1}{\gamma} \langle \mathbf{x}_r \times \mathbf{f}_r(\mathbf{x}) \rangle = \frac{1}{\gamma} \int d\mathbf{x}_r \langle \mathbf{x}_r \times \mathbf{f}_r(\mathbf{x}) | \mathbf{x}_r \rangle p_r(\mathbf{x}_r) = \frac{1}{\gamma} \int d\mathbf{x}_r \mathbf{x}_r \times \langle \mathbf{f}_r(\mathbf{x}) | \mathbf{x}_r \rangle p_r(\mathbf{x}_r) \quad (\text{S7})$$

We can further expand this expression by using $\mathbf{\Omega}_r = \mathbf{A}_{\text{eff}} + \mathbf{D}_{[r,r]} \mathbf{C}_{[r,r]}^{-1}$. (The expression for $\mathbf{\Omega}_r$ follows immediately from Eq. (4), since we require $\mathbf{j}_r(\mathbf{x}_r) = \mathbf{\Omega}_r \mathbf{x}_r p_r(\mathbf{x}_r)$.)

$$\frac{1}{\gamma} \langle \mathbf{f}_r(\mathbf{x}) | \mathbf{x}_r \rangle = \mathbf{A}_{\text{eff}} \mathbf{x}_r = \mathbf{\Omega}_r \mathbf{x}_r - \mathbf{D}_{[r,r]} \mathbf{C}_{[r,r]}^{-1} \mathbf{x}_r. \quad (\text{S8})$$

Combining this result with Eq. (S7), we arrive at

$$\frac{1}{\gamma} \langle \tau_{ij} \rangle = \int d\mathbf{x}_r \mathbf{x}_r \times (\mathbf{\Omega}_r \mathbf{x}_r) p_r(\mathbf{x}_r) - \int d\mathbf{x}_r \mathbf{x}_r \times (\mathbf{D}_{[r,r]} \mathbf{C}_{[r,r]}^{-1} \mathbf{x}_r) p_r(\mathbf{x}_r). \quad (\text{S9})$$

Using the explicit form of $\mathbf{\Omega}_r$ (see Eq. (S15)), we evaluate the first term in this expression,

$$\int d\mathbf{x}_r \mathbf{x}_r \times (\mathbf{\Omega}_r \mathbf{x}_r) p_r(\mathbf{x}_r) = \int d\mathbf{x}_r \omega_{ij} (x_i^2 + x_j^2) p_r(\mathbf{x}_r) = \omega_{ij} (c_{ii} + c_{jj}) = 2\omega_{ij}. \quad (\text{S10})$$

In addition, we confirm by direct calculation, that, as expected, the second term in Eq. (S9) vanishes:

$$\begin{aligned} - \int d\mathbf{x}_r \mathbf{x}_r \times (\mathbf{D}_{[r,r]} \mathbf{x}_r) p_r(\mathbf{x}_r) &= \int d\mathbf{x}_r (-x_j, x_i) \begin{pmatrix} d_{ii} & d_{ij} \\ d_{ij} & d_{jj} \end{pmatrix} \begin{pmatrix} x_i \\ x_j \end{pmatrix} p_r(\mathbf{x}_r) \\ &= \int d\mathbf{x}_r [-d_{ii} x_i x_j - d_{ij} x_j^2 + d_{ij} x_i^2 + d_{jj} x_i x_j] p_r(\mathbf{x}_r) \\ &= \underbrace{c_{ij}}_0 (d_{jj} - d_{ii}) + d_{ij} \underbrace{(c_{ii} - c_{jj})}_0 = 0 \end{aligned} \quad (\text{S11})$$

Altogether, this gives us the desired result:

$$\frac{1}{2\gamma} \frac{\langle \tau_{ij} \rangle}{\sqrt{\det \mathbf{C}_{[r,r]}}} = \omega_{ij} \quad (\text{S12})$$

DERIVATION OF EQ. (13)

Here we show that $\Pi_{\text{tot}} \geq \Pi_r$.

$$\begin{aligned} \frac{\Pi_{\text{tot}} - \Pi_r}{k_B} &= \int d\mathbf{x} \frac{\mathbf{j}^T(\mathbf{x}) \mathbf{D}^{-1} \mathbf{j}(\mathbf{x})}{p(\mathbf{x})} - \int d\mathbf{x}_r \frac{\mathbf{j}_r^T(\mathbf{x}_r) \mathbf{D}_{[r,r]}^{-1} \mathbf{j}_r(\mathbf{x}_r)}{p(\mathbf{x}_r)} \\ &= \frac{\gamma}{k_B} \sum_{j \in [l]} \int d\mathbf{x} \frac{v_j^2(\mathbf{x})}{(T + \alpha_j)} p(\mathbf{x}) + \frac{\gamma}{k_B} \sum_{i \in [r]} \left[\left(\int d\mathbf{x} \frac{v_i^2(\mathbf{x})}{(T + \alpha_i)} p(\mathbf{x}) \right) - \int d\mathbf{x}_r \frac{\langle v_i(\mathbf{x}) | \mathbf{x}_r \rangle^2}{(T + \alpha_i)} p(\mathbf{x}_r) \right] \\ &= \frac{\gamma}{k_B} \left\{ \sum_{j \in [l]} \int d\mathbf{x} \frac{v_j^2(\mathbf{x})}{(T + \alpha_j)} p(\mathbf{x}) + \sum_{i \in [r]} \int d\mathbf{x}_r \left[\left(\int d\mathbf{x}_1 \frac{v_i^2(\mathbf{x})}{(T + \alpha_i)} p(\mathbf{x}_1 | \mathbf{x}_r) p(\mathbf{x}_r) \right) - \frac{\langle v_i(\mathbf{x}) | \mathbf{x}_r \rangle^2}{(T + \alpha_i)} p(\mathbf{x}_r) \right] \right\} \\ &= \frac{\gamma}{k_B} \left(\sum_{j \in [l]} \frac{\langle v_j^2(\mathbf{x}) \rangle}{(T + \alpha_j)} + \sum_{i \in [r]} \int d\mathbf{x}_r \underbrace{\left(\langle v_i^2(\mathbf{x}) | \mathbf{x}_r \rangle - \langle v_i(\mathbf{x}) | \mathbf{x}_r \rangle^2 \right)}_{\geq 0} \frac{p(\mathbf{x}_r)}{(T + \alpha_i)} \right) \geq 0 \end{aligned} \quad (\text{S13})$$

where in the second line we use that \mathbf{D} is diagonal, $\mathbf{v}(\mathbf{x}) = \mathbf{j}(\mathbf{x})/p(\mathbf{x})$, and $\mathbf{j}_r(\mathbf{x}_r) = p(\mathbf{x}_r) \int d\mathbf{x}_1 \mathbf{v}_r(\mathbf{x}) p(\mathbf{x}_1 | \mathbf{x}_r) = p(\mathbf{x}_r) \langle \mathbf{v}_r(\mathbf{x}) | \mathbf{x}_r \rangle$, which follows from the derivation of Eq. (3).

DERIVATION OF EQ. (14)

Here we derive the expression for the partial entropy production rate in terms of the cycling frequencies (see Eq. (14)). It is convenient to substitute the current field $\mathbf{j} = \boldsymbol{\Omega}\mathbf{x}p(\mathbf{x})$ in Eq. (11), which gives

$$\begin{aligned}\Pi &= k_B \int d\mathbf{x} (\boldsymbol{\Omega}\mathbf{x})^T \mathbf{D}^{-1} (\boldsymbol{\Omega}\mathbf{x}) p(\mathbf{x}) = k_B \int d\mathbf{x} x_i \Omega_{ij}^T (\mathbf{D}^{-1})_{jl} \Omega_{lm} x_m p(\mathbf{x}) \\ &= k_B \Omega_{ij}^T (\mathbf{D}^{-1})_{jl} \Omega_{lm} c_{mi} = k_B \text{Tr} (\boldsymbol{\Omega}^T \mathbf{D}^{-1} \boldsymbol{\Omega} \mathbf{C}).\end{aligned}\quad (\text{S14})$$

Since the entropy production is invariant under coordinate transformations, we can use a more suitable coordinate system. In particular, we choose a set of coordinates such that $\mathbf{C} = \mathbf{I}$. In this set of coordinates, the entries of the matrix Ω_{ij} correspond to the cycling frequencies in the coordinates space of the i^{th} and j^{th} coordinates [S2]. Thus, in the 2D case $\boldsymbol{\Omega}_r$ is given by

$$\boldsymbol{\Omega}_r = \begin{pmatrix} 0 & \omega \\ -\omega & 0 \end{pmatrix} \quad (\text{S15})$$

Furthermore, in this coordinate system $\mathbf{C}_{[r,r]}$ and $\boldsymbol{\Omega}_r$ commute, yielding

$$\Pi_r^{(2)} = k_B \omega^2 \text{Tr} (\mathbf{C}_{[r,r]} \mathbf{D}_{[r,r]}^{-1}) \quad (\text{S16})$$

Note, this expression is invariant under coordinate transformations.

SYSTEM SIZE AND SPATIAL AVERAGE

We determined the scaling of cycling frequencies for a range of system sizes (Fig. S1A). By properly rescaling both axes (see Eq.(10)), we can collapse all data on a mastercurve, which is consistent with a power-law over at least two decades (Fig. S1B). This analysis suggests a universal behavior, which is not dependent on the size of the system. These results provides additional numerical evidence for a power law scaling.

To determine ensemble averages of the cycling frequencies in Fig.(3) and Fig.(4) we employ spatial averages. For an infinite heterogeneous system, the ensemble average is equivalent to a spatial average. In a finite system, we need to be careful when using spatial averages because of edge effects. We investigated this aspect in a 1D chain, for which edge effects will be stronger than in higher dimensional systems. We performed a spatial average over all the different beads at distance r in the system, where we excluded data from beads at distances < 10 from the edge of system. Using this procedure, we find results that are consistent with those obtained with the ensemble average. (Fig. S2)

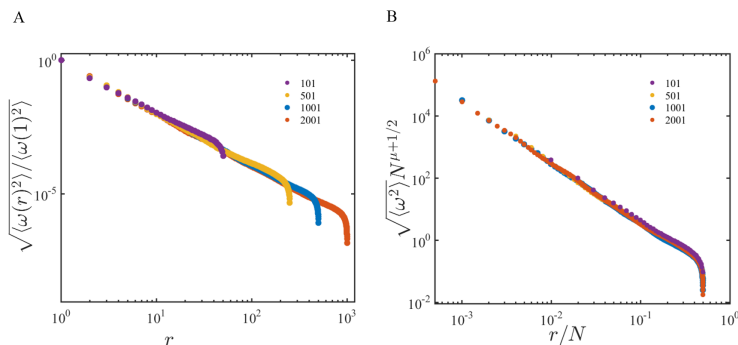


FIG. S1. Spatial scaling behavior of cycling frequencies. A) Scaling behavior of the frequency for different system sizes in the 1D chain (other parameters as in Fig. 3). B) Data collapse obtained by properly rescaling both axes.

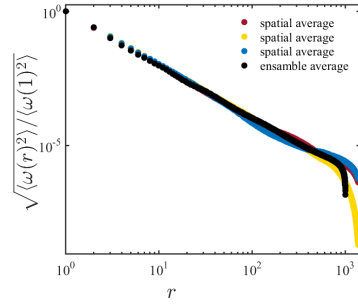


FIG. S2. Comparison between spatial and ensemble averages of the cycling frequencies for a 1D chain of size $N=1501$ (other parameters as in Fig. 3).

* These authors contributed equally

† C.broedersz@lmu.de

[S1] Y. L. Tong, *Springer Series in Statistics*, (Springer-Verlag, Berlin, 1990).

[S2] J. B. Weiss, *Tellus A* **3**, 55 (2003).

B Scaling behavior of nonequilibrium measures in internally driven elastic assemblies

This section is a reprint of the following publication:

Scaling behavior of nonequilibrium measures in internally driven elastic assemblies

Grzegorz Gradziuk, Federica Mura, and Chase P. Broedersz[†]

[†] corresponding author

Physical Review E **99**, 052406 (2019)

Scaling behavior of nonequilibrium measures in internally driven elastic assemblies

Grzegorz Gradziuk, Federica Mura, and Chase P. Broedersz*

Arnold-Sommerfeld-Center for Theoretical Physics and Center for NanoScience, Ludwig-Maximilians-Universität München, D-80333 München, Germany



(Received 14 January 2019; published 15 May 2019)

Detecting and quantifying nonequilibrium activity is essential for studying internally driven assemblies, including synthetic active matter and complex living systems such as cells or tissue. We discuss a noninvasive approach of measuring nonequilibrium behavior based on the breaking of detailed balance. We focus on “cycling frequencies”—the average frequency with which the trajectories of pairs of degrees of freedom revolve in phase space—and explain their connection with other nonequilibrium measures, including the area enclosing rate and the entropy production rate. We test our approach on simple toy models composed of elastic networks immersed in a viscous fluid with site-dependent internal driving. We prove both numerically and analytically that the cycling frequencies obey a power law as a function of distance between the tracked degrees of freedom. Importantly, the behavior of the cycling frequencies contains information about the dimensionality of the system and the amplitude of active noise. The mapping we use in our analytical approach thus offers a convenient framework for predicting the behavior of two-point nonequilibrium measures for a given activity distribution in the network.

DOI: [10.1103/PhysRevE.99.052406](https://doi.org/10.1103/PhysRevE.99.052406)

I. INTRODUCTION

The field of active matter has developed over recent decades to provide a physical description of classical many-body systems operating far from thermodynamic equilibrium [1–3]. A prominent class of such active matter are living systems: Schools of fish [4], flocks of birds [5], and colonies of bacteria [6,7] can all exhibit collective dynamics that are manifestly out of equilibrium. However, the non equilibrium activity of biological assemblies at smaller subcellular scales is not always straightforward to discern [8,9]. Examples include the stochastic fluctuations of biological assemblies such as chromosomes [10], the cytoskeleton [2,11–14], and cellular membranes [15–17]. Indeed, while these fluctuations can at first sight appear indistinguishable from thermal Brownian motion, they are in many cases driven by energy-consuming processes at molecular scales [1,2,8,9,18,19]. This molecular-scale activity can propagate to mesoscopic scales, giving rise to nonequilibrium dynamics that breaks detailed balance [9,20–25] or that violates the fluctuation dissipation theorem [12,15,16,26–28]. Soft-driven assemblies can also be realized in synthetic systems, including chemical fueled synthetic fibers [29], crystals of active colloidal particles [30], and artificial lipid membranes [31,32]. Numerous experimental studies showed how molecular nonequilibrium processes affect the mesoscopic mechanical properties of *in vivo* biological assemblies [2,11–13], *in vitro* reconstituted cytoskeletal networks [33–35], and synthetic materials [36]. It still remains unclear, however, how to characterize the nonequilibrium fluctuations of soft-driven assemblies.

To make further progress on characterizing active systems, various candidates for a reliable and informative nonequilibrium measure have been proposed. A natural and commonly used measure of the time-irreversibility of a process is the entropy production rate. In some cases, this measure is related to the energy dissipation in a system [37]. Recent studies made significant progress in inferring the entropy production rate from the observed trajectories [25,38,39]. In general, for complex systems it is unclear how to interpret measures of the partial entropy production rate or how to relate the measured quantities to the real entropy production rate of the full system. It is possible, however, to set a lower bound to the total entropy production from the observation of a few mesoscopic degrees of freedom [23,40–43]. An alternative approach of using area enclosing rates (AER) of stochastic trajectories in phase space as a metric for the breaking of detailed balance was presented in Refs. [44] and [45]. A closely related concept—the cycling frequencies of the stochastic trajectory—was used to analyze the nonequilibrium behavior emerging in the mode-space trajectories of a probe filament in an active gel [21,22] or the dynamics of a driven disordered elastic network near its isostatic point [24].

Despite the multitude of available nonequilibrium measures, it is still unclear how to use them to extract useful information about the nature of active driving in a system. The cycling frequencies can be used to investigate the nonequilibrium dynamics emerging on different lengthscales in driven elastic networks [23]. In particular, the cycling frequencies measured from trajectories of two probe particles in an internally driven elastic network display a power-law behavior as function of the distance between the particles, with an exponent that depends on the dimensionality of the system; the prefactor of this scaling law depends on the statistical properties of the internal driving. Thus, these experimentally

*C.broedersz@lmu.de

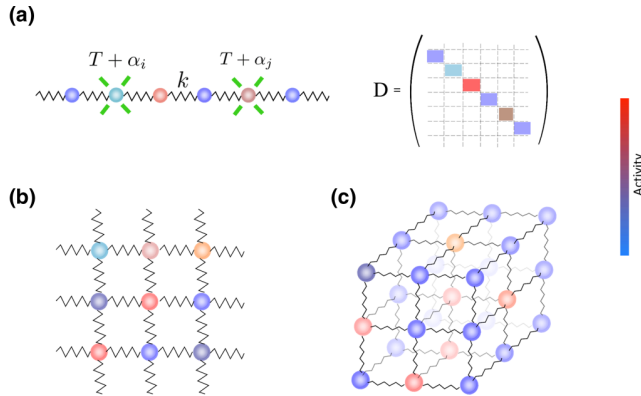


FIG. 1. (a) One-dimensional elastic chain of beads at temperature T with spatially varying white-noise driving intensity α_i , and the corresponding diffusion matrix D . The tracked pair of beads is indicated in green. (b) Two-dimensional and (c) three-dimensional elastic networks investigated in Sec. V A.

accessible cycling frequencies and their associated scaling behavior provide a promising candidate for a nonequilibrium measure that may provide access to properties of the internal driving.

In this work we present a detailed derivation of the scaling behavior of cycling frequencies for d -dimensional elastic networks with internal driving. Thus, we derive a theoretical framework that allows us to relate the cycling frequency to the lengthscale of the observation and to the properties of the network and of the active noise. Furthermore, we clarify the relation between the cycling frequencies and other nonequilibrium measures such as the area enclosing rate and the entropy production rate.

II. DRIVEN ELASTIC NETWORKS

We use overdamped networks of elastically coupled beads suspended in a viscous fluid (see Fig. 1) as a simple model for soft subcellular assemblies, such as a chromosome, a cell membrane, or the cytoskeleton [46–49]. For simplicity we choose units in which the elastic spring constant, the damping coefficient of the beads, and the Boltzmann constant k_B equal 1. The fluid is assumed to be at thermal equilibrium and the resulting thermal fluctuations in the system are thus modeled as Gaussian white noise processes acting independently on all the beads with the same amplitude T . Additional active force fluctuations, which in a biological system would be generated by enzymatic activity, drive the system out of thermal equilibrium. In real systems, the binding kinetics of enzymes such as molecular motors may depend on local structural properties of the network. Consequently, we expect the variance of the stochastic forces that these enzymes generate to depend on local features. We account for this possible spatial heterogeneity implicitly by implementing the active forces as independent Gaussian white noise processes with site-dependent amplitudes α_i . Here we shall only focus on the case of spatially uncorrelated intensities of the noise, but the theoretical framework we present in this paper can also be applied in other scenarios.

By modeling the active forces as “white,” we essentially restrict our model to systems in which the correlation times of the active driving are shorter than the intrinsic relaxation times of the network. This model is mathematically equivalent to embedding the beads in local thermal baths at temperatures $T + \alpha_i$ [50].

This simplified description allows us to study the dynamics of the system using a Fokker-Planck equation:

$$\partial_t p(\mathbf{x}, t) = -\nabla \cdot (\mathbf{A}\mathbf{x} - \mathbf{D}\nabla)p(\mathbf{x}, t) := -\nabla \cdot \mathbf{j}(\mathbf{x}, t), \quad (1)$$

where \mathbf{x} represents the displacements of the beads relative to their equilibrium positions, and $p(\mathbf{x}, t)$ is the probability distribution of \mathbf{x} at time t . We also assume that the forces are linear in \mathbf{x} , i.e., $\mathbf{f}(\mathbf{x}) = \mathbf{A}\mathbf{x}$ with a symmetric matrix \mathbf{A} , and $\mathbf{D} = \text{diag}\{T + \alpha_1, \dots, T + \alpha_N\}$ is the diffusion matrix. The right-hand side of Eq. (1) can be interpreted as the divergence of the probability current density $\mathbf{j}(\mathbf{x}, t) = (\mathbf{A}\mathbf{x} - \mathbf{D}\nabla)p(\mathbf{x}, t)$. At steady state, the nonvanishing dissipative probability currents constitute a measure of nonequilibrium dynamics in a system and thus play the key role in our approach.

III. CYCLING FREQUENCIES AND PHASE SPACE TORQUE

The steady-state probability currents, $\mathbf{j}(\mathbf{x})$, are mathematical objects that capture the presence of nonequilibrium activity by revealing time-irreversibility of the dynamics at the level of the Fokker-Planck equation. This time-irreversibility manifests through the emergence of a mean velocity field $\mathbf{v}(\mathbf{x})$ in the coordinate space, which is related to the probability current through $\mathbf{j}(\mathbf{x}) = \mathbf{v}(\mathbf{x})p(\mathbf{x})$ [51]. Therefore, from an experimental perspective, an ideal way to quantify the nonequilibrium dynamics of a system would be to measure such a velocity field $\mathbf{v}(\mathbf{x})$. However, inferring the full $\mathbf{v}(\mathbf{x})$ field is a challenge on its own. The most straightforward approaches require a discretization of the phase space. Such a measurement would require tracking many degrees of freedom for long time periods, which is difficult in practice.

Instead of inferring $\mathbf{v}(\mathbf{x})$ in full detail, one can alternatively measure some coarse-grained quantities related to $\mathbf{v}(\mathbf{x})$, which still retain key information about the nonequilibrium dynamics of the system. For instance, we could track a pair of degrees of freedom $\mathbf{x}_r = \{x_i, x_j\}$ and measure the time average of the angular velocity $\langle \dot{\beta}_{ij} \rangle$, or equivalently, the rate at which the trajectory revolves around the origin in this reduced two-dimensional subspace (Fig. 2). This simple measurement does not require any discretization of phase space or inference of the force field. We shall refer to $\langle \dot{\beta}_{ij} \rangle$ as the *cycling frequency*.

In general, $\langle \dot{\beta}_{ij} \rangle$ may contain only limited information about $\mathbf{v}(\mathbf{x})$. For linear systems, however, the mean phase space velocity can be written as [52]

$$\mathbf{v}(\mathbf{x}) = \mathbf{\Omega}\mathbf{x}, \quad \mathbf{\Omega} = \mathbf{A} + \mathbf{D}\mathbf{C}^{-1}, \quad (2)$$

where $\mathbf{C} = \langle \mathbf{x} \otimes \mathbf{x} \rangle$ is the steady-state covariance matrix obeying the Lyapunov equation

$$\mathbf{A}\mathbf{C} + \mathbf{C}\mathbf{A}^T = -2\mathbf{D}. \quad (3)$$

Equation (2) sets strong constraints on the structure of $\mathbf{v}(\mathbf{x})$: for dynamics projected on any two-dimensional subspace $\{x_i, x_j\}$ the probability currents have an elliptical structure.

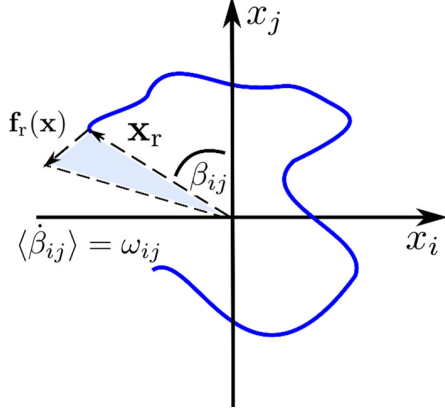


FIG. 2. Schematic trajectory in the coordinate space $[x_i, x_j]$ of two tracer beads. The light blue area enclosed in the triangle represents $\mathbf{x}_r \times \mathbf{f}_r(\mathbf{x})/2$ appearing in Eq. (6), which gives the area enclosing rate upon averaging over phase space.

The remaining information about the amplitude of the currents is set by the cycling frequencies $\langle \dot{\beta}_{ij} \rangle$.

To show this, we denote the velocity of the system in the reduced ij -subspace by $\mathbf{v}_r(\mathbf{x}) = \{v_i(\mathbf{x}), v_j(\mathbf{x})\}$. Note, what we observe while looking at the \mathbf{x}_r -subspace only is a conditional mean $\langle \mathbf{v}_r(\mathbf{x}) | \mathbf{x}_r \rangle$. Similar to Eq. (2), we find that $\langle \mathbf{v}_r(\mathbf{x}) | \mathbf{x}_r \rangle = \mathbf{\Omega}_r \mathbf{x}_r$, with $\mathbf{\Omega}_r = \mathbf{A}_{\text{eff}} + \mathbf{D}_{[r,r]} \mathbf{C}_{[r,r]}^{-1}$ [23]. Here \mathbf{A}_{eff} is a matrix such that $\langle \mathbf{f}_r(\mathbf{x}) | \mathbf{x}_r \rangle = \langle \{f_i(\mathbf{x}), f_j(\mathbf{x})\} | \mathbf{x}_r \rangle = \mathbf{A}_{\text{eff}} \mathbf{x}_r$; note, $\mathbf{C}_{[r,r]}$ and $\mathbf{D}_{[r,r]}$ are matrices of size $[2 \times 2]$, given by $\mathbf{C}_{[r,r]} = \{\{c_{ii}, c_{ij}\}, \{c_{ji}, c_{jj}\}\}$ and $\mathbf{D}_{[r,r]} = \{\{d_{ii}, d_{ij}\}, \{d_{ji}, d_{jj}\}\}$.

Next, we show that the eigenvalues of $\mathbf{\Omega}_r$ coincide with the cycling frequencies $\langle \dot{\beta}_{ij} \rangle$. First, note that $\langle \dot{\beta}_{ij} \rangle$ is invariant under orientation preserving linear transformations of the reduced subspace. We can therefore work in *covariance identity coordinates*, \mathbf{y}_r , such that $\mathbf{C}_{[r,r]} = \mathbf{I}$. In this basis, $\mathbf{\Omega}_r$ takes a particularly simple form [52]

$$\mathbf{\Omega}_r = \begin{pmatrix} 0 & \omega_{ij} \\ -\omega_{ij} & 0 \end{pmatrix}, \quad (4)$$

with the imaginary parts of its eigenvalues on the antidiagonal. This form of $\mathbf{\Omega}_r$ implies that for $\mathbf{C}_{[r,r]} = \mathbf{I}$, the probability current field has a circular structure. Using Eq. (4), we find that

$$\begin{aligned} \langle \dot{\beta}_{ij} | \mathbf{y}_r \rangle &= \left\langle \frac{\mathbf{y}_r \times \dot{\mathbf{y}}_r}{|\mathbf{y}_r|^2} \middle| \mathbf{y}_r \right\rangle = \frac{y_2 \langle \dot{y}_1 | \mathbf{y}_r \rangle - y_1 \langle \dot{y}_2 | \mathbf{y}_r \rangle}{y_1^2 + y_2^2} \\ &= \frac{y_2 \langle v_1(\mathbf{y}) | \mathbf{y}_r \rangle - y_1 \langle v_2(\mathbf{y}) | \mathbf{y}_r \rangle}{y_1^2 + y_2^2} = \omega_{ij}. \end{aligned} \quad (5)$$

This means that the conditional average of the angular velocity $\langle \dot{\beta}_{ij} | \mathbf{y}_r \rangle$ is \mathbf{y}_r -independent and equals ω_{ij} at all points in the reduced phase space. Hence, averaging over \mathbf{y}_r leads to $\langle \dot{\beta}_{ij} \rangle = \omega_{ij}$, with $\omega_{ij}^2 = \det \mathbf{\Omega}_r$.

Recently, new approaches have been developed to infer current fields in nonlinear systems by considering an expansion of the inferred force field [38]. Up to first order these methods reduce to calculating area enclosing rates, which are indeed closely related to the cycling frequencies, as we discuss further below.

One of our central objectives is to derive a relation between the observed currents and the properties of the system and the active driving. Given that the cycling frequencies are set by ω_{ij} —the imaginary parts of the eigenvalues of $\mathbf{\Omega}_r$ —we can make further progress by showing that for a general linear system [23]

$$\omega_{ij} = \frac{1}{2} \frac{\langle \mathbf{x}_r \times \mathbf{f}_r(\mathbf{x}) \rangle}{\sqrt{\det \mathbf{C}_r}}, \quad (6)$$

where $\langle \mathbf{x}_r \times \mathbf{f}_r(\mathbf{x}) \rangle = \langle x_i f_j(\mathbf{x}) - x_j f_i(\mathbf{x}) \rangle = (\mathbf{C}\mathbf{A}^T - \mathbf{A}\mathbf{C})_{ij}$ is the mean phase space torque (Fig. 2). Intuitively, Eq. (6) implies that for an overdamped linear system the mean phase space angular velocity is proportional to the mean phase space torque. A detailed derivation is presented in Ref. [23]. Moreover, in covariance identity coordinates Eq. (6) reduces to $\omega_{ij} = \frac{1}{2} (\mathbf{A}^T - \mathbf{A})_{ij} = \Omega_{ij}$, in accord with previous studies [21,22,52]. One can equivalently identify $(\mathbf{C}\mathbf{A}^T - \mathbf{A}\mathbf{C})_{ij}$ with mean area enclosing rates in the ij -subspace, as considered in [44]. Here, we focus on the cycling frequencies, since they are more directly related to the probability currents, which constitute the basis of our work. In some instances, however, the area enclosing rates turn out to be particularly advantageous to work with. In these cases we shall briefly discuss how switching to the area enclosing rates simplifies the analysis (see Sec. IV).

Since the cycling frequencies contain information about the amplitudes of the phase space probability currents, they can be related to the entropy production rate. For linear systems, in covariance identity coordinates, the full entropy production rate can be expressed as a weighted sum of the cycling frequencies squared: $\Pi = \sum_{i-\text{odd}}^n \omega_{i,i+1}^2 [(\mathbf{D}^{-1})_{i,i} + (\mathbf{D}^{-1})_{i+1,i+1}]$. However, in many experimental contexts it is typically impossible to track all the degrees of freedom or to resolve all steps of a process. This practical limitation motivated the introduction of various measures of reduced/apparent entropy production rate [23,40–43]. For the case of a two-point measurement, as the ones discussed in this paper, one can consider a reduced entropy production rate directly related to the cycling frequency: $\Pi_r^{(2)} = \omega_{ij}^2 \text{Tr}(\mathbf{C}_{[r,r]} \mathbf{D}_{[r,r]}^{-1})$, which gives a lower bound on the full contribution to the total entropy production rate from the observed pair of degrees of freedom [23].

IV. ONE-DIMENSIONAL CHAIN AND DIFFUSION EQUATION

While Eq. (6) sets a relation between the cycling frequencies observable in an experiment and the properties of both the network and the active noise distribution, it is not straightforward to explicitly derive these properties from the cycling frequencies. In the following sections, we use Eq. (6) to build a framework for extracting specific information about the system from the behavior of the cycling frequencies ω_{ij} .

We first consider the simplest case of a one-dimensional chain of $2N - 1$ beads coupled by harmonic springs. This example will help us build intuition for more complex lattices. To obtain insight into how nonequilibrium behavior manifests at different length scales, we consider a two-point nonequilibrium measure. Specifically, we study how the cycling

frequency in the subspace of displacements of two chosen beads $\{x_i, x_{i+r}\}$ depends on the distance r between these beads. Note that the distance r is expressed in the units of the lattice constant. We study the behavior of the cycling frequencies for two scenarios:

- (i) Active noise present only at single site,
- (ii) Random spatial distribution of activities $\{\alpha_i\}$.

In case (i) we plot the cycling frequency, $\omega_{\text{single}}(r)$, between the active bead and another bead at distance r . In case (ii) we consider an ensemble of active noise distributions $\{\alpha_i\}$, in which the amplitude of the active noise at each site is drawn randomly from a probability distribution p_α , with mean $\bar{\alpha}$ and variance σ_α^2 . The amplitudes α_i are spatially uncorrelated. We then calculate $\langle \omega^2(r) \rangle$ —the squared cycling frequency between two beads at distance r averaged over the activity distributions α_i . The first observation is that in both scenarios the cycling frequencies follow a power law as a function of distance, as shown in Fig. 3. The exponent in the random distribution scenario is independent of the probability distribution p_α of the intensities, but different from the single activity case.

To understand the origin of the power-law behavior and to calculate the exponents, we use Eq. (6) to derive analytical expressions for $\omega_{\text{single}}(r)$ and $\langle \omega(r)^2 \rangle$. In the case of a one-dimensional chain with spatially uncorrelated noise, the expression for the cycling frequency [Eq. (6)] reduces to

$$\omega_{ij} = \frac{\tilde{\partial}_2^2 c_{ij}}{\sqrt{\det \mathbf{C}_{[r,r]}}}, \quad (7)$$

where c_{ij} indicates the elements of the covariance matrix, and $\tilde{\partial}_2^2 c_{ij}$ denotes the discrete second derivative across rows: $\tilde{\partial}_2^2 c_{ij} = c_{i,j+1} - 2c_{i,j} + c_{i,j-1}$. Thus, this result reduces the problem of calculating ω_{ij} to finding the covariance matrix \mathbf{C} .

Motivated by the structure of \mathbf{D} , we decompose $\mathbf{C} = T\bar{\mathbf{C}} + \bar{\alpha}\mathbf{C}^*$ into equilibrium ($\bar{\mathbf{C}}$) and nonequilibrium (\mathbf{C}^*) parts [Fig. 4(a)]. For the one-dimensional chain, the Lyapunov equation [see Eq. (3)] is equivalent to

$$\tilde{\partial}_1^2 \bar{c}_{ij} + \tilde{\partial}_2^2 \bar{c}_{ij} = -2\delta_{ij}, \quad (8)$$

$$\tilde{\partial}_1^2 c_{ij}^* + \tilde{\partial}_2^2 c_{ij}^* = -2\delta_{ij} \frac{\alpha_i}{\bar{\alpha}}. \quad (9)$$

At equilibrium detailed balance is preserved, which implies $\tilde{\partial}_2^2 \bar{c}_{ij} = 0 \forall i \neq j$ [see Eq. (7)]. We can therefore replace $\tilde{\partial}_2^2 c_{ij}$ with $\tilde{\partial}_2^2 c_{ij}^*$ in Eq. (7). Then, expanding the expression for the cycling frequency in powers of $(\bar{\alpha}/T)$, we get

$$\omega_{ij} = \frac{\bar{\alpha}}{T} \frac{\tilde{\partial}_2^2 c_{ij}^*}{\sqrt{\det \bar{\mathbf{C}}_{[r,r]}}} + \mathcal{O}\left(\frac{\bar{\alpha}^2}{T^2}\right). \quad (10)$$

Up to linear order in $(\bar{\alpha}/T)$ the contributions from $\bar{\mathbf{C}}$ and \mathbf{C}^* separate; consequently, ω_{ij} becomes linear in $\{\alpha_i\}$. This linearity appearing in the limit of weak activity will later allow us to calculate cycling frequencies averaged over different realizations of the activity $\{\alpha_i\}$. Note, if instead of ω_{ij} , we consider the area enclosing rates (AER = $\bar{\alpha}\tilde{\partial}_2^2 c_{ij}^*$), the factor $\sqrt{\det \bar{\mathbf{C}}_{[r,r]}}$ does not enter, implying that the expression for

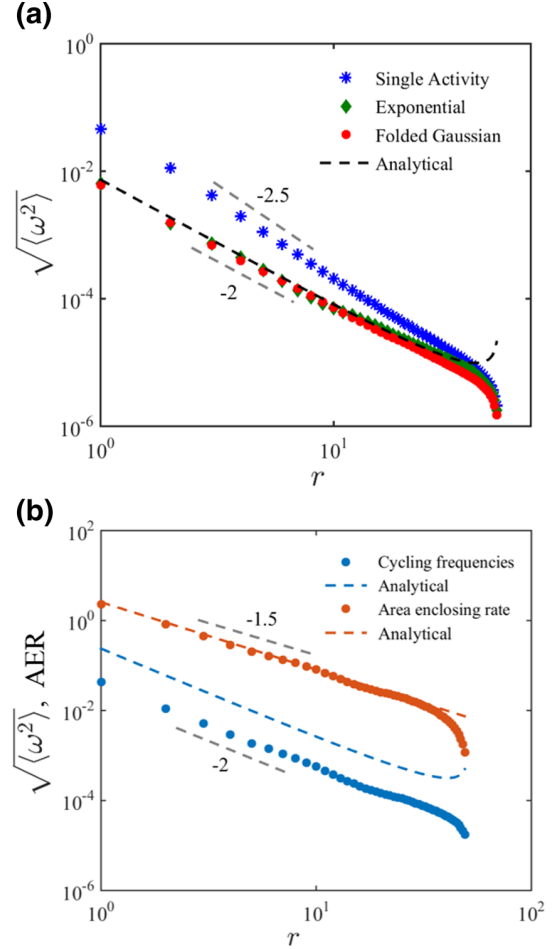


FIG. 3. (a) Scaling behavior of the cycling frequencies as a function of distance between the beads, obtained for a 1D chain with a single activity (blue stars) and with spatial distribution of activities with amplitudes drawn randomly from exponential (green diamonds) and folded Gaussian (red circles) distributions. (b) Comparison between the cycling frequencies (lower blue) and the Area Enclosing Rates (AER) (upper orange) above the weak noise limit ($\bar{\alpha}/T = 4$). All data points correspond to results obtained by numerically solving Lyapunov equation.

the area enclosing rates is linear in $\{\alpha_i\}$ irrespective of the magnitude of $\bar{\alpha}$.

A. Activity at a single site

To obtain insight into what determines the cycling frequencies in a concrete example, we first find the solution to Eq. (9) for the case of activity appearing only at a single site in the center of the chain. Later, we will use this solution to construct \mathbf{C}^* for a more general case. For now, let us assume that $\alpha_i = \alpha\delta_{iN}$ and $\bar{\alpha} = \alpha$.

We can think of Eq. (9) as a discretized stationary diffusion equation with a single source with a divergence of 2 in the middle of the \mathbf{C}^* matrix, and with absorbing boundary conditions at the edges. The absorbing boundaries in the diffusion equation reflect the fixed boundary conditions for the elastic chain. We denote by $r = \sqrt{(i-N)^2 + (j-N)^2}$ the distance

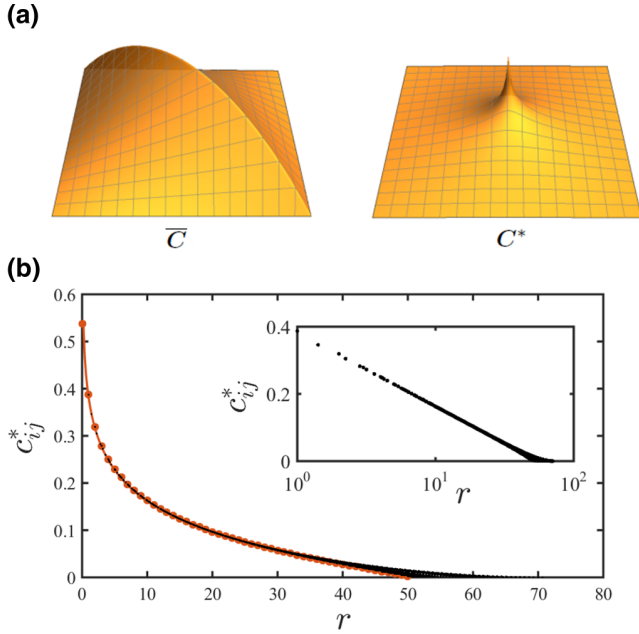


FIG. 4. (a) Profiles of the matrices $\bar{\mathbf{C}}$ and \mathbf{C}^* in the single activity case. For visual purposes, the discrete data points have been interpolated to a 2D surface. \bar{c}_{ij} is linear in both indices, resulting in $\omega_{ij} = 0$ for $\alpha_i = 0$. (b) Values of c_{ij}^* versus the distance from the center of the matrix $r = \sqrt{(i-N)^2 + (j-N)^2}$. Large orange points correspond to the entries at positions (i, N) . The inset depicts the same plot in log-linear scale.

from the center of \mathbf{C}^* . If we consider a continuous analog of our discrete problem and neglect the boundary conditions, then we can assume a rotational symmetry of the solution $c^*(r)$. The corresponding continuous diffusion equation takes the form: $\frac{1}{r} \partial_r r \partial_r c^*(r) = 0$. Consequently, $r \partial_r c^*(r) = -a$ and $c^*(r) = -a \ln(r) + b$.

One could also argue for $\partial_r c^*(r) \sim 1/r$ scaling of the “covariance current,” by demanding that the total “covariance flux” through a circle of radius r , centered at 0 is independent of r and equals 2—the divergence of the source. This also allows us to identify $a = 1/\pi$. The integration constant b is system-size dependent and has to be set such that the covariance vanishes at the edge of the covariance matrix.

The functional form that we obtain from this approximate analysis accurately describes the actual numerically obtained values of c_{ij}^* far from the boundaries [see Fig. 4(b)]. Note, the deviations that appear close to the boundaries are due to neglecting the absorbing boundary conditions and not due to the discrete nature of the problem. We can also consider a continuous limit of the problem, in which the chain is replaced by a string, by taking the limit $N \rightarrow \infty$, $k \rightarrow \infty$, while keeping $k/N = \text{const}$. In this limit the discrete diffusion equation is replaced by a continuous one, but the boundary effects still play the same role. We shall return to the continuous limit in Sec. VB, where we discuss more complex networks.

We can use the approximate form of $c^*(r)$ together with Eq. (10) to calculate $\omega_{\text{single}}(r)$. For large N , we can replace

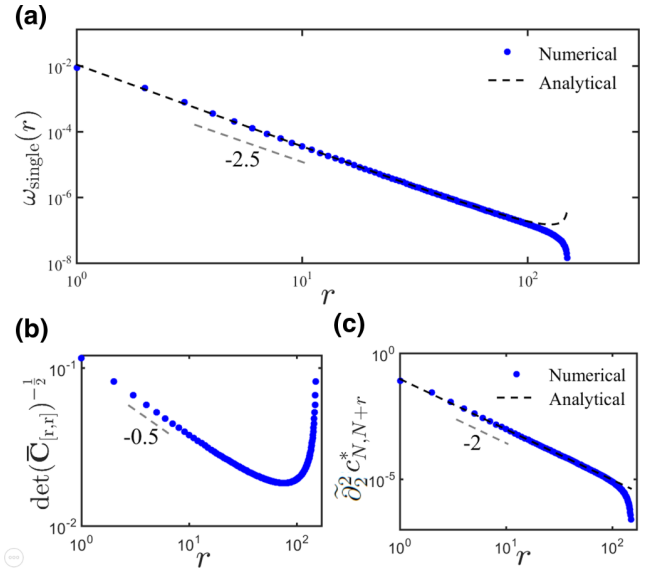


FIG. 5. (a) Scaling behavior of $\omega_{\text{single}}(r)$ as a function of the distance between the beads and comparison with the analytical prediction (dashed line) in Eq. (11). Below, the behavior of the (b) equilibrium and (c) nonequilibrium contributions to $\omega_{\text{single}}(r)$. The contribution presented in (c) coincides with the area enclosing rates. All data points correspond to results obtained by numerically solving Lyapunov equation.

$\tilde{\partial}_2^2 c_{N,N+r}^*$ with $\partial_r^2 c^*(r)$, to arrive at

$$\omega_{\text{single}}(r) = \frac{\alpha}{T} \frac{1}{\pi r^2} \frac{1}{\sqrt{\det \bar{\mathbf{C}}_{[r,r]}(r)}} + \mathcal{O}\left(\frac{\alpha^2}{T^2}\right). \quad (11)$$

Interestingly, it turns out that b , which is in general unknown, does not enter the equation for $\omega(r)$.

To find the equilibrium part $\bar{\mathbf{C}}$, we make the following observation. At equilibrium all cycling frequencies ω_{ij} must vanish, which combined with Eq. (7) gives: $\tilde{\partial}_2^2 \bar{c}_{ij} = 0 \forall i \neq j$. Using Eq. (8) at point (i, i) and the symmetry of $\bar{\mathbf{C}}$ we find $\tilde{\partial}_2^2 \bar{c}_{ii} = -1$. In general, we can therefore write the equation for $\bar{\mathbf{C}}$ as $\tilde{\partial}_2^2 \bar{c}_{ij} = -\delta_{ij}$. Note that this condition is equivalent to a discrete stationary diffusion equation in one dimension, with a single source at site i and with absorbing boundary conditions. This implies that \bar{c}_{ij} is linear in both indices and one can easily verify that $\bar{c}_{ij} = \min(i, j) - ij/(2N)$ satisfies Eq. (8). Using this solution, we find that $[\det \bar{\mathbf{C}}_{[r,r]}(r)]^{-\frac{1}{2}} = [\frac{1}{2}r(N-r)]^{-\frac{1}{2}} \sim r^{-\frac{1}{2}}$ for $r \ll N$. Therefore, $\omega_{\text{single}}(r) \sim r^{-\frac{3}{2}}$, as shown together with the numerical results in Fig. 5. The good agreement between the numerical and analytical results allows us to conclude that the scaling exponent is determined by the $\ln(r)$ -like profile of \mathbf{C}^* , which in turn is set by the dimensionality of the system. One could in principle find an analytical solution for $c^*(r)$ that accounts for the boundary conditions, but the $\ln(r)$ scaling captures the essential features.

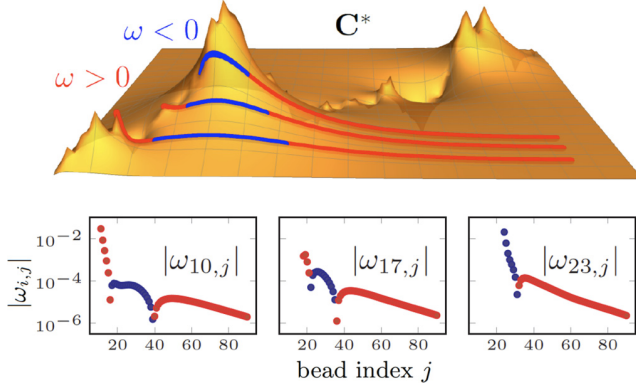


FIG. 6. Profile of \mathbf{C}^* in the case of spatially correlated amplitudes of the active noise, together with the lines $\{(i, j, c_{ij}^*)\}_{j=1, \dots, 2N-1}$ for $i = 10, 17, 23$. The color of a line indicates the sign of its curvature. The red (blue) points in the plots of $|\omega_{i,j}|$ correspond to positive (negative) cycling frequencies. Here, the profile of \mathbf{C}^* is presented for activities $\{\alpha_i - \bar{\alpha}\}$. This transformation of activities is justified in Appendix A.

B. Spatially varying activity

Equipped with the results from the previous section, we now consider a system with spatially varying activity. First, we will further clarify the connection between calculating cycling frequencies and solving a discretized steady-state diffusion equation for the covariance function. To this end, we consider a generic activity distribution $\{\alpha_i\}$ and plot the corresponding active part of the covariance matrix \mathbf{C}^* obtained by solving Eq. (9) (see Fig. 6). From the form of Eq. (7), we see

$$\begin{aligned} (\pi \bar{\alpha})^2 \langle [\tilde{\partial}_2^2 c_{-r,r}^*(\{\alpha_i\})]^2 \rangle &= \left\langle \left[\sum_z \frac{rz \alpha_z}{(r^2 + z^2)^2} \right] \left[\sum_{z'} \frac{r z' \alpha_{z'}}{(r^2 + z'^2)^2} \right] \right\rangle = \sum_z \frac{r^2 z^2 \langle \alpha_z^2 \rangle}{(r^2 + z^2)^4} + \sum_z \frac{rz \langle \alpha_z \rangle}{(r^2 + z^2)^2} \sum_{z' \neq z} \frac{r z' \langle \alpha_{z'} \rangle}{(r^2 + z'^2)^2} \\ &= \sum_z \frac{r^2 z^2 (\langle \alpha_z^2 \rangle - \langle \alpha_z \rangle^2)}{(r^2 + z^2)^4} \approx \sigma_\alpha^2 \int_{-\infty}^{\infty} \frac{r^2 z^2 dz}{(r^2 + z^2)^4} = \frac{\pi \sigma_\alpha^2}{16 r^3}. \end{aligned} \quad (14)$$

In the second line of this result, we used that $\sum_{z' \neq z} \frac{r z'}{(r^2 + z'^2)^2} = -\frac{rz}{(r^2 + z^2)^2}$ and approximated the sum by an integral. Evaluating the integral and rescaling $2r \rightarrow r$, we arrive at the final result:

$$\langle \omega^2(r) \rangle_\alpha = \frac{\sigma_\alpha^2}{T^2} \frac{1}{2\pi r^3} \frac{1}{\det \bar{\mathbf{C}}_{[r,r]}(r)}. \quad (15)$$

Given the asymptotic behavior $1/\det \bar{\mathbf{C}}_{[r,r]}(r) \sim r^{-1}$ for $r \ll N$ we conclude that in the limit of weak activity $\sqrt{\langle \omega^2(r) \rangle} \sim r^{-2}$ (see Fig. 3). Importantly, apart from reproducing the observed exponent of the power law, our result gives a correct prediction for the prefactor, which contains information about the variance of the active forces.

that the cycling frequencies $\{\omega_{ij}\}_{j=1, \dots, 2N-1}$ are proportional to the curvature of the line $\{(i, j, c_{ij}^*)\}_{j=1, \dots, 2N-1}$, as illustrated by the plots in Fig. 6. The connection with the steady-state diffusion equation [see Eq. (9)] allows us to understand how a given distribution of activities translates to a particular profile of the \mathbf{C}^* matrix and how this in turn determines the behavior of the cycling frequencies.

In general, the amplitudes of the active noise may be spatially correlated. Here, however, we restrict ourselves exclusively to the case of spatially uncorrelated activities, which is valid in the limit of distances larger than the correlation length of the amplitudes. To the “ i th” bead we assign a randomly sampled amplitude α_i . We assume all α_i to be pairwise independent and identically distributed with distribution $p(\alpha)$. For simplicity we index the beads so that the bead in the center of the system has index 0. To calculate $\omega(2r) = \omega_{-r,r}$, we need to determine $\tilde{\partial}_2^2 c_{-r,r}^*$. For a given activity distribution $\{\alpha_i\}$ we can exploit the linearity of Eq. (9) to obtain the corresponding $\mathbf{C}^*(\{\alpha_i\})$ as a superposition of single-source solutions. Thus, we can write

$$\tilde{\partial}_2^2 c_{-r,r}^*(\{\alpha_i\}) = \sum_z \tilde{\partial}_2^2 c_{-r,r}^*(\{\alpha_i \delta_{iz}\}). \quad (12)$$

For beads far enough from the boundary, we approximate $\mathbf{C}^*(\{\alpha_i \delta_{ij}\})$ by a logarithmic decay centered at (j, j) to obtain

$$\begin{aligned} \tilde{\partial}_2^2 c_{-r,r}^*(\{\alpha_i \delta_{iz}\}) &= \frac{1}{\pi} \frac{\alpha_z}{\bar{\alpha}} \frac{(r+z)^2 - (r-z)^2}{[(r+z)^2 + (r-z)^2]^2} \\ &= \frac{1}{\pi} \frac{\alpha_z}{\bar{\alpha}} \frac{rz}{(r^2 + z^2)^2}. \end{aligned} \quad (13)$$

Combining Eqs. (12) and (13), we calculate $\langle [\tilde{\partial}_2^2 c_{-r,r}^*(\{\alpha_i\})]^2 \rangle$, which is the main factor in the expression for $\langle \omega^2(2r) \rangle$.

V. d -DIMENSIONAL LATTICES

A. Cubic lattice

To explain the origin of the scaling behavior of $\omega(r)$ for multidimensional networks we now focus on the simplest possible case of a d -dimensional cubic lattice. Importantly, the calculation presented for this case also provides us with intuition for more complex lattices. Let us denote the bead indices corresponding to d independent directions with n_1, \dots, n_d . We will denote the elements of the covariance matrix \mathbf{C} as $c_{n_1, \dots, n_d; \bar{n}_1, \dots, \bar{n}_d} := c_{\mathbf{n}, \bar{\mathbf{n}}}$. We assume zero-restlength for the springs, so that the degrees of freedom corresponding to different directions decouple. Therefore, by \mathbf{C} we actually mean the covariance matrix of only these degrees of freedom that correspond to a single chosen direction, for instance the one corresponding to the index n_1 .

For this particular network, the Lyapunov equation is equivalent to

$$\left(\sum_{i=1}^d \tilde{\partial}_{n_i}^2 + \sum_{i=1}^d \tilde{\partial}_{\bar{n}_i}^2 \right) c_{\mathbf{n}, \bar{\mathbf{n}}} = -2d_{\mathbf{n}, \bar{\mathbf{n}}}. \quad (16)$$

Similar to the one-dimensional case, here we recognize a discretized stationary diffusion equation in $2d$ dimensions, with the divergence of the sources given by the elements of \mathbf{D} . For convenience we index the beads such that the one in the middle of the lattice is $(0, \dots, 0)$.

Our goal is to calculate the cycling frequency $\omega_{r, \dots, r; -r, \dots, -r} = \omega(2\sqrt{dr})$. Here we consider a particular case of relative position of the beads with respect to the principal directions of the lattice. It turns out, however, that the final result depends only on the distance between the beads. From Eq. (6), we find that

$$\omega_{r, \dots, r; -r, \dots, -r} \approx \frac{(\bar{\alpha}/T)}{\sqrt{\det \bar{\mathbf{C}}_{[r, r]}}} \sum_{i=1}^d \tilde{\partial}_{n_i}^2 c_{\mathbf{n}, \bar{\mathbf{n}}}^* \Big|_{r, \dots, r; -r, \dots, -r}. \quad (17)$$

Following the procedure used for the one-dimensional chain, we begin with finding the solution to a single source problem with one active bead at site $(0, \dots, 0)$. As before, we will then use this solution as a Green's function for our diffusion problem with a generic activity distribution.

Taking a continuous limit of the diffusion equation and neglecting the boundary conditions, we expect that $\partial_r c(r) \sim 1/r^{2d-1}$ and consequently $c(r) \sim 1/r^{2d-2}$, where r is the distance from the center of the $2d$ -dimensional covariance matrix. Therefore, for a single active bead at site $(0, \dots, 0)$, we obtain

$$c_{\mathbf{n}, \bar{\mathbf{n}}}^* = a_d \left(\sum_{i=1}^d n_i^2 + \sum_{i=1}^d \bar{n}_i^2 \right)^{-(d-1)} = a_d (\mathbf{n}^2 + \bar{\mathbf{n}}^2)^{-(d-1)}. \quad (18)$$

The constant $a_d = (d-2)!/(2\pi^d)$ can be obtained from the divergence theorem, as we did in the one-dimensional case.

The contribution to $\omega_{\mathbf{n}, \bar{\mathbf{n}}}$ from a single activity at site $(0, \dots, 0)$ is then given by (Appendix A)

$$\sum_{i=1}^d \tilde{\partial}_{n_i}^2 c_{\mathbf{n}, \bar{\mathbf{n}}}^* = 2d(d-1)a_d \frac{\mathbf{n}^2 - \bar{\mathbf{n}}^2}{(\mathbf{n}^2 + \bar{\mathbf{n}}^2)^{d+1}}. \quad (19)$$

Performing calculations analogous to those for the one-dimensional chain, we arrive at (Appendix A)

$$\langle \omega_{d=2}^2(r) \rangle_\alpha = \frac{\sigma_\alpha^2}{T^2} \frac{8}{5\pi^3 r^6} \frac{1}{\det \bar{\mathbf{C}}_{[r, r]}}, \quad (20)$$

$$\langle \omega_{d=3}^2(r) \rangle_\alpha = \frac{\sigma_\alpha^2}{T^2} \frac{27}{8\pi^4 r^9} \frac{1}{\det \bar{\mathbf{C}}_{[r, r]}}. \quad (21)$$

Importantly, we obtain exactly the same results when considering different directions across the lattice, such as $\omega_{(r, 0, \dots, 0), (-r, 0, \dots, 0)}$. In general, for a d -dimensional lattice we expect

$$\partial_r^2 c(r) \sim r^{-2d}, \quad (22)$$

$$\omega_{\text{single}, d}^2(r) \sim r^{-4d} / \det \bar{\mathbf{C}}_{[r, r]}(r), \quad (23)$$

$$\langle \omega_d^2(r) \rangle_\alpha \sim r^{-3d} / \det \bar{\mathbf{C}}_{[r, r]}(r). \quad (24)$$

For completeness we investigate the behavior of $\det \bar{\mathbf{C}}_{[r, r]}(r)$ for different dimensions. At equilibrium all cycling frequencies vanish, leading to

$$\sum_{i=1}^d \tilde{\partial}_{n_i}^2 \bar{c}_{\mathbf{n}, \bar{\mathbf{n}}} = 0 \quad \forall \mathbf{n} \neq \bar{\mathbf{n}}. \quad (25)$$

For all points on the diagonal of the covariance matrix $(\mathbf{n}, \bar{\mathbf{n}}) = (n_1, \dots, n_d; \bar{n}_1, \dots, \bar{n}_d)$ the diffusion equation [see Eq. (16)] reads

$$\sum_{i=1}^d \tilde{\partial}_{n_i}^2 \bar{c}_{\mathbf{n}, \bar{\mathbf{n}}} + \sum_{i=1}^d \tilde{\partial}_{\bar{n}_i}^2 \bar{c}_{\mathbf{n}, \bar{\mathbf{n}}} = -2. \quad (26)$$

Using the symmetry of the system, we conclude that the two sums in Eq. (26) are equal, which together with Eq. (25) imply that

$$\left(\sum_{i=1}^d \tilde{\partial}_{n_i}^2 \right) \bar{c}_{\mathbf{n}, \bar{\mathbf{n}}} = -\delta_{\mathbf{n}, \bar{\mathbf{n}}} \quad (27)$$

for all points $(\mathbf{n}, \bar{\mathbf{n}})$. This result can be interpreted in the following way: for a given $(\bar{n}_1, \dots, \bar{n}_d)$, $\bar{c}_{\mathbf{n}, \bar{\mathbf{n}}}$ as a function of (n_1, \dots, n_d) is a solution to a d -dimensional discretized stationary diffusion equation with a single source at position $(\bar{n}_1, \dots, \bar{n}_d)$, and with absorbing boundary conditions. Note, there is an interesting symmetry of the diffusion equation implied by the symmetry $\bar{c}_{\mathbf{n}, \bar{\mathbf{n}}} = \bar{c}_{\bar{\mathbf{n}}, \mathbf{n}}$: the solution at point \mathbf{n} from a source at point $\bar{\mathbf{n}}$ is equal to the solution at point $\bar{\mathbf{n}}$ from a source at point \mathbf{n} . While this property of the diffusion equation would be obvious in an infinite space, it surprisingly holds also in the presence of absorbing boundaries.

It can further be shown that

$$\bar{c}_{\mathbf{n}, \bar{\mathbf{n}}} \sim \ln[(n_1 - \bar{n}_1)^2 + (n_2 - \bar{n}_2)^2] \quad \text{for } d = 2,$$

$$\bar{c}_{\mathbf{n}, \bar{\mathbf{n}}} \sim \left[\sum_{i=1}^d (n_i - \bar{n}_i)^2 \right]^{-\left(\frac{d-2}{2}\right)} \quad \text{for } d > 2. \quad (28)$$

This result can also be understood using a simple dimensionality argument: A diffusion problem in d dimensions with a source forming a d_s -dimensional plane can be mapped to a $(d - d_s)$ -dimensional diffusion problem with a point source. In our case we are dealing with a diffusion problem in a $2d$ -dimensional space, with a d -dimensional source. Reducing the $2d$ -dimensional problem to a point source problem in d dimensions, we arrive exactly at Eq. (28). From this equation we conclude that for dimensions $d \geq 2$, the diagonal terms of $\bar{\mathbf{C}}_{[r, r]}(r)$ strongly dominate over the off-diagonal ones. In fact one can verify that for dimensions $d \geq 2$ and for systems large enough $\det \bar{\mathbf{C}}_{[r, r]}(r)$ depends on r only weakly and does not influence the scaling behavior of $\omega^2(r)$ anymore (see Fig. 7). This is a consequence of the shorter range of elastic interactions in higher dimensions.

It is important to note here that, as discussed after introducing Eq. (10), the area enclosing rates do not depend on $\det \bar{\mathbf{C}}_{[r, r]}$. This allows us to perform calculations analogous to the ones presented in this section, without assuming the limit of weak activities. As a result we predict a scaling $\sigma_\alpha r^{-3d/2}$

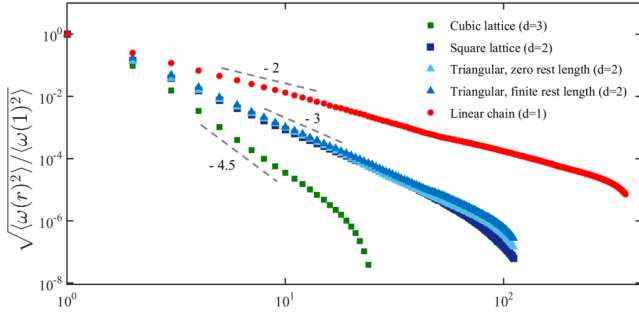


FIG. 7. Scaling behavior of the cycling frequencies as function of the distance between the beads. The results are obtained for different lattices and a folded Gaussian activity distribution [23]. Triangles, big squares, and small squares represent triangular, square, and cubic lattices, respectively. Light (dark) blue triangles represent triangular networks with zero (finite) rest length springs. In all cases we used $\frac{\alpha}{T} = 0.15$. For computational convenience we determined the ensemble average by performing a spatial average. All data points correspond to results obtained by numerically solving Lyapunov equation.

for the area enclosing rates even for high amplitudes of the active noise.

B. Generic lattices

In Sec. VA we investigated the simplest possible case of a d -dimensional zero-rest length cubic lattice \mathcal{L}^d . For such systems the Lyapunov equation for the covariance matrix could be viewed as a discretized steady-state diffusion equation defined on a space $\mathcal{L}^d \times \mathcal{L}^d \sim \mathcal{L}^{2d}$. For instance, for a two-dimensional square lattice we had to solve a diffusion equation in a four-dimensional cube. A natural question is how general the connection is between the Lyapunov equation and diffusion equations. It turns out that for many zero-rest length lattices there is simple procedure for translating a particular lattice structure to a corresponding diffusion equation for the covariance. The condition which allows us to identify the terms appearing in the Lyapunov equation with second derivatives, as in Eq. (9), is that at all sites of the lattice a spring pointing in one direction is accompanied by a spring pointing in the opposite direction. If this is the case, then we can directly read out the diffusion equation from the structure of the lattice, as illustrated in Fig. 8. Each such pair of springs gives rise to diffusive terms in the corresponding directions, with diffusion constant proportional to the spring constant.

In the case of finite rest length elastic networks with linearized forces, the same condition allows us to write the Lyapunov equation as a discretized second order partial differential equation for the covariance. Importantly, the displacements in x and y directions are no longer decoupled and one has to solve a differential equation for three different covariances: c^{xx} , c^{xy} , c^{yy} . An example of such an equation for a two-dimensional triangular lattice is included in Appendix B. Importantly, the structure of the network determines not only the equation for the covariance matrix but also the cycling frequencies according to Eq. (6).

For a wide range of networks, including randomly diluted networks [24], the condition given above is not satisfied and

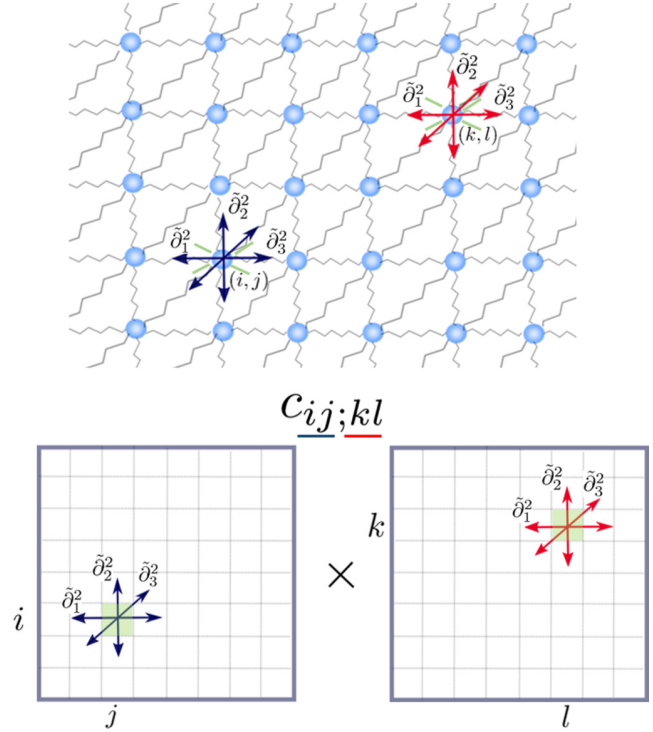


FIG. 8. An exemplary lattice for which the Lyapunov equation can be interpreted as a diffusion equation with nonisotropic diffusion. The presented lattice is equivalent to the triangular lattice, if we consider them in the zero-rest length case.

there is no straightforward way of translating the Lyapunov equation to a continuous diffusionlike equation for the covariance. Nevertheless, for a given network \mathcal{G} , which can be thought of as a graph, we can still interpret the Lyapunov equation as a Poisson equation on a graph $\mathcal{G} \times \mathcal{G}$ and relate the cycling frequency between a pair of degrees of freedom to the covariance flux through a corresponding vertex of $\mathcal{G} \times \mathcal{G}$. The theory of graph Laplacians, introduced by Kirchhoff in his study of the properties of resistor networks, has found applications in elasticity theory, graph theory, and computer science [53–56].

Our numerical calculations reveal that the exponents of the power laws for the cycling frequencies observed for various lattices are set by the dimensionality of the system and are independent of the detailed structure of the lattice [23]. Heuristically, this can be understood as follows: any d -dimensional rigid network, with a given average coordination number can be seen as an approximation to a continuous d -dimensional elastic medium. For such an elastic medium, a continuous diffusion equation, as the one we used to study d -dimensional cubic lattices, would be an exact equation for the covariance field, and we conjecture that the cycling frequencies for a continuous medium can be obtained by taking appropriate limits of our results for a discrete system. Note that a study of the cycling frequencies directly at the level of a continuous system would require introducing the Fokker-Planck equation for fields and make the analysis considerably more difficult. Since our results presented for the d -dimensional cubic lattice should coincide with the results for a d -dimensional

continuous medium, we argue that our analytical calculation captures the essential origins of the power-law phenomenon for all lattices that approximate a continuous medium well.

VI. CONCLUSIONS

Here we considered a simple model of an internally driven elastic assembly. Using this model, we investigated the properties of cycling frequencies—a two-point measure of nonequilibrium dynamics, which can be used in experimental and theoretical studies of active systems. We discussed how to relate the cycling frequencies to other commonly used nonequilibrium measures, such as the area enclosing rates or the reduced entropy production rate. Furthermore, based on our analytical approach, reinforced with numerical results, we predict that the cycling frequencies follow a power law as a function of distance between the two probes in an elastic network. The exponent of the power law depends on the dimensionality of the system, but not on the detailed structure of the network. In the case of a random spatial distribution of activities, we showed that the mean cycling frequencies $\sqrt{\langle \omega^2(r) \rangle}$ are proportional to the standard deviation of the intensities of the active noise σ_α . Interestingly, the case of a single-site activity gives a different exponent than the one with randomly distributed activities.

For more complex activity distributions, the connection between the Lyapunov equation and a diffusion equation, that we presented in Secs. IV and VB, provides some intuition for how the cycling frequencies in a system depend on the structure of the active noise. Since the diffusive terms in

the Lyapunov equation originate solely from the structure of the lattice, we expect that a similar framework can be used to study the behavior of the cycling frequencies for more complex distributions of the active noise, which include spatial correlations [57].

The analytical approach we developed aims at finding a mapping between the properties of the active noise and two-point nonequilibrium measures. Based on the results we obtained and their robustness to the detailed structure of a network, we argue that the cycling frequencies and the area enclosing rates are promising tools for studying the nature of the stochastic driving in an active elastic assembly. Examples of numerical studies of actively driven elastic assemblies in which the nonequilibrium measures presented in our work could be applied include [58–61]. Experimentally our approach can be tested on reconstituted actomyosin networks [33–35] and other noise-driven biological [10,15,16] or synthetic systems [29–32,36], which can be well approximated by an elastic assembly at steady state. Such experiments could be performed in chromosomes, membranes, or tissues, using embedded colloidal particles or fluorescently tagged cellular organelles.

ACKNOWLEDGMENTS

We thank F. Gnesotto, B. Remlein, and P. Ronceray for many stimulating discussions. This work was supported by the German Excellence Initiative via the program NanoSystems Initiative Munich (NIM), the Graduate School of Quantitative Biosciences Munich (QBM), and was funded by the Deutsche Forschungsgemeinschaft (DFG, German Research Foundation), Grant No. 418389167.

APPENDIX A: CALCULATION FOR A D-DIMENSIONAL ZERO-RESTLENGTH CUBIC LATTICE

First we find the profile of the C^* matrix for the case of a single activity at site $(0, \dots, 0)$. Neglecting the boundary conditions and assuming a rotational symmetry of the solution we find

$$c_{\mathbf{n},\bar{\mathbf{n}}}^* = a_d \left(\sum_{i=1}^d n_i^2 + \sum_{i=1}^d \bar{n}_i^2 \right)^{-(d-1)}, \quad \text{with } a_d = \frac{(d-2)!}{2\pi^d}, \quad (\text{A1})$$

$$\partial_{n_i} c_{\mathbf{n},\bar{\mathbf{n}}}^* = -(d-1)a_d \frac{2n_i}{(n_1^2 + \dots + \bar{n}_d^2)^d}, \quad (\text{A2})$$

$$\partial_{n_i}^2 c_{\mathbf{n},\bar{\mathbf{n}}}^* = d(d-1)a_d \frac{4n_i^2}{(n_1^2 + \dots + \bar{n}_d^2)^{d+1}} - (d-1)a_d \frac{2}{(n_1^2 + \dots + \bar{n}_d^2)^d} \quad (\text{A3})$$

$$= \frac{2(d-1)a_d}{(n_1^2 + \dots + \bar{n}_d^2)^{d+1}} [2dn_i^2 - (n_1^2 + \dots + \bar{n}_d^2)]. \quad (\text{A4})$$

Adding contributions from the all the second derivatives appearing in Eq. (17) we get

$$\sum_{i=1}^d \partial_{n_i}^2 c_{\mathbf{n},\bar{\mathbf{n}}}^* = 2d(d-1)a_d \frac{[(n_1^2 + \dots + n_d^2) - (\bar{n}_1^2 + \dots + \bar{n}_d^2)]}{(n_1^2 + \dots + \bar{n}_d^2)^{d+1}} = 2d(d-1)a_d \frac{\mathbf{n}^2 - \bar{\mathbf{n}}^2}{(\mathbf{n}^2 + \bar{\mathbf{n}}^2)^{d+1}}. \quad (\text{A5})$$

To get an expression for $\sum_{i=1}^d \partial_{z_i}^2 c$ in the case of one active bead at site (z_1, \dots, z_d) , one simply has to substitute $n_i \rightarrow (n_i - z_i)$, $\bar{n}_i \rightarrow (\bar{n}_i - z_i)$ in Eq. (A5). Therefore, the contribution to ω from an activity α_{z_1, \dots, z_d} at site (z_1, \dots, z_d) reads

$$\sum_{i=1}^d \partial_{n_i}^2 c_{r, \dots, r; -r, \dots, -r} = 2d(d-1)a_d \frac{\sum_{i=1}^d (r - z_i)^2 - \sum_{i=1}^d (-r - z_i)^2}{\left(\sum_{i=1}^d (r - z_i)^2 + \sum_{i=1}^d (-r - z_i)^2 \right)^{d+1}} \alpha_{z_1, \dots, z_d} \quad (\text{A6})$$

$$= 2d(d-1)a_d \frac{\sum_{i=1}^d (-4rz_i)}{\left(2r^2d + 2\sum_{i=1}^d z_i^2\right)^{d+1}} \alpha_{z_1, \dots, z_d} \quad (\text{A7})$$

$$= -\frac{d(d-1)a_d}{2^{d-2}} \frac{\sum_{i=1}^d rz_i}{\left(r^2d + \sum_{i=1}^d z_i^2\right)^{d+1}} \alpha_{z_1, \dots, z_d}. \quad (\text{A8})$$

Finally, we can proceed to calculating $\langle \omega^2(2\sqrt{d}r) \rangle$:

$$\left\langle \left(\sum_{z_1, \dots, z_d} \frac{(\sum_{i=1}^d rz_i) \alpha_{z_1, \dots, z_d}}{\left(r^2d + \sum_{i=1}^d z_i^2\right)^{d+1}} \right) \left(\sum_{\bar{z}_1, \dots, \bar{z}_d} \frac{(\sum_{i=1}^d r\bar{z}_i) \alpha_{\bar{z}_1, \dots, \bar{z}_d}}{\left(r^2d + \sum_{i=1}^d \bar{z}_i^2\right)^{d+1}} \right) \right\rangle \quad (\text{A9})$$

$$\stackrel{(1)}{=} \sum_{z_1, \dots, z_d} \frac{(\sum_{i=1}^d rz_i)^2 \sigma_\alpha^2}{\left(r^2d + \sum_{i=1}^d z_i^2\right)^{2d+2}} \stackrel{(2)}{=} \sum_{z_1, \dots, z_d} \frac{\sum_{i=1}^d r^2 z_i^2 \sigma_\alpha^2}{\left(r^2d + \sum_{i=1}^d z_i^2\right)^{2d+2}} \quad (\text{A10})$$

$$\approx^{\text{cont.}} \int_{z_1, \dots, z_d} \frac{\sum_{i=1}^d r^2 z_i^2 \sigma_\alpha^2}{\left(r^2d + \sum_{i=1}^d z_i^2\right)^{2d+2}}. \quad (\text{A11})$$

Step (1) follows from $\langle \alpha_{z_1, \dots, z_d} \alpha_{\bar{z}_1, \dots, \bar{z}_d} \rangle = \sigma_\alpha^2 \delta_{z_1, \bar{z}_1} \cdots \delta_{z_d, \bar{z}_d}$. Thereby we have assumed that $\bar{\alpha} = 0$. This can be achieved by replacing the noise amplitudes α_i with $\alpha_i - \bar{\alpha}$. This transformation is justified, because any shift of the active noise amplitudes by a constant value does not affect $\tilde{\partial}^2 c_{ij}^*$ (compare with $\tilde{\partial}^2 \bar{c}_{ij} = 0 \forall i \neq j$). Note that $\alpha_i - \bar{\alpha}$ are introduced just for convenience and one should not think of them as of any noise amplitudes. Step (2) results from the fact that the terms odd in z_i sum up to 0. In the last step we approximated the sum by an integral.

APPENDIX B: CALCULATION FOR FINITE RESTLENGTH TRIANGULAR LATTICE

Here we derive equation for the covariance matrix for the case of a finite restlength triangular lattice. We index the beads in the lattice as shown in Fig. 9. Let us denote by f_{ij}^x and f_{ij}^y the x and y components of the force acting on bead (i, j) , and by x_{ij} , y_{ij} the x and y displacements of bead (i, j) . Expanding the force up to linear order in displacements we find

$$\begin{aligned} f_{ij}^x &= \alpha(x_{i-1, j-1} + x_{i+1, j+1} - 2x_{i, j} + x_{i-1, j} + x_{i+1, j} - 2x_{i, j}) + (x_{i, j-1} + x_{i, j+1} - 2x_{i, j}) \\ &\quad - \beta(y_{i-1, j-1} + y_{i+1, j+1} - 2y_{i, j}) + \beta(y_{i-1, j} + y_{i+1, j} - 2y_{i, j}), \\ f_{ij}^y &= \gamma(y_{i-1, j-1} + y_{i+1, j+1} - 2y_{i, j} + y_{i-1, j} + y_{i+1, j} - 2y_{i, j}) \\ &\quad - \delta(x_{i-1, j-1} + x_{i+1, j+1} - 2x_{i, j}) + \delta(x_{i-1, j} + x_{i+1, j} - 2x_{i, j}), \end{aligned}$$

with $\alpha = 1/4$, $\beta = \sqrt{3}/4$, $\gamma = 3/4$, $\delta = \sqrt{3}/4$. It is convenient to rewrite the Lyapunov equation in the following way:

$$-2\mathbf{D} = \mathbf{A}\mathbf{C} + \mathbf{C}\mathbf{A} = \langle \mathbf{A}\mathbf{x}\mathbf{x}^T + \mathbf{x}(\mathbf{A}\mathbf{x})^T \rangle = \langle \mathbf{f}\mathbf{x}^T + \mathbf{x}\mathbf{f}^T \rangle. \quad (\text{B1})$$

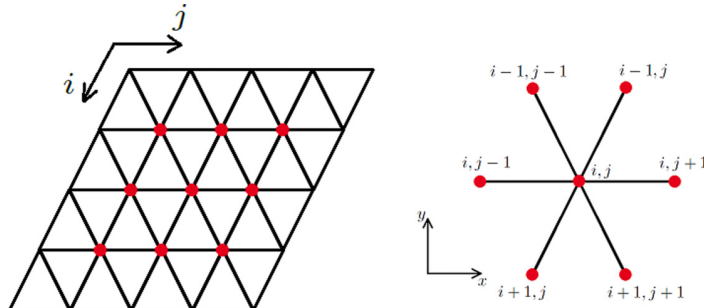


FIG. 9. Triangular lattice and indexing of beads.

Let us denote the elements of the covariance matrix by: $\langle x_{ij}x_{kl} \rangle = c_{ij,kl}^{xx}$, $\langle x_{ij}y_{kl} \rangle = c_{ij,kl}^{xy}$, $\langle y_{ij}y_{kl} \rangle = c_{ij,kl}^{yy}$ and introduce the discrete derivative operators:

$$\begin{aligned}\tilde{\partial}_1^2 c_{ij,kl} &= c_{i-1,j,k,l} - 2c_{i,j,k,l} + c_{i+1,j,k,l}, & \tilde{\partial}_1^2 c_{ij,kl} &= c_{i,j,k-1,l} - 2c_{i,j,k,l} + c_{i,j,k+1,l}, \\ \tilde{\partial}_2^2 c_{ij,kl} &= c_{i,j-1,k,l} - 2c_{i,j,k,l} + c_{i,j+1,k,l}, & \tilde{\partial}_2^2 c_{ij,kl} &= c_{i,j,k,l-1} - 2c_{i,j,k,l} + c_{i,j,k,l+1}, \\ \tilde{\partial}_3^2 c_{ij,kl} &= c_{i-1,j-1,k,l} - 2c_{i,j,k,l} + c_{i+1,j+1,k,l}, & \tilde{\partial}_3^2 c_{ij,kl} &= c_{i,j,k-1,l-1} - 2c_{i,j,k,l} + c_{i,j,k+1,l+1}.\end{aligned}$$

Then, the Lyapunov equation translates to

$$\langle f_{ij}^x x_{kl} + x_{ij} f_{kl}^x \rangle = [\alpha(\tilde{\partial}_3^2 + \tilde{\partial}_1^2) + \tilde{\partial}_2^2] c_{ij,kl}^{xx} - \beta(\tilde{\partial}_3^2 - \tilde{\partial}_1^2) c_{ij,kl}^{yx} + [\alpha(\tilde{\partial}_3^2 + \tilde{\partial}_1^2) + \tilde{\partial}_2^2] c_{ij,kl}^{xx} - \beta(\tilde{\partial}_3^2 - \tilde{\partial}_1^2) c_{ij,kl}^{xy} = -2\delta_{(ij),(kl)} d_{ij}, \quad (\text{B2})$$

$$\langle f_{ij}^x y_{kl} + x_{ij} f_{kl}^y \rangle = [\alpha(\tilde{\partial}_3^2 + \tilde{\partial}_1^2) + \tilde{\partial}_2^2] c_{ij,kl}^{xy} - \beta(\tilde{\partial}_3^2 - \tilde{\partial}_1^2) c_{ij,kl}^{yy} + \gamma(\tilde{\partial}_3^2 + \tilde{\partial}_1^2) c_{ij,kl}^{xy} - \delta(\tilde{\partial}_3^2 - \tilde{\partial}_1^2) c_{ij,kl}^{xx} = 0, \quad (\text{B3})$$

$$\langle f_{ij}^y y_{kl} + y_{ij} f_{kl}^y \rangle = [\alpha(\tilde{\partial}_3^2 + \tilde{\partial}_1^2) + \tilde{\partial}_2^2] c_{ij,kl}^{yy} - \beta(\tilde{\partial}_3^2 - \tilde{\partial}_1^2) c_{ij,kl}^{yx} + \gamma(\tilde{\partial}_3^2 + \tilde{\partial}_1^2) c_{ij,kl}^{yx} - \delta(\tilde{\partial}_3^2 - \tilde{\partial}_1^2) c_{ij,kl}^{xx} = 0, \quad (\text{B4})$$

$$\langle f_{ij}^y y_{kl} + y_{ij} f_{kl}^y \rangle = \gamma(\tilde{\partial}_3^2 + \tilde{\partial}_1^2) c_{ij,kl}^{yy} - \delta(\tilde{\partial}_3^2 - \tilde{\partial}_1^2) c_{ij,kl}^{xy} + \gamma(\tilde{\partial}_3^2 + \tilde{\partial}_1^2) c_{ij,kl}^{yy} - \delta(\tilde{\partial}_3^2 - \tilde{\partial}_1^2) c_{ij,kl}^{yx} = -2\delta_{(ij),(kl)} d_{ij}. \quad (\text{B5})$$

If we want to move to a continuous picture, then we replace $\tilde{\partial}_1^2 \rightarrow \partial_1^2$, $\tilde{\partial}_2^2 \rightarrow \partial_2^2$, $\tilde{\partial}_3^2 \rightarrow (\partial_1 + \partial_2)^2$. In this picture c^{xx} , c^{xy} , c^{yx} , c^{yy} should be seen as functions on a four-dimensional cube.

One can also write down equations for the cycling frequencies using

$$\omega_{x_{ij}, y_{kl}} = \frac{\langle f_{ij}^x y_{kl} - x_{ij} f_{kl}^y \rangle}{2\sqrt{\det \mathbf{C}_{[r,r]}}} \stackrel{\mathbf{D}\text{-diag.}}{=} \frac{\langle f_{ij}^x y_{kl} \rangle}{\sqrt{\det \mathbf{C}_{[r,r]}}}. \quad (\text{B6})$$

In the last step we used the Lyapunov equation together with the fact that \mathbf{D} is a diagonal matrix.

-
- [1] É. Fodor and M. Cristina Marchetti, *Phys. A Stat. Mech. Appl.* **504**, 106 (2018).
- [2] F. Jülicher, K. Kruse, J. Prost, and J. F. Joanny, *Phys. Rep.* **449**, 3 (2007).
- [3] M. C. Marchetti, J. F. Joanny, S. Ramaswamy, T. B. Liverpool, J. Prost, M. Rao, and R. A. Simha, *Rev. Mod. Phys.* **85**, 1143 (2013).
- [4] A. Filella, F. Nadal, C. Sire, E. Kanso, and C. Eloy, *Phys. Rev. Lett.* **120**, 198101 (2018).
- [5] M. Ballerini, N. Cabibbo, R. Candelier, A. Cavagna, E. Cisbani, I. Giardina, V. Lecomte, A. Orlandi, G. Parisi, A. Procaccini, M. Viale, and V. Zdravkovic, *Proc. Natl. Acad. Sci. USA* **105**, 1232 (2008).
- [6] N. C. Damton, L. Turner, S. Rojevsky, and H. C. Berg, *Biophys. J.* **98**, 2082 (2010).
- [7] S. Thutupalli, M. Sun, F. Bunyak, K. Palaniappan, and J. W. Shaevitz, *J. R. Soc. Interface* **12**, 20150049 (2015); [arXiv:1410.7230](https://arxiv.org/abs/1410.7230).
- [8] F. C. MacKintosh and C. F. Schmidt, *Curr. Opin. Cell Biol.* **22**, 29 (2010).
- [9] F. S. Gnesotto, F. Mura, J. Gladrow, and C. P. Broedersz, *Rep. Prog. Phys.* **81**, 066601 (2018).
- [10] S. C. Weber, A. J. Spakowitz, and J. A. Theriot, *Proc. Natl. Acad. Sci. USA* **109**, 7338 (2012).
- [11] A. W. C. Lau, B. D. Hoffmann, A. Davies, J. C. Crocker, and T. C. Lubensky, *Phys. Rev. Lett.* **91**, 198101 (2003).
- [12] M. Guo, A. J. Ehrlicher, M. H. Jensen, M. Renz, J. R. Moore, R. D. Goldman, J. Lippincott-Schwartz, F. C. MacKintosh, and D. A. Weitz, *Cell* **158**, 822 (2014).
- [13] N. Fakhri, A. D. Wessel, C. Willms, M. Pasquali, D. R. Klopfenstein, F. C. MacKintosh, and C. F. Schmidt, *Science* **344**, 1031 (2014).
- [14] C. P. Brangwynne, G. H. Koenderink, F. C. MacKintosh, and D. A. Weitz, *J. Cell Biol.* **183**, 583 (2008).
- [15] T. Betz, M. Lenz, J.-F. Joanny, and C. Sykes, *Proc. Natl. Acad. Sci. USA* **106**, 15320 (2009).
- [16] H. Turlier, D. A. Fedosov, B. Audoly, T. Auth, N. S. Gov, C. Sylkes, J.-F. Joanny, G. Gompper, and T. Betz, *Nat. Phys.* **12**, 513 (2016).
- [17] E. Ben-Isaac, Y. K. Park, G. Popescu, F. L. H. Brown, N. S. Gov, and Y. Shokef, *Phys. Rev. Lett.* **106**, 238103 (2011).
- [18] D. Needleman and Z. Dogic, *Nat. Rev. Mater.* **2**, 17048 (2017).
- [19] R. Suzuki, C. A. Weber, E. Frey, and A. R. Bausch, *Nat. Phys.* **11**, 839 (2015).
- [20] C. Battle, C. P. Broedersz, N. Fakhri, V. F. Geyer, J. Howard, C. F. Schmidt, and F. C. MacKintosh, *Science* **352**, 604 (2016).
- [21] J. Gladrow, N. Fakhri, F. C. MacKintosh, C. F. Schmidt, and C. P. Broedersz, *Phys. Rev. Lett.* **116**, 248301 (2016).
- [22] J. Gladrow, C. P. Broedersz, and C. F. Schmidt, *Phys. Rev. E* **96**, 022408 (2017).
- [23] F. Mura, G. Gradziuk, and C. P. Broedersz, *Phys. Rev. Lett.* **121**, 038002 (2018).
- [24] F. S. Gnesotto, B. M. Remlein, and C. P. Broedersz, [arXiv:1809.04639v1](https://arxiv.org/abs/1809.04639v1) (2018).
- [25] J. Li, J. M. Horowitz, T. R. Gingrich, and N. Fakhri, *Nat. Commun.* **10**, 1666 (2019).
- [26] D. Mizuno, C. Tardin, C. F. Schmidt, and F. C. MacKintosh, *Science* **315**, 370 (2007).

- [27] P. Martin, A. J. Hudspeth, and F. Jülicher, *Proc. Natl. Acad. Sci. USA* **98**, 14380 (2001).
- [28] É. Fodor, M. Guo, N. S. Gov, P. Visco, D. A. Weitz, and F. van Wijland, *Europhys. Lett.* **110**, 48005 (2015).
- [29] J. H. v. E. Job Boekhoven, Wouter E. Hendriksen, Ger J. M. Koper, Rienk Eelkema, *Science* **349**, 1075 (2015).
- [30] J. Palacci, S. Sacanna, A. P. Steinberg, D. J. Pine, and P. M. Chaikin, *Science* **339**, 936 (2013).
- [31] J.-B. Manneville, P. Bassereau, D. Lévy, and J. Prost, *Phys. Rev. Lett.* **82**, 4356 (1999).
- [32] J.-B. Manneville, P. Bassereau, S. Ramaswamy, and J. Prost, *Phys. Rev. E* **64**, 021908 (2001).
- [33] J. Liu, M. L. Gardel, K. Kroy, E. Frey, B. D. Hoffman, J. C. Crocker, A. R. Bausch, and D. A. Weitz, *Phys. Rev. Lett.* **96**, 118104 (2006).
- [34] G. H. Koenderink, Z. Dogic, F. Nakamura, P. M. Bendix, F. C. MacKintosh, J. H. Hartwig, T. P. Stossel, and D. A. Weitz, *Proc. Natl. Acad. Sci. USA* **106**, 15192 (2009).
- [35] J. Alvarado, M. Sheinman, A. Sharma, F. C. MacKintosh, and G. H. Koenderink, *Soft Matter* **13**, 5624 (2017).
- [36] O. J. N. Bertrand, D. K. Fygenson, and O. A. Saleh, *Proc. Natl. Acad. Sci. USA* **109**, 17342 (2012).
- [37] U. Seifert, *Rep. Prog. Phys.* **75**, 126001 (2012).
- [38] A. Frishman and P. Ronceray, [arXiv:1809.09650](https://arxiv.org/abs/1809.09650) (2018).
- [39] D. S. Seara, V. Yadav, I. Linsmeier, A. P. Tabatabai, P. W. Oakes, S. M. A. Tabei, S. Banerjee, and M. P. Murrell, *Nat. Commun.* **9**, 4948 (2018).
- [40] É. Roldán, J. Barral, P. Martin, J. M. R. Parrondo, and F. Jülicher, [arXiv:1803.04743v3](https://arxiv.org/abs/1803.04743v3).
- [41] G. Bisker, M. Polettini, T. R. Gingrich, and J. M. Horowitz, *J. Stat. Mech. Theory Exp.* (2017) 093210.
- [42] M. Esposito, *Phys. Rev. E* **85**, 041125 (2012).
- [43] M. Polettini and M. Esposito, *Phys. Rev. Lett.* **119**, 240601 (2017).
- [44] A. Ghanta, J. C. Neu, and S. Teitworth, *Phys. Rev. E* **95**, 032128 (2017).
- [45] J. P. Gonzalez, J. C. Neu, and S. W. Teitworth, *Phys. Rev. E* **99**, 022143 (2019).
- [46] M. G. Yucht, M. Sheinman, and C. P. Broedersz, *Soft Matter* **9**, 7000 (2013).
- [47] C. P. Broedersz and F. C. MacKintosh, *Rev. Mod. Phys.* **86**, 995 (2014).
- [48] D. Osmanović and Y. Rabin, *Soft Matter* **13**, 963 (2017).
- [49] X. Mao and T. C. Lubensky, *Annu. Rev. Condens. Matter Phys.* **9**, 413 (2018).
- [50] G. Falasco, M. Baiesi, L. Molinaro, L. Conti, and F. Baldovin, *Phys. Rev. E* **92**, 022129 (2015).
- [51] H. Risken, *The Fokker-Planck Equation* (Springer, Berlin, 1996).
- [52] J. B. Weiss, *Tellus A* **55**, 208 (2003).
- [53] B. Mohar, in *Graph Theory, Combinatorics and Applications*, edited by Y. Alavi, G. Chartrand, O. R. Ollermann, and A. J. Schwenk (Wiley, New York, 1991), pp. 871–898.
- [54] S. E. Schaeffer, *Comput. Sci. Rev.* **1**, 27 (2007).
- [55] M. E. Fisher, *J. Comb. theory* **1**, 105 (1966).
- [56] G. Kirchhoff, *Ann. Phys.* **148**, 497 (1847).
- [57] F. Mura, G. Gradziuk, and C. P. Broedersz (unpublished).
- [58] J. Harder, C. Valeriani, and A. Cacciuto, *Phys. Rev. E* **90**, 062312 (2014).
- [59] S. A. Mallory, C. Valeriani, and A. Cacciuto, *Phys. Rev. E* **92**, 012314 (2015).
- [60] Y. Li and P. R. ten Wolde, [arXiv:1902.02684](https://arxiv.org/abs/1902.02684) (2019).
- [61] A. Kaiser, S. Babel, B. Ten Hagen, C. Von Ferber, and H. Löwen, *J. Chem. Phys.* **142**, 124905 (2015).

C Irreversibility in linear systems with colored noise

This section is a reprint of the following publication:

Irreversibility in linear systems with colored noise

Grzegorz Gradziuk, Gabriel Torregrosa, and Chase P. Broedersz[†]

[†] corresponding author

Physical Review E **105**, 024118 (2022)

Irreversibility in linear systems with colored noise

Grzegorz Gradziuk and Gabriel Torregrosa

*Arnold-Sommerfeld-Center for Theoretical Physics and Center for NanoScience,
Ludwig-Maximilians-Universität München, D-80333 München, Germany*

Chase P. Broedersz*

*Arnold-Sommerfeld-Center for Theoretical Physics and Center for NanoScience,
Ludwig-Maximilians-Universität München, D-80333 München, Germany and*

Department of Physics and Astronomy, Vrije Universiteit Amsterdam, 1081 HV Amsterdam, The Netherlands

(Dated: January 19, 2022)

Time-irreversibility is a distinctive feature of non-equilibrium dynamics and several measures of irreversibility have been introduced to assess the distance from thermal equilibrium of a stochastically driven system. While the dynamical noise is often approximated as white, in many real applications the time correlations of the random forces can actually be significantly long-lived compared to the relaxation times of the driven system. We analyze the effects of temporal correlations in the noise on commonly used measures of irreversibility and demonstrate how the theoretical framework for white noise driven systems naturally generalizes to the case of colored noise. Specifically, we express the auto-correlation function, the area enclosing rates, and mean phase space velocity in terms of solutions of a Lyapunov equation and in terms of their white noise limit values.

I. INTRODUCTION

The Langevin equation, first introduced to simplify the description of Brownian motion [1, 2], has become a standard tool for studying stochastic systems in fields ranging from physics, chemistry and electronics [3] to climate [4] and population dynamics [5]. In the original context the random force, or the dynamical noise, was assumed to be delta-correlated in time, owing to the time scale separation between the dynamics of the Brownian particle and the dynamics of fluid molecules. This assumption was later lifted to account for possible time-correlations in the noise and memory effects, leading to the formulation of a generalized Langevin equation [6, 7]. Subsequently, the area of investigation expanded to systems out of thermal equilibrium, both synthetic [8–10] and natural ones [11–16], setting up the challenge of quantifying the irreversibility of the dynamics and linking this irreversibility to heat dissipation and entropy production rate [17, 18]. To tackle this problem of measuring the “distance from thermal equilibrium” experimentalists have employed a combination of optical and magnetic tweezers-based microrheology combined with time-lapse microscopy [8, 13, 14, 19–21]. These and other experiments revealed deviations from the Fluctuation-Dissipation theorem that allowed estimating the energy dissipation rates in certain biological systems [22–24]. Simultaneous work on the theoretical side resulted in the foundation of stochastic thermodynamics and discovery of a multitude of fluctuation theorems, exposing the connections between dissipation and irreversibility [17, 25]. Such connections have recently been investigated also in case of time-correlated dynamical noise [26, 27].

Despite the spectacular success of the white noise approximation at modelling the stochastic nature of both equilibrium and non-equilibrium processes, a more complex description is indeed needed when the correlation time of the noise becomes significant, as compared to the natural relaxation times of the analyzed system. In fact, temporal correlations in the noise can qualitatively change the dynamics, e.g., they can lead to stochastic resonance [28] and induce phase transitions in the stationary probability distributions [29].

While increasing the range of applicability and the abundance of phenomena, accounting for time-correlations in the noise largely complicates the mathematical treatment of the dynamics. The loss of Markovianity precludes a straightforward mapping to a Fokker-Planck formalism, in which the time evolution of the probability density and resulting correlations between the degrees of freedom could be calculated. To circumvent this obstacle, numerous approximation schemes and perturbative approaches have been developed for specific regimes of the correlation time of the noise [30–33]. Furthermore, it has been shown, that in certain cases, despite the non-Markovianity of the dynamics, an exact, generalized Fokker-Planck equation with an effective diffusion matrix can be formulated under certain assumptions about the initial preparation of the system, statistics of the noise, or linearity of the dynamics [32, 34]. For a comprehensive review of the topic we refer the reader to [32].

Here, we abstain from calculating the full probability distribution and instead take a perspective focused on the time-irreversibility of the dynamics. The most fundamental, or direct measures of irreversibility compare the probabilities of observing a forward vs. backward trajectory. Here, we focus on a set of indirect, but commonly used measures of irreversibility based on the probability currents and temporal correlations of the trajectory. We

* c.p.broedersz@vu.nl

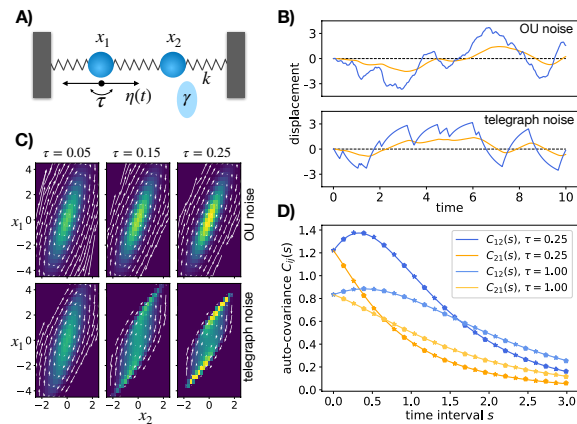


FIG. 1. A) Schematics of the two-bead model with bead 1 driven by a colored noise with correlation time τ . B) Sample trajectories of bead displacements x_1 (blue) and x_2 (orange) for bead 1 driven with OU noise (upper plot) and telegraph noise (lower plot), with $\tau = 0.25$. C) Probability density plots for (x_1, x_2) , with OU noise (upper row) and telegraph noise (lower row) for increasing correlation time of the noise. The white arrows represent the mean velocity field. D) Off-diagonal elements of the auto-covariance function $C_{ij}(s) = \langle x_i(t)x_j(t+s) \rangle$ for OU noise (stars) and telegraph noise (pentagons). For the diagonal elements of $\mathbf{C}(s)$ see Appendix.

show how such measures depend on the correlations of the driving noise, in particular its correlation time. We first introduce a class of linear systems for which analytical solutions can be obtained. Then, we demonstrate how the formulas for the irreversibility measures known for white noise driven systems [35–37] naturally generalize to the colored noise case and discuss the physical mechanism behind this generalization. Finally, we present an example application of the new formulas to a model system of a driven soft biological network [37], that in the context of irreversibility has up to now only been studied within the white noise approximation.

II. LINEAR SYSTEMS WITH COLORED NOISE

Linear analysis lies at the heart of physics. To reduce the complexity one commonly considers small fluctuations around a fixed point of the deterministic dynamics, for which the restoring force is approximately a linear function of the displacements. In relation to non-equilibrium dynamics and measures of irreversibility, such linear analysis has been applied in diverse contexts: driven biological assemblies [37–39], population dynamics [40], climate oscillations [4, 41, 42], or electronic circuits [36, 43].

As in these works, we consider an overdamped system for which the deterministic force is a linear function of the instantaneous position in phase space $\mathbf{x}(t)$ at time t . The deterministic velocity can thus be written as $\mathbf{A}\mathbf{x}$, where

\mathbf{A} includes a constant mobility tensor. The existence of a steady state requires the real parts of all the eigenvalues of \mathbf{A} to be negative. Here, we do not require \mathbf{A} to be symmetric, therefore allowing for non-conservative forces. The Langevin equation then takes the form

$$\dot{\mathbf{x}}(t) = \mathbf{A}\mathbf{x}(t) + \sqrt{2\mathbf{D}_\alpha}\boldsymbol{\eta}_\alpha(t) \quad (1)$$

with possibly colored noise $\boldsymbol{\eta}_\alpha$ characterized by a time-correlation function \mathcal{G}_α :

$$\langle \boldsymbol{\eta}_\alpha(t) \rangle = 0, \quad \langle \boldsymbol{\eta}_\alpha(t)\boldsymbol{\eta}_\beta^\top(t') \rangle = \mathbb{1}\delta_{\alpha,\beta}\mathcal{G}_\alpha(t-t'). \quad (2)$$

Here, α indexes the pairwise independent sources of the dynamical noise and summation over repeating indices is assumed. The matrix \mathbf{D}_α is an equivalent of the diffusion matrix and describes the amplitude and correlations of the noise acting on different degrees of freedom. These correlations encoded in \mathbf{D}_α can be thought of as spatial correlations of the random forces, if $\mathbf{x}(t) = \{x_i(t)\}$ describes the dynamics of components of a spatially extended system. We allow in general for a set of pairwise independent noise terms $\{\sqrt{2\mathbf{D}_\alpha}\boldsymbol{\eta}_\alpha\}$ with corresponding correlations $\{\mathbf{D}_\alpha\}$, $\{\mathcal{G}_\alpha\}$. However, due to the linearity of the system one can always analyse the contributions from each statistically independent noise term separately and then superpose the results. Thereby, for simplicity we consider from now on a single, non-indexed noise term $\sqrt{2\mathbf{D}}\boldsymbol{\eta}(t)$.

It is crucial to note that $\mathcal{G}(t)$ and \mathbf{D} together with Eq. (2) do not define the noise uniquely – they restrict the noise correlations only up to second order, leaving the higher order moments unconstrained. In fact, two noises characterized by exactly the same $\mathcal{G}(t)$ and \mathbf{D} can lead to qualitatively different dynamics and steady state statistics, as illustrated in Fig. 1. On the contrary, the irreversibility measures discussed in this paper, as well as any other two-point correlation function, are indeed fully determined by $\mathcal{G}(t)$ and \mathbf{D} , as we shall see later. Given the linear dynamics, two systems sharing equal $\mathcal{G}(t)$ and \mathbf{D} can only differ in higher order correlations of $\mathbf{x}(t)$. To illustrate the above points, we present two commonly employed examples of colored noise that share the same time-correlation function.

One of the most common implementations of colored noise defines the dynamics of the noise via an Ornstein-Uhlenbeck (OU) process:

$$\dot{\boldsymbol{\eta}}(t) = -\frac{1}{\tau}\boldsymbol{\eta}(t) + \boldsymbol{\xi}(t) \quad (3)$$

$$\langle \xi_i(t)\xi_j(t') \rangle = \delta_{ij}\delta(t-t'), \quad (4)$$

where $\boldsymbol{\xi}(t)$ is vector of normalized Gaussian white noises. The time-correlations of $\boldsymbol{\eta}(t)$ decay exponentially:

$$\mathcal{G}(s) = \frac{1}{2\tau}e^{-|s|/\tau}, \quad (5)$$

which allows to identify τ as the correlation time. A clear advantage of the OU noise is that after including the dynamics of the noise (Eq. (3)) in the description, one arrives at a Markovian system driven by a Gaussian white

noise. This largely simplifies the analysis and for a linear system implies in particular that the conditional probability density $p(\mathbf{x}, t | \mathbf{x}_0, t_0)$ is Gaussian, independently of the value of τ (see Fig. 1). Owing to its simplicity, OU noise is widely employed to model the persistent motion of active Brownian particles [33, 44–46].

The assumption about the noise being Gaussian is often legitimate: it is the case, for example, when the random force effectively describes an aggregate action of a large number of factors (such as the collisions of fluid molecules with a Brownian particle), as rationalized by the Central Limit Theorem. In other contexts, however, the noise statistics can drastically differ from Gaussian. As a glaring example, consider a random force that switches between a discrete set of values. Similar stochastic dynamics is exhibited in nature by myosin motors [8, 14, 47, 48] exerting step-like contractile forces on the cytoskeleton. In such systems the noise may be more adequately modelled with a telegraph process [49]:

$$\eta_i(t) = \frac{(-1)^{n_i(t)}}{\sqrt{2\tau}}, \quad (6)$$

where $\{n_i(t)\}$ are pairwise independent Poisson processes with transition rate $1/(2\tau)$. The time correlation function $\mathcal{G}(s)$ for the telegraph noise, as defined by Eq. (6), is an exponential decay, identical to the one associated to the OU noise (Eq. (5)). Even though these two types of noise give rise to very different trajectories and steady state probability distributions, they result in identical auto-covariance functions (see Fig. 1), which will be discussed in detail in the following section.

Finally, let us remark that we use a convention in which the time correlation function of the noise is normalized to 1, namely: $\int_{-\infty}^{\infty} \mathcal{G}(t) dt = 1$, corresponding to noise of power 1. This choice, implying that $\mathcal{G}(t) \xrightarrow{\tau \rightarrow 0} \delta(t)$, allows us to study the effects of transition from white to time-correlated noise, while keeping the power of the noise fixed.

III. AUTO-COVARIANCE FUNCTION

The auto-covariance function is a standard quantity used in the analysis of time series and in particular the time-irreversibility of the dynamics. Comparing the auto-covariance with the response function can reveal deviations from the Fluctuation-Dissipation theorem [8, 12, 16, 50], which can be further connected to the heat dissipation rate through the Harada-Sasa relation [51, 52]. The auto-covariance is defined as

$$\mathbf{C}(t, t+s) = \langle \mathbf{x}(t) \mathbf{x}^\top(t+s) \rangle. \quad (7)$$

Under steady state conditions, the covariance function becomes translation invariant in time and we can write $\mathbf{C}(t, t+s) := \mathbf{C}(s)$. By definition, the covariance function fulfils $\mathbf{C}^\top(s) = \mathbf{C}(-s)$. For the purpose of calculations,

this property allows us to assume without loss of generality that $s > 0$, since the covariance for negative time differences $-s$ can be obtained by transposition of $\mathbf{C}(s)$. Time reversibility additionally requires $\mathbf{C}(s) = \mathbf{C}(-s)$, implying that $\mathbf{C}(s)$ must be a symmetric matrix. Note, however, to fulfill $\mathbf{C}(s) = \mathbf{C}^\top(s)$ does not in general require the system to be at equilibrium. In fact, any time correlations of the noise in Eq. (1) not accompanied by a corresponding memory kernel in the deterministic term inevitably violate the Fluctuation-Dissipation Theorem [7].

To derive an equation for $\mathbf{C}(s)$ note that for a linear system one can write a formal solution for the time trajectory:

$$\mathbf{x}(t) = \int_{-\infty}^t e^{\mathbf{A}(t-t')} \sqrt{2\mathbf{D}} \boldsymbol{\eta}(t') dt' \quad (8)$$

and for the associated covariance matrix

$$\mathbf{C}(t, t+s) = \int_{-\infty}^t dt' \int_{-\infty}^{t+s} dt'' e^{\mathbf{A}(t-t')} 2\mathbf{D} \mathcal{G}(t'-t'') e^{\mathbf{A}^\top(t+s-t'')}. \quad (9)$$

While mathematically correct, Eq. (9) does not provide a simple interpretation of how the time correlations in the noise affect the covariance function. A more insightful relation is obtained by using the steady state assumption and time translation invariance. Eq. (9) combined with the steady state property $\partial_t \mathbf{C}(t, t+s) = 0$ leads to (see Appendix):

$$\mathbf{A}\mathbf{C}(s) + \mathbf{C}(s)\mathbf{A}^\top = -[\mathbf{B}(s)\mathbf{D} + \mathbf{D}\mathbf{B}^\top(-s)], \quad (10)$$

where $\mathbf{B}(s)$ is defined as

$$\mathbf{B}(s) = 2 \int_0^\infty dt e^{\mathbf{A}t} \mathcal{G}(t+s) \quad \forall s \in \mathbb{R}. \quad (11)$$

For reasons that will become clear later, we refer to \mathbf{B} as the spreading matrix. First, let us consider a few limiting cases. In the limit of white noise ($\tau \rightarrow 0$) the equal-time covariance matrix $\mathbf{C}_w(s=0) := \mathbf{C}_w$ fulfils

$$\mathbf{A}\mathbf{C}_w + \mathbf{C}_w\mathbf{A}^\top = -2\mathbf{D}, \quad (12)$$

which is the well known Lyapunov equation [41]. The product $\mathbf{A}\mathbf{C}_w$ can be identified with the matrix of Onsager coefficients \mathbf{L} and the Lyapunov equation itself with $\mathbf{L} + \mathbf{L}^\top = -2\mathbf{D}$ [53]. Comparing Eq. (10) with Eq. (12) leads to a key observation: the covariance $\mathbf{C}(s)$ can be calculated by solving a Lyapunov equation with an effective diffusion matrix. This modified diffusion matrix $\tilde{\mathbf{D}}(s)$ is set by the spreading matrix $\mathbf{B}(s)$ via

$$\tilde{\mathbf{D}}(s) = \frac{1}{2}[\mathbf{B}(s)\mathbf{D} + \mathbf{D}\mathbf{B}^\top(-s)]. \quad (13)$$

Note that for time irreversible dynamics and $s \neq 0$ the effective diffusion matrix $\tilde{\mathbf{D}}(s)$ can in general be non-symmetric, resulting in a covariance function non-symmetric in time. The non-symmetry of the effective

diffusion matrix does not allow for identifying $\tilde{\mathbf{D}}(s)$ as a covariance matrix of some effective white noise. Conversely, when considering the equal-time covariance (setting $s = 0$), we find a symmetric effective diffusion matrix

$$\tilde{\mathbf{D}} = \frac{1}{2}[\mathbf{B}\mathbf{D} + \mathbf{D}\mathbf{B}^\top], \quad (14)$$

which can indeed be interpreted as a covariance matrix of an effective noise. Therefore, the equal-time covariance $\mathbf{C}(s = 0) := \mathbf{C}$ for a system with time correlated noise and diffusion matrix \mathbf{D} remains unchanged, if one replaces the colored noise with a white noise with an appropriate effective diffusion matrix $\tilde{\mathbf{D}}$. In this sense, for linear systems the temporal and spatial correlations in the noise are equivalent at the level of covariance matrix. This is of particular importance for the case of Gaussian colored noise (e.g. Ornstein-Uhlenbeck noise), for which the stationary probability density is known to be Gaussian. In this case the covariance matrix \mathbf{C} calculated for the system with the effective white noise defines the exact stationary probability distribution of a colored noise system: $p(\mathbf{x}) \sim \exp[-\mathbf{x}^\top \mathbf{C}^{-1} \mathbf{x} / 2]$. This special case of Gaussian noise was solved in [32], where a generalized Fokker-Planck equation for $p(\mathbf{x}, t)$ is derived. In the long time limit the diffusion matrix of the generalized Fokker-Planck equation converges to our effective diffusion matrix $\tilde{\mathbf{D}}$ defined as in Eq. (14). Importantly, even though with Gaussian noise the stationary probability densities are identical in the coloured- and effective white-noise systems, the actual dynamics can be very different. Moreover, non-Gaussian noise can result in $p(\mathbf{x})$ qualitatively different from Gaussian (see Fig. 1), while, remarkably, the covariance matrix \mathbf{C} is the same as for the effective white-noise system.

Having presented the partial correspondence between temporal and spatial correlations in the noise for linear systems, let us now discuss the physical origin of this connection. Consider two degrees of freedom x_i and x_j that are coupled in some way, directly or indirectly. That is a displacement in x_i results in a displacement of x_j , with a magnitude and time dependence encoded by \mathbf{A} . When a persistent force is exerted on the i th degree of freedom, it is followed by a displacement in x_j , which leads to correlations in the force instantaneously experienced by i and j . The way these correlations enter in the effective diffusion matrix $\tilde{\mathbf{D}}$ is specified by Eq. (14) and the spreading matrix \mathbf{B} . The multiplication by \mathbf{B} results in spreading of the elements of $\tilde{\mathbf{D}}$, as exemplified in Fig. 2. The directions of spreading are set by the \mathbf{A} matrix, while the range of spreading is controlled by the correlation time τ , or more generally, by the width of $\mathcal{G}(t)$. These two key quantities define \mathbf{B} in terms of an integral, but an explicit expression can be found in certain cases. For the ubiquitous case of exponentially decaying time-correlations, as in Eq. (5), one finds

$$\mathbf{B} = (\mathbf{1} - \tau \mathbf{A})^{-1}. \quad (15)$$

The derivation and expressions for $\mathbf{B}(s)$ are presented in

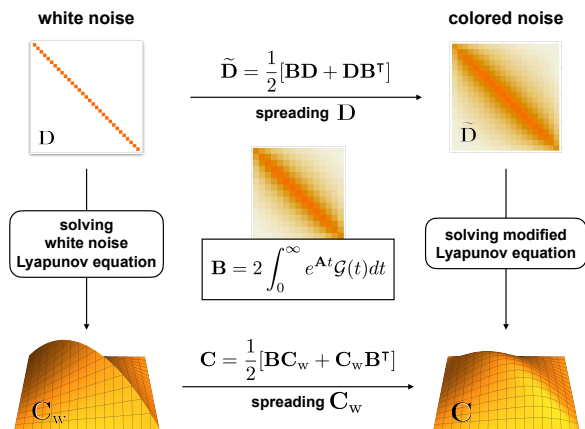


FIG. 2. Schematic procedure of obtaining the auto-covariance matrix $\mathbf{C}(s)$ in the colored noise case. Here shown for $s = 0$, for a 1-dimensional chain of harmonically coupled beads, with each bead driven by independent noise with correlations decaying exponentially in time. The two possible sequences of steps marked by the arrows lead to equal results for $\mathbf{C}(s)$. These two alternative ways include "spreading" either \mathbf{D} , or \mathbf{C}_w using the \mathbf{B} matrix.

the Supplementary Information. Notably, Eq. (10) and the derived expressions for $\mathbf{B}(s)$ are exact and make no assumptions on the noise correlation time τ being small or large.

We close this section by noting that instead of first calculating the effective diffusion matrix and solving the Lyapunov equation with $\tilde{\mathbf{D}}(s)$, one can equivalently first find the equal-time white-noise covariance matrix \mathbf{C}_w (by replacing $\mathcal{G}(s)$ with $\delta(s)$ in the original problem and solving Eq. (12)) and calculate the covariance function $\mathbf{C}(s)$ as

$$\mathbf{C}(s) = \frac{1}{2}[\mathbf{B}(s)\mathbf{C}_w + \mathbf{C}_w\mathbf{B}^\top(-s)]. \quad (16)$$

The equivalence of the two approaches is visualised in Fig. 2 for a specific system comprised of a chain of harmonically coupled overdamped beads, with $s = 0$. A proof based on simple algebra and $\mathbf{A}\mathbf{B} = \mathbf{B}\mathbf{A}$ is presented in the appendix.

IV. MEAN VELOCITY AND AREA ENCLOSING RATES

In the previous section we considered two point time covariance functions as indicators of time irreversible dynamics. However, already mean values of instantaneous quantities can reveal time-irreversibility. Consider the instantaneous velocity $\mathbf{v}(t)$ and its mean value at a certain point in phase space $\langle \mathbf{v}(\mathbf{x}) \rangle := \langle \mathbf{v}(t) | \mathbf{x}(t) = \mathbf{x} \rangle$. Upon time reversal the velocity changes sign, and therefore time-reversibility requires $\langle \mathbf{v}(\mathbf{x}) \rangle = 0$. This fact has been used to define a class of measures of equilibrium based

on non-vanishing probability fluxes [15, 36, 38, 39]. For a linear system driven by white noise the mean phase space velocity is known to be a linear function of \mathbf{x} [41]:

$$\langle \mathbf{v}(\mathbf{x}) \rangle = \boldsymbol{\Omega}_w \mathbf{x}, \quad \boldsymbol{\Omega}_w = (\mathbf{A} + \mathbf{D}\mathbf{C}_w^{-1}) \quad (17)$$

Note that since for overdamped systems with white noise the velocities are not well defined in terms of the time derivative of the position, one defines $\langle \mathbf{v}(\mathbf{x}) \rangle$ through $\langle \mathbf{v}(\mathbf{x}) \rangle = \mathbf{j}(\mathbf{x})/p(\mathbf{x})$, where $\mathbf{j}(\mathbf{x})$ is the probability current. To avoid the difficulty of measuring the average velocity $\langle \mathbf{v}(\mathbf{x}) \rangle$ at every point in phase space, one can define a more coarse grained measure of irreversibility known as the area enclosing rate [54]:

$$\mathcal{A} = \frac{1}{2} \langle \dot{\mathbf{x}}\mathbf{x}^\top - \mathbf{x}\dot{\mathbf{x}}^\top \rangle. \quad (18)$$

This entity can be traced back to the works of Mori and Kubo [6, 7], where it was used in the derivation of the Generalised Langevin Equation. Recently \mathcal{A} has received renewed attention as a measure of irreversibility [36, 37, 42, 43, 55], it has been connected to the entropy production rate, and applied in an irreversibility-oriented dimensionality reduction scheme [56]. Measuring \mathcal{A} is in fact equivalent to finding a linear expansion of the mean velocity field $\langle \mathbf{v}(\mathbf{x}) \rangle$ [57]. It has been demonstrated that for a white noise-driven linear system \mathcal{A} can be expressed in terms of the covariance matrix as

$$\mathcal{A}_w = \frac{1}{2} [\mathbf{A}\mathbf{C}_w - \mathbf{C}_w\mathbf{A}^\top]. \quad (19)$$

Moreover, in this specific case the mean velocity field and area enclosing rates are related via

$$\boldsymbol{\Omega}_w = \mathcal{A}_w \mathbf{C}_w^{-1}. \quad (20)$$

Hitherto, to our knowledge, the computation of $\mathbf{v}(\mathbf{x})$ and \mathcal{A} was mostly limited to systems driven by white noise. Following the same line of thought as for the auto-covariance function, we would like to investigate how the mean phase space velocity and the area enclosing rates change as the correlation time of the noise increases and becomes comparable with the relaxation times of the system, or larger.

Let us begin by considering a linear system driven by an Ornstein-Uhlenbeck noise. In this simple case, the complete dynamics, that include the time evolution of the noise, constitute a white noise linear system. Hence, the probability distribution is Gaussian and consequently the conditional average $\langle \mathbf{v}|\mathbf{x} \rangle$ is also a linear function of \mathbf{x} . More specifically, we show that (see Appendix):

$$\langle \mathbf{v}(\mathbf{x}) \rangle = \boldsymbol{\Omega}_{\text{OU}} \mathbf{x}, \quad \text{with} \quad \boldsymbol{\Omega}_{\text{OU}} = (\mathbb{1} + \tau \mathbf{D}\mathbf{C}_w^{-1})^{-1} \boldsymbol{\Omega}_w. \quad (21)$$

This expression shows explicitly how the mean velocity $\langle \mathbf{v}(\mathbf{x}) \rangle$ departs from the white noise values as the correlation time of the noise τ increases. Alternatively, $\boldsymbol{\Omega}_{\text{OU}}$ can be expressed in a way equivalent to Eq. (20), as demonstrated in the appendix, where we also give an exact expression for the joint probability $p(\mathbf{x}, \mathbf{v})$.

For other types of noise $\langle \mathbf{v}(\mathbf{x}) \rangle$ does not in general show a simple linear dependence on \mathbf{x} . Nevertheless, a compact formula can still be found for the area enclosing rates. This is obtained by substituting the formal solution (Eq. (8)) into Eq. (18) (for details see the Appendix). One then finds

$$\mathcal{A} = \frac{1}{2} [\mathbf{B}\mathbf{A}\mathbf{C}_w - \mathbf{C}_w\mathbf{A}^\top\mathbf{B}^\top], \quad (22)$$

that only depends on the correlation function of the noise $\mathcal{G}(s)$ (encoded in \mathbf{B}) and on \mathbf{D} (encoded in \mathbf{C}_w). This implies, in particular, that two qualitatively different noises (such as OU and telegraph) will yield exactly the same \mathcal{A} , if their two-point correlations given by \mathbf{D} and $\mathcal{G}(s)$ coincide. This property is a direct consequence of the linearity of the dynamics and \mathcal{A} being a second order correlation. Eq. (22) differs from the white noise formula by \mathbf{A} being replaced with an effective force matrix $\mathbf{B}\mathbf{A}$ (see Fig. 3).

At this point it is important to emphasise that the results in Eq. (21) and Eq. (22) are not perturbative and hold for arbitrarily large values of the correlation time τ . Therefore, they allow us to study not only the departure from the white noise behavior, but the full τ -dependence.

Finally, let us demonstrate a relationship between the area enclosing rates \mathcal{A} and the auto-covariance function $\mathbf{C}(s)$ discussed in the preceding section. As discussed in [36], when dealing with a discrete-time signal with time resolution $1/\Delta t$, one has to approximate the velocity in Eq. (18) with a finite difference, leading to:

$$\begin{aligned} \mathcal{A}_{ij} &= \frac{1}{2\Delta t} \langle [x_i(t + \Delta t) - x_i(t)]x_j(t) \\ &\quad - x_i(t)[x_j(t + \Delta t) - x_j(t)] \rangle \\ &= \frac{1}{2\Delta t} (C_{ij}(\Delta t) - C_{ij}(-\Delta t)). \end{aligned} \quad (23)$$

For systems driven by time correlated noise only, for which the auto-covariance function is differentiable, we can conclude that $\mathcal{A} = \frac{d}{ds}\mathbf{C}(s)|_{s=0}$. Consistently, for time reversible dynamics, $\mathbf{C}(s)$ is an even function with derivative 0 at $s = 0$. When the dynamics includes a white noise component, $\mathbf{C}(s)$ is no longer differentiable at $s = 0$, yet the symmetrized difference in Eq. (23) converges to a finite value in the limit of $\Delta t \rightarrow 0$.

V. EXAMPLE APPLICATION AND EMERGENT LENGTH-SCALE

In this last section we show how the framework developed in this article can be applied to a physical problem and offer insights inaccessible within a white noise approximation. As a working example we use a toy-model that was recently employed to study the non-equilibrium behavior across length scales in active biological assemblies [37, 39, 55]. There, the viscoelastic medium mimicking the cytoskeleton was modelled as a lattice of overdamped beads connected by springs and embedded in a

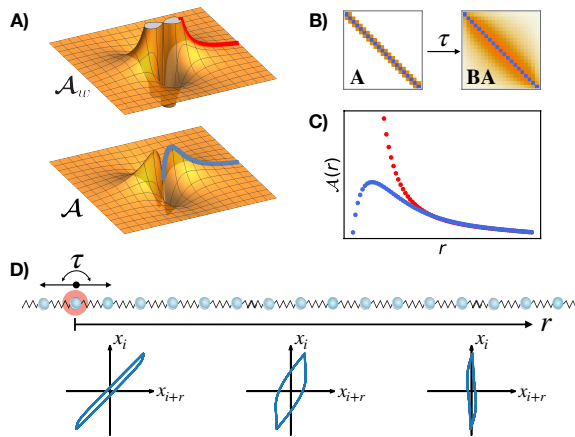


FIG. 3. Area enclosing rates for the 1-dimensional chain of harmonically coupled beads, with only the central bead "m" driven ($D_{ij} = \delta_{im}\delta_{jm}$). A) Plots of the area enclosing rate matrices for the white noise (top) and the colored noise (bottom) scenarios. The blue and red lines are the same as in panel C). B) The deterministic force matrix \mathbf{A} and the effective force matrix \mathbf{AB} , which enters in Eq. (22). C) Plots of the area enclosing rate for the driven bead and a bead at distance r , for white (red) and colored (blue) noise. D) Phase space trajectories of the displacements of bead i , driven by a deterministic periodically switching force, and a bead at distance r , for increasing values of r .

viscous fluid. The activity of molecular motors was implemented as a collection of dipole forces delta-correlated in time. Here we revisit this model, lift the assumption about white noise activity and discuss the resulting changes in the non-equilibrium behavior. For simplicity we focus on a 1-dimensional version of this model - a chain of beads.

In the previous works it has been shown that with a single activity in the chain, the area enclosing rate measured for two degrees of freedom: the agitated bead x_i and a bead at distance r , x_{i+r} , displays a power law as a function of the distance r . Importantly, with a collection of active agents in the chain, a similar scaling behavior is observed for the mean squared area enclosing rate $\langle \mathcal{A}^2(r) \rangle := \langle \mathcal{A}_{i,i+r}^2 \rangle_i$ measured for pairs of beads at distance r from each other (see Fig. 4). Note, while each $\mathcal{A}_{i,i+r}$ itself is a temporal average, $\langle \dots \rangle_i$ denotes a spatial average, or equivalently an average over an ensemble of activity distributions. Both results assumed the active forces to be delta-correlated in time, or in our formulation $\mathcal{G}(t) = \delta(t)$, and were essentially derived using Eq. (19).

Now, equipped with the colored noise formula (Eq. (22)) we can study the effects of the time correlations of the active forces. We assume force correlations to decay exponentially with time, as in Eq. (5), which among others can represent a telegraph process. The results presented in Fig. 3 (single activity) and in Fig. 4 (distribution of activities) show a qualitative change in both cases. The functional dependence of $\mathcal{A}_{i,i+r}$ and

$\langle \mathcal{A}^2(r) \rangle$ on the distance r is no longer monotonic. At a certain distance the area enclosing rates reach a pronounced maximum followed by a power law decay at large distances. In fact, the behavior for large r (power law decay with exponent -7) coincides with the one predicted theoretically for white noise activity in [37]. Heuristically, for large distances the relaxation times become much larger than the correlation time of active forces and it is justified to treat the active noise as "white". The origin of the maximum can be qualitatively explained in the single activity case with the stereotypical trajectories sketched in Fig. 3D). For short distances from the activity both beads experience a large displacement, but since the passive bead reacts almost immediately to the displacement of the driven one, the loops enclosed by the trajectory are very narrow, leading to small \mathcal{A} . At large distances the displacements of the passive bead are small and \mathcal{A} starts decreasing. A trade-off between the size of displacements and the delay between them gives rise to a maximum at moderate values of r . The exact position of the maximum turns out to scale as $\sqrt{\tau}$, as confirmed by the collapse in Fig. 4. We suspect this specific scaling, $r_{\max} \sim \sqrt{\tau}$, to be related to the distance up to which displacements propagate when applying a point force persistently over time τ . Despite the specificity of the considered system, the simple qualitative explanation of the origin of the maximum suggests that analogous behavior can be expected in other scenarios. Although it's difficult to argue for a biological relevance of \mathcal{A} reaching a maximum at a certain distance, the fact itself that a time scale τ gives rise to a specific length scale is rather remarkable.

VI. CONCLUSIONS

In this paper we showed how temporal correlations in the noise can affect the irreversibility of a systems' linear dynamics. To this end, we considered a class of linear systems described by a Langevin equation and driven by colored noise classified by its auto-covariance, which encodes both temporal and spatial correlations. We demonstrated that the formulas commonly employed to calculate standard measures of irreversibility, such as the auto-covariance or the area enclosing rates, naturally generalize to the case of colored noise. The expressions we derive are exact and valid for arbitrary correlations of the noise, allowing to study the full dependence of the irreversibility measures on the correlation time of the noise, and not only the departure from the white noise limit.

We discussed how noise scenarios that share the same two-point correlations can lead to drastically different dynamics and steady state probability distribution, while yielding equal results for certain measures of irreversibility. We also showed that for any colored noise model there exists a corresponding white noise model with appropriately modified spatial correlations, which lead to the same covariance matrix. In practice, when modelling

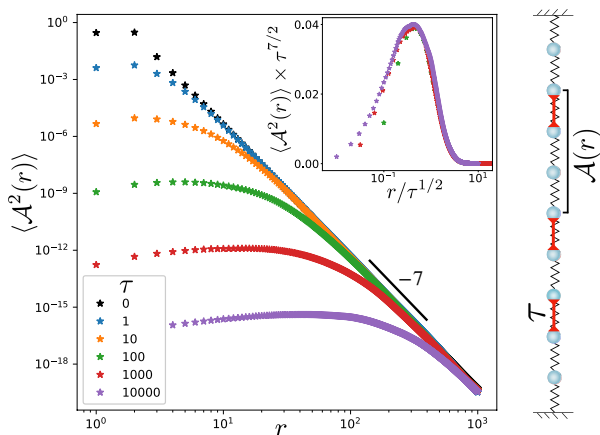


FIG. 4. Plots of the mean squared area enclosing rate for pairs of beads at distance r . The chain of beads is driven by homogeneously distributed and statistically independent force dipoles acting on pairs of neighboring beads ($i, i + 1$) with randomly chosen amplitudes $\sqrt{\alpha_i}$. Specifically, $D_{ij} = \delta_{ij}(\alpha_i + \alpha_{i-1}) - \delta_{i-1,j}\alpha_{i-1} - \delta_{i,j-1}\alpha_i$, where $\sqrt{\alpha_i}$ are drawn independently from a distribution (here a folded Gaussian distribution, however, only the variance of the distribution matters). For each dipole the force correlations decay exponentially in time with correlation time τ , as for the telegraph noise. The black markers ($\tau = 0$) correspond to white noise. Inset: collapse of the appropriately rescaled curves from the main plot in a linear-log scale. Only the curves for $\tau = \{10^2, 10^3, 10^5\}$, for which the maximum appears at a distance larger than the lattice spacing, are plotted.

a noisy or driven system, the detailed statistics of the

noise at play are unknown and one has to model the noise just based on its primary features. In such cases it is crucial to know how robust the results are to changes in the specific implementation of the noise. For the case of Ornstein-Uhlenbeck noise, customarily employed to model persistent forces, we find exact expressions for the probability distribution and mean phase space velocity in terms of solutions for the white noise limit.

Finally, we presented an example application of the derived formulas and revisited a model for irreversible dynamics in driven biological network, which up to now was only analyzed within the white noise approximation. We now allowed for time correlations in the active driving, leading to a qualitative change of behavior of the irreversibility measures at moderate distances. The introduced time correlations in the noise give rise to a specific length scale marked by a maximum of the irreversibility measures. The significance of this and analogous length scales potentially emerging in other non-equilibrium contexts remains an open question.

ACKNOWLEDGMENTS

We thank D. Brückner, F. Gnesotto, F. Mura and P. Ronceray for many stimulating discussions. This work was funded by the Deutsche Forschungsgemeinschaft (DFG, German Research Foundation) under Germany's Excellence Strategy—EXC-2094 - 390783311, by the DFG grant 418389167 and by the DFG Excellence cluster ORIGINS.

-
- [1] P. Langevin, C. R. Acad. Sci. **146**, 530 (1908).
[2] D. S. Lemons and A. Gythiel, American Journal of Physics **65**, 1079 (1997).
[3] W. T. Coffey, Y. P. Kalmykov, and J. T. Waldron, *The Langevin Equation* (World Scientific, Singapore, 1996).
[4] K. Hasselmann, Tellus **28**, 473 (1976).
[5] R. M. Nisbet and W. S. C. Gurney, *Modeling Fluctuating Populations* (Wiley, New York, 1982).
[6] H. Mori, Progress of Theoretical Physics **33** (1965).
[7] R. Kubo, Rep. Prog. Phys **29**, 255 (1966).
[8] D. Mizuno, C. Tardin, C. F. Schmidt, and F. C. MacKintosh, Science **315**, 370 (2007).
[9] S. Ciliberto, A. Imparato, A. Naert, and M. Tanase, Physical Review Letters **110**, 180601 (2013).
[10] J. R. Howse, R. A. Jones, A. J. Ryan, T. Gough, R. Vafabakhsh, and R. Golestanian, Physical Review Letters **99**, 048102 (2007), arXiv:0706.4406.
[11] P. Martin, A. J. Hudspeth, and F. Jülicher, Proceedings of the National Academy of Sciences of the United States of America **98**, 14380 (2001).
[12] A. W. C. Lau, B. D. Hoffman, A. Davies, J. C. Crocker, and T. C. Lubensky, Phys. Rev. Lett. **91**, 198101 (2003).
[13] T. Betz, M. Lenz, J.-F. Joanny, and C. Sykes, Proceedings of the National Academy of Sciences **106**, 15320 (2009).
[14] M. Guo, A. J. Ehrlicher, M. H. Jensen, M. Renz, J. R. Moore, R. D. Goldman, J. Lippincott-Schwartz, F. C. MacKintosh, and D. A. Weitz, Cell **158**, 822 (2014).
[15] C. Battle, C. P. Broedersz, N. Fakhri, V. F. Geyer, J. Howard, C. F. Schmidt, and F. C. MacKintosh, Science **352**, 604 (2016).
[16] H. Turlier, D. A. Fedosov, B. Audoly, T. Auth, N. S. Gov, C. Sykes, J. F. Joanny, G. Gompper, and T. Betz, Nature Physics **12**, 513 (2016).
[17] U. Seifert, Reports on Progress in Physics **75**, 126001 (2012), arXiv:1205.4176.
[18] É. Roldán, *Irreversibility and Dissipation in Microscopic Systems* (Springer, Cham, 2014).
[19] S. Ciliberto, S. Joubaud, and A. Petrosyan, Journal of Statistical Mechanics: Theory and Experiment **2010** (2010), arXiv:1009.3362.
[20] F. Ritort, Advances in Chemical Physics **137**, 31 (2008), arXiv:0705.0455.
[21] F. S. Gnesotto, F. Mura, J. Gladrow, and C. P. Broedersz, Reports on Progress in Physics **81**, 066601 (2018), arXiv:1710.03456.
[22] S. Toyabe, T. Okamoto, T. Watanabe-Nakayama, H. Taketani, S. Kudo, and E. Muneyuki, Physical Re-

- view Letters **104**, 198103 (2010).
- [23] É. Fodor, W. W. Ahmed, M. Almonacid, M. Bussonnier, N. S. Gov, M. H. Verlhac, T. Betz, P. Visco, and F. Van Wijland, Europhysics Letters **116**, 30008 (2016), arXiv:1511.00921.
- [24] T. Ariga, M. Tomishige, and D. Mizuno, Physical Review Letters **121**, 218101 (2018), arXiv:1704.05302.
- [25] K. Sekimoto, *Stochastic Energetics* (Springer, Berlin, 2010).
- [26] É. Fodor, R. L. Jack, and M. E. Cates, Annual Review of Condensed Matter Physics **13**, 215 (2022), arXiv:2104.06634.
- [27] J. O’Byrne, Y. Kafri, J. Tailleur, and F. van Wijland, arXiv preprint , 2104.03030 (2021), arXiv:2104.03030.
- [28] L. Gammaitoni, P. Hänggi, P. Jung, and F. Marchesoni, Reviews of Modern Physics **70**, 223 (1998).
- [29] K. Kitahara, W. Horsthemke, R. Lefever, and Y. Inaba, Progress of Theoretical Physics **64**, 1233 (1980).
- [30] N. G. Van Kampen, Physics Reports **24**, 171 (1976).
- [31] P. Jung and P. Hänggi, Physical Review A **35**, 4464 (1987).
- [32] P. Hänggi and P. Jung, Adv. Chem. Phys. **89**, 239 (1995).
- [33] É. Fodor, C. Nardini, M. E. Cates, J. Tailleur, P. Visco, and F. Van Wijland, Physical Review Letters **117**, 038103 (2016), arXiv:1604.00953.
- [34] P. Hänggi, Zeitschrift für Physik B Condensed Matter and Quanta **31**, 407 (1978).
- [35] J. B. Weiss, Physical Review E **76**, 061128 (2007), arXiv:0711.2250.
- [36] J. P. Gonzalez, J. C. Neu, and S. W. Teitworth, Physical Review E **99**, 22143 (2019).
- [37] F. Mura, G. Gradziuk, and C. P. Broedersz, Soft Matter **15**, 8067 (2019), arXiv:1905.13663.
- [38] J. Gladrow, N. Fakhri, F. C. MacKintosh, C. F. Schmidt, and C. P. Broedersz, Phys. Rev. Lett. **116**, 248301 (2016).
- [39] F. Mura, G. Gradziuk, and C. P. Broedersz, Physical Review Letters **121**, 38002 (2018), arXiv:1803.02797.
- [40] A. J. McKane and T. J. Newman, Physical Review Letters **94**, 218102 (2005), arXiv:0501023 [q-bio].
- [41] J. B. Weiss, Tellus A: Dynamic Meteorology and Oceanography **55**, 208 (2003).
- [42] J. B. Weiss, B. Fox-Kemper, D. Mandal, N. D. Arin, and R. K. P. Zia, Journal of Statistical Physics **179**, 1010 (2020).
- [43] A. Ghanta, J. C. Neu, and S. Teitworth, Physical Review E **95**, 032128 (2017).
- [44] P. Romanczuk, M. Bär, W. Ebeling, B. Lindner, and L. Schimansky-Geier, European Physical Journal: Special Topics **202**, 1 (2012).
- [45] U. Marini Bettolo Marconi and C. Maggi, Soft Matter **11**, 8768 (2015), arXiv:1507.03443.
- [46] G. Szamel, E. Flenner, and L. Berthier, Physical Review E **91**, 062304 (2015), arXiv:1501.01333.
- [47] F. C. MacKintosh and A. J. Levine, Phys. Rev. Lett. **100**, 18104 (2008), arXiv:0704.3794.
- [48] C. P. Brangwynne, G. H. Koenderink, F. C. Mackintosh, and D. A. Weitz, Phys. Rev. Lett. **100**, 118104 (2008).
- [49] M. Kac, The Rocky Mountain Journal of Mathematics **4**, 497 (1974).
- [50] P. Martin, A. J. Hudspeth, and F. Jülicher, Proceedings of the National Academy of Sciences **98**, 14380 (2001).
- [51] T. Harada and S. I. Sasa, Physical Review Letters **95**, 130602 (2005), arXiv:0502505 [cond-mat].
- [52] T. Harada and S. I. Sasa, Physical Review E **73**, 026131 (2006), arXiv:0510723 [cond-mat].
- [53] L. Onsager, Physical Review **38**, 2265 (1931).
- [54] This antisymmetrized form is only of relevance for the white noise case, where it makes the expression independent of the applied integration convention. With colored noise one can unambiguously write $\mathcal{A} = \langle \dot{\mathbf{x}}\mathbf{x}^\top \rangle$.
- [55] G. Gradziuk, F. Mura, and C. P. Broedersz, Physical Review E **99**, 052406 (2019), arXiv:1901.03132.
- [56] F. S. Gnesotto, G. Gradziuk, P. Ronceray, and C. P. Broedersz, Nature Communications **11**, 5378 (2020), arXiv:2001.08642.
- [57] A. Frishman and P. Ronceray, Physical Review X **10**, 21009 (2020), arXiv:1809.09650.

Appendices

A. DERIVATION OF AUTO-COVARIANCE FUNCTION

Consider a linear system with a time-correlated driving force described with the following equation of motion:

$$\dot{\mathbf{x}}(t) = \mathbf{A}\mathbf{x}(t) + \sqrt{2\mathbf{D}}\boldsymbol{\eta}(t), \quad \text{with} \quad \langle \boldsymbol{\eta}(t) \rangle = 0, \quad \langle \boldsymbol{\eta}(t)\boldsymbol{\eta}^\top(t') \rangle = \mathbf{1}\mathcal{G}(t-t') \quad (24)$$

The formal solution can be written as

$$\mathbf{x}(t) = \int_{-\infty}^t e^{\mathbf{A}(t-t')} \sqrt{2\mathbf{D}}\boldsymbol{\eta}(t') dt' \quad (25)$$

Similarly, we can formally express the auto-covariance function as

$$\mathbf{C}(t, t+s) = \langle \mathbf{x}(t)\mathbf{x}^\top(t+s) \rangle = \int_{-\infty}^t dt' \int_{-\infty}^{t+s} dt'' e^{\mathbf{A}(t-t')} 2\mathbf{D}\mathcal{G}(t'-t'') e^{\mathbf{A}^\top(t+s-t'')} \quad (26)$$

Note that by the definition, at the steady state the auto-covariance function $\mathbf{C}(s) := \mathbf{C}(t, t+s)$ has the property $\mathbf{C}(-s) = \mathbf{C}^\top(s)$, so in the following we can assume without loss of generality that $s > 0$, unless specified otherwise.

Using the following lemma for differentiation:

$$\partial_t \int_{-\infty}^t dt' \int_{-\infty}^{t+s} dt'' f(t, t', t'') = \int_{-\infty}^t dt' \int_{-\infty}^{t+s} dt'' \partial_t f(t, t', t'') + \int_{-\infty}^{t+s} dt'' f(t, t, t'') + \int_{-\infty}^t dt' f(t, t', t+s) \quad (27)$$

and using the fact that at the stationary state $\partial_t \mathbf{C}(s) = 0$, we derive an equation for the auto-covariance:

$$\partial_t \mathbf{C}(t, t+s) = 0 = \mathbf{A}\mathbf{C}(s) + \mathbf{C}(s)\mathbf{A}^\top + \int_{-\infty}^{t+s} dt'' 2\mathbf{D}e^{\mathbf{A}^\top(t+s-t'')} \mathcal{G}(t-t'') + \int_{-\infty}^t dt' e^{\mathbf{A}(t-t')} 2\mathbf{D}\mathcal{G}(t'-t-s) \quad (28)$$

$$0 = \mathbf{A}\mathbf{C}(s) + \mathbf{C}(s)\mathbf{A}^\top + \underbrace{\mathbf{D} \int_{-\infty}^t dt' 2e^{\mathbf{A}^\top(t-t')} \mathcal{G}(t-t'-s)}_{\mathbf{B}^\top(-s)} + \underbrace{\int_{-\infty}^t dt' 2e^{\mathbf{A}(t-t')} \mathcal{G}(t-t'+s) \mathbf{D}}_{\mathbf{B}(s)} \quad (29)$$

$$\mathbf{A}\mathbf{C}(s) + \mathbf{C}(s)\mathbf{A}^\top = -[\mathbf{D}\mathbf{B}^\top(-s) + \mathbf{B}(s)\mathbf{D}] \quad (30)$$

Where we have used the time symmetry of the time correlation function of the noise $\mathcal{G}(t) = \mathcal{G}(-t)$ and defined the 'spreading matrix' $\mathbf{B}(s)$:

$$\mathbf{B}(s) = \int_0^\infty dt' 2e^{\mathbf{A}t'} \mathcal{G}(t'+s) \quad \text{for all } s \in \mathbb{R} \quad (31)$$

It is instructive to consider a set of limiting cases for Eq. (30).

1. Calculating the covariance matrix $\mathbf{C} := \mathbf{C}(0)$ for time-correlated noise:

$$\mathbf{A}\mathbf{C} + \mathbf{C}\mathbf{A}^\top = -(\mathbf{D}\mathbf{B}^\top + \mathbf{B}\mathbf{D}) \quad \text{with} \quad \mathbf{B} := \mathbf{B}(0) = 2 \int_0^\infty dt' e^{\mathbf{A}t'} \mathcal{G}(t'). \quad (32)$$

2. Calculating the auto-covariance function $\mathbf{C}_w(s)$ for white noise ($\mathcal{G}(t) = \delta(t)$):

$$\mathbf{A}\mathbf{C}_w(s) + \mathbf{C}_w(s)\mathbf{A}^\top = -2\mathbf{D}e^{\mathbf{A}^\top s} \quad (33)$$

3. Calculating the covariance matrix \mathbf{C}_w for white noise:

$$\mathbf{A}\mathbf{C}_w + \mathbf{C}_w\mathbf{A}^\top = -2\mathbf{D} \quad (34)$$

which reduces to solving the standard Lyapunov equation.

There is an interesting relation between case 3 and Eq. (30). Substituting the expression for \mathbf{D} from Eq. (34) into Eq. (30) one obtains

$$\mathbf{A}\mathbf{C}(s) + \mathbf{C}(s)\mathbf{A}^\top = \frac{1}{2} [\mathbf{B}(s)\mathbf{A}\mathbf{C}_w + \mathbf{B}(s)\mathbf{C}_w\mathbf{A}^\top + \mathbf{A}\mathbf{C}_w\mathbf{B}^\top(-s) + \mathbf{C}_w\mathbf{A}^\top\mathbf{B}^\top(-s)] \quad (35)$$

$$= \mathbf{A} \left[\frac{1}{2} (\mathbf{B}(s)\mathbf{C}_w + \mathbf{C}_w\mathbf{B}^\top(-s)) \right] + \left[\frac{1}{2} (\mathbf{B}(s)\mathbf{C}_w + \mathbf{C}_w\mathbf{B}^\top(-s)) \right] \mathbf{A}^\top \quad (36)$$

and using the uniqueness of the solution of the Lyapunov equation we conclude that

$$\mathbf{C}(s) = \frac{1}{2} [\mathbf{B}(s)\mathbf{C}_w + \mathbf{C}_w\mathbf{B}^\top(-s)] \quad (37)$$

For an exponentially correlated noise, with $\mathcal{G}(t) = \frac{1}{2\tau} e^{-|t|/\tau}$, such that $\mathcal{G}(t) \xrightarrow{\tau \rightarrow 0} \delta(t)$, both $\mathbf{B}^\top(-s)$ and $\mathbf{B}(s)$ can be calculated analytically.

$$\mathbf{B}^\top(-s) = \int_0^\infty 2e^{\mathbf{A}^\top t'} \mathcal{G}(t'-s) dt' = \underbrace{\frac{1}{\tau} \int_0^s e^{\mathbf{A}^\top t'} e^{-\frac{s-t'}{\tau}} dt'}_{\text{(I)}} + \underbrace{\frac{1}{\tau} \int_s^\infty e^{\mathbf{A}^\top t'} e^{-\frac{t'-s}{\tau}} dt'}_{\text{(II)}} \quad (38)$$

We calculate terms (I) and (II) separately:

$$(I) = \frac{1}{\tau} \int_0^s e^{\mathbf{A}^\top(s-t')} e^{-\frac{t'}{\tau}} dt' = \frac{1}{\tau} e^{\mathbf{A}^\top s} \int_0^s e^{-(\mathbf{A}^\top + \frac{\mathbb{1}}{\tau})t'} dt' = \frac{1}{\tau} e^{\mathbf{A}^\top s} \left[- \left(\mathbf{A}^\top + \frac{\mathbb{1}}{\tau} \right)^{-1} e^{-(\mathbf{A}^\top + \frac{\mathbb{1}}{\tau})t'} \right]_0^s \quad (39)$$

$$= \frac{1}{\tau} e^{\mathbf{A}^\top s} \left(\mathbf{A}^\top + \frac{\mathbb{1}}{\tau} \right)^{-1} \left(\mathbb{1} - e^{-(\mathbf{A}^\top + \frac{\mathbb{1}}{\tau})s} \right) = e^{\mathbf{A}^\top s} \frac{s \mathbb{1} - e^{-(\mathbb{1} + \tau \mathbf{A}^\top) \frac{s}{\tau}}}{\tau (\mathbb{1} + \tau \mathbf{A}^\top) \frac{s}{\tau}} \quad (40)$$

Since the matrix $(\mathbb{1} + \tau \mathbf{A}^\top)$ may in general be non-invertible the result above should be interpreted in terms of evaluating the analytic function $f(x) = \frac{1-e^{-x}}{x}$ for a matrix argument $(\mathbb{1} + \tau \mathbf{A}^\top) \frac{s}{\tau}$.

$$(II) = \frac{1}{\tau} \int_0^\infty e^{\mathbf{A}^\top(t'+s)} e^{-\frac{t'}{\tau}} dt' = \frac{1}{\tau} e^{\mathbf{A}^\top s} \int_0^\infty e^{(\mathbf{A}^\top - \frac{\mathbb{1}}{\tau})t'} dt' = -\frac{1}{\tau} e^{\mathbf{A}^\top s} \left(\mathbf{A}^\top - \frac{\mathbb{1}}{\tau} \right)^{-1} = e^{\mathbf{A}^\top s} (\mathbb{1} - \tau \mathbf{A}^\top)^{-1} \quad (41)$$

Similarly, we calculate $\mathbf{B}(s)$:

$$\mathbf{B}(s) = \int_0^\infty 2e^{\mathbf{A}t'} \mathcal{G}(t'+s) dt' = \frac{1}{\tau} e^{\mathbf{A}t'} e^{-\frac{|t'+s|}{\tau}} = e^{-\frac{s}{\tau}} \frac{1}{\tau} \int_0^\infty e^{(\mathbf{A} - \frac{\mathbb{1}}{\tau})t'} dt' = e^{-\frac{s}{\tau}} (\mathbb{1} - \tau \mathbf{A})^{-1} \quad (42)$$

Altogether, the equation for the auto-covariance function reads

$$\mathbf{A}\mathbf{C}(s) + \mathbf{C}(s)\mathbf{A}^\top = -\mathbf{D}e^{\mathbf{A}^\top s} \left[(\mathbb{1} - \tau \mathbf{A}^\top)^{-1} + \frac{\mathbb{1} - e^{-(\mathbb{1} + \tau \mathbf{A}^\top) \frac{s}{\tau}}}{\mathbb{1} + \tau \mathbf{A}^\top} \right] - e^{-\frac{s}{\tau}} (\mathbb{1} - \tau \mathbf{A})^{-1} \mathbf{D} \quad (43)$$

and in the case $s = 0$ the equation reduces to

$$\mathbf{A}\mathbf{C} + \mathbf{C}\mathbf{A}^\top = -[\mathbf{D}(\mathbb{1} - \tau \mathbf{A}^\top)^{-1} + (\mathbb{1} - \tau \mathbf{A})^{-1} \mathbf{D}]. \quad (44)$$

B. EXAMPLE PLOTS OF THE AUTO-COVARIANCE FUNCTION

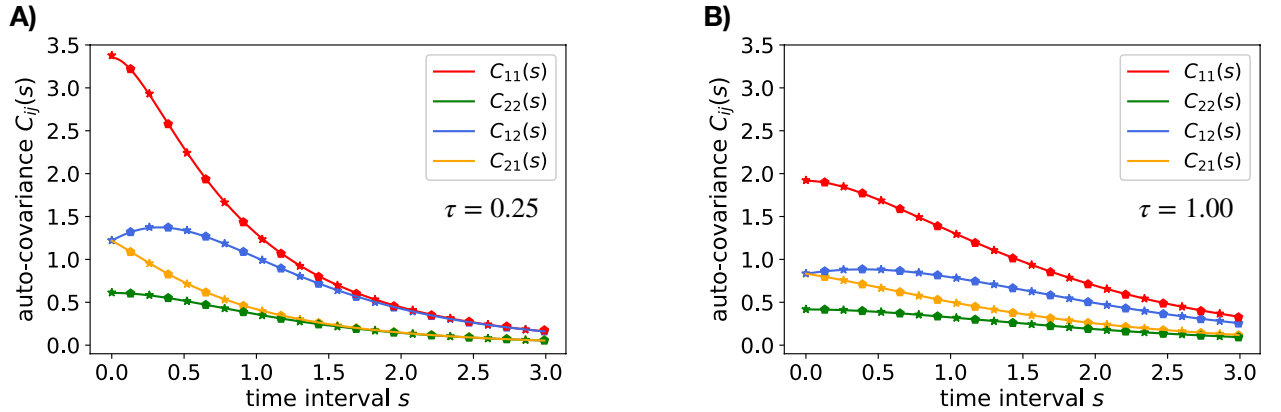


FIG. 5. Plots of the auto-covariance function for a simple two-bead system, as in Fig. 1 of the main text, obtained for the same set of parameters: $k = 1$, $\gamma = 1$, $D_{ij} = 8\delta_{i,1}\delta_{j,1}$. The correlation times of the driving are $\tau = 0.25$ (panel **A**) and $\tau = 1.00$ (panel **B**). The solid lines are the theoretical curves. The data points represent values inferred from a simulation with OU noise (stars) and telegraph noise (pentagons).

C. DERIVATION OF THE FORMULA FOR \mathcal{A}

The area enclosing rates are defined as

$$\mathcal{A} = \frac{1}{2} \langle \dot{\mathbf{x}}\mathbf{x}^\top - \mathbf{x}\dot{\mathbf{x}}^\top \rangle. \quad (45)$$

This antisymmetrized form is used only to make the expression independent of the integration convention in the case of white noise. For colored noise, where no ambiguity in terms of integration occurs, it is enough to calculate $\langle \dot{\mathbf{x}}\mathbf{x}^\top \rangle$. We will confirm this by showing that $\langle \dot{\mathbf{x}}\mathbf{x}^\top \rangle$ itself is antisymmetric. Taking the expression for $\dot{\mathbf{x}}$ from Eq. (1) we get

$$\langle \dot{\mathbf{x}}\mathbf{x}^\top \rangle = \mathbf{A} \underbrace{\langle \mathbf{x}\mathbf{x}^\top \rangle}_{\mathbf{C}} + \sqrt{2\mathbf{D}} \langle \boldsymbol{\eta}(t)\mathbf{x}^\top(t) \rangle. \quad (46)$$

Substituting the formal solution for $\mathbf{x}(t)$ we evaluate the second term:

$$\sqrt{2\mathbf{D}} \langle \boldsymbol{\eta}(t)\mathbf{x}^\top(t) \rangle = \int_{-\infty}^t \sqrt{2\mathbf{D}} \langle \boldsymbol{\eta}(t)\boldsymbol{\eta}^\top(t') \rangle \sqrt{2\mathbf{D}} e^{\mathbf{A}^\top(t-t')} dt' = \int_{-\infty}^t 2\mathbf{D} e^{\mathbf{A}^\top(t-t')} \mathcal{G}(t-t') dt' = \mathbf{D}\mathbf{B}^\top \quad (47)$$

Combining it with the first term we get

$$\mathbf{A} = \mathbf{A}\mathbf{C} + \mathbf{D}\mathbf{B}^\top = \frac{1}{2}(\mathbf{A}\mathbf{C} - \mathbf{C}\mathbf{A}^\top) + \frac{1}{2}(\mathbf{D}\mathbf{B}^\top - \mathbf{B}\mathbf{D}). \quad (48)$$

As mentioned before, this expression is already antisymmetric. The first term is identical to the white noise expression, with \mathbf{C}_w replaced by \mathbf{C} . The correction term $(\mathbf{D}\mathbf{B}^\top - \mathbf{B}\mathbf{D})$ contributes to \mathcal{A}_{ij} only if the degrees of freedom x_i, x_j are coupled (directly or indirectly) and if the active noise acts directly on at least one of them. The above expression can be rewritten in an alternative form after making use of $2\mathbf{C} = \mathbf{B}\mathbf{C}_w + \mathbf{C}_w\mathbf{B}^\top$ (Eq. (37)) and $2\mathbf{D} = \mathbf{A}\mathbf{C}_w + \mathbf{C}_w\mathbf{A}^\top$ (Eq. (34)), and the fact that matrices \mathbf{A} and \mathbf{B} commute:

$$\mathbf{A} = \frac{1}{4} [\mathbf{A}\mathbf{B}\mathbf{C}_w + \mathbf{A}\mathbf{C}_w\mathbf{B}^\top - \mathbf{B}\mathbf{C}_w\mathbf{A}^\top - \mathbf{C}_w\mathbf{B}^\top\mathbf{A}^\top - \mathbf{A}\mathbf{C}_w\mathbf{B}^\top - \mathbf{C}_w\mathbf{A}^\top\mathbf{B}^\top + \mathbf{B}\mathbf{A}\mathbf{C}_w + \mathbf{B}\mathbf{C}_w\mathbf{A}^\top] \quad (49)$$

$$= \frac{1}{2} [\mathbf{B}\mathbf{A}\mathbf{C}_w - \mathbf{C}_w\mathbf{A}^\top\mathbf{B}^\top]. \quad (50)$$

D. MEAN VELOCITY FIELD WITH OU NOISE

Consider a linear system driven by OU noise, described by the Langevin equation

$$\begin{pmatrix} \dot{\mathbf{x}} \\ \dot{\boldsymbol{\eta}} \end{pmatrix} = \begin{pmatrix} \mathbf{A} & \sqrt{2\mathbf{D}} \\ 0 & -\mathbb{1}/\tau \end{pmatrix} \begin{pmatrix} \dot{\mathbf{x}} \\ \dot{\boldsymbol{\eta}} \end{pmatrix} + \frac{1}{\tau} \begin{pmatrix} 0 \\ \boldsymbol{\xi} \end{pmatrix}, \quad (51)$$

where $\boldsymbol{\xi}(t)$ is Gaussian white noise satisfying $\langle \boldsymbol{\xi}(t)\boldsymbol{\xi}^\top(t') \rangle = \mathbb{1}\delta(t-t')$. The instantaneous velocity can be then written as $\mathbf{v} = \mathbf{A}\mathbf{x} + \sqrt{2\mathbf{D}}\boldsymbol{\eta}$. The covariance matrix for the whole system $\{\mathbf{x}, \boldsymbol{\eta}\}$ including the noise dynamics satisfies the Lyapunov equation:

$$\begin{pmatrix} \mathbf{A} & \sqrt{2\mathbf{D}} \\ 0 & -\mathbb{1}/\tau \end{pmatrix} \begin{pmatrix} \mathbf{C}_{\mathbf{x}\mathbf{x}} & \mathbf{C}_{\mathbf{x}\boldsymbol{\eta}} \\ \mathbf{C}_{\boldsymbol{\eta}\mathbf{x}} & \mathbf{C}_{\boldsymbol{\eta}\boldsymbol{\eta}} \end{pmatrix} + \begin{pmatrix} \mathbf{C}_{\mathbf{x}\mathbf{x}} & \mathbf{C}_{\mathbf{x}\boldsymbol{\eta}} \\ \mathbf{C}_{\boldsymbol{\eta}\mathbf{x}} & \mathbf{C}_{\boldsymbol{\eta}\boldsymbol{\eta}} \end{pmatrix} \begin{pmatrix} \mathbf{A}^\top & 0 \\ \sqrt{2\mathbf{D}} & -\mathbb{1}/\tau \end{pmatrix} = \begin{pmatrix} 0 & 0 \\ 0 & -\mathbb{1}/\tau^2 \end{pmatrix}. \quad (52)$$

This equation can be split into three equations for $\{\mathbf{C}_{\mathbf{x}\mathbf{x}}, \mathbf{C}_{\boldsymbol{\eta}\mathbf{x}}, \mathbf{C}_{\boldsymbol{\eta}\boldsymbol{\eta}}\}$. One of them is

$$-\frac{1}{\tau}\mathbf{C}_{\boldsymbol{\eta}\boldsymbol{\eta}} - \frac{1}{\tau}\mathbf{C}_{\boldsymbol{\eta}\boldsymbol{\eta}} = -\frac{\mathbb{1}}{\tau^2} \implies \mathbf{C}_{\boldsymbol{\eta}\boldsymbol{\eta}} = \frac{\mathbb{1}}{2\tau}. \quad (53)$$

Another equation, allowing us to find $\mathbf{C}_{\boldsymbol{\eta}\mathbf{x}}$ is

$$-\frac{1}{\tau}\mathbf{C}_{\boldsymbol{\eta}\mathbf{x}} + \mathbf{C}_{\boldsymbol{\eta}\mathbf{x}}\mathbf{A}^\top + \mathbf{C}_{\boldsymbol{\eta}\boldsymbol{\eta}}\sqrt{2\mathbf{D}} = 0. \quad (54)$$

Substituting the derived expression for $\mathbf{C}_{\boldsymbol{\eta}\boldsymbol{\eta}}$ and rearranging the terms we find

$$\mathbf{C}_{\boldsymbol{\eta}\mathbf{x}} = \sqrt{\frac{\mathbf{D}}{2}}(\mathbb{1} - \tau\mathbf{A}^\top)^{-1} = \sqrt{\frac{\mathbf{D}}{2}}\mathbf{B}^\top. \quad (55)$$

Because the joint probability distribution $p(\mathbf{x}, \boldsymbol{\eta})$ has to be multivariate normal, the mean value of the OU noise $\boldsymbol{\eta}$ conditioned on the position \mathbf{x} can be calculated as

$$\langle \boldsymbol{\eta}|\mathbf{x} \rangle = \underbrace{\langle \boldsymbol{\eta} \rangle}_0 + \mathbf{C}_{\boldsymbol{\eta}\mathbf{x}}(\mathbf{C}_{\mathbf{x}\mathbf{x}})^{-1}\mathbf{x}. \quad (56)$$

Consistently with the notation of the main text we will write $\mathbf{C}_{\mathbf{xx}} := \mathbf{C}$. The mean velocity $\mathbf{v}(\mathbf{x})$ is then obtained as

$$\mathbf{v}(\mathbf{x}) = \langle \mathbf{v} | \mathbf{x} \rangle = \mathbf{A}\mathbf{x} + \sqrt{2\mathbf{D}} \langle \boldsymbol{\eta} | \mathbf{x} \rangle = (\mathbf{A} + \sqrt{2\mathbf{D}} \mathbf{C}_{\boldsymbol{\eta}\mathbf{x}} (\mathbf{C}_{\mathbf{xx}})^{-1}) \mathbf{x} = \underbrace{(\mathbf{A} + \mathbf{D}\mathbf{B}^T \mathbf{C}^{-1})}_{\boldsymbol{\Omega}_{\text{OU}}} \mathbf{x}. \quad (57)$$

Comparing with Eq. (48), we conclude that with the Ornstein-Uhlenbeck noise the mean velocity can be written as $\langle \mathbf{v} | \mathbf{x} \rangle = \boldsymbol{\Omega}_{\text{OU}} \mathbf{x}$, where $\boldsymbol{\Omega}_{\text{OU}} \mathbf{x} = \mathcal{A} \mathbf{C}^{-1}$, just as for a white noise driven system.

An alternative expression for $\boldsymbol{\Omega}_{\text{OU}}$ in case of the OU noise can be found by first calculating the exact probability distribution $p(\mathbf{x}, \mathbf{v})$ and expressing it in terms of the white noise covariance matrix \mathbf{C}_w . To this end we followed a perturbative scheme based on an expansion in powers of $\tau^{\frac{1}{2}}$ that was presented in [33], employing the identity $\mathbf{A}\mathbf{C}_w + \mathbf{C}_w\mathbf{A}^T = -2\mathbf{D}$. With linear forces, as in our case, the expansion terminates at order $n = 4$ leading to an exact expression:

$$p(\mathbf{x}, \mathbf{v}) = \mathcal{N} \exp \left\{ -\frac{1}{2} (\mathbf{x}^T \ \mathbf{v}^T) \begin{pmatrix} \mathbf{C}_w^{-1} + \tau \mathbf{A}^T \mathbf{D}^{-1} \mathbf{A} & -\tau (\mathbf{C}_w^{-1} + \mathbf{A}^T \mathbf{D}^{-1}) \\ -\tau (\mathbf{C}_w^{-1} + \mathbf{D}^{-1} \mathbf{A}) & \tau \mathbf{D}^{-1} + \tau^2 \mathbf{C}_w^{-1} \end{pmatrix} \begin{pmatrix} \mathbf{x} \\ \mathbf{v} \end{pmatrix} \right\} \quad (58)$$

$$:= \mathcal{N} \exp \left\{ -\frac{1}{2} (\mathbf{x}^T \ \mathbf{v}^T) \begin{pmatrix} \mathbf{C}_{\mathbf{xx}} & \mathbf{C}_{\mathbf{xv}} \\ \mathbf{C}_{\mathbf{vx}} & \mathbf{C}_{\mathbf{vv}} \end{pmatrix}^{-1} \begin{pmatrix} \mathbf{x} \\ \mathbf{v} \end{pmatrix} \right\}, \quad (59)$$

where \mathcal{N} is a normalization constant. Additionally, the decomposition of the full covariance matrix using Schur complement gives:

$$[(\mathbf{C}^{-1})_{\mathbf{vv}}]^{-1} (\mathbf{C}^{-1})_{\mathbf{vx}} = -\mathbf{C}_{\mathbf{vx}} (\mathbf{C}_{\mathbf{xx}})^{-1}. \quad (60)$$

Equipped with these results, we can calculate the conditioned mean velocity as:

$$\langle \mathbf{v} | \mathbf{x} \rangle = \mathbf{C}_{\mathbf{vx}} (\mathbf{C}_{\mathbf{xx}})^{-1} \mathbf{x} = -[(\mathbf{C}^{-1})_{\mathbf{vv}}]^{-1} (\mathbf{C}^{-1})_{\mathbf{vx}} \mathbf{x} = (\tau \mathbf{D}^{-1} + \tau^2 \mathbf{C}_w^{-1})^{-1} \tau (\mathbf{C}_w^{-1} + \mathbf{D}^{-1} \mathbf{A}) \mathbf{x} \quad (61)$$

$$= (\mathbb{1} + \tau \mathbf{D} \mathbf{C}_w^{-1})^{-1} (\mathbf{A} + \mathbf{D} \mathbf{C}_w^{-1}) \mathbf{x} = (\mathbb{1} + \tau \mathbf{D} \mathbf{C}_w^{-1})^{-1} \boldsymbol{\Omega}_w \mathbf{x}. \quad (62)$$

From this we conclude that for a linear system driven by OU noise

$$\langle \mathbf{v}(\mathbf{x}) \rangle = \boldsymbol{\Omega}_{\text{OU}} \mathbf{x}, \quad \text{with} \quad \boldsymbol{\Omega}_{\text{OU}} = (\mathbb{1} + \tau \mathbf{D} \mathbf{C}_w^{-1})^{-1} \boldsymbol{\Omega}_w. \quad (63)$$

D Learning the non-equilibrium dynamics of Brownian movies

This section is a reprint of the following publication:

Learning the non-equilibrium dynamics of Brownian movies

Federico S. Gnesotto, Grzegorz Gradziuk, Pierre Ronceray[†], and Chase P. Broedersz[†]

[†] corresponding author

Nature Communications **11**, 5378 (2020)

Learning the Non-equilibrium Dynamics of Brownian Movies

Federico S. Gnesotto,¹ Grzegorz Gradziuk,¹ Pierre Ronceray,^{2,*} and Chase P. Broedersz^{1,3,*}

¹*Arnold-Sommerfeld-Center for Theoretical Physics and Center for NanoScience,
Ludwig-Maximilians-Universität München, D-80333 München, Germany.*

²*Center for the Physics of Biological Function, Princeton University, Princeton, NJ 08544, USA*

³*Department of Physics and Astronomy, Vrije Universiteit Amsterdam, 1081 HV Amsterdam, The Netherlands*

(Dated: February 7, 2022)

Abstract: Time-lapse microscopy imaging provides direct access to the dynamics of soft and living systems. At mesoscopic scales, such microscopy experiments reveal intrinsic thermal and non-equilibrium fluctuations. These fluctuations, together with measurement noise, pose a challenge for the dynamical analysis of these Brownian movies. Traditionally, methods to analyze such experimental data rely on tracking embedded or endogenous probes. However, it is in general unclear, especially in complex many-body systems, which degrees of freedom are the most informative about their non-equilibrium nature. Here, we introduce an alternative, tracking-free approach that overcomes these difficulties via an unsupervised analysis of the Brownian movie. We develop a dimensional reduction scheme selecting a basis of modes based on dissipation. Subsequently, we learn the non-equilibrium dynamics, thereby estimating the entropy production rate and time-resolved force maps. After benchmarking our method against a minimal model, we illustrate its broader applicability with an example inspired by active biopolymer gels.

INTRODUCTION

Over the last two centuries, fundamental insights have been gleaned about the physical properties of biological and soft matter systems by using microscopes to image their dynamics [1, 2]. At the micrometer scale and below, however, this dynamics is inherently stochastic, as ever-present thermally driven Brownian fluctuations give rise to short-time displacements [3–6]. This random motion makes such “Brownian movies” appear jiggly and erratic; this randomness is further exacerbated by measurement noise and limited resolution intrinsic to, e.g., fluorescence microscopy [7]. In light of all these sources of uncertainty, how can one best make use of measured Brownian movies of a systems dynamics, to learn the underlying physics of the fluctuating and persistent forces?

In addition to thermal effects, active processes can strongly impact the stochastic dynamics of a system [8–12]. Recently, there has been a growing interest in quantifying and characterizing the non-equilibrium nature of the stochastic dynamics in active soft and living systems [13–25]. In cells, molecular-scale activity, powered for instance by ATP hydrolysis, controls mesoscale non-equilibrium processes in assemblies such as cilia [26, 27], flagella [28], chromosomes [29], protein droplets [30] or cytoskeletal networks [31–34]. The irreversible nature of such non-equilibrium processes can lead to measurable dissipative currents in a phase space of mesoscopic degrees of freedom [9, 17, 18, 35–38]. Such dissipative currents can be quantified by the entropy production rate [39], which is a measure of the irreversibility of the dynamics [40]. New approaches have been developed to measure this rate in real systems [22, 24], shedding light

onto the structure of dissipative processes [19] and their impact on the dynamics of living matter [20]. However, it remains an outstanding challenge to accurately infer the entropy production rate by analyzing Brownian movies of such systems.

Traditional approaches to measure microscopic forces and analyze time-lapse microscopy data typically rely on tracking the position or shape of well-defined probes such as tracer beads, fluorescent proteins and filaments, or simply on exploiting the natural contrast of the intracellular medium to obtain such tracks [14–17, 29, 31, 34, 41–44]. The tracer trajectories can be studied through stochastic analysis techniques to extract an effective model for their dynamics and infer quantities like the entropy production rate [19, 20, 22, 24, 45–48]. There are, however, many cases in which tracking is impractical [49, 50], due to limited resolution or simply because there are no recognizable objects to use as tracers. Another, more fundamental limitation of tracking is that one then mostly learns about the dynamics of the tracked object—not of the system as a whole. Indeed, the dissipative power in a system might not couple directly to the tracked variables, and a priori, it might not be clear which coordinates will be most informative about such dissipation. This raises the question how one can identify which degrees of freedom best encode the forces and non-equilibrium dissipation in a given system.

Here we propose an alternative to tracking: learning the dynamics and inferring the entropy production rate directly from the unsupervised analysis of Brownian movies. We first decompose the movie into generic principal modes of motion, and predict which ones are the most likely to encode useful information through a “Dissipative Component Analysis” (DCA). This allows us to perform a dimensional reduction, leading to a representation of the movie as a stochastic trajectory in this component space. Finally, we employ a recently intro-

* ronceray@princeton.edu, c.broedersz@lmu.de

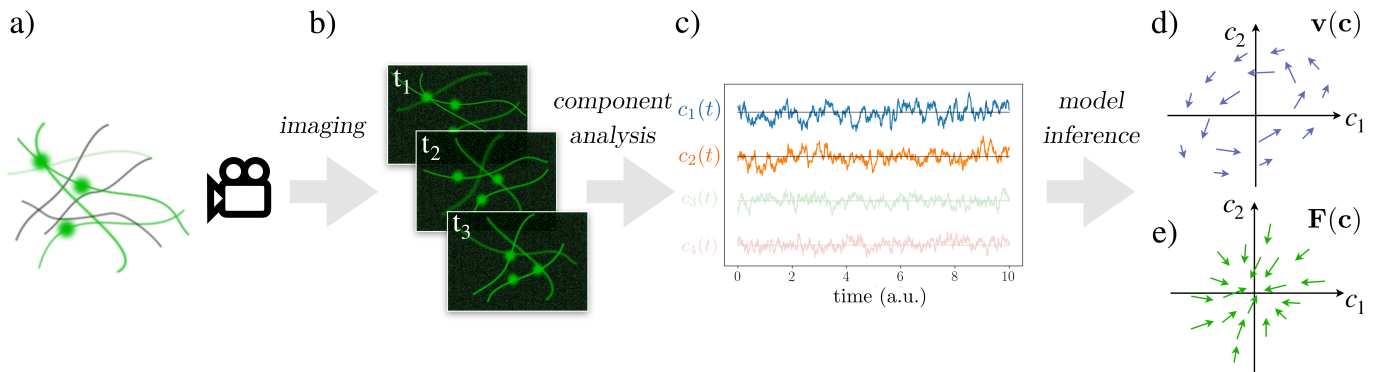


FIG. 1. **Schematic illustration of our approach to learn non-equilibrium dynamics from a Brownian movie.** a) Sketch of a network of biopolymers (black) with embedded fluorescent filaments and beads (green). b) Image-frames of the fluorescent components in panel a) at three successive time points. c) The time trajectories of the projection coefficients $c_1(t), c_2(t), \dots$: the coefficients and respective trajectories discarded by the dimensional reduction are faded. Sketch of the the inferred velocity $\mathbf{v}(\mathbf{c})$ (d) and of the force field $\mathbf{F}(\mathbf{c})$ (e) in the space $\{c_1, c_2\}$.

duced method, Stochastic Force Inference (SFI) [24], to analyze such trajectories. Our approach not only yields an estimate of the entropy production rate of a Brownian movie, which is a controlled lower bound to the system’s total entropy production rate, but also important dynamical information such as a time-resolved force map of the imaged system. Thus, our approach may provide an alternative to methods that use microcopic force sensors [43, 44, 51, 52]. In this article, we first present the method in its generality, then benchmark it on a simple two-beads model. Finally, we demonstrate the potential of our approach on simulated semi-realistic fluorescence microscopy movies of out-of-equilibrium biopolymer networks.

RESULTS

Principle of the method

We begin by describing a tracking-free method to infer the dynamical equations of a system from raw image sequences. This approach allows us to determine a bound on the dissipation of a system, as well as the force-field in image space.

Our starting point is the assumption that the physical system we observe (Fig. 1a)—such as a cytoskeletal network or a fluctuating membrane—can be described by a configurational state vector $\mathbf{x}(t)$ at time t , undergoing steady-state Brownian dynamics in an unspecified d -dimensional phase space:

$$\frac{d\mathbf{x}}{dt} = \Phi(\mathbf{x}) + \sqrt{2\mathbf{D}(\mathbf{x})}\xi(t), \quad (1)$$

where $\Phi(\mathbf{x})$ is the drift field, $\mathbf{D}(\mathbf{x})$ is the diffusion tensor field, and throughout this article $\xi(t)$ is a Gaussian white noise vector ($\langle \xi(t) \rangle = 0$ and $\langle \xi_i(t)\xi_j(s) \rangle = \delta_{ij}\delta(t-s)$). Note that when diffusion is state-dependent,

$\sqrt{2\mathbf{D}(\mathbf{x})}\xi(t)$ is a multiplicative noise term: we employ the Itô convention for the drift, *i.e.* $\Phi(\mathbf{x}) = \mathbf{F}(\mathbf{x}) + \nabla \cdot \mathbf{D}(\mathbf{x})$, where $\mathbf{F}(\mathbf{x})$ is the product of the mobility matrix and the physical force in the absence of Brownian noise [53, 54].

Our goal is to learn as much as possible about the process described by Eq. (1) from an experimental observation. In particular, we aim to measure if, and how far, the system is out-of-equilibrium by determining the irreversible nature of its dynamics. This irreversibility is quantified by the system’s entropy production rate [39]

$$\dot{S}_{\text{total}} = \langle \mathbf{v}(\mathbf{x})\mathbf{D}^{-1}(\mathbf{x})\mathbf{v}(\mathbf{x}) \rangle, \quad (2)$$

where $\langle \cdot \rangle$ denotes a steady-state average, throughout this article we set Boltzmann’s constant $k_B = 1$, and $\mathbf{v}(\mathbf{x})$ is the mean phase space velocity field quantifying the presence of irreversible currents. Specifically, using the steady-state Fokker-Planck equation one can write $\mathbf{v}(\mathbf{x}) = \mathbf{F}(\mathbf{x}) - \mathbf{D}(\mathbf{x})\nabla \log P(\mathbf{x})$, where $P(\mathbf{x})$ is the steady-state probability density function, and flux balance imposes that $\nabla \cdot (P\mathbf{v}) = 0$.

The input of our method consists of a discrete time-series of microscopy images of the physical system $\{\mathcal{I}(t_0), \dots, \mathcal{I}(t_N)\}$ —a “Brownian movie” (Fig. 1b). Each image $\mathcal{I}(t)$ is an imperfect representation of the state $\mathbf{x}(t)$ of the physical system as a bitmap, *i.e.* a $L \times W$ array of real-valued pixel intensities [55]. Specifically, we model the imaging apparatus as a noisy nonlinear map $\mathcal{I}(t) = \bar{\mathcal{I}}(\mathbf{x}(t)) + \mathcal{N}(t)$, where \mathcal{N} is a temporally uncorrelated random array representing measurement noise (such as the fluctuations in registered fluorescence intensities), and $\bar{\mathcal{I}}(\mathbf{x})$ is the “ideal image” returned on average by the microscope when the system’s state is \mathbf{x} . We assume that the map $\mathbf{x} \mapsto \bar{\mathcal{I}}(\mathbf{x})$ is time-independent (*i.e.* that the microscope settings are fixed and stable).

Importantly, if no information is lost by the imaging process, the ideal image $\bar{\mathcal{I}}(t)$ undergoes a Brownian dynamics equation determined by the nonlinear transform-

mation of Eq. (1) through the map $\mathbf{x} \mapsto \bar{\mathcal{I}}(\mathbf{x})$, as prescribed by Itô’s lemma [56]. In general, however, there is information loss and this map is not invertible: due to finite optical resolution or because some elements are simply not visible, the imaging may not capture the full high-dimensional state of the system. For this reason, the dynamics in image space are not uniquely specified by the ideal image value $\bar{\mathcal{I}}$; they also depend on “hidden” degrees of freedom \mathbf{x}_h not captured by the image. In this case, a Markovian dynamical equation for $\bar{\mathcal{I}}$ alone does not exist, but by including the dynamics of \mathbf{x}_h , we can write

$$\frac{d}{dt}(\bar{\mathcal{I}}, \mathbf{x}_h) = \varphi(\bar{\mathcal{I}}, \mathbf{x}_h) + \sqrt{2\mathcal{D}(\bar{\mathcal{I}}, \mathbf{x}_h)}\xi(t). \quad (3)$$

Here $(\bar{\mathcal{I}}, \mathbf{x}_h)$ is a column vector composed of pixel intensities $\bar{\mathcal{I}}$ and hidden degrees of freedom \mathbf{x}_h , $\varphi(\bar{\mathcal{I}}, \mathbf{x}_h)$ and $\mathcal{D}(\bar{\mathcal{I}}, \mathbf{x}_h)$ are the drift field and diffusion tensor, respectively, in the combined space of pixel intensities and hidden variables. Our Brownian movie analysis allows us to infer the mean image drift $\varphi(\bar{\mathcal{I}}) := \langle \varphi_{\mathcal{I}}(\bar{\mathcal{I}}, \mathbf{x}_h) | \bar{\mathcal{I}} \rangle$ and mean image diffusion tensor $\mathcal{D}(\bar{\mathcal{I}}) := \langle \mathcal{D}_{\mathcal{I}}(\bar{\mathcal{I}}, \mathbf{x}_h) | \bar{\mathcal{I}} \rangle$, averaged over the degrees of freedom \mathbf{x}_h lost in the imaging process. From drift and diffusion fields we can directly obtain the mean image force field $\mathcal{F}(\bar{\mathcal{I}}) = \varphi(\bar{\mathcal{I}}) - \nabla \cdot \mathcal{D}(\bar{\mathcal{I}})$. Similar to force and diffusion fields, the phase space velocity field $\mathbf{v}(\mathbf{x})$ in the d -dimensional physical phase space, transforms into a velocity field $\mathcal{V}(\bar{\mathcal{I}})$ in the $L \times W$ -dimensional image space—again, averaged over unobserved degrees of freedom. The corresponding currents result in an apparent entropy production rate associated to the image dynamics [57],

$$\dot{S}_{\text{apparent}} = \langle \mathcal{V}(\bar{\mathcal{I}}) \mathcal{D}^{-1}(\bar{\mathcal{I}}) \mathcal{V}(\bar{\mathcal{I}}) \rangle. \quad (4)$$

Importantly, $\dot{S}_{\text{apparent}} \leq \dot{S}_{\text{total}}$: the apparent entropy production rate is a lower bound to the total one. Indeed, all transformations involved in the analysis process – imaging through the nonlinear map $\mathbf{x} \mapsto \bar{\mathcal{I}}(\mathbf{x})$, masking the hidden degrees of freedom, and averaging over their value – have nonincreasing effects on the entropy production rate (see Supplementary Note 8). The measure of $\dot{S}_{\text{apparent}}$ thus provides direct insight into the dissipative processes in the physical system.

The goal of our method is to reconstruct the mean image-space dynamics $(\mathcal{F}(\bar{\mathcal{I}}), \mathcal{D}(\bar{\mathcal{I}}))$, and in particular the corresponding entropy production rate (Eq. (4)). However, doing so in the high-dimensional image space is unpractical and would require unrealistic amounts of data. We therefore need to reduce the dimensionality of our system to a tractable number of relevant degrees of freedom.

Because each image represents a physical state of the system, we expect that the ideal images $\bar{\mathcal{I}}(t)$ all share similar structural features. Consequently, the Brownian movie occupies only a smaller subspace in the space of all configurations of pixel intensities. To restrict ourselves to the manifold of images representing the physical states

and to reduce the noise, we first perform a standard dimensionality reduction procedure: for simplicity, we employ Principal Component Analysis (PCA). As we shall see later, this standard procedure can be reinforced with an analysis that provides an additional basis transformation to select the most dissipative components. The idea behind this approach is to find an appropriate basis, in which pairs of components can be hierarchically ordered according to how much they are expected to contribute to the total entropy production rate. It then becomes possible to truncate the basis and reduce the dimensionality of the problem, while retaining maximum information about the system’s irreversible dynamics.

We truncate the basis of components according to two criteria: 1) Noise floor—due to the finite amount of data and the measurement noise present in the Brownian movie, some modes are indistinguishable from the measurement noise. We only keep modes that rise above this noise floor. 2) Time resolution of the dynamics—we only consider the components whose statistical properties are consistent with Brownian dynamics, i.e. such that the short-time diffusive behavior can be resolved through the noise. In low-dimensional systems, these criteria can be extended with an additional restriction based on estimating the dimensionality of the set of images in the Brownian movie.

Our task is now reduced to inferring the mean dynamics in component space,

$$\Phi(\mathbf{c}) := \langle \Phi_{\mathbf{c}}(\mathbf{c}, \mathbf{x}_h) | \mathbf{c} \rangle, \quad \mathcal{D}(\mathbf{c}) := \langle \mathcal{D}_{\mathbf{c}}(\mathbf{c}, \mathbf{x}_h) | \mathbf{c} \rangle \quad (5)$$

where $\mathbf{c}(t) = (c_1(t), c_2(t), \dots, c_n(t))$ are the components obtained after a linear transformation of the images (see Fig. 1c), $\mathcal{D}_{\mathbf{c}}$ is the restriction of the diffusion tensor to the \mathbf{c} -space, and the hidden degrees of freedom \mathbf{x}_h now also include those present in the image, but left out after the components’ truncation. This procedure has reduced the system’s dynamics to that of a smaller number of components, making it possible to learn $\Phi(\mathbf{c})$ and $\mathcal{D}(\mathbf{c})$.

To this end, we employ a recently introduced method, Stochastic Force Inference [24] (SFI), for the inverse Brownian dynamics problem. Briefly, this procedure is based on a least-squares approximation of the diffusion and drift fields using a basis of known functions (such as polynomials). This method is data-efficient, not limited to low-dimensional signals or equilibrium systems, robust against measurement noise, and provides estimates of the inference error, making it well suited for our purpose. In practice, we use SFI in two ways: 1) we infer the velocity field $\mathbf{v}(\mathbf{c})$ (Fig. 1d) and the diffusion field $\mathcal{D}(\mathbf{c})$, which we use to measure the entropy production rate. 2) We infer the drift field $\Phi(\mathbf{c})$, compute the image force $\mathbf{F}(\mathbf{c}) = \Phi(\mathbf{c}) - \nabla \cdot \mathcal{D}(\mathbf{c})$ (Fig. 1e), and thus reconstruct the dynamics of the components. To render this deterministic dynamics more intelligible, we can transform $\mathbf{F}(\mathbf{c})$ back into image space by inverting the $\mathcal{I} \mapsto \mathbf{c}$ linear transformation: this results in a pixel force-map, which indicates at each time step which pixel intensities tend to increase or decrease. This provides, we argue, a way to

gain insight into the dynamics of Brownian systems and disentangle deterministic forces from Brownian motion without tracking.

Our analysis framework can thus be schematically summarized as: imaging \rightarrow component analysis \rightarrow model inference (Fig. 1). This procedure allows the inference of entropy production rate and reconstruction of the dynamical equations from image sequences of a Brownian system.

A minimal example: two-beads Brownian movies

Next, we test the performance of our procedure on a simple non-equilibrium model: two coupled beads moving in one dimension. The beads are coupled by Hookean springs with stiffness k and experience Stokes drag with friction coefficient γ , due to the surrounding fluid (Fig. 2a). In this two-bead model, the time-evolution of the bead displacements $\mathbf{x}(t) = (x_1(t), x_2(t))$ obeys the overdamped Langevin Eq. (1), with $\mathbf{F}(\mathbf{x}) = \mathbf{K}\mathbf{x}$ and $K_{ij} = (1 - 3\delta_{ij})k\gamma^{-1}$. The system is driven out of thermodynamic equilibrium by imposing different temperatures on the two beads: $D_{ij} = \delta_{ij}k_B T_i \gamma^{-1}$ [9, 22, 58–60]. First, we obtain position trajectories for the two beads by discretizing their stochastic dynamics using an Euler integration scheme (see Supplementary Note 1). Then, we use these position trajectories to construct a noisy Brownian movie (Fig. 2b) (cf. Supplementary Note 2 and Supplementary Movie 1). Note that by construction, the steady-state dynamics of the two-beads system in image space is governed by a non-linear Langevin equation with multiplicative noise.

We seek to reduce the dimensionality of the data and to filter out measurement noise by finding relevant components. To this end, we employ Principal Component Analysis (PCA) [61] and determine the basis of n principal components $\mathbf{pc}_1, \mathbf{pc}_2, \dots, \mathbf{pc}_n$ to expand each image around the time-averaged image $\langle \mathcal{I} \rangle$: $\mathcal{I}(t) = \langle \mathcal{I} \rangle + \sum_{i=1}^n c_i(t) \mathbf{pc}_i$. The dynamics of the projection coefficients are on average governed by the drift field $\Phi(\mathbf{c})$ and diffusion tensor $\mathbf{D}(\mathbf{c})$ (see Eq. (5)).

In the simulated data of the two-bead model, the first four principal components satisfy criteria 1) and 2) introduced above (Fig. 2c). Interestingly, \mathbf{pc}_1 and \mathbf{pc}_2 resemble the in-phase and out-of-phase motion of the two beads, respectively, and should suffice to reproduce the dynamics of $(x_1(t), x_2(t))$. The components \mathbf{pc}_3 and \mathbf{pc}_4 appear to mostly represent the isolated fluctuations of the hot and cold beads and mainly account for the nonlinear details of the image representation. Together, the first four components allow for an adequate reconstruction of the original images (Fig. 2d, Supplementary Figure 1).

From the recorded trajectories in $\mathbf{pc}_1 \times \mathbf{pc}_2$ space we can already infer key features of the system's dynamics using SFI. Specifically, we infer the force and diffusion fields (Fig. 2e). In the phase space spanned by the first two principal components, we identify a stable fixed point

at $(0, 0)$ (Fig. 2e). As may be expected in this case, the \mathbf{pc}_1 -direction (in-phase motion) is less stiff than the \mathbf{pc}_2 direction (out-of-phase motion).

The temperature difference between the two beads results in phase-space circulation, as revealed by the inferred mean velocity field (Fig. 2f). To quantitatively assess the irreversibility associated with the presence of such phase space currents, we estimate the entropy production rate of the system \hat{S} , which converges for long enough measurement time (Fig. 2g-inset). Strikingly, already with two principal components we find good agreement between the inferred and the exact entropy production rate, capturing from $78 \pm 25\%$ at $T_c T_h^{-1} = 0.5$ to $88 \pm 7\%$ of the entropy production rate at $T_c T_h^{-1} = 0.2$ (Fig. 2g). Furthermore, the difference between the exact and inferred entropy production rate is consistent with the typical inference error predicted by SFI. As expected, the estimate of the entropy production rate increases with the number of included components. Note that including more modes than the dimension of the physical phase space (in this case 2) can lead to an overestimate of \hat{S} (Fig. 2g). In such low-dimensional systems, one can further restrict the number of included components based on estimating the dimensionality of the set of images in the Brownian movie.

We can also use the information contained in the first four principal components to quantitatively infer forces in image-space via the relation $\hat{\mathcal{F}}(\mathcal{I}(t)) = \sum_{i=1}^4 \hat{F}_i(\mathbf{c}(t)) \mathbf{pc}_i$. Note that while two modes were sufficient to infer \hat{S} , more modes are needed to reconstruct the full images and image-force fields as a linear combination of modes. When inferring forces we always subtract from the drift the spurious force $\nabla \cdot \mathbf{D}(\mathbf{c})$ arising in overdamped Itô stochastic differential equations with multiplicative noise [53, 54]. For comparison purposes, the exact image force field is obtained directly from the simulated data as: $\hat{\mathcal{F}}_{\text{ex}}(t) = \{\bar{\mathcal{I}}[\mathbf{x}(t) + \mathbf{F}(\mathbf{x}(t))\Delta t] - \bar{\mathcal{I}}(\mathbf{x}(t))\} \Delta t^{-1}$. Remarkably, we find good qualitative agreement between inferred and exact image force fields for specific realizations of the system, as shown in the kymographs in Fig. 2i (see also Supplementary Movies 2 and 3). Moreover, we find a strong correlation (Pearson correlation coefficient $\rho = 0.93$) between inferred and exact image-forces. To further quantify the performance of force inference, we compute the relative squared error on the inferred image force field $\sigma_{\hat{\mathcal{F}}}^2 = \sum_t \|\hat{\mathcal{F}}(t) - \hat{\mathcal{F}}_{\text{ex}}(t)\|^2 \left(\sum_t \|\hat{\mathcal{F}}(t)\|^2 \right)^{-1}$, which in this case is modest, $\sigma_{\hat{\mathcal{F}}}^2 = 0.14$ (Fig. 2h).

Thus, with sufficient information, we can use our approach to accurately predict at any instant of time the physical force fields in image space from the Brownian movie, even if the system is out of equilibrium. Moreover, the results for this simple two-bead system demonstrate the validity of our approach: we reliably infer the non-equilibrium dynamics of this system. Arguably, direct tracking of the two beads is, in this case, a more straightforward approach. However, this changes when

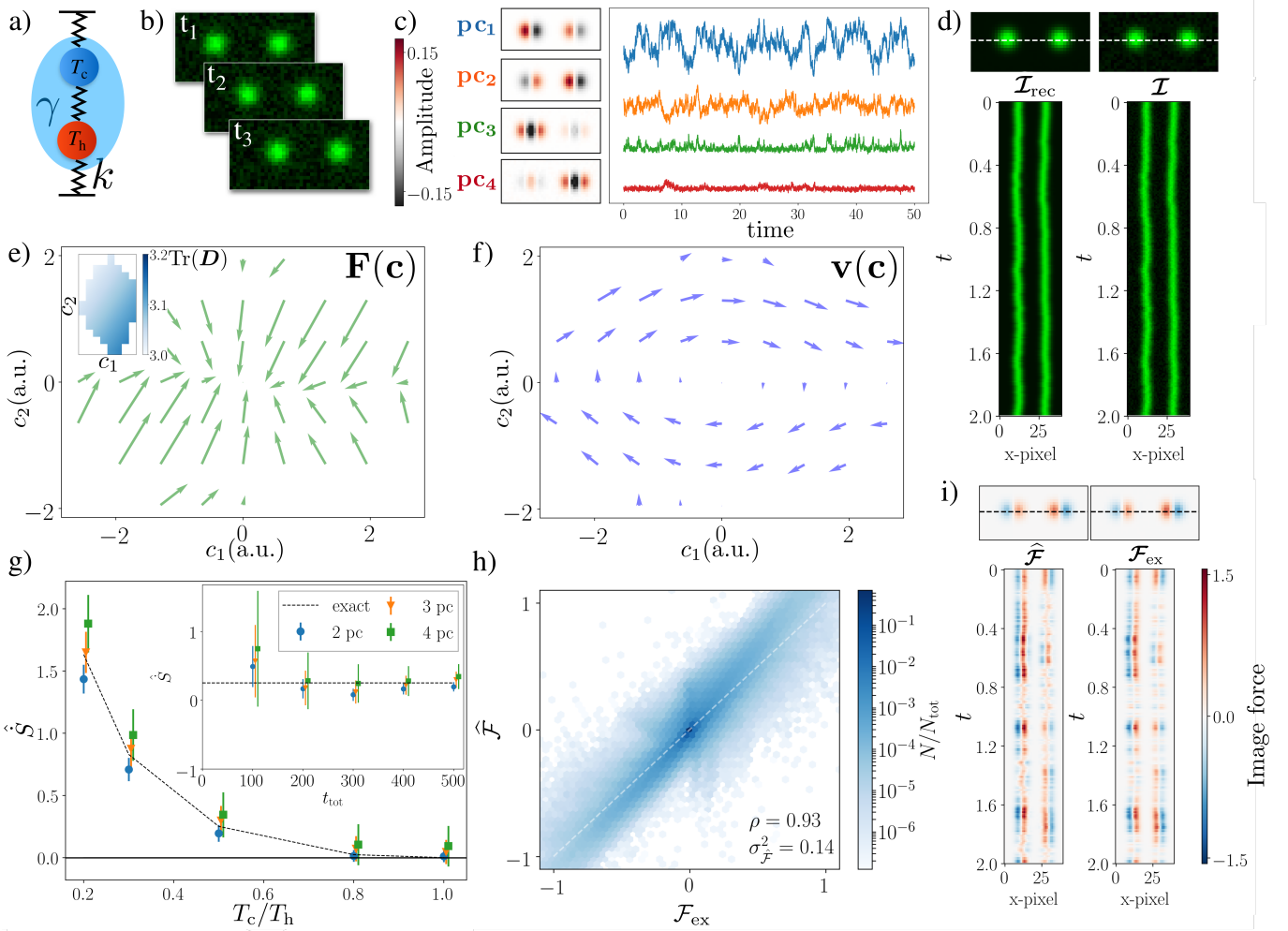


FIG. 2. **Benchmarking the Brownian movie learning approach with a simple toy model** a) Schematic of the two-bead model. The temperature of the hot bead $T_h = 1$ is fixed and the temperature of the cold bead $T_c \leq 1$ is varied. b) 40×20 Frames of the noisy (10% noise) Brownian movie for the two bead-model at successive time-points c) The first 4 principal components (in arbitrary units) with time-traces of respective projection coefficients. The color map displays negative values in black and positive values in red. d) Snapshot \mathcal{I}_{rec} of the reconstructed movie, reconstructed with the first four principal components, and snapshot \mathcal{I} of the original movie (right), together with associated kymographs. Pixel intensity ranges from 0 (black) to 1 (bright green). We compare pixel intensities along the superimposed horizontal dashed line. Force field (e) and mean phase space velocity (f) in the space of the first two principal components $\{c_1, c_2\}$. Arrows are scaled for visualization purposes. Inset e): trace of diffusion tensor $\text{Tr}(\mathbf{D})$ with the same axis scaling. g) Inferred entropy production rate \hat{S} for varying temperature ratio $T_c T_h^{-1}$ and number of included principal components. Inset: \hat{S} as a function of trajectory length for a fixed $T_c T_h^{-1} = 0.5$. The error bars represent an estimate of the root-mean-square deviation between the true apparent entropy production rate and the inferred value (see Methods). h) Scatter plot of the elements of the exact image force field \mathcal{F}_{ex} vs. the inferred image force field $\hat{\mathcal{F}}$ for different pixels and time points (data has been binned for visualization purposes). Results are obtained using the first four principal components. i) Comparison of inferred $\hat{\mathcal{F}}$ and exact \mathcal{F}_{ex} image-space force fields, together with associated kymographs.

considering more general soft assemblies comprised of many degrees of freedom.

Dissipative Component Analysis

To expand the scope of our approach, we next consider a more complex scenario inspired by cytoskeletal

assemblies: a network of elastic filaments (Fig. 3a). The filaments are modeled as Hookean springs represented as bonds connecting neighboring nodes of a triangular network. We randomly remove bonds to introduce spatial disorder in the system. The state of the network as a whole, represented by the set $\{\mathbf{x}_i\}$ of two-dimensional displacement of each node i , undergoes Langevin dynamics (Eq. (1)). In this case, the force acting on node i is

$\mathbf{F}_i(\mathbf{x}) = -\sum_{j \sim i} \frac{k_{ij}}{\gamma} (\|\mathbf{x}_{i,j}(t)\| - \ell_0) \hat{\mathbf{x}}_{i,j}$, where $k_{ij} = k$ if the bond is present, $k_{ij} = 0$ if it is not, $\mathbf{x}_{i,j} = \mathbf{x}_i - \mathbf{x}_j$, $\hat{\mathbf{x}}_{i,j}$ is the corresponding unit vector, and the sum runs over the nearest-neighbor nodes j of node i . Rigid boundary conditions are imposed to avoid rotations and diffusion of the system as a whole. Finally, we drive the system out of equilibrium by randomly setting a fraction of the network nodes at an elevated temperature, as illustrated in Fig. 3a.

To study an experimentally relevant scenario, we generate a Brownian movie of a random filamentous network (Supplementary Note 2), which is only partially imaged (black frame in Fig. 3a) with measurement noise and at a limited optical resolution (Supplementary Note 6, 7). To simulate limited optical resolution, we blur the image-frames of the movie with a Gaussian filter (Fig. 3b and Supplementary Movie 4). In this spatially extended system, generated from an underlying dynamics with 800 degrees of freedom, it is not obvious based on the recorded Brownian movie (80×80 pixels) how to select and analyze the relevant degrees of freedom.

We start our movie-based analysis by employing PCA to reduce the dimensionality of the image data (Fig. 3c). For this set of simulation data, our truncation criteria indicate that the maximum number of retainable components is roughly 200 (Supplementary Note 5 and Supplementary Figure 3). Although we greatly reduced dimensionality of the image data using this truncation, it is still intractable to infer dynamics in a 200-dimensional space due to limited statistics. However, even a subset of these modes may suffice to glean useful information about the system’s non-equilibrium dynamics. Therefore, as a first attempt, we infer the dynamics in increasingly larger PC-space via SFI. This allows us to infer the retained percentage of entropy production rate $\hat{S}/\dot{S}_{\text{ex}}$ in the observed region (See Supplementary Note 2) as a function of the number of principal components considered (Fig. 3e). In contrast to the two-beads case, we observe that in this more realistic scenario we recover less than 4% of the entropy production rate of the observed system with the first 30 PCs. Indeed, PCA is designed to find modes that capture the most variance in the image data, and large variance does not necessarily imply large dissipation. Thus, in this case, PCA fails at selecting components that capture a substantial fraction of the entropy production rate.

Our goal is to infer the system’s non-equilibrium dynamics. We thus propose an alternative way of reducing data dimensionality that spotlights the time-irreversible contributions to the dynamics, which we term Dissipative Component Analysis (DCA). DCA represents a principled approach to determine the most dissipative pairs of modes for a linear system with state-independent noise (see Supplementary Note 3). For such a linear system, there exists a set of component pairs for which the entropy production rate can be expressed as a sum of independent positive-definite contributions, which can be ranked by magnitude. After a suitable truncation, this

basis ensures that the components with the largest entropy production rate are selected. While the approach is only rigorous for a linear system with state-independent noise, we demonstrate below that this method also performs well for more general scenarios.

DCA relies on the measurement of an intuitive trajectory-based non-equilibrium quantity: the area enclosing rate (AER) matrix $\dot{\mathbf{A}}$ associated to a general set of coordinates \mathbf{y} . The elements of the AER matrix, in Itô convention, are defined by [24, 38, 62–64]

$$\dot{A}_{ij} = \frac{1}{2} \langle y_j \dot{y}_i - y_i \dot{y}_j \rangle, \quad (6)$$

where y_i denotes the i -th coordinate centered around its mean value and $\langle \cdot \rangle$ a time average. This non-equilibrium measure quantifies the average area enclosed by the trajectory in phase space per unit time. Importantly, the AER is tightly linked to the entropy production rate. Specifically, for a linear system $\dot{S} = \text{Tr}(\dot{\mathbf{A}}\mathbf{C}^{-1}\dot{\mathbf{A}}^T\mathbf{D}^{-1})$ where the covariance matrix $C_{ij} = \langle y_i y_j \rangle$. DCA identifies a basis of vector pairs $\{(\mathbf{dc}_1, \mathbf{dc}_2); (\mathbf{dc}_3, \mathbf{dc}_4); \dots\}$ that simultaneously transforms \mathbf{C} to the identity and diagonalizes $\dot{\mathbf{A}}\dot{\mathbf{A}}^T$ (see Supplementary Note 3). By doing so, DCA naturally separates the entropy production rate into independent contributions that can be readily ordered by magnitude, *i.e.* $\dot{S} = \dot{S}_{\mathbf{dc}_1, \mathbf{dc}_2} + \dot{S}_{\mathbf{dc}_3, \mathbf{dc}_4} + \dots$ with $\dot{S}_{\mathbf{dc}_1, \mathbf{dc}_2} > \dot{S}_{\mathbf{dc}_3, \mathbf{dc}_4} > \dots$. Truncating the basis of dissipative components using the aforementioned criteria, allows us to identify a limited number of components that are assured to maximally contribute to the dissipation of the system. This is analogous to PCA, where the diagonalization of the covariance matrix \mathbf{C} allows one to select the components which capture most of the variance.

To test the performance of DCA, we revisit the network simulations. We first perform PCA to reduce noise and dimensionality. Subsequently, we perform DCA with the first 200 principal component coefficients as input. The dissipative components exhibit a different spatial structure than the principal components, as they aim to maximize different quantities (Fig. 3d). Strikingly, DCA allows us to recover a larger portion of the entropy production rate of the observed region (almost 10% with 30 components), performing consistently better than the PCA-based approach, as shown in Fig. 3e. Finally, we note that the performance of our approach improves substantially in systems with smaller fluctuations in which the image-space dynamics is closer to linear (Fig. 3e and Supplementary Movie 8).

In non-equilibrium systems our DCA-based method infers non-zero entropy production rates, even with poor optical resolution (Fig. 3f, Supplementary Note 6, and Supplementary Figure 4) and with strong measurement noise (Supplementary Note 7 and Supplementary Figure 5). At the same time we measure no dissipation in equilibrium systems. Thus, this example illustrates the potential applicability of our approach to real experiments on biological assemblies.

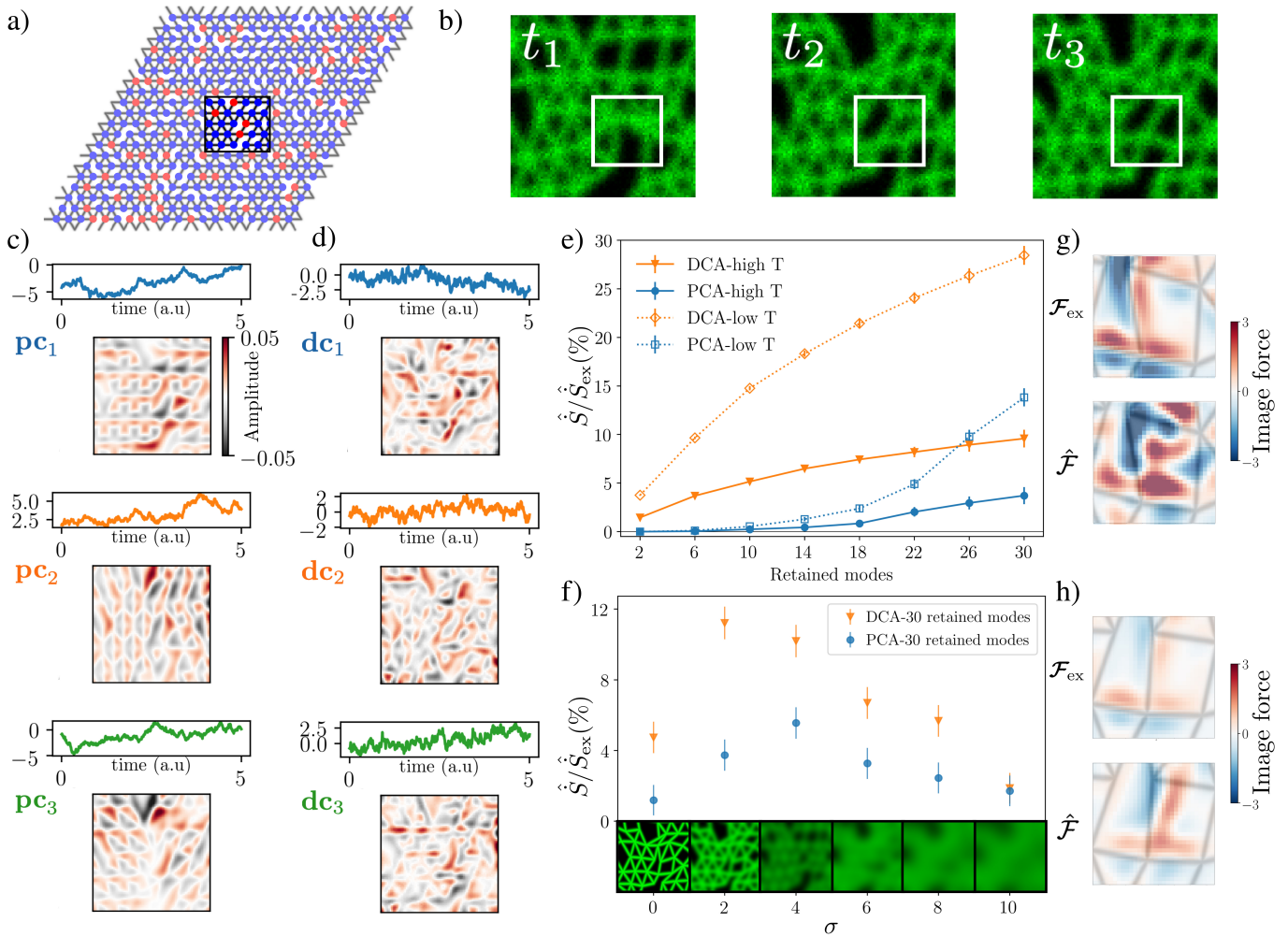


FIG. 3. **Learning the non-equilibrium dynamics of Brownian movies of simulated filamentous networks** a) The 20×20 filamentous network generated in the Brownian dynamics simulation with 20% random bond removal and heterogeneous temperatures: node temperatures are randomly set to T_{hot} with probability 0.2, or else to $T_{\text{cold}} = 0.2 T_{\text{hot}}$. The black frame indicates the observed region of the system which is analyzed with our movie-based method. b) Three time frames of the Brownian movie of the observed region of the system (80×80 pixels, $T_{\text{hot}} = 0.25$). c-d) Trajectory of the projection coefficient c_i in arbitrary units together with associated image-component for PCA (c) and DCA (d) for the observed region defined in panel a). Scale bar applies to all image-components. e) The recovered entropy production rate $\hat{S}/\dot{S}_{\text{ex}}$ for the observed region as a function of the number of components included in the analysis. For the high and low temperature cases $T_{\text{hot}} = 0.25$ and $T_{\text{hot}} = 0.05$, respectively. See Supplementary Note 5 and Supplementary Figure 2 for additional data at equilibrium and convergence of the estimates with total time. f): The recovered entropy production rate $\hat{S}/\dot{S}_{\text{ex}}$ as a function of the blurring parameter σ for 30 retained PCs and DCs. We show a corresponding blurred frame above every x -axis tick. The error bars in panels e,f) represent an estimate of the root-mean-square deviation between the true apparent entropy production rate and the inferred value (see Methods). g,h) Comparison of the exact image-force \mathcal{F}_{ex} to the inferred one $\hat{\mathcal{F}}$ at a selected instant of time for the region of interest in the white frame in panel b) for the high (g) and low (h) temperature cases. The underlying network structure is drawn in grey as a guide to the eye.

Our inference approach reveals additional information about the dynamics in the system, such as force field estimates. These force fields provide insight into the spatial structure of the instantaneous deterministic forces in the system at a given configuration. In image space, these forces describe the dynamics of the pixel: positive and negative image forces represent a deterministic force acting to respectively raise and lower pixel values,

which reflect the forces acting on the position and shape of the objects being imaged. To investigate to what extent our movie-based learning approach reconstructs the elastic forces exerted by the network's filaments, we exploit the short range of the interactions in the system to facilitate extracting information about local forces from local dynamics in image space. We consider a small region of interest (white frame in Fig. 3b, Supplementary

Movie 5) and compare the inferred force field in image space to the exact one. For this purpose, we employ PCA in our dimensional reduction scheme, which can be used both in and out of equilibrium. Inferring image force fields with high accuracy for this complex example is challenging (Pearson correlation coefficient between exact and inferred images force $\rho = 0.37$ for the high temperature case and $\rho = 0.56$ for the low temperature case). Nonetheless, despite the network disorder, large fluctuations, many hidden degrees of freedom, limited optical resolution, and measurement noise, we find that the inferred force field in image space can capture the basic features of the exact force field, as shown in Fig. 3g,h (Supplementary Movies 6-11). Finally, we emphasize that our approach is scalable: force inference on a small spatial region of interest can be applied to arbitrarily large systems, as long as the interactions are local.

DISCUSSION

We considered the dynamics of movies of time-lapse microscopy data. Under the assumptions outlined in the first section of the Results, these movies undergo Brownian dynamics in image space: the image-field obeys an overdamped Langevin equation of the form of Eq. (3). Rather than tracking selected degrees of freedom, we propose to analyze the Brownian movie as a whole.

Our approach is based on constructing a reduced set of relevant degrees of freedom to reduce dimensionality, by combining PCA with a new method that we term Dissipative Component Analysis (DCA). In the limit of a linear system with state-independent noise, DCA provides a principled way of constructing and ranking independent dissipative modes. The order at which we truncate is an important trade-off parameter of this method: on the one hand we wish to significantly reduce the dimensionality of the data, on the other hand we need to include enough components to retain the information necessary to infer the system’s dynamics. After the dimensional reduction, we infer the stochastic dynamics of the system, revealing the force field, phase space currents, and the entropy production rate in this basis. This information can then be mapped back to image-space to provide estimators for the stochastic dynamics of the Brownian movie. We illustrated our approach on simulated data of a minimal two-beads model and on complex filamentous networks in both equilibrium and non-equilibrium settings, and showed that it is robust in the presence of measurement noise and with limited optical resolution. Beyond providing controlled lower bounds of the entropy production rates directly from the Brownian movie, our approach yields estimates of the force-fields in image space for an instantaneous snapshot of the system and we demonstrated that this approach can be scaled up to large systems. Thus, we provide in principle an alternative to microscopic force and stress sensing methods [43, 44, 51, 52].

We focused here on a class of soft matter systems termed “active viscoelastic solids” [9, 65]. Such systems include active biological materials such as cytoskeletal assemblies [31, 33, 34, 66], membranes [16, 67, 68], chromosomes [29], protein droplets [30], as well as active turbulent solids [69] and colloidal systems [10]. Although these structures are constantly fluctuating both due to energy-consuming processes (*e.g.* rapid contractions generated by molecular motors) and thermal motion, they do not exhibit macroscopic flow. Useful insights into the properties of such systems have been obtained via different non-invasive techniques. Typically, these techniques employ time traces of tracked objects to extract information about the active processes governing the non-equilibrium behavior [16–20, 60, 67]. Often, however, it is not a priori obvious which physical degrees of freedom should be tracked, how tracking can be performed in fragile environments, and to what extent the dynamical information about the system of interest is encoded in the measured trajectories [49]. While tracking-free approaches have been proposed to obtain rheological information of a system under equilibrium conditions [50], our approach offers an alternative to tracking that can provide information on dissipative modes and the instantaneous force fields of a fluctuating non-equilibrium system.

In summary, we presented a viable alternative to traditional analysis techniques of high-resolution video-microscopy of soft living assemblies. Indeed, we envision experimental scenarios where our approach may serve as a guide, providing insights by disentangling the deterministic and stochastic components of the dynamics, and by helping to identify the source of thermal and active forces as well as the dissipation in the system. Overall, our movie-based approach constitutes an adaptable tool that paves the road for a systematic, non-invasive and tracking-free analysis of time-lapse data of soft and living systems.

METHODS

Parameters for Fig. 2: We use $k = 2$, $\gamma = 1$, $k_B = 1$. Panels c)-d)-e)-f)-h)-i) have been obtained with $T_c T_h^{-1} = 0.5$ and for a trajectory of length $t_{\text{tot}} = 10^5 \Delta t$, $\Delta t = 0.01$. Panel g) with $t_{\text{tot}} = 5 \times 10^4 \Delta t$. We employed a first order polynomial basis for the inference of forces and diffusion fields using SFI. The noise-corrected estimator was used to infer the diffusion fields [24].

Parameters for Fig. 3: All results have been obtained with a trajectory of 10^6 time steps, $\Delta t = 0.005$ and 80×80 -pixels frames for the observed region of the full network. We employed a first order polynomial basis for the inference of forces and diffusion fields using Stochastic Force Inference, and noise-corrected diffusion estimates. The high temperature case is shown in g) using 50 PCs and the low temperature case is shown in h) using 20 PCs.

The error bars on the entropy production rates in Figs. 2, 3 are obtained as a self-consistent estimate of $\langle (\dot{S}_{\text{apparent}} - \hat{S})^2 \rangle^{0.5}$, where $\langle \cdot \rangle$ represents the average over the realizations of the noise. For details see [24].

DATA AVAILABILITY

The datasets generated during and/or analysed during the current study are available from the corresponding authors on reasonable request.

CODE AVAILABILITY

The Python code generating the data and implementing the analysis presented in the manuscript is available at <https://github.com/ronceray/NonequilibriumBrownianMovies>.

ACKNOWLEDGEMENTS

We thank C. Schmidt, F. Mura, S. Ceolin and I. Graf for many stimulating discussions. This work was

Funded by the Deutsche Forschungsgemeinschaft (DFG, German Research Foundation) under Germany's Excellence Strategy – EXC-2094 – 390783311 and by the DFG grant 418389167.

AUTHOR CONTRIBUTIONS

P.R. and C.P.B. conceived the project. F.G. wrote the new codes developed in this manuscript and performed all simulations and Brownian movies analysis. P.R. provided support for the SFI analysis and G.G. largely developed the derivations underlying the DCA analysis. All authors contributed conceptually to developing the Brownian movie analysis and DCA frameworks, interpreting the results, and writing the paper.

COMPETING INTERESTS

The authors declare no competing interests.

-
- [1] Stephens, D. J. & Allan, V. J. Light Microscopy Techniques for Live Cell Imaging. *Science* **300**, 82–86 (2003).
- [2] Sahl, S. J., Hell, S. W. & Jakobs, S. Fluorescence nanoscopy in cell biology. *Nat Rev Mol Cell Biol* **18**, 685–701 (2017).
- [3] Brown, R. XXVII. *A brief account of microscopical observations made in the months of June, July and August 1827, on the particles contained in the pollen of plants; and on the general existence of active molecules in organic and inorganic bodies.* *The Philosophical Magazine* **4**, 161–173 (1828).
- [4] Einstein, A. Über die von der molekularkinetischen Theorie der Wärme geforderte Bewegung von in ruhenden Flüssigkeiten suspendierten Teilchen. *Ann. Phys.* **322**, 549–560 (1905).
- [5] Smoluchowski, M. Zur kinetischen theorie der brownischen molekularbewegung und der suspensionen. *Annalen der Physik* **326**, 756–780 (1906).
- [6] Frey, E. & Kroy, K. Brownian motion: A paradigm of soft matter and biological physics. *Annalen der Physik* **14**, 20–50 (2005).
- [7] Waters, J. C. Accuracy and precision in quantitative fluorescence microscopy. *The Journal of Cell Biology* **185**, 1135–1148 (2009).
- [8] MacKintosh, F. C. & Schmidt, C. F. Active cellular materials. *Current Opinion in Cell Biology* **22**, 29–35 (2010).
- [9] Gnesotto, F. S., Mura, F., Gladrow, J. & Broedersz, C. P. Broken detailed balance and non-equilibrium dynamics in living systems: A review. *Rep. Prog. Phys.* **81**, 066601 (2018).
- [10] Aranson, I. S. Active colloids. *Phys.-Usp.* **56**, 79 (2013).
- [11] Cates, M. E. & Tailleur, J. Motility-Induced Phase Separation. *Annual Review of Condensed Matter Physics* **6**, 219–244 (2015).
- [12] Fodor, É. *et al.* How Far from Equilibrium Is Active Matter? *Phys. Rev. Lett.* **117**, 038103 (2016).
- [13] Martínez, I. A., Bisker, G., Horowitz, J. M. & Parrondo, J. M. R. Inferring broken detailed balance in the absence of observable currents. *Nat Commun* **10**, 1–10 (2019).
- [14] Guo, M. *et al.* Probing the Stochastic, Motor-Driven Properties of the Cytoplasm Using Force Spectrum Microscopy. *Cell* **158**, 822–832 (2014).
- [15] Fakhri, N. *et al.* High-resolution mapping of intracellular fluctuations using carbon nanotubes. *Science* **344**, 1031–1035 (2014).
- [16] Turlier, H. *et al.* Equilibrium physics breakdown reveals the active nature of red blood cell flickering. *Nature Physics* **12**, 513–519 (2016).
- [17] Battle, C. *et al.* Broken detailed balance at mesoscopic scales in active biological systems. *Science* **352**, 604–607 (2016).
- [18] Gladrow, J., Fakhri, N., MacKintosh, F. C., Schmidt, C. F. & Broedersz, C. P. Broken Detailed Balance of Filament Dynamics in Active Networks. *Phys. Rev. Lett.* **116**, 248301 (2016).
- [19] Mura, F., Gradziuk, G. & Broedersz, C. P. Nonequilibrium Scaling Behavior in Driven Soft Biological Assemblies. *Phys. Rev. Lett.* **121**, 038002 (2018).

- [20] Seara, D. S. *et al.* Entropy production rate is maximized in non-contractile actomyosin. *Nature Communications* **9**, 1–10 (2018).
- [21] Ma, R., Klindt, G. S., Riedel-Kruse, I. H., Jülicher, F. & Friedrich, B. M. Active Phase and Amplitude Fluctuations of Flagellar Beating. *Phys. Rev. Lett.* **113**, 048101 (2014).
- [22] Li, J., Horowitz, J. M., Gingrich, T. R. & Fakhri, N. Quantifying dissipation using fluctuating currents. *Nat Commun* **10**, 1666 (2019).
- [23] Sanchez, T., Chen, D. T. N., DeCamp, S. J., Heymann, M. & Dogic, Z. Spontaneous motion in hierarchically assembled active matter. *Nature* **491**, 431–434 (2012).
- [24] Frishman, A. & Ronceray, P. Learning force fields from stochastic trajectories. *Phys. Rev. X* **10**, 021009 (2020).
- [25] Roldán, É. & Parrondo, J. M. R. Estimating Dissipation from Single Stationary Trajectories. *Phys. Rev. Lett.* **105**, 150607 (2010).
- [26] Sanchez, T., Welch, D., Nicastro, D. & Dogic, Z. Cilia-Like Beating of Active Microtubule Bundles. *Science* **333**, 456–459 (2011).
- [27] Battle, C., Ott, C. M., Burnette, D. T., Lippincott-Schwartz, J. & Schmidt, C. F. Intracellular and extracellular forces drive primary cilia movement. *PNAS* **112**, 1410–1415 (2015).
- [28] Riedel-Kruse, I. H., Hilfinger, A., Howard, J. & Jülicher, F. How molecular motors shape the flagellar beat. *HFSP Journal* **1**, 192–208 (2007).
- [29] Weber, S. C., Spakowitz, A. J. & Theriot, J. A. Non-thermal ATP-dependent fluctuations contribute to the in vivo motion of chromosomal loci. *Proceedings of the National Academy of Sciences* **109**, 7338–7343 (2012).
- [30] Brangwynne, C. P., Mitchison, T. J. & Hyman, A. A. Active liquid-like behavior of nucleoli determines their size and shape in *Xenopus laevis* oocytes. *PNAS* **108**, 4334–4339 (2011).
- [31] Mizuno, D., Tardin, C., Schmidt, C. F. & MacKintosh, F. C. Nonequilibrium Mechanics of Active Cytoskeletal Networks. *Science* **315**, 370–373 (2007).
- [32] Brangwynne, C. P., Koenderink, G. H., MacKintosh, F. C. & Weitz, D. A. Cytoplasmic diffusion: Molecular motors mix it up. *J Cell Biol* **183**, 583–587 (2008).
- [33] Koenderink, G. H. *et al.* An active biopolymer network controlled by molecular motors. *PNAS* **106**, 15192–15197 (2009).
- [34] Brangwynne, C. P., Koenderink, G. H., MacKintosh, F. C. & Weitz, D. A. Nonequilibrium Microtubule Fluctuations in a Model Cytoskeleton. *Phys. Rev. Lett.* **100**, 118104 (2008).
- [35] Pajmans, J., Bosman, M., ten Wolde, P. R. & Lubensky, D. K. Discrete gene replication events drive coupling between the cell cycle and circadian clocks. *PNAS* **113**, 4063–4068 (2016).
- [36] Kimmel, J. C., Chang, A. Y., Brack, A. S. & Marshall, W. F. Inferring cell state by quantitative motility analysis reveals a dynamic state system and broken detailed balance. *PLOS Computational Biology* **14**, e1005927 (16-gen-2018).
- [37] Wan, K. Y. & Goldstein, R. E. Time Irreversibility and Criticality in the Motility of a Flagellate Microorganism. *Phys. Rev. Lett.* **121**, 058103 (2018).
- [38] Zia, R. K. P., Weiss, J. B., Mandal, D. & Fox-Kemper, B. Manifest and Subtle Cyclic Behavior in Nonequilibrium Steady States. *Journal of Physics: Conference Series* **750**, 012003 (2016).
- [39] Seifert, U. Stochastic thermodynamics, fluctuation theorems and molecular machines. *Rep. Prog. Phys.* **75**, 126001 (2012).
- [40] Crooks, G. E. Entropy production fluctuation theorem and the nonequilibrium work relation for free energy differences. *Phys. Rev. E* **60**, 2721–2726 (1999).
- [41] Crocker, J. C. & Grier, D. G. Methods of Digital Video Microscopy for Colloidal Studies. *Journal of Colloid and Interface Science* **179**, 298–310 (1996).
- [42] Levine, A. J. & Lubensky, T. C. One- and Two-Particle Microrheology. *Phys. Rev. Lett.* **85**, 1774–1777 (2000).
- [43] Sawada, Y. *et al.* Force Sensing by Mechanical Extension of the Src Family Kinase Substrate p130Cas. *Cell* **127**, 1015–1026 (2006).
- [44] Grashoff, C. *et al.* Measuring mechanical tension across vinculin reveals regulation of focal adhesion dynamics. *Nature* **466**, 263–266 (2010).
- [45] Mura, F., Gradziuk, G. & Broedersz, C. P. Mesoscopic non-equilibrium measures can reveal intrinsic features of the active driving. *Soft Matter* **15**, 8067–8076 (2019).
- [46] Brückner, D. B. *et al.* Stochastic nonlinear dynamics of confined cell migration in two-state systems. *Nature Physics* **15**, 595–601 (2019).
- [47] Selmeçzi, D., Mosler, S., Hagedorn, P. H., Larsen, N. B. & Flyvbjerg, H. Cell Motility as Persistent Random Motion: Theories from Experiments. *Biophysical Journal* **89**, 912–931 (2005).
- [48] Stephens, G. J., Johnson-Kerner, B., Bialek, W. & Ryu, W. S. Dimensionality and Dynamics in the Behavior of *C. elegans*. *PLOS Computational Biology* **4**, e1000028 (25-apr-2008).
- [49] Seara, D. S., Machta, B. B. & Murrell, M. P. Dissipative signatures of dynamical phases and transitions. *arXiv:1911.10696 [cond-mat, physics:physics, q-bio]* (2019). 1911.10696.
- [50] Edera, P., Bergamini, D., Trappe, V., Giavazzi, F. & Cerbino, R. Differential dynamic microscopy microrheology of soft materials: A tracking-free determination of the frequency-dependent loss and storage moduli. *Phys. Rev. Materials* **1**, 073804 (2017).
- [51] Lucio, A. A., Ingber, D. E. & Campàs, O. Chapter 20 - Generation of biocompatible droplets for in vivo and in vitro measurement of cell-generated mechanical stresses. In Paluch, E. K. (ed.) *Methods in Cell Biology*, vol. 125 of *Biophysical Methods in Cell Biology*, 373–390 (Academic Press, 2015).
- [52] Han, Y. L. *et al.* Cell contraction induces long-ranged stress stiffening in the extracellular matrix. *PNAS* **115**, 4075–4080 (2018).
- [53] Lau, A. W. C. & Lubensky, T. C. State-dependent diffusion: Thermodynamic consistency and its path integral formulation. *Phys. Rev. E* **76**, 011123 (2007).
- [54] Risken, H. & Frank, T. *The Fokker-Planck Equation: Methods of Solution and Applications*. Springer Series in Synergetics (Springer-Verlag, Berlin Heidelberg, 1996), 2 edn.
- [55] We neglect the discretization effect induced by the finite number of pixel intensities here.
- [56] Øksendal, B. *Stochastic Differential Equations: An Introduction with Applications*. Universitext (Springer-Verlag, Berlin Heidelberg, 2003), 6 edn.

- [57] Note that we consider here only the entropy production rate associated to apparent currents. The irreversible dynamics of unobserved degrees of freedom has repercussion on non-Markovian effects in the dynamics, which result in other contributions to the entropy production [25], which we neglect here.
- [58] Crisanti, A., Puglisi, A. & Villamaina, D. Nonequilibrium and information: The role of cross correlations. *Phys. Rev. E* **85**, 061127 (2012).
- [59] Bérut, A., Imparato, A., Petrosyan, A. & Ciliberto, S. Theoretical description of effective heat transfer between two viscously coupled beads. *Phys. Rev. E* **94**, 052148 (2016).
- [60] Gnesotto, F. S., Remlein, B. M. & Broedersz, C. P. Nonequilibrium dynamics of isostatic spring networks. *Phys. Rev. E* **100**, 013002 (2019).
- [61] Bishop, C. M. *Pattern Recognition and Machine Learning*. Information Science and Statistics (Springer, New York, 2006).
- [62] Ghanta, A., Neu, J. C. & Teitworth, S. Fluctuation loops in noise-driven linear dynamical systems. *Phys. Rev. E* **95**, 032128 (2017).
- [63] Gonzalez, J. P., Neu, J. C. & Teitworth, S. W. Experimental metrics for detection of detailed balance violation. *Phys. Rev. E* **99**, 022143 (2019).
- [64] Gradziuk, G., Mura, F. & Broedersz, C. P. Scaling behavior of nonequilibrium measures in internally driven elastic assemblies. *Phys. Rev. E* **99**, 052406 (2019).
- [65] Fletcher, D. A. & Geissler, P. L. Active Biological Materials. *Annu. Rev. Phys. Chem.* **60**, 469–486 (2009).
- [66] Jensen, M. H., Morris, E. J. & Weitz, D. A. Mechanics and dynamics of reconstituted cytoskeletal systems. *Biochimica et Biophysica Acta (BBA) - Molecular Cell Research* **1853**, 3038–3042 (2015).
- [67] Betz, T., Lenz, M., Joanny, J.-F. & Sykes, C. ATP-dependent mechanics of red blood cells. *PNAS* **106**, 15320–15325 (2009).
- [68] Ben-Isaac, E. *et al.* Effective Temperature of Red-Blood-Cell Membrane Fluctuations. *Phys. Rev. Lett.* **106**, 238103 (2011).
- [69] Hemingway, E. J. *et al.* Active Viscoelastic Matter: From Bacterial Drag Reduction to Turbulent Solids. *Phys. Rev. Lett.* **114**, 098302 (2015).

Supplementary Information

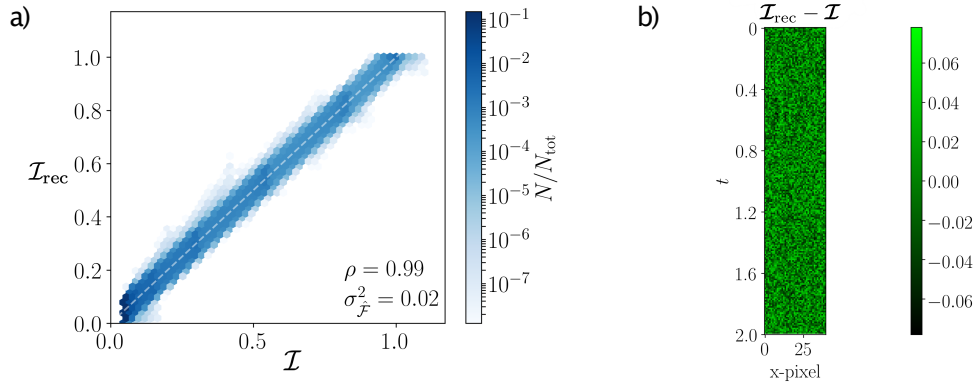
Learning the Non-Equilibrium Dynamics of Brownian Movies

Federico S. Gnesotto and Grzegorz Gradziuk
*Arnold-Sommerfeld-Center for Theoretical Physics and Center for NanoScience,
Ludwig-Maximilians-Universität München, D-80333 München, Germany.*

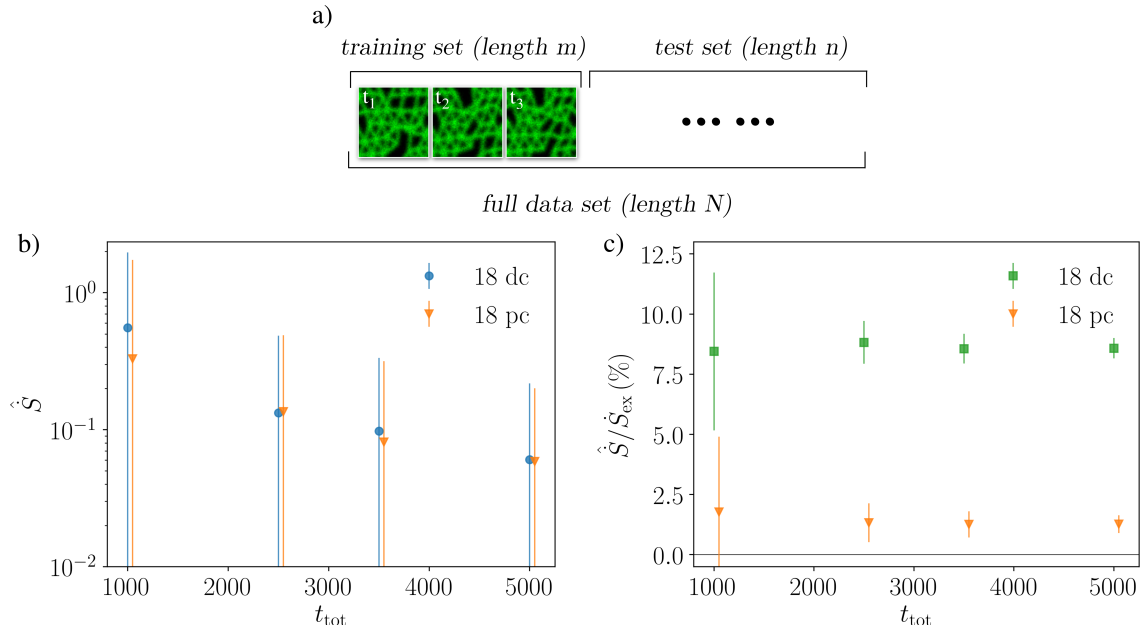
Pierre Ronceray*
*Center for the Physics of Biological Function,
Princeton University, Princeton, NJ 08544, USA*

Chase P. Broedersz*
*Arnold-Sommerfeld-Center for Theoretical Physics and Center for NanoScience,
Ludwig-Maximilians-Universität München, D-80333 München, Germany. and
Department of Physics and Astronomy, Vrije Universiteit Amsterdam, 1081 HV Amsterdam, The Netherlands*

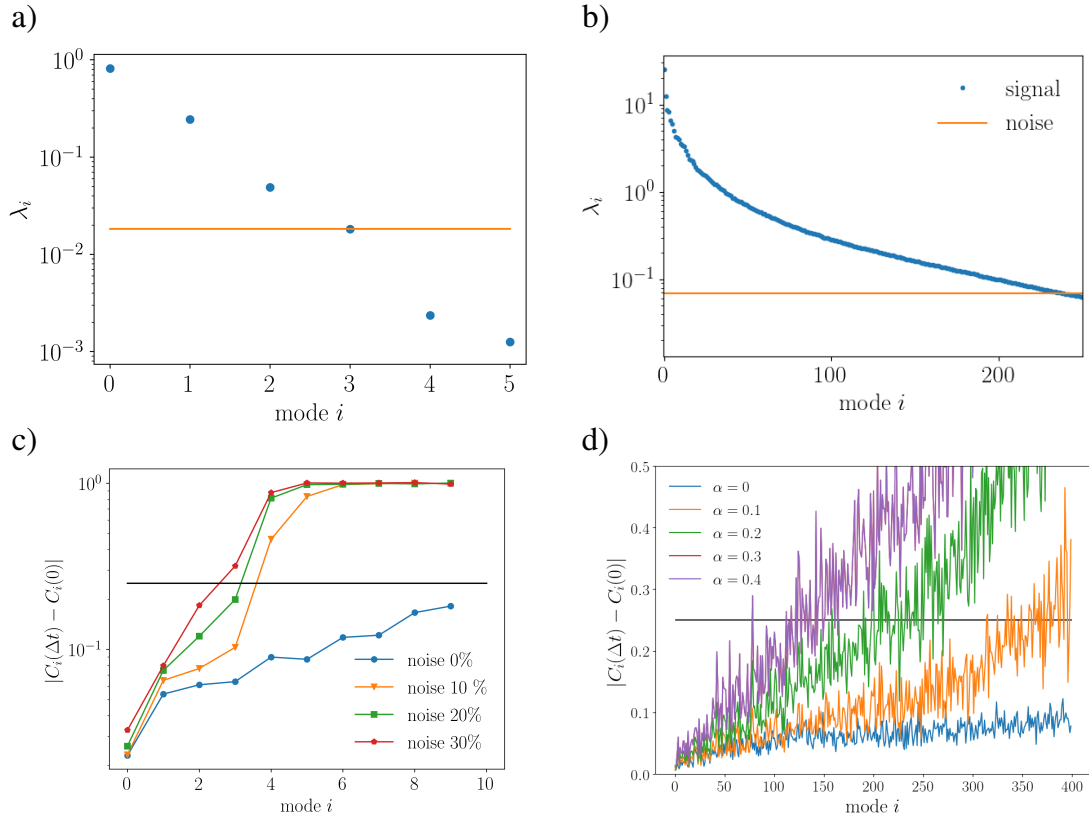
* ronceray@princeton.edu, c.broedersz@lmu.de



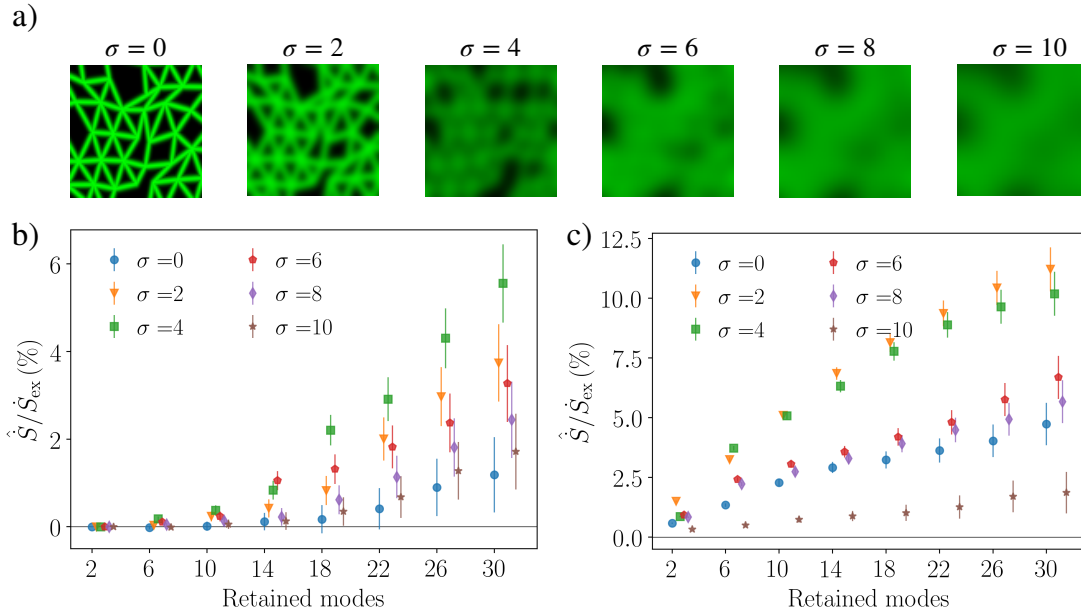
Supplementary Figure 1. **Two-beads Brownian movie: Comparison between reconstructed and exact images** Here we compare the exact two-beads images \mathcal{I} to the reconstructed images \mathcal{I}_{rec} using PCA (see main text Fig. 2d). We do so with a scatter plot of the pixel values at different time points and with a kymograph of the difference between exact and reconstructed images, as shown in Supplementary Figure 1. Overall, we find that the first four PCA modes allow for an accurate reconstruction of the images in the Brownian movie for this two-beads model. a) Scatter plot of reconstructed (with 4 principle components) image-pixel values \mathcal{I}_{rec} and exact image-pixel values \mathcal{I} using PCA. The Pearson correlation coefficient ρ and the relative squared error $\sigma_{\mathcal{I}}^2$ (see main text for definition) are shown. Data is the same as in Fig. 2d of the main text. b) Kymograph of the difference between reconstructed (with 4 principle components) and exact pixel values along the horizontal line shown in Fig. 2d of the main text.



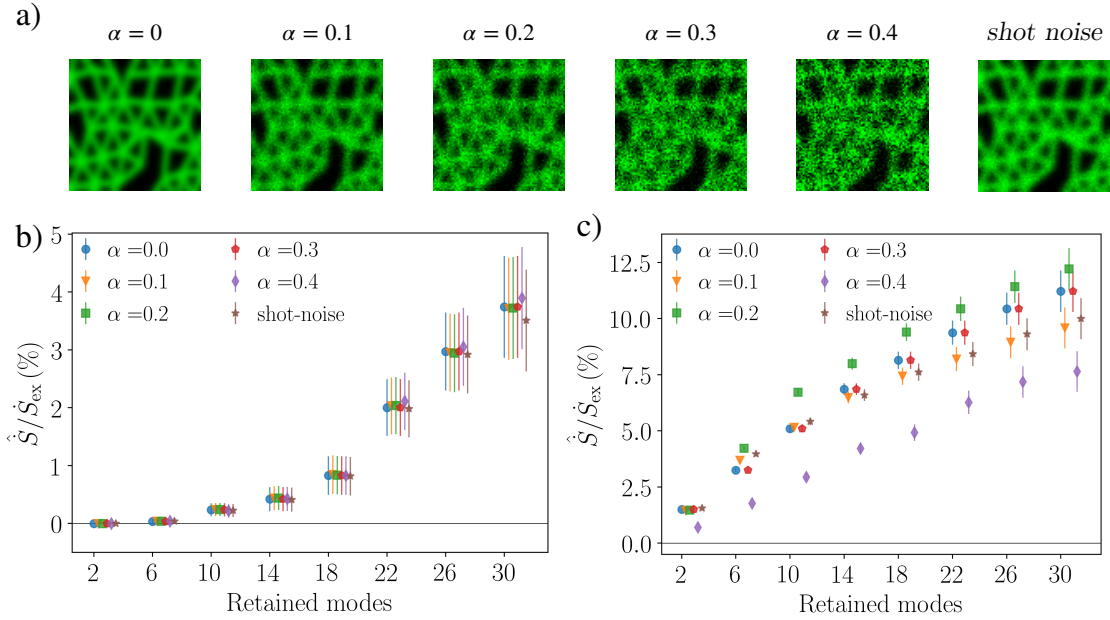
Supplementary Figure 2. **Dependence of Entropy Production Rates on the trajectory length** a): Schematic of the training/test set splitting procedure: the full trajectory (length N) is split into a training set (length m) and into a test set (length n). b) Decay to zero of the entropy production rate bias (estimated with 18 principled components (pc)-blue dots and 18 principled components (pc)-orange triangles) as a function of the trajectory length at equilibrium. c) Convergence of the entropy production rate (estimated with 18 pc-orange triangles and 18 dc-green squares) as a function of the trajectory length. The error bars in panels b,c) represent an estimate of the root-mean-square deviation between the true apparent entropy production rate and the inferred value (see Methods). The parameters of the simulations and noise level are the same as in Fig. 3 of the main text. Equilibrium is obtained by setting all temperatures equal to $T_0 = 0.05$.



Supplementary Figure 3. **Detecting the noise floor** a-b): Eigenvalues λ_i of the covariance matrix for the data \mathbf{X} (blue markers) together with the noise floor (largest eigenvalue of $\mathbf{X}_{\text{shuffled}}$ -orange line) for the two-beads model (a) and the focus-region of the 20×20 network analyzed in Fig. 3 of the main text (b). In panel (a) the noise level on the image is 10%, in panel (b) $\alpha = 0.1$. c-d): Decrease (absolute value) of the autocorrelation function of principal component coefficients after one time-step at different noise levels for the two-bead model (c) and the focus-region of the filamentous network (d). The solid line indicates the 25% level used in our criterion. Panels a,c (Panels b,d): same simulation parameters as Fig. 2 (Fig. 3) of the main text.



Supplementary Figure 4. **Inferring entropy production rates of Brownian movies with image blurring** a) Image-frames (80×80) of the analyzed patch for different values of the blurring parameter σ . b-c) Percentage of recovered entropy production rate $\hat{S}/\hat{S}_{\text{ex}}$ vs retained modes with PCA (b) and DCA (c) for varying σ . The error bars represent an estimate of the root-mean-square deviation between the true apparent entropy production rate and the inferred value (see Methods). All results have been obtained for a trajectory of 10^6 time steps, $\Delta t = 0.005$ and 80×80 frames. DCA was performed on the first 200 principle components for $\sigma = 2$, on the first 100 principle components for $\sigma = 4$, on the first 50 principle components for $\sigma = 6$, on the first 40 principle components for $\sigma = 8$, and on the first 34 principle components for $\sigma = 10$. Stochastic Force Inference was used with a first order polynomial basis for the inference of the diffusion tensor and of the force field. The noise-corrected diffusion estimator was employed.



Supplementary Figure 5. **Inferring entropy production rates of Brownian movies with imaging noise** a) Image-frames (80×80) of the analyzed patch for different values of the white gaussian noise parameter α and for shot noise. The built-in python-numpy functions for generation of normal and poisson distributed numbers are employed to generate the noise. b-c) Percentage of recovered entropy production rate $\hat{S}/\dot{S}_{\text{ex}}$ vs retained modes with PCA (b) and DCA (c) for varying α and for shot noise. The error bars represent an estimate of the root-mean-square deviation between the true apparent entropy production rate and the inferred value (see Methods). All results have been obtained for a trajectory of 10^6 time steps, $\Delta t = 0.005$ and 80×80 frames. DCA was performed on the first 200 principle components for $\alpha = 0, 0.1$ and for the shot noise case, on the first 150 principle components for $\alpha = 0.2$, on the first 100 principle components for $\alpha = 0.3$, on the first 50 principle components for $\alpha = 0.4$. Stochastic Force Inference was used with a first order polynomial basis for the inference of the diffusion tensor and the force field. The noise-corrected diffusion estimator was employed.

SUPPLEMENTARY NOTE 1
NUMERICALLY INTEGRATING THE BROWNIAN DYNAMICS

We simulate the stochastic dynamics of the two-beads model by numerically integrating the overdamped Langevin equation for the beads' displacements $\mathbf{x} = (x_1, x_2)$ (Eq. 1 main text), with $\mathbf{F}(\mathbf{x}) = \mathbf{K}\mathbf{x}$, $K_{ij} = (1 - 3\delta_{ij})k/\gamma$, $D_{ij} = \delta_{ij}k_B T_i/\gamma$. We discretize the equation of motion for the two beads using an Euler scheme with discretization step Δt . Thus, the discretized equation of motion after n time steps for the i -th bead reads: $x_i((n+1)\Delta t) = x_i(n\Delta t) + \sum_{j=1,2} K_{ij}x_j(n\Delta t)\Delta t + \sum_{j=1,2} \sqrt{2D_{ij}\Delta t}\xi_j$, where ξ_j is a random number drawn from a normal distribution with mean zero and variance one. We initialize the simulation with the beads in their rest state and we only record the positions of the beads after an equilibration time $t_{\text{eq}} = 10^5 \Delta t$ to allow the dynamics to reach steady state. The parameters for the results of Fig. 2 of the main text are: $\Delta t = 0.01$, $k = 2$, $\gamma = 1$, $k_B = 1$, $T_1 = 1$ and $0.2 < T_2 \leq 1$.

The dynamics of the 20×20 spring network is generated in a similar way. In this case, we discretize the overdamped Langevin equation for the nodes' positions \mathbf{x} with time step $\Delta t = 0.005$. For the network the elastic force acting on node i reads: $\mathbf{F}_i(\mathbf{x}) = -\sum_{j \sim i} \frac{k_{ij}}{\gamma} (\|\mathbf{x}_{i,j}(t)\| - \ell_0) \hat{\mathbf{x}}_{i,j}$, where $k_{ij} = k$ if the bond is present, $k_{ij} = 0$ if it is not, $\mathbf{x}_{i,j} = \mathbf{x}_i - \mathbf{x}_j$ is the unit vector between nodes i and j , the sum runs over nearest-neighbor nodes j of i , $k = 4$, and $\ell_0 = \gamma = k_B = 1$. In Fig. 3 of the main text, we randomly choose $1/5$ of the nodes to have higher temperature $T_{\text{hot}} = 0.25$, while the rest has a lower temperature $T_{\text{cold}} = 0.05$ ($T_{\text{hot}} = 0.05$ and $T_{\text{cold}} = 0.01$ in the low temperature case). Additionally, we randomly dilute the bonds of the network with probability $1/5$. The simulation is initialized with the network in its rest state and we wait an equilibration time $t_{\text{eq}} = 10^5 \Delta t$ before recording trajectories.

SUPPLEMENTARY NOTE 2
GENERATING THE BROWNIAN MOVIES

We first outline the procedure to generate a Brownian movie for the two-beads model (see Fig. 2 of the main text). The input consists of the numerically generated position trajectories of the two beads. We then transform the trajectories from position space to image space into pixel units (we used a 40×20 pixel grid). Specifically, we set the image pixel intensities at a given time point by centering a radially symmetric Gaussian function centered at the bead's position, with amplitude 1 and variance 9 pixels. Finally, to simulate measurement noise in a simple way, we add uncorrelated white noise sampled uniformly from $[0, a]$ ($a = 0.1$, i.e. in Fig. 2 of the main text) independently at each pixel. As in real imaging devices, pixels are saturated at intensity 1.

Next, we briefly detail how we generate a movie for a region inside a 20×20 network. The $N \times 800$ -dimensional position array (N is the number of recorded time steps), which is the output of the numerical integration of the Langevin equation, is transferred to a custom Python routine that, at each time step, directly plots all the lines connecting neighboring nodes within the selected smaller region (grey frame of Fig. 3a of the main text) onto a 80×80 pixel grid. In this routine, pixel intensities decay with the distance from each such line as a Gaussian function with amplitude 0.8 and a variance of 2 pixels. Additionally, to simulate limited optical resolution of the imaging device, we blur the images as described in Supplementary Note 6. To simulate measurement noise, we add white gaussian noise as described in Supplementary Note 7. Note, from our Brownian dynamics simulation we can compute the exact entropy production rate (in natural units with $k_B = 1$) $\dot{S}_{\text{tot}} = 786$ of the full 20×20 network. To estimate the exact entropy production rate \dot{S}_{ex} of the observed region in the Brownian movie, we assume the spatial density of entropy production rate to be approximately uniform throughout the whole 20×20 network. The exact entropy production rate for the observed region is then $\dot{S}_{\text{ex}} \approx \dot{S}_{\text{tot}} A_{\text{obs}}/A_{\text{tot}}$, where $A_{\text{tot}} = 381.5$ is the area of the full network measured in natural units, and $A_{\text{obs}} = 24.5$ the area of the observed region. From this we obtain $\dot{S}_{\text{ex}} = 786 \times 24.5/381.5 \approx 50.5$ for the network, which is the value we employ throughout the manuscript.

SUPPLEMENTARY NOTE 3
INFERRING THE DISSIPATIVE MODES: DISSIPATIVE COMPONENT ANALYSIS

The aim of Dissipative Component Analysis (DCA) is to infer a set of modes that maximize dissipation or, more precisely, the entropy production rate. This method is a principled approach only for a linear dynamical

system with constant diffusion. However, as we demonstrate in the main text, this method can be successfully employed in high-dimensional situations when dealing with image-data, when the dynamics is close to linear (close to the stable fixed points of the system). In such cases DCA can reduce the dimensionality by exploiting the non-equilibrium character of the system, as outlined below.

We consider a generic linear system described by an n -dimensional column-vector of coordinates \mathbf{y} that obeys the Langevin equation

$$\frac{d\mathbf{y}(t)}{dt} = \mathbf{K}\mathbf{y}(t) + \sqrt{2\mathbf{D}}\boldsymbol{\xi}(t), \quad (1)$$

where \mathbf{K} is the interaction matrix and \mathbf{D} the diffusion matrix. Note that \mathbf{D} and \mathbf{K} may in general not satisfy detailed balance and the system may thus be out of equilibrium.

As a preliminary step we perform principal component analysis (PCA) on data obtained simulating the time-evolution described by Eq. 1 for N time-steps: we first compute the covariance matrix $\mathbf{C} = \frac{1}{N} \sum_{t=1}^N (\mathbf{y}(t) - \langle \mathbf{y} \rangle) \cdot (\mathbf{y}^T(t) - \langle \mathbf{y} \rangle^T)$, where $\langle \mathbf{y} \rangle = \frac{1}{N} \sum_{t=1}^N \mathbf{y}(t)$. We then retain the first $m < n$ eigenvectors of \mathbf{C} (see Supplementary Note 5 for details on the truncation criteria), ordered by magnitude of the associated eigenvalues, and use them to construct the $m \times n$ transformation matrix \mathbf{E} . The time evolution of the system projected onto the PC-coordinates is then $\mathbf{y}_{\text{pca}}(t) = \mathbf{E}^T \mathbf{y}(t)$. In this basis, the covariance matrix \mathbf{C}_{pca} is diagonal with the ordered eigenvalues as diagonal entries. This preliminary step is useful for two reasons: it reduces dimensionality and it conveniently filters out measurement noise from the images. Next, we transform the data into covariance identity coordinates (cic), in which the covariance matrix is the identity. This is accomplished by $\mathbf{y}_{\text{cic}}(t) = \mathbf{C}_{\text{pca}}^{-1/2} \mathbf{E}^T \mathbf{y}(t)$.

In the next step, we focus on the non-equilibrium character of the system and compute the area-enclosing-rate matrix (AER) $\dot{\mathbf{A}}$ in CIC coordinates [1–3]:

$$\dot{A}_{\text{cic},ij} = \frac{1}{2t_{\text{tot}}} \sum_{t=1}^N [y_{\text{cic},i}(t)\Delta y_{\text{cic},j}(t) - y_{\text{cic},j}(t)\Delta y_{\text{cic},i}(t)], \quad (2)$$

where $t_{\text{tot}} = N\Delta t$ is the total simulation time and Δy_i denotes the displacement of the i -th coordinate between two successive time-steps. Each element \dot{A}_{ij} of the AER matrix corresponds to the area that the trajectory encloses on average in the plane (y_i, y_j) per unit time. This area enclosing rate quantifies broken detailed balance in the system and is zero in thermal equilibrium. Having defined the AER allows us to conveniently write the total entropy production of the system as [2, 4]:

$$\dot{S} = \text{Tr}(\dot{\mathbf{A}}_{\text{cic}} \dot{\mathbf{A}}_{\text{cic}}^T \mathbf{D}_{\text{cic}}^{-1}), \quad (3)$$

where $\mathbf{D}_{\text{cic}} := \frac{1}{2t_{\text{tot}}} \sum_t \Delta \mathbf{y}_{\text{cic}}(t) \Delta \mathbf{y}_{\text{cic}}^T(t)$. It is now key to observe that the matrix product $\dot{\mathbf{A}}_{\text{cic}} \dot{\mathbf{A}}_{\text{cic}}^T$, appearing in the expression for the entropy production rate Eq. 3, is real and symmetric and thus admits a real orthonormal basis of eigenvectors. Moreover, since $\dot{\mathbf{A}}_{\text{cic}}$ is antisymmetric, all non-zero eigenvalues of $\dot{\mathbf{A}}_{\text{cic}} \dot{\mathbf{A}}_{\text{cic}}^T$ are two-fold degenerate. Furthermore, note that the orthonormal basis of $\dot{\mathbf{A}}_{\text{cic}} \dot{\mathbf{A}}_{\text{cic}}^T$ is unique up to rotations in the two-dimensional eigenspaces that correspond to the same eigenvalue. Importantly, in these special covariance identity coordinates (scic), the total entropy production rate reads

$$\dot{S} = \sum_{i \in \text{odd}} \lambda_i [(D_{\text{scic}}^{-1})_{ii} + (D_{\text{scic}}^{-1})_{i+1, i+1}], \quad (4)$$

with λ_i being the eigenvalues of $\dot{\mathbf{A}}_{\text{cic}} \dot{\mathbf{A}}_{\text{cic}}^T$. We refer to the corresponding eigenvectors as the dissipative components.

SUPPLEMENTARY NOTE 4 DEPENDENCE OF ENTROPY PRODUCTION RATES ON THE TRAJECTORY LENGTH

The entropy production rate is a semi-positive definite quantity: at steady state $\dot{S} \geq 0$. Given finite-length data, the estimate of the entropy production rate will be biased. While this bias can be computed analytically for homogeneous diffusion coefficients [5], this may be difficult for space-dependent diffusion coefficients and in the presence of measurement noise. Given that we are here concerned with finite-size data of systems

with multiplicative noise partially corrupted by measurement noise, we use the following approach to reduce the bias of the entropy production rate and, correspondingly, to avoid overfitting: We separate our data set of length N into two independent and successive sets, a training set of length m and a test set of length $n = N - m$. The results in Fig. 3 of the main text are obtained with $m = N/10$. We first infer relevant components using the training set, and we then project the test set onto these components and infer the corresponding entropy production rate, as shown in Supplementary Figure 2a. Although entropy production rate estimates remain weakly positively biased for short trajectories, the bias approaches zero for long trajectories, as shown in Supplementary Figure 2b for the analyzed region of the 20×20 spring network with uniform temperatures (equilibrium). Note, however that our error bar estimates always intersect zero for all trajectory lengths (Supplementary Figure 2b). When the network is out of equilibrium, the entropy production rate estimates converge to non-zero values for long trajectories, as shown in

SUPPLEMENTARY NOTE 5 DIMENSIONAL REDUCTION: TRUNCATION CRITERIA

For the Brownian-movie learning procedure it is important to reduce the dimensionality of image data to a more tractable number of components. Therefore, we require criteria to decide on the maximum number of components that we consider in our analysis of the stochastic dynamics. Two main limiting effects arise due to the finite length of trajectories and measurement noise.

1) Noise floor

We start by asking what is the maximum number of components that we can distinguish from a noise floor set by the imaging noise and the finite length of the data. Our image data is a matrix \mathbf{X} of t_{tot} (total simulation time) rows and $L \times W$ (total number of pixels in a single image) columns. We first estimate the principal components — the normalized eigenvectors of the covariance matrix of image data — and sort these components according to the magnitude of the corresponding eigenvalues. To determine the noise floor, we eliminate temporal correlations in the image data by shuffling the values of \mathbf{X} separately along each of its columns [6]. What we obtain is a shuffled data set $\mathbf{X}_{\text{shuffled}}$ for which we can also compute principal components and eigenvalues. The largest eigenvalue of the covariance matrix of $\mathbf{X}_{\text{shuffled}}$ yields the noise floor. Thus, we truncate the basis of principal components to exclude components with eigenvalues below this noise floor. To illustrate this procedure, a plot of the eigenvalues for \mathbf{X} together with the noise threshold is shown in Supplementary Figure 3 a-b for the two beads model and for the filamentous network.

2) Resolution of the dynamics

Criterion 1) ensures that the components are distinguishable from imaging noise, which is a static property of the data. The Brownian-movie analysis is concerned with the dynamics. We thus want to make sure that we can resolve the dynamics of the components selected with criterion 1). This is a necessary condition to infer force and diffusion fields in image-space. A criterion for selecting components whose dynamics can be resolved using SFI is based on computing the autocorrelation function of the projection coefficients (\mathbf{c} in the main text) centered around their average value ($c_i(t) \rightarrow c_i(t) - \langle c_i \rangle$):

$$C_i(n\Delta t) = \frac{\sum_{t=1}^{N-n\Delta t} c_i(t+n\Delta t)c_i(t)}{\sum_{t=1}^N c_i^2(t)}. \quad (5)$$

We are only able to resolve the dynamics if $c_i(t)$ does not decorrelate too fast, i.e. if $C_i(n\Delta t)$ does not decay to zero in a time comparable to the time-step Δt . We therefore employ the following criterion: we only retain components for which $|C_i(\Delta t) - C_i(0)| < 0.25$. We applied criterion 2) to the two-beads data and to the network data and plot the results in Supplementary Figure 3 c-d. Criterion 2) is clearly sensitive both to the time resolution Δt and to the signal to noise ratio in the trajectories.

SUPPLEMENTARY NOTE 6
ENTROPY PRODUCTION RATE INFERENCE FOR INCREASING IMAGE-BLURRING

The imaging of a physical system will be subject to a finite resolution, which will induce image blurring. Here, we test the performance of our inference method as we increase the blurring of the object of interest in the Brownian movie, as shown in Supplementary Figure 4a. Blurring of the original image ($\sigma=0$) is obtained by applying the standard gaussian filter of the scikit-image python library. The blurring parameter σ corresponds to the standard deviation of the gaussian kernel. Our estimates of the recovered entropy production rates are affected by high levels of blurring of the structure of interest, as shown in Supplementary Figure 4b-c. Interestingly, when blurring is modest ($\sigma = 2, 4$) our method recovers more entropy production rate than without any blurring ($\sigma = 0$), possibly because the image-space dynamics is expected to become more linear with a slightly blurred system. If blurring is further increased and objects in the movie start to overlap ($\sigma > 4$), the $\widehat{S}/\widehat{S}_{\text{ex}}$ estimates start to decline. Remarkably however, both PCA and DCA still yield non-zero estimates of \widehat{S} with very strong blurring $\sigma = 10$, if a sufficient number of modes ($\gtrsim 10$) are retained. Furthermore, for this example DCA outperforms PCA, also for blurred Brownian movies.

SUPPLEMENTARY NOTE 7
ENTROPY PRODUCTION RATE INFERENCE FOR INCREASING NOISE LEVEL

In this section, we test the robustness of our entropy production inference method to increasing levels of measurement noise in the image-frames. To simulate imaging noise, we consider two different white-noise contributions: we include an intensity-dependent contribution $\mathcal{N}_{\mathcal{I}}$, and a white gaussian noise \mathcal{N}_0 , which is independent of the intensity at each pixel. Thus, the intensity of each frame $\mathcal{I}(t)$ is given by:

$$\mathcal{I}(t) = \bar{\mathcal{I}}(t) + \mathcal{N}_{\mathcal{I}}(t) + \mathcal{N}_0(t), \quad (6)$$

where $\bar{\mathcal{I}}$ is the ideal image, and the intensity-dependent white noise $\mathcal{N}_{\mathcal{I}}$ is drawn from a normal distribution of zero mean and standard deviation $\alpha\sqrt{\bar{\mathcal{I}}(t) + \mathcal{N}_0(t)}$ (negative values of $\bar{\mathcal{I}}(t) + \mathcal{N}_0(t)$ are truncated at zero), where $\mathcal{N}_0(t)$ the background white noise term drawn independently at each time step from a normal distribution of zero mean and standard deviation $\alpha/10$. Negative pixel intensities are truncated at zero. Additionally, to simulate the case of shot noise in the imaging apparatus, we also consider additive Poisson-distributed noise with a mean and variance equal to the intensity at each pixel $\bar{\mathcal{I}}(t)$.

Examples of noisy image frames are shown in Supplementary Figure 5a. The estimated entropy production rate via DCA and PCA are robust to modest levels of white gaussian noise in the image ($\alpha = 0.1, 0.2, 0.3$), as well as to shot noise, as shown in Supplementary Figure 5b-c. For $\alpha = 0.4$ we are probing the limit of our inference method (our truncation criteria allows us to perform DCA only with the first 50 principle components) and, although we are still able estimate a significant amount of entropy production, the performance decreases.

SUPPLEMENTARY NOTE 8
PROOF OF LOWER BOUND ON THE ENTROPY PRODUCTION RATE

A common problem in the inference of the entropy production rate is that we only observe a part of the system, which typically makes it impossible to infer the exact value of the total entropy production rate. However, even with hidden degrees of freedom one can still find a non-trivial lower bound to the total entropy production rate. Here we offer a proof to demonstrate this for a class of systems described by a Langevin equation with multiplicative Gaussian white noise.

Let us denote by $\mathbf{D}(\mathbf{x})$ the diffusion matrix. We split the system into observed part "o" and hidden part "h", such that the diffusion matrix has the form

$$\mathbf{D} = \begin{pmatrix} D_{oo} & D_{oh} \\ D_{ho} & D_{hh} \end{pmatrix} \quad (7)$$

Denoting by $\mathbf{v}(\mathbf{x}) = (\mathbf{v}_o(\mathbf{x}), \mathbf{v}_h(\mathbf{x}))$ the mean phase space velocity, by $\tilde{\mathbf{v}}_o(\mathbf{x}_o) = \langle \mathbf{v}_o(\mathbf{x}) | \mathbf{x}_o \rangle$ the apparent mean phase space velocity, and by $\tilde{\mathbf{D}}_{oo}(\mathbf{x}_o) = \langle \mathbf{D}_{oo}(\mathbf{x}) | \mathbf{x}_o \rangle$ the apparent diffusion matrix of the observed

subsystem, we define the apparent entropy production rate as

$$\dot{S}_{\text{app}} = \langle \tilde{\mathbf{v}}_o (\tilde{\mathbf{D}}_{oo})^{-1} \tilde{\mathbf{v}}_o \rangle \quad (8)$$

The total entropy production rate of the system is calculated as

$$\dot{S} = \langle \mathbf{v} \mathbf{D}^{-1} \mathbf{v} \rangle \quad (9)$$

We aim to show that $\dot{S}_{\text{app}} \leq \dot{S}$. The proof follows in two steps. First, given that the function $\pi(\mathbf{D}, \mathbf{v}) = \mathbf{v} \mathbf{D}^{-1} \mathbf{v}$ restricted to positive definite matrices \mathbf{D} is multivariate convex (Lemma 1), the Jensen inequality implies:

$$\dot{S}_{\text{app}} = \langle \tilde{\mathbf{v}}_o (\tilde{\mathbf{D}}_{oo})^{-1} \tilde{\mathbf{v}}_o \rangle \leq \langle \mathbf{v}_o (\mathbf{D}_{oo})^{-1} \mathbf{v}_o \rangle \quad (10)$$

Second, we demonstrate that (Lemma 2):

$$\forall \mathbf{v} \in \mathbb{R}^n \quad \mathbf{v}_o (\mathbf{D}_{oo})^{-1} \mathbf{v}_o \leq \mathbf{v} \mathbf{D}^{-1} \mathbf{v} \quad (11)$$

Put together, Lemma's 1 and 2 imply:

$$\dot{S}_{\text{app}} = \langle \tilde{\mathbf{v}}_o (\tilde{\mathbf{D}}_{oo})^{-1} \tilde{\mathbf{v}}_o \rangle \leq \langle \mathbf{v} \mathbf{D}^{-1} \mathbf{v} \rangle = \dot{S} \quad (12)$$

Proof of Lemma 1

Let $\mathbf{v} \in \mathbb{R}^n$ and $\mathbf{D} \in \mathbb{R}^{n^2}$. The function $\pi : \mathbb{R}^n \times \mathbb{R}^{n^2} \rightarrow \mathbb{R}$ is defined by $\pi(\mathbf{v}, \mathbf{D}) = \mathbf{v} \mathbf{D}^{-1} \mathbf{v} = v_\mu D_{\mu\nu}^{-1} v_\nu$, using the Einstein summation convention. Let $\mathcal{H}^\pi[\mathbf{v}, \mathbf{D}]$ denote the Hessian of π at point (\mathbf{v}, \mathbf{D}) . Let us also denote by \mathcal{S}_n the space of symmetric matrices of size $n \times n$ and by \mathcal{S}_n^+ the subset of positive definite matrices. Note that \mathcal{S}_n is a linear subspace of \mathbb{R}^{n^2} and that \mathcal{S}_n^+ is a convex set.

We need to prove that $\pi|_{\mathbb{R}^n \times \mathcal{S}_n^+}$ is a convex function. Because \mathcal{S}_n is a linear subspace of \mathbb{R}^{n^2} , it is enough to prove that at every point $(\mathbf{v}, \mathbf{D}) \in \mathbb{R}^n \times \mathcal{S}_n^+$ the Hessian $\mathcal{H}^\pi[\mathbf{v}, \mathbf{D}]$ is positive semi-definite on $\mathbb{R}^n \times \mathcal{S}_n$, that is:

$$\forall (\mathbf{v}, \mathbf{D}) \in \mathbb{R}^n \times \mathcal{S}_n^+ \quad \forall (\mathbf{w}, \mathbf{P}) \in \mathbb{R}^n \times \mathcal{S}_n \quad (\mathbf{w}, \mathbf{P}) \mathcal{H}^\pi[\mathbf{v}, \mathbf{D}] (\mathbf{w}, \mathbf{P}) \geq 0 \quad (13)$$

In order to verify this condition we first calculate the full Hessian \mathcal{H}^π defined as:

$$\mathcal{H}^\pi = \begin{pmatrix} \frac{\partial^2 \pi}{\partial \mathbf{v} \partial \mathbf{v}} & \frac{\partial^2 \pi}{\partial \mathbf{v} \partial \mathbf{D}} \\ \frac{\partial^2 \pi}{\partial \mathbf{D} \partial \mathbf{v}} & \frac{\partial^2 \pi}{\partial \mathbf{D} \partial \mathbf{D}} \end{pmatrix} := \begin{pmatrix} \mathbf{A} & \mathbf{B} \\ \mathbf{B}^\top & \mathbf{C} \end{pmatrix} \quad (14)$$

Let us calculate the first derivatives of $\pi(\mathbf{D}, \mathbf{v})$:

$$\frac{\partial \pi}{\partial v_a} = D_{a\nu}^{-1} v_\nu + D_{\nu a}^{-1} v_\nu \quad (15)$$

$$\frac{\partial \pi}{\partial D_{ij}} = -v_\mu D_{\mu i}^{-1} D_{j\nu}^{-1} v_\nu \quad (16)$$

and the elements of the Hessian:

$$A_{ab} = \frac{\partial^2 \pi}{\partial v_a \partial v_b} = 2D_{ab}^{-1} \quad (17)$$

$$B_{a,ij} = \frac{\partial^2 \pi}{\partial v_a \partial D_{ij}} = -[D_{ai}^{-1} D_{j\nu}^{-1} + D_{\nu i}^{-1} D_{ja}^{-1}] v_\nu \quad (18)$$

$$C_{ij,kl} = \frac{\partial^2 \pi}{\partial D_{ij} \partial D_{kl}} = v_\mu v_\nu [D_{\mu k}^{-1} D_{li}^{-1} D_{j\nu}^{-1} + D_{\mu i}^{-1} D_{jk}^{-1} D_{l\nu}^{-1}] \quad (19)$$

We can now proceed by verifying the condition expressed in Eq. (13).

$$\begin{aligned}
(\mathbf{w}, \mathbf{P})\mathcal{H}^\pi[\mathbf{v}, \mathbf{D}](\mathbf{w}, \mathbf{P}) &= 2w_a D_{ab}^{-1} w_b - 2P_{ij} w_a [D_{ai}^{-1} D_{j\nu}^{-1} + D_{\nu i}^{-1} D_{ja}^{-1}] v_\nu \\
&\quad + P_{ij} P_{kl} v_\mu v_\nu [D_{\mu k}^{-1} D_{li}^{-1} D_{j\nu}^{-1} + D_{\mu i}^{-1} D_{jk}^{-1} D_{l\nu}^{-1}]
\end{aligned} \tag{20}$$

$$\begin{aligned}
&= 2\mathbf{w}\mathbf{D}^{-1}\mathbf{w} - 2\mathbf{w}\mathbf{D}^{-1}\mathbf{P}\mathbf{D}^{-1}\mathbf{v} - 2\mathbf{w}\mathbf{D}^{-1}\mathbf{P}^\top\mathbf{D}^{-1}\mathbf{v} \\
&\quad + 2\mathbf{v}\mathbf{D}^{-1}\mathbf{P}\mathbf{D}^{-1}\mathbf{P}\mathbf{D}^{-1}\mathbf{v}
\end{aligned} \tag{21}$$

Using that $\mathbf{P} \in \mathcal{S}_n$, meaning that we only consider directions within the subspace of symmetric matrices, and renaming $\mathbf{x} := \mathbf{P}\mathbf{D}^{-1}\mathbf{v}$, we simplify the above expression to

$$2[\mathbf{w}\mathbf{D}^{-1}\mathbf{w} - 2\mathbf{w}\mathbf{D}^{-1}\mathbf{x} + \mathbf{x}\mathbf{D}^{-1}\mathbf{x}] = 2(\mathbf{w} - \mathbf{x})\mathbf{D}^{-1}(\mathbf{w} - \mathbf{x}) \geq 0 \tag{22}$$

which holds due to \mathbf{D} being positive definite. \square

Proof of Lemma 2

First, let us note that the inequality $\mathbf{v}_o(\mathbf{D}_{oo})^{-1}\mathbf{v}_o \leq \mathbf{v}\mathbf{D}^{-1}\mathbf{v} \forall \mathbf{v} \in \mathbb{R}^n$ is equivalent to

$$\begin{pmatrix} (\mathbf{D}^{-1})_{oo} - (\mathbf{D}_{oo})^{-1} & (\mathbf{D}^{-1})_{oh} \\ (\mathbf{D}^{-1})_{ho} & (\mathbf{D}^{-1})_{hh} \end{pmatrix} \succeq 0 \tag{23}$$

To simplify the notation let us introduce $\mathbf{Q} := \mathbf{D}^{-1}$. Since \mathbf{D} is positive definite, we also have $\mathbf{Q} \succ 0$ and in particular $\mathbf{Q}_{hh} \succ 0$. Rewriting the above condition in terms of \mathbf{Q} we get:

$$\begin{pmatrix} \mathbf{Q}_{oo} - [(\mathbf{Q}^{-1})_{oo}]^{-1} & \mathbf{Q}_{oh} \\ \mathbf{Q}_{ho} & \mathbf{Q}_{hh} \end{pmatrix} \succeq 0 \tag{24}$$

Using Schur's decomposition, we can write $(\mathbf{Q}^{-1})_{oo} = (\mathbf{Q}_{oo} - \mathbf{Q}_{oh}(\mathbf{Q}_{hh})^{-1}\mathbf{Q}_{ho})^{-1}$. Substituting this in the equation above we get:

$$\begin{pmatrix} \mathbf{Q}_{oh}(\mathbf{Q}_{hh})^{-1}\mathbf{Q}_{ho} & \mathbf{Q}_{oh} \\ \mathbf{Q}_{ho} & \mathbf{Q}_{hh} \end{pmatrix} \succeq 0 \tag{25}$$

To check the positive semi-definiteness of this matrix we can apply it to an arbitrary vector $\mathbf{v} = (\mathbf{v}_o, \mathbf{v}_h)$. The matrix in Eq. (25) is positive semi-definite if and only if

$$\mathbf{v}_o \mathbf{Q}_{oh} (\mathbf{Q}_{hh})^{-1} \mathbf{Q}_{ho} \mathbf{v}_o + 2\mathbf{v}_o \mathbf{Q}_{oh} \mathbf{v}_h + \mathbf{v}_h \mathbf{Q}_{hh} \mathbf{v}_h \geq 0 \tag{26}$$

To simplify this expression let us substitute $\mathbf{w}_h = \mathbf{Q}_{ho} \mathbf{v}_o$. This gives us:

$$\mathbf{w}_h (\mathbf{Q}_{hh})^{-1} \mathbf{w}_h + 2\mathbf{w}_h \cdot \mathbf{v}_h + \mathbf{v}_h \mathbf{Q}_{hh} \mathbf{v}_h \geq 0 \tag{27}$$

Finally we substitute $\mathbf{w}_h = \mathbf{Q}_{hh} \mathbf{x}$, $\mathbf{v}_h = \mathbf{y}$, to get:

$$\mathbf{x} \mathbf{Q}_{hh} \mathbf{x} + 2\mathbf{x} \mathbf{Q}_{hh} \mathbf{y} + \mathbf{y} \mathbf{Q}_{hh} \mathbf{y} \geq 0 \iff \tag{28}$$

$$(\mathbf{x} + \mathbf{y}) \mathbf{Q}_{hh} (\mathbf{x} + \mathbf{y}) \geq 0 \tag{29}$$

which holds, due to \mathbf{Q}_{hh} being positive definite. \square

SUPPLEMENTARY REFERENCES

-
- [1] Ghanta, A., Neu, J. C. & Teitworth, S. Fluctuation loops in noise-driven linear dynamical systems. *Physical Review E* **95**, 032128 (2017).
 - [2] Mura, F., Gradziuk, G. & Broedersz, C. P. Nonequilibrium Scaling Behavior in Driven Soft Biological Assemblies. *Physical Review Letters* **121**, 038002 (2018).
 - [3] Gonzalez, J. P., Neu, J. C. & Teitworth, S. W. Experimental metrics for detection of detailed balance violation. *Physical Review E* **99**, 022143 (2019).
 - [4] Gradziuk, G., Mura, F. & Broedersz, C. P. Scaling behavior of nonequilibrium measures in internally driven elastic assemblies. *Physical Review E* **99**, 052406 (2019).
 - [5] Frishman, A. & Ronceray, P. Learning force fields from stochastic trajectories. *Phys. Rev. X* **10**, 021009 (2020).
 - [6] Berman, G. J., Choi, D. M., Bialek, W. & Shaevitz, J. W. Mapping the stereotyped behaviour of freely moving fruit flies. *Journal of The Royal Society Interface* **11**, 20140672 (2014).

Acknowledgements

It's the first time in a long time that I'm really happy about there being so much left to write!

Chase, many centuries ago, when I had to find a master project to work on, I somehow didn't imagine joining any other group. Actually, it quickly turned out that I didn't imagine joining your group either, or at least I didn't imagine it correctly. From the very first day you ruined my idea of what a thesis supervisor is. You always had time and endless reserves of truly contagious enthusiasm. I really enjoyed invading your office space to share fun facts, as well as all the laughter-filled blackboard discussions. I also never really imagined doing a PhD at all, so me being here is all your fault. Thank You! :)

Fede, I'm really thankful for how you welcomed me in the group. You made the work pure fun, so that even at the very beginning, when I had no idea what to do, it didn't seem like a problem. I only wish you hadn't graduated so quickly! Btw. when are we meeting for Catan?

Fede, thanks for showing me the office life and educating me on the Brain Salad Surgery, Watermelon In Easter Hay, the New Trolls and other crucial topics. I really appreciated your determination to learn polish (some part of it). This made me feel at home. When are you making fritelle again?

David, la pierdolatsch! Jesteś piękna! Of course you also showed me the office life! I'm still searching for the missing messages, I'll make sure to find them before leaving the office for good. Tiramisu!

Thanks Tom, I wish we could have shared the office for more time! Thanks to Gabriel and Steven for showing me the other side of a master project and especially to Gabriel for teaching me to how pronounce my name correctly. Thanks to Joris for taking me on board when I couldn't look at my own stuff anymore. Thanks Pierre, the group's satellite – it was great to have you around from time to time. Thanks Isabella for being the most kind and modest being. Thanks Felix for the jokes, Salbei, discussions about Münzen and above all loads of cookies and wisdom every Thursday! Borislav, we should meet up for some more singing. Thanks to all Broedersz and Frey group for the discussions and the APS tours and Christmas parties.

Nothing teaches you more than when you have to teach yourself. Thanks to Chase, Erwin, all the co-tutors and students, many of which stayed around for much longer, at least two are in Amsterdam now. I really enjoyed our tutorials, I hope you also keep them

in good memory.

Huge thanks to you, whoever you are, that made Antholz possible, be it by driving a car, booking stuff, preparing your presentation, or organising a hike. Thanks to Frau Brunner for taking good care of us. If it were just for Antholz, still it would be worth doing a PhD.

Thanks to all the Italians and generalised Italians that I've had around me, who made the life in Munich great. Special thanks to Fra for hosting me at the true capital of Lazio, Fra for crushing the ASP problems, Harry and Charlotte for bringing me to Welcome, Fede for advanced algebraic topology discussions and Ceci for teaching me the time uncertainty principle.

Thank you Siddhant for adding lots of spice, flavour and smell to my PhD experience and of course for showing me the truth. Thank you Pablito, mostly for leading me to my greatest finding.

Od Grzegorza ukłony i różne wyrazy dla szanownego grona doktorów z Roboty, ze szczególnym uwzględnieniem doktora inżyniera, niezrównanego kompana do narzekania i już on wie czego. Gracias a Rosario Esperanza y a Francisco José por hospedarme en Vélez y por el alquiler del despacho.

Dziękuję mojej rodzinie za to, że zawsze we mnie wierzy i wspiera, nawet w tak nieprzychylnych pomysłach jak robienie doktoratu. Elo elo 3 2 0 siora!

Gracias kochi por tu apoyo, nadie sabe mejor que tú lo que me ha costado. Eres la mejor! :*